

Miniature Wireless Neural Implants

Mohammad Meraj Ghanbari

Electrical Engineering and Computer Sciences
University of California, Berkeley

Technical Report No. UCB/EECS-2024-195

<http://www2.eecs.berkeley.edu/Pubs/TechRpts/2024/EECS-2024-195.html>

December 1, 2024



Copyright © 2024, by the author(s).
All rights reserved.

Permission to make digital or hard copies of all or part of this work for personal or classroom use is granted without fee provided that copies are not made or distributed for profit or commercial advantage and that copies bear this notice and the full citation on the first page. To copy otherwise, to republish, to post on servers or to redistribute to lists, requires prior specific permission.

Miniature Wireless Neural Implants

by

Mohammad Meraj Ghanbari

A dissertation submitted in partial satisfaction of the

requirements for the degree of

Doctor of Philosophy

in

Engineering – Electrical Engineering and Computer Sciences

in the

Graduate Division

of the

University of California, Berkeley

Committee in charge:

Associate Professor Rikky Muller, Chair

Professor Michel M. Maharbiz

Associate Professor Evan Miller

Fall 2022

Miniature Wireless Neural Implants

Copyright 2022
by
Mohammad Meraj Ghanbari

Abstract

Miniature Wireless Neural Implants

by

Mohammad Meraj Ghanbari

Doctor of Philosophy in Engineering – Electrical Engineering and Computer Sciences

University of California, Berkeley

Associate Professor Rikky Muller, Chair

In this work, we present miniature wireless neural implants capable of recording and transmitting neural activity from deeply-seated peripheral nerves. In order to reduce implant-induced trauma and the likelihood of post-implant infection and to enable minimally-invasive implantation techniques, such as injection, the primary design goals of these implants are miniaturization and wireless operation in a multi-implant setting.

These implants are comprised of an integrated circuit and a piezoceramic (used as an acoustic antenna). The piezoceramic, piezo, dominates the overall volume of the implant. Therefore, here, we provide a systematic design approach for the geometry of the implant piezo and operation frequency to minimize the overall volume of the implant.

These miniature implants harvest energy from ultrasound wavelets launched by an external interrogator. They also communicate data through the same ultrasound link using a technique known as backscattering. A critical design aspect of an ultrasonic backscatter communication link is the response of the piezo acoustic reflection coefficient Γ with respect to the variable shunt impedance, Z_E , of the implant uplink modulator. Due to the complexity of the piezo governing equations and multi-domain, electro-acoustical nature of the piezo, $\Gamma(Z_E)$ has often been characterized numerically and the implant uplink modulator has been designed empirically resulting in sub-optimal performance in terms of data rate and linearity. Here, we present experimentally validated closed-form expressions for $\Gamma(Z_E)$ under various boundary conditions. We conclude that Γ is approximately linearly proportional to the voltage across the piezo when operating at the series or parallel resonant frequencies. We further demonstrate two linear uplink backscatter modulators and incorporate them into the active rectifier of the implant ICs. One of these modulators perform end-to-end linear analog modulation, while the other implements quasi-digital m-level ASK modulator to provide immunity to carrier noise while achieving a substantially higher data rate (by a factor of $\log_2(m)$) relative to the commonly-used on-off keying modulation.

Moreover, a key aspect of the wireless communication channel for these miniature neural implants is the multiple-access feature of the link. Therefore, we demonstrate integration of code-division and time-division multiple-access (CDMA and TDMA) into the uplink commu-

nication protocols of these implants. These protocols allow communications with a network of these implants using a single-element low-cost external interrogator. The functionality of both of the proposed implants are experimentally verified.

Dedicated to my mother, Nosrat Bashardanesh.

Contents

Contents	ii
List of Figures	iv
List of Tables	xii
1 Miniature Wireless Implants	1
1.1 Introduction	1
1.2 Neural Implants	3
1.3 Challenges	5
1.4 Thesis Contribution	8
1.5 Thesis Organization	9
2 Ultrasonic Wireless Power Transmission	11
2.1 Background on Piezoelectricity	11
2.2 Acoustic Wireless Power Transmission	18
2.3 Power Receiver Design	24
2.4 Design Case Study	28
2.5 Summary	32
3 Ultrasonic Wireless Data Transmission	34
3.1 Power+Data Transmission Protocols	36
3.2 Channel Equivalent Circuit Model	42
3.3 Simplified Implant Piezo Model	48
3.4 Backscatter Bandwidth	51
3.5 Measurement and Model Verification	53
3.6 Summary	56
4 A mm-Scale Free-Floating Neural Recording Implant with Linear AM CDMA Uplink	58
4.1 Introduction	58
4.2 CDMA Pulse-Echo Protocol	59
4.3 Linear Echo Modulation	61

4.4	Hardware Implementation	62
4.5	Hardware Verification	69
4.6	Summary	77
5	High Throughput Ultrasonic Multi-implant Readout Using a Machine-Learning Assisted CDMA Receiver	79
5.1	Introduction	79
5.2	ML-Assisted CDMA Decoder	79
5.3	Experimental Results	81
5.4	Summary	84
6	A mm-Scale Free-Floating Neural Recording Implant with M-level ASK TDMA Uplink	86
6.1	Introduction	86
6.2	Hardware Implementation	89
6.3	Experimental Verification	113
6.4	Summary	127
7	Summary and Future Research Directions	131
7.1	Summary	131
7.2	Future Research Directions	132
	Bibliography	136
	Glossary	143

List of Figures

1.1	Existing trade-offs between four commonly used neural recording methods. ^b The lifetime metric for the fMRI method cannot be fairly compared to that of the other methods since fMRI takes only short ‘snapshots’ of the neural activity. Such short recordings, however, can be taken over many years and thus we consider the lifetime of fMRI to be similar to that of EEG.	2
1.2	Example electrodes. Adapted from (a) Utah Microelectrode Arrays [59], (b) Neuralink’s ultrathin polymer threads [57], (c) syringe-inserted foldable meshes [86].	3
1.3	Recently published miniature neural implants. From left to right adapted from [43], [33], [72], [24], [13], [44].	4
1.4	Examples of high-channel-count neural interfaces. From left to right adapted from Neuralink [57], Neuropixels 2.0 by IMEC [76] and Argo by Paradromics [69].	5
1.5	Concept of active prosthetic arm control using a distributed network of ultrasonically powered peripheral nerve implants.	7
2.1	(a) piezo as a three-port network, and (b) Redwood’s equivalent circuit model. .	15
2.2	(a) Electrical impedance of a lossless unloaded piezo around its fundamental resonance mode. The series f_s and parallel f_p resonant frequencies are defined where the imaginary component of the impedance becomes zero. (b) The electrical impedance of the same piezo with non-zero acoustic loading.	16
2.3	Ratio of f_s/f_p for the TE resonance mode as a function of (piezo coupling constant) ²	17
2.4	Concept of acoustic wireless power transmission. The flow of energy is shown by the arrow. The external transducer converts the electrical energy supplied by V_s to acoustic energy which travels through the acoustic medium and finally converted back to electrical energy and delivered to the implant modeled by R_L . $Z_{B,EXTERNAL}$ and $Z_{B,IMPLANT}$ are the acoustic termination impedances of the back face of the external and implant piezos, respectively.	19

2.5	(a) Radiation profile of an unfocused single-element external transducer with aperture D . The generated beam has an inherent focal area at one Rayleigh distance away from the transducer. FEM simulated axial pressure intensity (normalized to that at the Rayleigh distance) profile and the lateral intensity at the Rayleigh distance for $D = 6$ mm operating at 3 MHz. Rayleigh distance and far-field divergence angle θ_d (b) for $D = 6$ mm at various frequencies and (c) at 3 MHz and various apertures.	21
2.6	Comparison of unfocused, spherically and cylindrically focused external transducers.	22
2.7	3D simulated intensity profiles (with equal-intensity isosurfaces) of (a) an unfocused, and (b) a cylindrically focused external transducer with focal depth of 9 mm. The diameter of both transducers is 6 mm. Operation frequency is 3 MHz.	23
2.8	Comparison of simulated axial and lateral intensity profiles of an unfocused and cylindrically focused external transducers designed with various focal depths (4 mm, 9 mm, 14 mm). The diameter of all transducers is 6 mm. Operation frequency is 3 MHz. All intensities are normalized to the far-field peak intensity of the unfocused transducer.	24
2.9	(a) Implant piezo geometry and its Thevenin equivalent circuit at resonance. Finite Element Simulation (FEM) results of the (b) series resonant frequency, (c) parallel resonant frequency, (d) resistance and (e) open circuit voltage with an incident pressure intensity of 720 mW/cm^2 for various piezo thicknesses and aspect ratios. (f) Simulated V_{Th} and R_{Th} values in (d) and (e) were used to calculate the available power per unit volume of the implant piezo (volumetric efficiency) at f_s and f_p . (g) Relative available power at f_s and f_p and its correlation with piezo resonant modes: Longitudinal Expander (LE) and Width Expander (WE) resonant modes determined using the effective electromechanical coupling factor of the piezo, k_{eff} . (h) A design example when operating at f_s with a relatively small impedance mismatch results in a smaller piezo volume compared to operating at f_p with a perfect piezo-load impedance matching. (i) A design example when operating at f_s with a relatively large impedance mismatch results in a larger piezo volume compared to operating at f_p with a perfect piezo-load impedance matching. Note: In all plots, each aspect ratio is shown using a unique marker (<i>e.g.</i> , Δ for $AR = 1/2$)	25
2.10	The generic ultrasonic implant model.	29
2.11	The piezo (a) open-circuit voltage, (b) impedance, and (c) calculated maximum available power with the unity aspect ratio (AR) at 7200 W/m^2 of local ultrasound intensity. The estimated maximum available power at the neuron dimensions is significant. (d) Designed piezo geometries and a comparison to prior art.	30
2.12	Axial intensity of an unfocused radial external transducer with a Rayleigh distance of 20 mm.	32
3.1	A single-piezo ultrasonic biosensing implant with backscatter uplink modulator.	35

3.2	Previously reported power and uplink protocols for (a) continuous power and data communication with a dual-piezo implant. Single-piezo implant protocols include (b) active drive: sequential power harvesting and uplink data transmission, and (c) pulse-echo scheme: simultaneous power harvesting and uplink echo modulation.	37
3.3	Multiple access protocols using (a) FDMA on main carrier, (b) FDMA on sub-carriers, (c) CDMA on subcarriers.	39
3.4	An example of a TDMA protocol for a pulse-echo channel with two implants	40
3.5	(top) A typical ultrasound pulse with analog echo modulation (AM); (bottom) comparison between Analog and Digital echo modulation schemes and their corresponding bounce diagrams	41
3.6	(a) Typical backscatter communication channel, and (b) timing diagram of each interrogation event.	42
3.7	FEM simulation of channel path loss. (a) Simulation setup. Simulated (b) forward, (c) backward, and (d) round-trip path loss for various implant thicknesses (with aspect ratio of 1) and TX radii. (e) Optimal TX radius and relative contribution of spreading and attenuation components of the path loss.	44
3.8	(a) end-to-end equivalent circuit model of channel. Simulated (b) transient response of channel (c) received echo signal. Received echo vs. Z_E at (d) the series resonant and (e) parallel resonant frequencies.	46
3.9	Proposed piezo electro-acoustical model (a) coupling the Thevenin equivalent circuit model of the piezo to its acoustic reflection coefficient. Expressions for reflection coefficient at parallel and series resonant frequencies for two common backing boundary conditions are listed in (b)-(e).	48
3.10	(a) Non-idealities that degrade $\Delta\Gamma_{Max}$. FEM simulation results show (b) decreasing the piezo AR initially enhances $\Delta\Gamma_{Max}$ as the piezo resonance mode changes from width expander (WE) to longitudinal expander (LE), but for $AR < 1$, $\Delta\Gamma_{Max}$ starts dropping due to diffraction. The simulated fractional bandwidth of the piezo follows a similar pattern. (c) Simulated available power and backscatter bandwidth for a piezo with an AR of unity.	51
3.11	(a) 4-level ASK backscatter modulation with non-equidistant echo levels due to a suboptimal selection of linearly-spaced modulating Z'_E . (b) optimal 4-level ASK backscatter modulation with equidistant echo levels with nonlinearly-spaced modulating Z_E . (c) Numerically simulated bit error rates for (a), (b) and OOK; 1.5 MHz carrier frequency is used.	52
3.12	Experimental setup.	54
3.13	Measured and simulated piezo impedance.	55
3.14	(a) simulated and (b) measured frequency response of the modulation index of the piezo for resistive. (c) simulated and (d) measured frequency response of the modulation index of the piezo for capacitive terminations. Comparison of simulated, measured and predicted Γ_{norm} at (e) f_s and (f) f_p for resistive loads. Comparison of simulated, measured and predicted Γ_{norm} at (g) f_s and (h) f_p for capacitive loads.	56

4.1	Untethered neural recording from deep regions of the peripheral/central nervous system using ultrasonically powered neural recording implant.	59
4.2	Various ultrasound operating protocols: (a) continuous mode operation where OOK is used for uplink data transmission (b) pulse-echo mode with classic AM uplink data transmission; (c) pulse-echo mode with simultaneous interrogation of two implants using orthogonally encoded AM.	60
4.3	Conceptual Γ - R_E curve showing significant nonlinearity.	62
4.4	Simplified block diagram of the IC.	63
4.5	(a) Schematic diagram of power management blocks (b) chip-level timing diagram shown with 2 subcarrier cycles.	64
4.6	LNA topology and timing diagram.	65
4.7	(a) Fully complimentary OTA topology used in the LNA (b) power-gated charger of the input terminals of the OTA.	66
4.8	Linear gm-cell architecture.	67
4.9	(a) Conceptual echo amplitude modulation using synchronous up-conversion current mixer (b) reusing active rectifier as synchronous mixer (c) nonlinearity induced by the rectifying modulator.	68
4.10	(a) Fully packaged implant micrograph (b) IC micrograph (c) dimensions of the fully packaged implant (d) power consumption breakdown.	70
4.11	Measured ENIG electrode impedance (mean of measurements for 6 electrode pairs); (inset) single electrode model.	71
4.12	(a) benchtop measurement setup, (b) single-mote <i>in vitro</i> measurement setup . .	71
4.13	Benchtop measurement result showing amplitude modulation of the input voltage of the rectifier for (a) five consecutive sample pulses for a 313 Hz, 20 mV _{PP} input signal (b) first interrogation event where startup time and the subcarrier signal are visible (c) the demodulated input-referred signal.	72
4.14	(a) The static input-output (defined as the input voltage of the rectifier) linearity curve of the chip. (b) power spectral density of the reconstructed signal shown in Figure 4.13.	73
4.15	Noise measurement. (a) the noise spectral density of the carrier alone and that obtained from the chip: noise is dominated by the carrier noise. (b) effect of chopping in reducing the low-frequency noise contents of the main carrier. . . .	74
4.16	Single-mote <i>in vitro</i> measurement results. Implant is interrogated at 8 kS/s at 5 cm of depth (a-b) two received echo signals each translating into a sample shown in (e), (c) their corresponding AM demodulation (d) common-mode rejection of received echoes (e) reconstructed 313 Hz signal (f) SNR of received signal (noise dominated by carrier noise) and (g) measured SNR and equivalent uplink data rate vs. input range of the implant.	75
4.17	(a) 800 ms stream of pre-recorded neural signal recorded (at 10 kS/s) and wirelessly transmitted by the mote at 45 mm of depth. Comparison of reconstructed data between (b) single and (c) multiple action potential events.	76

4.18	Measured piezo-interrogator relative misalignment characterization in (a) vertical (b) horizontal y-axis (c) horizontal x-axis dimensions	76
4.19	Simultaneous power up and data transmission of two implants at depth of 50 mm and separation of 2 mm. (a): <i>in vitro</i> measurement setup. (b): reconstructed signals at the external interrogator. (c-d) spectra of the reconstructed signals (e-f) measured SNDR and SFDR of each channel versus vertical misalignment between the notes	77
5.1	Illustration of bit expansion and resulted Inter Symbol Interference (ISI): transmission of a ‘101’ for various cycles/bit configurations.	80
5.2	Block diagram of machine-learning assisted CDMA decoder.	81
5.3	(a) Setup for automated data collection and (b) generation	82
5.4	Simultaneous data transmission of 4 implants using OOK CDMA modulation. Measured waveforms received by external transducer for data rates of (a) 56 kbps and (b) 392 kbps.	83
5.5	(a) Measured bit error rate (BER) vs. total data rate of the channel. (b) Measured bit error rate (BER) vs. received signal-to-noise (SNR) ratios for various total channel data rates.	84
6.1	The ulnar and median nerves are centimeters apart around the wrist and each control the movement of a particular finger. Concept of distributed miniature wireless neural implants shown in the right. Each implant is ultrasonically powered and communicated and uses a transverse intrafascicular multichannel electrode (TIME) for enhanced nerve selectivity.	87
6.2	Contours show the maximum achievable data rate as a function of cycles/symbol and carrier frequency using OOK modulation in a pulse-echo protocol. Performance of prior art with OOK uplink using pulse-echo and continuous-time protocols.	88
6.3	Simplified block diagram of the implant system, comprising a bulk piezo for power harvesting and data communications, an external capacitor for energy storage and the DustNet IC.	90
6.4	Simplified timing diagram of the proposed protocol when two implants are in operation is shown in top. The two implants are assumed to have the same distance to the external interrogator. Critical signals of each implant are also illustrated. The pattern of the envelope of mode 0 and mode 1 pulses are also shown.	92
6.5	Minimum required C_{store} for a given total chip current at various depths of operation. The open-circuit piezo voltage and its series resistance are assumed to be 2 V and 2 k Ω , respectively. Target $VRECT_{min}$ is 1.2 V.	94

6.6	(a) OOK echo modulation using two distant (open/short) piezo electrical terminations. (b) Linearly spaced piezo termination results in heavily overlapped echo levels (and high BER) due to the inherent nonlinearity of Γ vs. Z_E . (c) Equidistant echo levels can be achieved by nonlinearly-spaced Z_E values. Note that the x-axis in these plots is log-scale, and operation at the series resonance frequency is assumed.	96
6.7	(a) ASK4 linear echo modulation shown conceptually, i.e., $\Gamma \propto VPZ \propto I_{DATA}$ (b) Simplified circuit diagram of the current-mode echo modulator consisting of two matched iDACs and a pair of cross-coupled NMOS clamp. Signal flow is shown from the input of the SAR ADC to the piezo terminals.	97
6.8	(a) Simplified circuit diagram of the proposed modulating active rectifier and (b) its common-gate high-speed comparators. The circuit has two modes: active rectifier (Figure 6.9) and linear echo (piezo load) modulator (Figure 6.10). . . .	98
6.9	(a) During active rectification, the load modulating devices (M_5 and M_6) are disabled and the piezo current is properly steered through the PMOS pass transistors, M_1 and M_2 , in both the (b) negative and (c) positive half cycles of the harvested piezo voltage to charge C_{store}	99
6.10	(a) For echo modulation, the non-inverting outputs of the comparators are forced to a high-state, disabling both the PMOS pass transistors, M_1 and M_2 , disconnecting C_{store} and protecting its stored charge from the large modulating current drawn from the piezo terminals. Quasi digital data in terms of current I_{DATA} is drawn from the piezo causing a linear voltage drop in both (b) negative and (c) positive half cycles of the piezo effectively modulating the envelope of the echo.	99
6.11	Ultrasound ON detector. Control signals v_p^- and v_n^- are the inverting output terminal of the high-speed rectifier comparators.	100
6.12	Downlink demodulator block diagram. The received VPZ carries both data and clock. The extracted (and hence synchronous) main clock is divided to generate the symbol sampling clock.	101
6.13	Clock extraction from VPZ using a high-speed comparator with a built-in hysteresis.	102
6.14	Simplified circuit diagram of the envelope detector.	103
6.15	Simplified circuit diagram of PTAT reference generator and the POR.	104
6.16	Simplified circuit diagram of the classic low-dropout regulator. The loop amplifier is modelled by a G_m -cell and its parasitic output load R_a and C_a . Load is modelled by a constant current sink I_L	105
6.17	(left) Simplified circuit diagram of the common-gate compensated low-dropout regulator. (right) The root-locus of the loop-gain for decreasing I_L is shown in (a). The bode diagram of the loop-gain for (b) relatively large I_L and (d) relatively small I_L . The bode-diagram of the output impedance is shown in (c).	106
6.18	The circuit implementation of the CG-compensated LDO.	108

6.19	(a) Simplified block diagram of the analog front-end. (b) timing diagram of critical switches. (c) Simplified circuit diagram of the input biasing network. Simplified circuit diagram of the (d) first and (e) second G_m cells.	109
6.20	Transfer function of the integrating sampler with the integration period of T_s has a -3dB bandwidth at $\approx 0.44/T_s$, and notches at integer multiples of $1/T_s$	109
6.21	(a) Constant- g_m biasing of G_{m0} , and (b) implementation of the local oscillator to achieve PVT tolerant open-loop gain.	110
6.22	Simplified circuit model of the integrating sampler using (a) a single-stage and (b) a two-stage integrator.	112
6.23	Layout of the prototype chip, and the breakdown of the simulated current consumption of the subblocks.	114
6.24	Simplified block diagram of the benchtop measurement setup.	114
6.25	<i>VRECT</i> , analog supply and the 0.55 V supply during start-up. <i>VPZ</i> is initiated at time 0.	116
6.26	Mode 0 operation with inter-pulse gaps during which the chip only relies on charge stored on C_{store} . The slope of the linear voltage drop of <i>VRECT</i> determines the total current consumption of the chip that is $5.6 \mu\text{A}$	117
6.27	Mode 0 pulse showing various states of the internal FSM showing the chip locking into symbol width and performing demodulation.	118
6.28	(a) A mode 0 pulse. (b) The close-up of the uplink segment of the pulse where the uplink header and payload are identifiable. The uplink modulation index is set to 5% in this pulse. The same uplink segment when the chip is programmed through the downlink segment of the pulse to use (c) 25% and (d) 50% uplink modulation index.	119
6.29	An uplink segment is shown with various symbol widths. Possible choices are (a) 4 cycles/symbol, (b) 8 cycles/symbol, (c) 12 cycles/symbol, and (d) 16 cycles/symbol.	120
6.30	Sample Mode 1 pulses using (a) ASK2, (b) ASK4, (c) ASK8 and (d) ASK16 in the uplink segment.	121
6.31	Mode 1 uplink transmitting LFSR data. (top) Histogram of the ASK2 levels. (middle) The reconstructed LFSR data and (bottom) the golden LFSR data.	122
6.32	Mode 1 uplink transmitting LFSR data. (top) Histogram of the ASK4 levels. (middle) The reconstructed LFSR data and (bottom) the golden LFSR data.	123
6.33	Mode 1 uplink transmitting LFSR data. (top) Histogram of the ASK8 levels. (middle) The reconstructed LFSR data and (bottom) the golden LFSR data.	124
6.34	Mode 1 uplink transmitting LFSR data. (top) Histogram of the ASK16 levels. (middle) The reconstructed LFSR data and (bottom) the golden LFSR data.	125
6.35	Functional verification of TDMA using a single test chip. The chip is programmed with (top) $N_{implants} = 1$, (middle) (top) $N_{implants} = 2$, and (bottom) $N_{implants} = 4$. For each configuration, the implant correctly decides when to activate its uplink modulator.	126

6.36	(a) A 10 mV_{pp} , 2 Hz sine wave recorded, transmitted and reconstructed. (b) the spectrum of the reconstructed sine wave. (c) Measured input-referred noise spectral density of the implant. Measured input-referred integrated noise is $24\text{ }\mu\text{V}_{rms}$.	128
6.37	Measured linearity of the combined AFE and ADC (a) full-scale input ramp, and (b) its histogram (the first and last bins are removed for better visibility). (c) INL and DNL.	129
7.1	A conceptual diagram for the continuous pulse-echo communication scheme.	133
7.2	A conceptual diagram of a three-piezo implant to reduce sensitivity to angular misalignment.	134
7.3	Concept of closed-loop neuromodulation using miniature wireless implants.	135

List of Tables

4.1	Performance Comparison Table	78
5.1	Comparison of Recently Published Ultrasound Links	85
6.1	Summary of ASK modulation Configurations	97

Acknowledgments

This dissertation is the culmination of over six years of research, development and collaboration. In this effort, I received continuous support from individuals who not only helped me shape the contents of this dissertation but also profoundly influenced the contents of my character. I truly believe I am a better version of myself today because of these individuals and I am forever indebted to all of them. In particular, I am grateful to Prof. Rikky Muller, my PhD adviser, for her whole-hearted support throughout the course of my PhD. I appreciate her empowering and transformational advising style that fosters creativity that I believe is indispensable to research. I also appreciate Rikky's invaluable input and technical advice that played a major role in sculpting the body of work presented in this dissertation. This work would not have been made possible without her dedication and support. I am grateful to my qualification exam committee, Prof. Michel Maharbiz, Prof. Evan Miller and Prof. Mekhail Anwar for eagerly listening to my talk and providing insightful feedback regarding the direction of this research. I am thankful to Prof. Maharbiz and Prof. Miller for reading this dissertation as well.

During the first two years of my PhD, I closely worked with Dr. Ben Johnson on the StimDust project. I am very thankful to Ben for raising some fundamental questions about the underlying mechanisms of ultrasound backscattering and wireless power transmission the answer to which laid the foundations for the ultrasonic implants developed in this work.

I cannot thank David Piech enough for all the time he selflessly devoted to help me with the ultrasound measurements of the first chip I taped out. I still vividly remember the two all-nighters we pulled for the ISSCC submission in 2018. I remember we had a lot of 'fun' with the leaking tank at Li Ka Shing Center, but David never gave up until we got the nicest sine wave ever transmitted over our ultrasound links.

I feel very fortunate to have met exceptionally talented people during my time at Berkeley. Sina Faraji Alamouti and I shared a lot of moments together over the course of our programs. Together, we worked on six class projects, taped out two chips, and coauthored seven papers. Sina is a talented circuit designer with a never-ending desire to learn. I admire Sina in many ways, but what amazes me most about him is his one-of-a-kind sense of empathy and generosity towards others. I am grateful to Sina for his continuous support and all the technical/non-technical discussions we had over the past couple of years. I am very grateful to Cem Yalcin for his substantial contribution to the tapeout of the chips presented in this dissertation. I am also thankful to Cem for all the tips and tricks he shared with me in his layout masterclass. I am grateful to Braeden Benedict, Rahul Kumar, and Aviral Pandey for their diligence and support throughout the DustNet project. I would also like to thank Nathan Tesema Ersaro for the many hours he spent in the Marvell Nanofabrication lab for micro-dicing the piezoceramics I needed for my experiments. I will have to extend my thanks to my other fellow graduate students – Ryan Kaveh, Justin Doong, Adelson Chua, Carolyn Schwendeman, Liz Murray, Mahsa Sadeghi, Rozhan Rabbani, Alex Moreno – Dr. Burak Eminoglu and Dr. Soner Sonmezoglu for helping me along the way with reviewing my manuscripts and helping with the measurements.

I am grateful to Shirley Salanio and the staff at BWRC – Candy Corpus, Mikaela Cavizo-Briggs, Jeffrey Anderson-Lee, and Brian Richards – for their incredible support over the course of my PhD.

The research presented in this dissertation was financially supported by DARPA, NSF, Hellman Fellows Fund, Apple PhD Fellowship, UC Berkeley EECS department fellowship, the sponsors of BWRC and TSMC. I am grateful to all these funding sources and agencies for supporting this research.

Before joining Berkeley, I had the privilege to work with Dr. Simone Gambini, one of the most brilliant people I have ever met in my life. It was Simone who really introduced me to IC design in the first place. I feel very fortunate he trusted my abilities and trained me with his very unique style of teaching. I am certain I would not be writing this dissertation without having met Simone. I have the utmost respect for him.

I'm grateful to my decades-long friendship with Ali Taraz and Amir Halaji. I think of both of you as my brothers.

Finally, I am most grateful to my wonderful family for their unconditional love and endless support. Mom, you dedicated your entire life to me, and your departure from life left a very deep void in mine. I wish I could hold and feel the warmth of your hands one last time. I dedicate this dissertation to you. I miss you so much. Dad, it is very hard to find a man of your calibre. You are truly an inspiration to me for your generosity and kindness. You have my eternal gratitude for instilling your strong work ethic and determination into me. My two sweet sisters, Atefeh and Azadeh, you are the most loving, caring and supportive sisters I could ever ask for. Thank you for bringing so much joy and delight to the family. My amazing in-laws, Jila, Djavad, Hamoon and Sahar, I am grateful to all of you for always giving me your support regardless of the circumstances.

Negin, you are the brightest star in my life. You are my tower of strength. You are my potion of endurance. I would not be the person that I am today without all your sacrifices and love. *I thank you from the bottom of my heart.*

Chapter 1

Miniature Wireless Implants

1.1 Introduction

The human nervous system is perhaps the most astonishing and paradoxical engineering masterpiece. It performs complex signal processing tasks (e.g., real-time audio and visual decoding) on a vast amount of information using a basic integrate-and-threshold function. This basic operation was first described by a simple set of differential equations [29] that won Hodgkin and Huxley a Nobel Prize in Physiology in 1963 and has since driven an ongoing effort to holistically understand the nervous system using a bottom-up approach. Such an understanding is a key element in prevention, early diagnosis and targeted treatment of a spectrum of neurological disorders, e.g. Alzheimer, depression and seizure, as well as providing alternate treatment options for restoring sight and motor function with active prostheses. Nevertheless, despite significant advances in neuroscience research in recent years, the underlying mechanisms of the prime features of the nervous system (e.g., memory, plasticity, perception and emotion) are under active research, and our understanding of the internal mechanics and processing of the human nervous system is at best partial. This is in part due to lack of a golden technology to *continuously* and *holistically* monitor the activity of neurons (or nerves in the peripheral nervous system, PNS) without disrupting their organic operation and compromising the integrity of the biological soft tissue. The key aspects of this ‘golden’ technology are highlighted as follows:

- **continuous operation:** having a decades-long uninterrupted life time for continuous monitoring of neural activity,
- **spatial resolution:** monitoring the activity of all individual neurons/nerves that are functionally closely interrelated,
- **non/minimally invasive:** having the least amount of impact on live tissue upon application, and

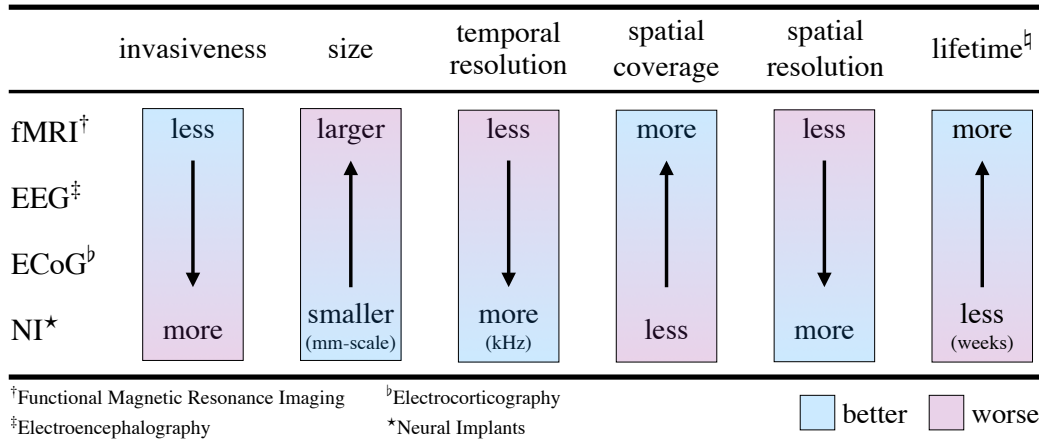


Figure 1.1: Existing trade-offs between four commonly used neural recording methods. [‡]The lifetime metric for the fMRI method cannot be fairly compared to that of the other methods since fMRI takes only short ‘snapshots’ of the neural activity. Such short recordings, however, can be taken over many years and thus we consider the lifetime of fMRI to be similar to that of EEG.

- **signal quality:** neural activity recording with a greater than 40 dB of signal-to-noise (SNR) ratio and 10 kHz of signal acquisition bandwidth.

The existing trade-offs among the most commonly used neural activity recording methods (i.e., functional Magnetic Resonance Imaging (fMRI), electroencephalography (EEG), electrocorticography (ECoG) and neural implants) are shown in Figure 1.1. Unfortunately, all of these methods are far behind the golden technology in multiple fronts, and therefore there is ample opportunity in advancing the current state-of-the-art in certain areas. Compared to other methods, *in situ* neural recording using neural implants is uniquely advantageous with regards to the quality of the recorded signal and fine spatial resolution that enable single-neuron activity monitoring using spike sorting computation methods. Neural implants, however, have small spatial coverage (a few mm) and are the most invasive method of all and consequently suffer from very short lifetimes that currently limit their applications to basic neuroscience research. The primary focus of this thesis is enhancing the longevity and spatial coverage of neural implants by means of scaling, miniaturization and long-range wireless connectivity. The immediate application of this work is long-term recording of neural activity from deeply-seated nerves.

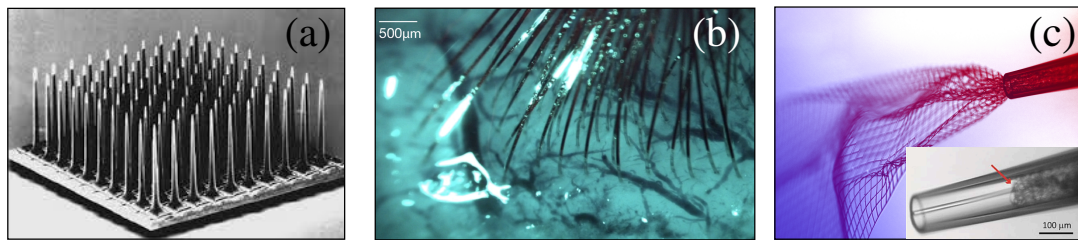
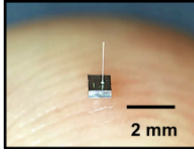
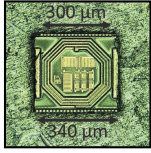
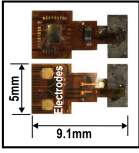
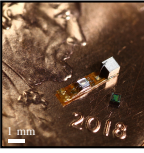
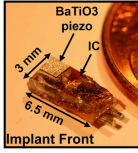
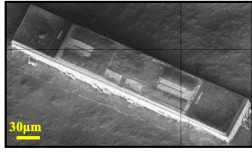


Figure 1.2: Example electrodes. Adapted from (a) Utah Microelectrode Arrays [59], (b) Neuralink’s ultrathin polymer threads [57], (c) syringe-inserted foldable meshes [86].

1.2 Neural Implants

In its simplest form, a neural implant is comprised of two elements: 1. electrode(s) and 2. data acquisition system. An electrode is a passive bio-compatible device that is strictly implanted in live tissue to conduct the electrical activity of the tissue to the data acquisition system. Many types of electrodes have been developed over the years for various purposes. The Utah microelectrode array (MEA) [59], a microfabricated polysilicon electrode array that enables neural recording from 100 electrodes at a $400\text{-}\mu\text{m}$ pitch, shown in Figure 1.2(a), is often used for neuromodulation of targets in both central nervous system (CNS) [28] and PNS [82]. Histological studies, however, have shown that large rigid structures, such as the Utah MEA, in the brain cause glial cells [18], which perform maintenance functions in the brain, to coat the foreign bodies, form scar tissue, and insulate the electrodes, reducing the amplitude and bandwidth of the neural signal. Moreover, relative micromotions between implanted rigid electrodes and soft tissue widen the dead-zones in the vicinity of the electrodes and further degrade the signal quality over time [63]. For PNS targets, these electrode micromotions are more frequent making the longevity of such electrodes even shorter to only few weeks.

One approach to remedy this is use of thin, flexible electrodes, such as Neuralink’s ultrathin polymer threads [57] shown in Figure 1.2(b). Another approach is syringe-inserted foldable mesh electrodes [86], Figure 1.2(c), that have the advantage of not requiring surgical implantation. Miniature *Active* electrodes that *float* in tissue can potentially alleviate the problem of implantation trauma and long-term tissue scarring [70, 24, 44, 43] as they are intended to blend in and move in harmony with tissue and minimally displace it thanks to their (sub)mm-scale dimensions. A few examples of some recently published neural implants are shown in Figure 1.3 along with some of their key features. Compared to their passive counterparts, active electrodes (or equivalently neural implants) need to incorporate two other main features: 1. low-noise signal acquisition (or neuromodulation in general) and 2. wireless connectivity. Moreover, since batteries do not provide sufficient energy at such form factors and periodically need to be surgically replaced, neural implants often deploy wireless power transmission (WPT) as well. Multitude of approaches for wirelessly delivering

	Neurograin	Microbead	MagNI	Neural Dust	TBioCAS'18	MOTE
						
Wireless	RF*	RF*	ME [†]	US [‡]	US [‡]	Optical
Application	recording/stimulation	stimulation	stimulation	recording	stimulation	recording
Target	brain	brain	spinal cord	peripheral	peripheral	brain
Range [mm]	5 – 8*	6.6	30	50	105	6

*Radio Frequency [†]Magnetoelectric [‡]Ultrasound *Requires relay coils

Figure 1.3: Recently published miniature neural implants. From left to right adapted from [43], [33], [72], [24], [13], [44].

power to and communicating with such miniaturized devices have been explored (Figure 3). Common wireless powering modalities utilize inductive or electromagnetic coupling [43, 33], magnetoelectric [72], acoustic [24, 13] and optical sources [44]. To implant an entire device in a minimally invasive fashion, the electronics must fit within the dimensions of syringes and stents, requiring the entire neural implant, power source/antenna, assembly, interconnect, and encapsulation to have dimensions on the scale of 2 mm or less.

Increasing the number of recording channels enables advanced signal processing techniques such as spike sorting and classification which provide critical information about the status of the nervous system. For instance, in short-term human studies that demonstrated active control of prosthetic arms using recorded neural signals from the peripheral nervous system [16, 67, 14, 82], it has been shown that increasing the number of recording sites on *different* neural pathways, (e.g. medial and ulnar nerves) provides considerably more controllable degrees of freedom on the prosthetic arm, translating into more natural hand gestures. Therefore, the general trend has been to record from as many neurons/nerves as possible by scaling the number of sensing sites.

The current state of the art has scaled to thousands of channels, with examples provided in Figure 1.4. Neuralink’s 1,024-channel recording and stimulation chip connects to flexible, thread-like electrodes through feedthroughs in a custom hermetic package [57]. IMEC’s Neuropixels 2.0 probe [76] integrates 5,120 electrodes directly over circuitry in a long shank structure that is etched directly from a CMOS substrate. Paradromics’s Argo system [69] has more than 65,000 flexible wire electrodes bonded to a 256×256 amplifier array. These many channel counts, however, are unheard of in miniature neural implants due to the distributed nature of the sensor nodes and available power constraints imposed by WPT and the small form factor as discussed in detail below.


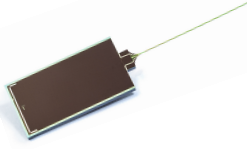

Neuralink	IMEC Neuropixels 2.0	Paradromics Argo
		
1,024 channels	5,120 channels	65,536 channels
Wireless	Wireline	Wireline
Bidirectional	Recording	Recording

Figure 1.4: Examples of high-channel-count neural interfaces. From left to right adapted from Neuralink [57], Neuropixels 2.0 by IMEC [76] and Argo by Paradromics [69].

1.3 Challenges

Designing wireless sub-mm scale implants with centimeters-deep operation ranges presents power delivery and data transmission challenges. The following is an overview of the challenges involved in wireless links across various energy modalities.

Electromagnetic/RF links

Electromagnetic (inductive/RF) power coupling is the most common form of wireless power delivery. It is commercially used in devices such as cochlear implants and peripheral nerve stimulators and has been extensively proposed for powering neural implants. Sequential inductive coupling (using an implanted high-Q tertiary coil) was presented in [83] for transcranial power transmission to epicortical free-floating implants at a depth of 20 mm. Recently, [42, 43] demonstrated WPT and uplink data communication with a network of free-floating implants at a depth of 1 cm using a random time-division multiple access (TDMA) protocol and a tertiary coil similar to [83] for power transmission. RF wireless power delivery and frequency division multiple access (FDMA) downlink were proposed in [33] to communicate with an ensemble of sub-mm scale neural stimulators.

Well-characterized on-chip inductors with moderate quality factors are widely integrated on Silicon and greatly simplify the assembly of electromagnetically powered implants [33]. Since the dimensions of on-chip antennas are proportional to the wavelength, implementing mm-scale electromagnetic resonators requires operating at a relatively high frequency, e.g. >1 GHz. Such a high operation frequency provides a generous uplink bandwidth that can be leveraged to scale the number of implants as far as uplink data transmission is concerned [43]. However, GHz-range operation frequency sets strict limits on the transmitted power and implant operation depth due to considerable tissue absorption as discussed in detail in [70]. Due to this limitation, the wireless operation range of mm-scale implants deploying

electromagnetic wireless power delivery does not extend beyond a few mm and are most useful for epicortical recording. It should also be noted that sequential inductive coupling cannot be extended to deep tissue PNS recording since the tertiary coil has a large form factor and the implants must be on the same plane (similar to [55, 26]).

Other forms of wireless powering include optical or infrared powering [44], magnetoelectric power transfer [84, 72] and acoustic/ultrasound [24, 81, 71, 75].

Optical links

Although μm -scale form factors are achievable through optical links using micro-fabricated on-chip photo detectors and LEDs, the harvested power on such scales is limited to single-digit μW due to high tissue attenuation which limits the operation range to a few mm. An example of an optically powered neural implant is presented in [44] which is the smallest free-floating neural recording implant reported in literature, but its maximum theoretical operation depth does not exceed 6 mm making it better suited to epicortical recording.

Magnetic links

Recently, coupled magneto-piezoelectric devices were proposed in [84, 72] as an energy harvesting device for wireless power delivery to deep implants. This technique utilizes two mechanically coupled resonators, i.e., a magnetoelectric element and a piezoelectric element, as the energy harvester. The magnetoelectric element resonates in presence of a variable magnetic field which in turn forces the piezoelectric element to vibrate and generate electricity. This method exploits the relatively small attenuation of the B-field in tissue/skull and therefore offers high energy densities at depth which is particularly useful for transcranial wireless power transmission to neural implants. Although, this is appealing for transferring energy to deep power hungry implants (e.g., neural stimulating implants), the operation frequency used in this scheme is a few kHz (imposed by the dimensions of the magnetoelectric device) which leaves little bandwidth for data-rate intensive uplinks required by neural recording implants specially in multi-channel/multi-site recording settings.

Acoustic links

In the past few years, ultrasound has also emerged as a viable modality for powering and communicating with implants [24, 81, 71, 75]. Such implants utilize a small ultrasound transducer that converts ultrasound-induced mechanical vibrations to electrical energy. Similarly to electromagnetic/RF links, simultaneous power and bidirectional communication across a single wireless acoustic link has also been demonstrated (known as ultrasound backscattering). Because the volume of piezoelectric transducers dominate that of the implant, using a single transducer for both power harvesting and data transmission substantially reduces the overall volume of implants.

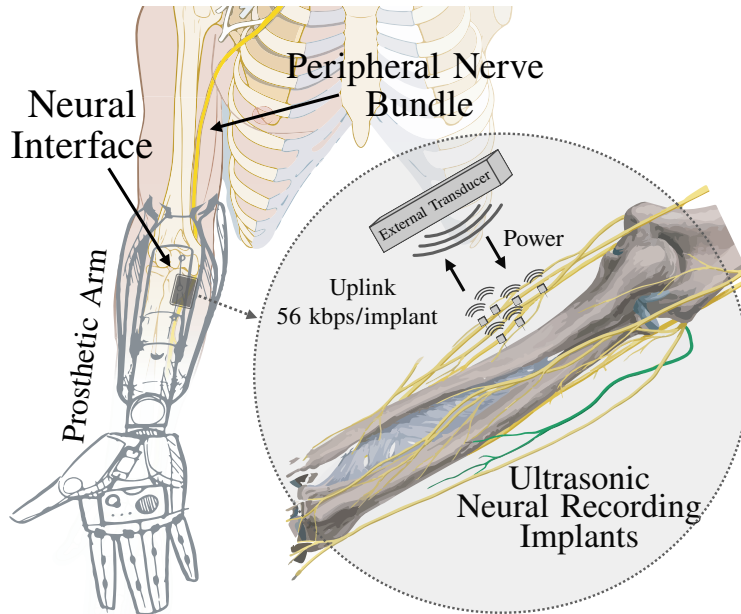


Figure 1.5: Concept of active prosthetic arm control using a distributed network of ultrasonically powered peripheral nerve implants.

The speed of sound in tissue is almost 5 orders of magnitude smaller than that of the electromagnetic waves, and therefore mm-scale acoustic resonators can be designed to operate at considerably lower frequencies, e.g. MHz range, compared to their electromagnetic counterparts. Since the acoustic attenuation coefficient is <3 dB/(cm·MHz) for most soft tissues [3], acoustic waves with mm-scale wavelengths propagate more efficiently than electromagnetic waves (e.g., up to 9 dB/cm at 1 GHz for muscle [38]). Unlike electromagnetic WPT, this enables safe power delivery to deep anatomical areas, e.g. most peripheral nerves. While the skull distorts and attenuates the incident ultrasound wave pattern, power can be delivered to implants in the brain through thinned skull [78, 21].

It has been shown that the optimal carrier frequency for ultrasonic implants is in the range of 1–2 MHz as far as the implant size and the end-to-end efficiency of the wireless power delivery link are concerned [12]. Although, MHz-range carrier frequency provides a much larger uplink bandwidth relative to the optical and magnetic links described earlier, it can hardly support the uplink data rate required for tens of neural recording implants. For instance, assuming that 20 single-channel neural recording implants are needed for capturing neural information from the severed nerves of an amputated arm for inferring thoughts to control a robotic arm as shown in Figure 1.5. The minimum required information rate per implant is ~ 50 kb/s, (7 bits of sensitivity and 7 kS/s). Therefore, the wireless channel needs to have an overall data rate of at least 1 Mbps which is the same order of magnitude as the carrier frequency (of say 1 MHz) translating into only 1 cycle/symbol if the common on-off

keying modulation is used. This simple example excludes communication protocol overheads and assumes a continuous wireless uplink. In fact with a backscatter uplink protocol the channel capacity is halved which means the symbol width must not be longer than 0.5 of a cycle which is an impractically small number. This example clearly illustrates the insufficiency of bandwidth of power-data acoustic links for scaling the number of miniature neural recording implants in ultrasonic links.

1.4 Thesis Contribution

The main objective of this work is scaling the number of ultrasonically-powered neural implants which strictly requires 1. miniaturization of each sensor node, 2. enhancing the channel utilization of (backscatter) ultrasound uplinks, and 3. incorporating multiple-access protocols in uplink communication. We provide various tools and analytical methods that advance the state-of-the-art in all these three aspects while using a single-element external transducer. In particular, we present a design procedure for the geometry and the operation frequency of the ultrasound link that minimizes the volume of the power harvesting element of the implant. Given ultrasound backscatter/pulse-echo communication inherently results in the smallest implant volume, we discuss the underlying mechanisms of ultrasound backscattering, provide a SPICE-friendly circuit model of a generic ultrasound link, and derive simple yet powerful closed-form expressions that relate the electrical termination impedance of the piezo to its acoustic reflection coefficient, Γ . These closed-form expressions are then used to design two ultrasound uplink modulators: 1. a highly linear AM backscatter modulator and 2. an M-level amplitude shift keying (ASK) modulator. Thanks to its large linear range, the first modulator enables spectrally efficient AM modulation while accommodating code-division multiple-access protocol. The second modulator uses a quasi digital m-level ASK scheme to improve the robustness of the uplink to carrier noise while improving the uplink data rate by $\log_2(m)$ compared to commonly used on-off keying (OOK). Incorporating time-division multiple-access protocol is also demonstrated in conjunction with the second modulator. These two modulators are then implemented in implant prototypes whose complete hardware implementation is discussed along with their experimental verification. The first implant prototype is the first demonstration of simultaneous power-delivery and communication with multiple implants at depths larger than 45 mm, while the extended channel utilization in the second implant enables power-delivery and communication with 4 miniature implants.

List of Publications

- Ghanbari, M.M., Piech, D.K., Shen, K., Alamouti, S.F., Yalcin, C., Johnson, B.C., Carmena, J.M., Maharbiz, M.M. and Muller, R., 2019, February. 17.5 A 0.8 mm³ Ultrasonic Implantable Wireless Neural Recording System with Linear AM Backscat-

tering. In 2019 IEEE International Solid-State Circuits Conference-(ISSCC) (pp. 284–286). IEEE.

- Ghanbari, M.M., Piech, D.K., Shen, K., Alamouti, S.F., Yalcin, C., Johnson, B.C., Carmena, J.M., Maharbiz, M.M. and Muller, R., 2019. A Sub-mm³ Ultrasonic Free-Floating Implant for Multi-Mote Neural Recording. *IEEE Journal of Solid-State Circuits*, 54(11), pp.3017–3030.
- Alamouti, S.F.*, Ghanbari, M.M.*, Ersumo, N.T. and Muller, R., 2020, July. High Throughput Ultrasonic Multi-implant Readout Using a Machine-Learning Assisted CDMA Receiver. In 2020 42nd Annual International Conference of the IEEE Engineering in Medicine & Biology Society (EMBC) (pp. 3289–3292). IEEE.
- Ghanbari, M.M. and Muller, R., 2020. Optimizing Volumetric Efficiency and Backscatter Communication in Biosensing Ultrasonic Implants. *IEEE Transactions on Biomedical Circuits and Systems*, 14(6), pp.1381–1392.
- Benedict, B. C., Ghanbari, M.M., Alamouti, S.F., Ersumo, N.T., and Muller, R., 2021, May. Time Reversal Beamforming for Powering Ultrasonic Implants. In 2021 10th International IEEE/EMBS Conference on Neural Engineering (NER). IEEE.
- Muller, R., Ghanbari, M.M., and Zhou, A. (2021). Miniaturized Wireless Neural Interfaces: A tutorial. *IEEE Solid-State Circuits Magazine*, 13(4), 88–97.
- Benedict, B.C., Ghanbari, M.M. and Muller, R., 2022. Phased Array Beamforming Methods for Powering Biomedical Ultrasonic Implants. In 2022 *IEEE Transactions on Ultrasonics, Ferroelectrics, and Frequency Control*, vol. 69, no. 10, pp. 2756–2765.

1.5 Thesis Organization

The rest of this thesis is organized as follows:

- **Chapter 2:** In this chapter, the fundamentals of piezoelectricity are reviewed, and the concept of acoustic wireless power transmission using piezoelectric (piezo) transducers is briefly discussed. Then the geometrical design of the implant piezoceramic transducer is discussed in detail while special attention is paid to the optimization of the volumetric efficiency of the piezo. The design method presented in this chapter minimizes the overall volume of the piezo for a given required harvested power. This chapter concludes with a realistic design example of an ultrasonically-powered neural stimulating implant.
- **Chapter 3:** In this chapter, the underlying mechanisms of ultrasound backscattering is discussed in detail. A CAD-friendly circuit model is presented to facilitate simulation of the ultrasound link, and lastly an analytical study is used to obtain a set of simple

closed-form expressions for describing the relationship between the reflection coefficient Γ and the termination electrical impedance of the implant piezo under various acoustic loading and resonance frequencies. These simple expressions lay the groundwork for designing highly linear uplink modulators introduced in later chapters.

- **Chapter 4:** Hardware implementation and experimental verification of an ultrasonically powered mm-scale neural recording implant that uses linear AM backscattering and code-division multiple-access (CDMA) protocol are presented in this chapter. This miniature implant achieves state-of-the-art noise-power performance and is the first demonstration of multi-site neural recording using ultrasonically-powered implants from the depths of greater than 45 mm.
- **Chapter 5:** A machine-learning assisted CDMA decoder is introduced in this chapter that significantly improves the bit error rate (BER) of digitally-encoded active uplinks. Simultaneous uplink communication from 4 implants is also demonstrated and experimentally characterized using this decoder.
- **Chapter 6:** Due to unavailability of a more spectrally-efficient backscatter modulator, almost all prior art uses the most basic on-off keying (OOK) modulation scheme in backscatter ultrasound links. In this chapter, we introduce an m-level amplitude shift keying (ASK) backscatter uplink modulator circuit along with a time-division multiple-access (TDMA) protocol to increase the channel utilization by $\log_2(m)$ in an effort to increase the number of implants that can be supported with a MHz-range carrier frequency. Hardware implementation and experimental functional verification of this implant are also presented.
- **Chapter 7:** This chapter concludes the thesis with the summary of the results and important future research directions.

Some of the figures in this chapter were adapted from the following article:

R. Muller, **M. M. Ghanbari**, and A. Zhou. “Miniaturized Wireless Neural Interfaces: A tutorial.” *IEEE Solid-State Circuits Magazine* 13, no. 4 (2021): 88–97.

Personal contribution: I drafted the last section of this article, generated the majority of the figures and discussed/reviewed the contents of the final manuscript with the co-authors.

Acknowledgements: All authors contributed to the draft of the original manuscript. R. Muller reviewed the manuscript and provided advice on the technical aspects of the work. R. Muller was the principal investigator of this work.

Chapter 2

Ultrasonic Wireless Power Transmission

Wireless power transmission is a key feature of miniature neural implants for it obviates the need for bulky batteries that have limited lifetime and require frequent replacements post implantation. Any type of wireless power transmission requires an energy carrier wave/field whose energy modality (e.g., inductive, acoustic, magnetic etc.) should be chosen carefully for the application of interest. For deeply-seated neural implants, the size of the implant, depth of operation and communication bandwidth are of paramount importance. For such implants, *acoustic* energy modality is arguably an optimal choice due to its low propagation loss in tissue (<2 dB/(cm · MHz)) and relatively small propagation speed (that enables sub-mm scale resonators at MHz-range operation frequencies) [70].

A typical acoustic wireless power transmission link is comprised of an external acoustic transmitter and an implant receiver both of which are commonly realized by piezoelectric (piezo) transducers [24, 70, 71, 75, 62] that are complex electromechanical devices. In this chapter, we briefly review the fundamentals of piezoelectricity at various levels of abstraction that are frequently referred to throughout this work. Then, acoustic wireless power transmission using external single-element unfocused, spherically-focused, cylindrically-focused and phased array piezo transducers are described and compared. We then focus on the geometrical design of the implant piezo transducer and provide a design process that minimizes the volume of the implant piezo. The next chapter deals with wireless data transmission through acoustic links when using piezos as acoustic antennas.

2.1 Background on Piezoelectricity

A piezoelectric material, due to its asymmetric molecular structure, has a non-zero dipole moment whose magnitude changes as a function of mechanical strain. Similarly, an electric field that is aligned with the poling direction of a piezoelectric material strengthens/weakens the dipole moments of its unit molecular cells and results in mechanical strain (or stress

depending on the existing mechanical boundary conditions). Therefore in a piezoelectric material, there is a coupling between the mechanical (stress T , and strain S) and the electrical properties (electric E , and displacement D fields) of the material that is described by one of the four sets of constitutive relations of piezoelectricity (discussed below). Provided that acoustic waves are in essence due to mechanical vibrations (characterized by force F and particle velocity v) of the molecules of the propagation medium, a piezoelectric material is in fact an electroacoustical transducer as well. Therefore, piezoelectric transducers can both transmit and receive acoustic waves that make them a perfect choice as acoustic antennas for wireless power transmission to miniature implants.

Piezoelectric transducers are elastic mechanical objects that are made in a variety of shapes such as rectangular/circular plates, bars, rings, cuboids etc. Elastic objects depending on their geometry and boundary conditions have a tendency to move/resonate in certain modes. For instance, the fundamental resonance mode of a rectangular plate laid on the xy plane with clamped edges is a paraboloid whose vertex oscillates along the z axis. Similarly, piezoelectric transducers (objects) have certain resonant modes that generally fall into two categories of low- and high-frequency resonant modes [9]. The low-frequency resonant modes involve motion along the major dimension of the transducer (for instance, a bar resonating along its length, or a circular plate resonating along its radius). On the contrary, a high-frequency resonance mode is often excited along the minor dimension, e.g. the thickness of a plate. Most commercially-available single-element external transducers are high-frequency resonators while the implant piezo transducers depending on their geometry resonate in either low-frequency mode, high-frequency mode or a combination of the two (that is known as mode coupling). Therefore, it is important to understand these relevant piezo resonance modes in order to accurately model and predict their behaviour. We first briefly discuss the piezoelectricity constitutive relations, derive important design equations and present a piezo equivalent circuit that most accurately models the high-frequency piezo resonance mode, known as thickness-extensional (TE), that is the main resonance mode of the single-element circular external transducers commonly used for wireless power delivery. We, then, provide the equivalent circuit model for a low-frequency longitudinal-expander (LE) mode that is more relevant to the geometries/shapes of implant piezos with a major dimension (large aspect ratios). Implant piezos without any major dimension do not have a single/distinct resonance mode and therefore are most accurately modeled by numerical methods such as finite element method (FEM) solvers.

Thickness-Extensional (TE) Resonance Mode

The piezoelectric constitutive relations in which strain S and electric field E are used as independent variables are described as

$$T = C^E S - eE, \quad (2.1)$$

$$D = eS + \epsilon^S E, \quad (2.2)$$

in which e , C^E and ϵ^S are the piezoelectric stress constant, piezoelectric elastic stiffness constant (at constant or zero E , hence the superscript), and piezoelectric permittivity (at constant or zero strain), respectively. Because most piezoelectric materials are anisotropic, C^E , e and ϵ^S are generally defined as tensors, but for the resonance modes of interest here (poling and motion along certain axes) they can be replaced by a single constant with negligible error. The constitutive relations and the acoustic wave equation (see below) can be used to derive an equivalent three-port circuit model of the piezo as shown below.

From (2.1) and (2.2), it is straightforward to see how a piezoelectric material is different from a non-piezoelectric elastic material. That is, according to the Hooke's law, the total internal stress of a linear elastic material T_t is related to its strain by

$$T_t = CS, \quad (2.3)$$

where C is the elastic stiffness constant. Comparing (2.1) and (2.3), it can be seen that eE in (2.1) is the component of stress that is contributed by the applied electric field across the piezoelectric material. Similarly, the electric displacement field of a dielectric material is

$$D = \epsilon E, \quad (2.4)$$

where ϵ is the permittivity of the dielectric material. Comparing (2.2) and (2.4), we find that eS in (2.2) is the additional polarization caused by the strain-induced dipole moment in a piezoelectric material.

The piezo constitutive relations can be solved for T in terms of S and D as follows

$$T = C^D S - hD, \quad (2.5)$$

where C^D and h are respectively the stiffened elastic and transmitting constants given by

$$C^D = C^E \left(1 + \frac{e^2}{C^E \epsilon^S}\right) = C^E (1 + K^2), \quad (2.6)$$

$$h = \frac{e}{\epsilon^S}, \quad (2.7)$$

where $K > 0$ is the piezoelectric coupling constant. Equation (2.6) means that, interestingly, an open-circuit piezoelectric has a larger (by a factor of $(1 + K^2)$) elastic stiffness constant (and therefore is stiffer) compared to a short-circuit piezo with elastic constant of just C^E . In a similar fashion, strain S can be eliminated from the constitutive relations to arrive at

$$D = \frac{e}{C^E} T + \epsilon^T E, \quad (2.8)$$

$$\epsilon^T = \epsilon^S (1 + K^2), \quad (2.9)$$

which means that relative to the permittivity of a strain-free piezoelectric material ϵ^S , that of a stress-free piezoelectric material ϵ^T is elevated by $1 + K^2$ which is the direct consequence of the additional strain-induced polarization.

The constitutive relations in conjunction with Newton's second law of motion and the conservation of mass can be used to properly model the piezo with a three port network as follows [35]. Newton's second law of motion can be described for any particle in a piezoelectric material along displacement axis of z as

$$\frac{\partial T}{\partial z} = \rho \frac{\partial v}{\partial t} = j\omega\rho v, \quad (2.10)$$

where ρ and v are the mass density of the material and the particle velocity, respectively. It can be also shown that the spatial gradient of the particle velocity along the axis of motion is equal to the temporal gradient of strain using the conservation of mass inside the material as

$$\frac{\partial v}{\partial z} = \frac{\partial S}{\partial t} = j\omega S. \quad (2.11)$$

Taking partial derivative of both sides of (2.5) with respect to z , and noting that $\partial D/\partial z = 0$ (because there is no free charge inside piezoelectric material), T and S can be eliminated from (2.10) and (2.11) to obtain the wave equation for the particle velocity inside the piezoelectric material

$$\frac{\partial^2 v}{\partial z^2} + \frac{\omega^2 \rho}{C^D} v = 0, \quad (2.12)$$

that describes moving waves of the form $e^{\pm j\beta z}$ with the wave propagation constant β and wave velocity V_a of

$$\beta = \omega \sqrt{\frac{\rho}{C^D}}, \quad (2.13)$$

$$V_a = \sqrt{\frac{C^D}{\rho}}. \quad (2.14)$$

The solution to the particle velocity wave equation for a piezo element with length l can be combined with

$$I = j\omega AD, \quad (2.15)$$

where A is the cross section area of the piezo, to relate the mechanical (force and particle velocity) and electrical (voltage and current) properties of the piezo as

$$\begin{bmatrix} F_1 \\ F_2 \\ V_3 \end{bmatrix} = \begin{bmatrix} \frac{Z_C}{j\tan(\beta l)} & \frac{Z_C}{j\sin(\beta l)} & \frac{N}{j\omega C_0} \\ \frac{Z_C}{j\sin(\beta l)} & \frac{Z_C}{j\tan(\beta l)} & \frac{N}{j\omega C_0} \\ \frac{N}{j\omega C_0} & \frac{N}{j\omega C_0} & \frac{1}{j\omega C_0} \end{bmatrix} \begin{bmatrix} v_1 \\ v_2 \\ I_3 \end{bmatrix}, \quad (2.16)$$

where the radiation impedance Z_C , strain-free capacitance of the piezo C_0 , and N are

$$Z_C = Z_0 A = \rho V_a A = A \sqrt{\rho C^D}, \quad (2.17)$$

$$C_0 = \epsilon^S \frac{A}{l}, \quad (2.18)$$

$$N = h C_0 = \frac{eA}{l}. \quad (2.19)$$

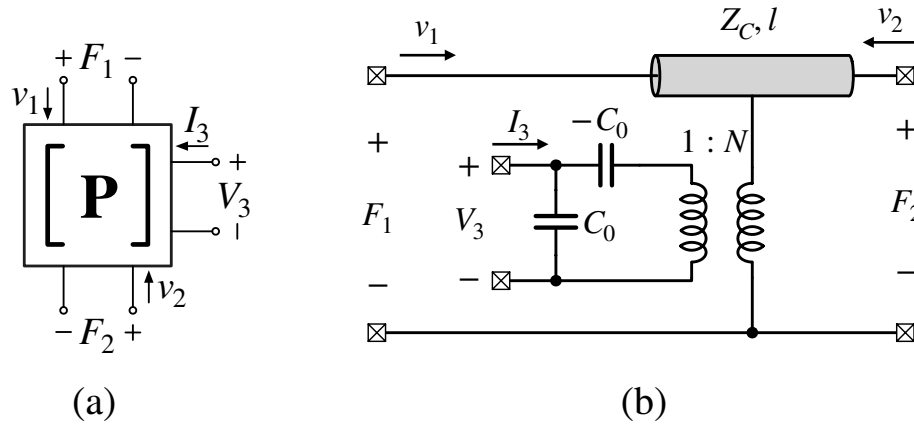


Figure 2.1: (a) piezo as a three-port network, and (b) Redwood's equivalent circuit model.

Z_0 is the specific acoustic impedance of the material which is the product of the mass density and wave propagation speed in that material, i.e., stiffened piezo in this case. The set of equations described in (2.16) are used to treat the piezo as a three-port *blackbox* network with two acoustic ports (force F_i , particle velocity v_i) and an electric port (voltage V , current I) that completely describe the electromechanical coupling of the piezo. For a thickness-extensional resonance mode where the poling direction of the piezo and the direction of motion are along the z axis (in material coordinates, axis 3), the tensors e , ϵ^S and C^E can be respectively replaced by the associated constants e_{33} , ϵ_{33}^S and C_{33}^E to drastically simplify the model.

The mathematical description of a TE-mode resonating piezo in (2.16) can be converted into an equivalent circuit model which was first proposed by Mason [49] and further developed into the famous KLM model [37]. A slightly modified version of the Mason's equivalent model was proposed by Redwood [66], shown in Figure 2.1, which is more SPICE friendly because it elegantly uses a single transmission line (with length l and characteristic impedance Z_C) to model the three nonlinear complex impedances in Mason's model that are otherwise challenging to model/simulate by circuit simulators.

TE-mode Impedance

One of the most important aspects of a piezoelectric device is its resonance frequencies that can be analytically derived using the piezo three-port network described by (2.16) or simulated using the Redwood's equivalent circuit model for known piezoelectric material, dimensions, and termination impedances.

The electrical impedance ($Z_3 = V_3/I_3$) of an unloaded piezo (in vacuum, short-circuit at both acoustic terminals, that is $F_1 = F_2 = 0$) can be found by eliminating v_1 and v_2 in

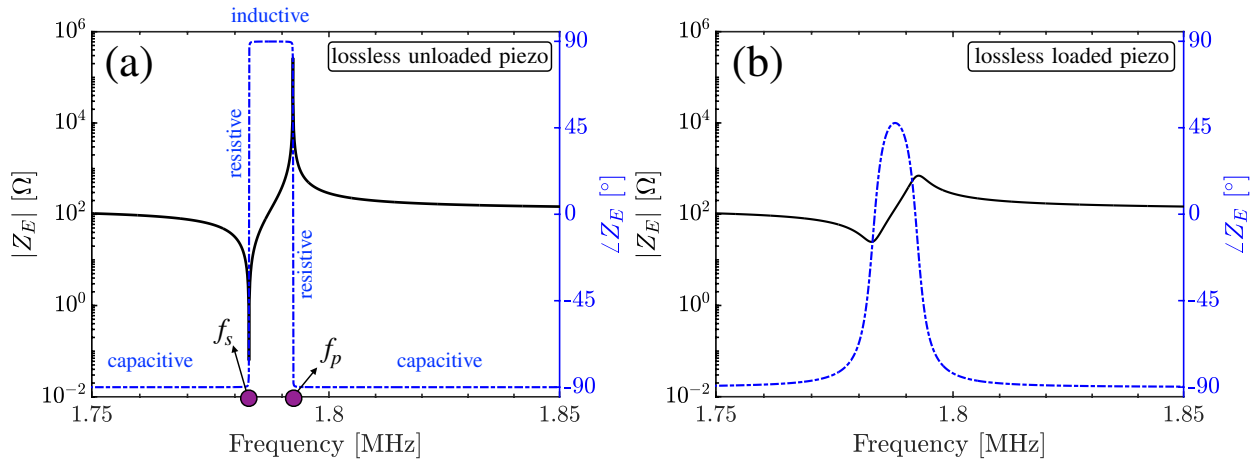


Figure 2.2: (a) Electrical impedance of a lossless unloaded piezo around its fundamental resonance mode. The series f_s and parallel f_p resonant frequencies are defined where the imaginary component of the impedance becomes zero. (b) The electrical impedance of the same piezo with non-zero acoustic loading.

(2.16), that is

$$Z_3 = \frac{V_3}{I_3} = \frac{1}{j\omega C_0} \left(1 - k_t^2 \frac{\tan(\beta l/2)}{\beta l/2} \right), \quad (2.20)$$

where $k_t^2 = K^2/(1 + K^2)$ is the piezoelectric coupling constant for a piezo that has little to no motion transverse to the poling direction. A typical electrical impedance of a lossless unloaded (acoustic ports are terminated with zero acoustic impedance) piezo is shown in Figure 2.2(a). The impedance of an unloaded piezo is purely real at two distinct frequencies known as series f_s and parallel f_p resonance frequencies. At frequencies smaller than f_s and larger than f_p , the piezo is essentially a capacitor and at frequencies between the two resonance frequencies the piezo behaves as an inductor. Because the piezo is assumed lossless and is acoustically unloaded, the quality factor of the piezo at the two resonance frequencies is very large. Acoustic loading of the piezo dampens the resonance by dissipation of energy at the acoustic ports which in turn reduces the quality factor as shown in Figure 2.2(b).

At f_p the electrical impedance of an unloaded piezo is infinite. It is straightforward to find this frequency using (2.20), that is when $\beta l = \pi$, as follows

$$f_p = \frac{V_a}{2l}. \quad (2.21)$$

Therefore, for a given piezo material, the parallel resonance frequency of the TE-mode is inversely proportional to the thickness l of the piezo. Also, for a given thickness, stiffer and less dense materials have higher parallel resonance frequencies. It is possible to show

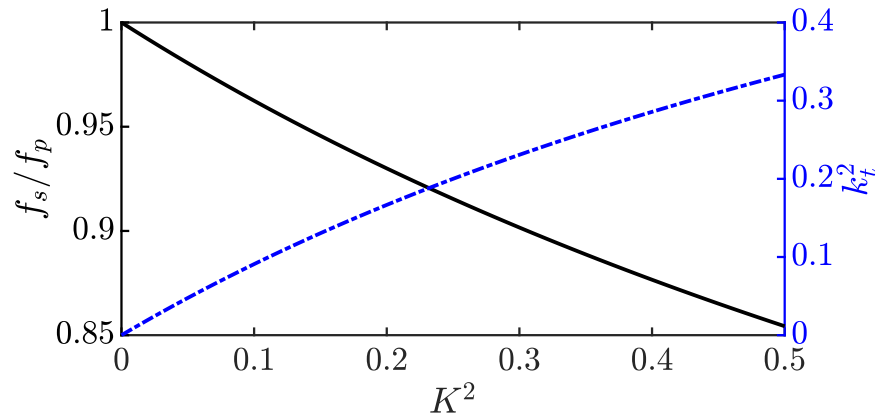


Figure 2.3: Ratio of f_s/f_p for the TE resonance mode as a function of (piezo coupling constant)²

that the series resonance frequency, defined as the frequency at which the impedance of the unloaded piezo is zero, is given by [35] (2.20), that is when $\beta l = \pi$, as follows

$$f_s \approx f_p \sqrt{1 - \frac{8}{\pi^2} k_t^2}. \quad (2.22)$$

The piezoelectric coupling constant K is primarily material dependent and is in the range of $0 < K^2 < 0.5$. Therefore, as shown in Figure 2.3, f_s can be up to only 15% smaller than f_p in a TE mode resonating piezo, and this can be used to quickly identify whether the piezo is resonating in the TE-mode mode or not by just inspecting the impedance plot and finding the ratio f_s/f_p of the piezo. Also, notice that (2.21) is the fundamental parallel resonance frequency of the piezo, and that the piezo also has higher-order parallel resonance at all the odd harmonics of f_p (and of course f_s following (2.22)) as well.

Longitudinal-Expander (LE) Resonance Mode

The TE resonance mode best models the behaviour of a piezoelectric transducer that has little motion in the direction perpendicular to its poling direction. This is satisfied when the width/length of the piezo is many wavelengths larger than its thickness or alternatively when the piezo is transversely clamped. Neither of these two conditions are satisfied for implant piezo transducers because due to fabrication and implant size limitations such piezos commonly have a rectangular cuboid shape whose length, width and thickness are almost the same order of magnitude.

The resonance motion of a bar-shaped implant piezo (length=width<thickness) can be modelled by longitudinal-expander (LE) mode when the piezo is mainly strained along its major dimension (thickness in this case) which is also parallel to the poling direction of

the piezo. In this case, a great deal of similarity between the LE- and TE-mode equivalent circuits results if stress T and charge density D are used as the independent variables for the constitutive relations of the piezo as follows

$$S = s^D T + g D, \quad (2.23)$$

$$E = -g T + \nu^T D, \quad (2.24)$$

where g and ν are known as piezo voltage and dielectric constants. In fact, it is shown in [9] that the same Redwood's equivalent circuit model, in Figure 2.1, can be used for the LE mode as long as correct material constants are used to calculate C_0 , V_a and N as follows

$$d_{33} = \frac{g_{33}}{\nu_{33}^T} \quad (2.25)$$

$$k_{33}^2 = \frac{d_{33}^2}{s_{33}^E \epsilon_{33}^T} \quad (2.26)$$

$$C_0 = A \epsilon_s s^T (1 - k_{33}^2) / l \quad (2.27)$$

$$V_a = \sqrt{\frac{1}{\rho s_{33}^D}} \quad (2.28)$$

$$N = \frac{A d_{33}}{l s_{33}^E} \quad (2.29)$$

where d_{33} and k_{33} are piezoelectric constant and piezo longitudinal coupling factor. In other words, the same equivalent three-port network described by (2.16) can be used to model both the LE- and TE-mode resonances. Nevertheless, the resonance behaviour of piezos whose width to thickness ratios is around unity cannot be categorized as either LE or TE and should be analyzed using finite element method (FEM) solvers as shown later in this chapter.

2.2 Acoustic Wireless Power Transmission

In the previous section, we briefly described the effect of piezoelectricity and derived a three-port equivalent network that is suitable for modeling the TE- and LE-resonance modes of piezo devices. With the help of the three-port piezo equivalent network, the conceptual diagram in Figure 2.4 demonstrates the process of acoustic wireless power transmission. For acoustic wireless power transmission, *three* elements are required: 1. a transmitting (external) transducer 2. a receiving (implant) transducer and 3. an acoustic medium. The external and implant transducers are modeled by their respective three-port equivalent networks. For simplicity, it is assumed that the back surfaces of these transducers are terminated by $Z_{B,EXTERNAL}$ and $Z_{B,IMPLANT}$, respectively. In this case, the external transducer receives electric energy from the electric source V_S and converts it to acoustic energy that is emitted through its front facing acoustic port. The acoustic energy travels through the medium,

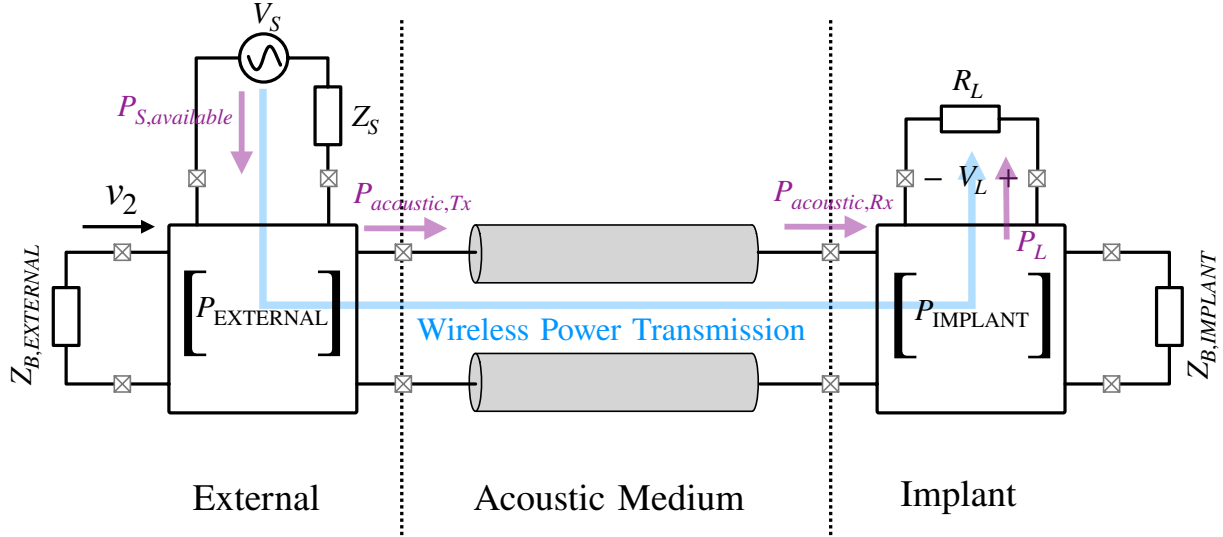


Figure 2.4: Concept of acoustic wireless power transmission. The flow of energy is shown by the arrow. The external transducer converts the electrical energy supplied by V_s to acoustic energy which travels through the acoustic medium and finally converted back to electrical energy and delivered to the implant modeled by R_L . $Z_{B,EXTERNAL}$ and $Z_{B,IMPLANT}$ are the acoustic termination impedances of the back face of the external and implant piezos, respectively.

modeled by a pair of transmission lines, to reach the acoustic port of the implant piezo. The distance between the external and the implant piezos determine the length of the transmission lines whose characteristic impedance is $Z_C = \rho_m V_m$, where ρ and V_m are the density and speed of sound of the acoustic medium, respectively. The transmission line models can also include losses in the medium by including a loss factor. The implant piezo converts the acoustic energy back to electric energy and delivers it to the implant integrated circuit (IC) here simply modeled by R_L .

An efficient wireless power transmission link optimizes the link end-to-end efficiency η defined as

$$\eta = \eta_{E,Tx} \cdot \eta_{Tx,Rx} \cdot \eta_{Rx,E}, \quad (2.30)$$

in which,

$$\eta_{E,Tx} = \frac{P_{acoustic,Tx}}{P_{S,available}}, \quad (2.31)$$

$$\eta_{Tx,Rx} = \frac{P_{acoustic,Rx}}{P_{acoustic,Tx}}, \quad (2.32)$$

$$\eta_{Rx,E} = \frac{P_L}{P_{acoustic,Rx}}, \quad (2.33)$$

where $P_{S,available}$ is the available electric power from source V_S , $P_{acoustic,Tx}$ is the available acoustic power at the output of the external transducer, $P_{acoustic,Rx}$ is the available acoustic power at the input of the implant piezo, and P_L is the electric power delivered to the implant electric load, R_L . Provided that the system shown in Figure 2.4 is highly asymmetric (due to the relative sizes of the external transducer and the implant piezo), the back propagation of acoustic waves from the implant to the external transducer can be ignored and efficiency optimization performed on each component of η individually. $\eta_{E,Tx}$ is the electric to acoustic conversion efficiency of the external transducer that is affected by the electric and acoustic impedance matching quality at the electric and transmitting acoustic ports of the external transducer. $\eta_{Tx,Rx}$ is a measure of the focusing ability of the external transducer to the aperture of the implant piezo, and $\eta_{Rx,L}$ is the acoustic to electric conversion efficiency of the implant piezo. Optimization of $\eta_{E,Tx}$ and $\eta_{Tx,Rx}$ is outside the scope of this work and discussed elsewhere [35, 12]. Nevertheless, we briefly review common types of single-element external transducers and describe their associated design parameters and existing trade-offs below. A design procedure that co-optimizes $\eta_{Rx,E}$ and implant piezo volume is presented in the next section.

Unfocused Transducers

The simplest and most commonly used transducer is perhaps the unfocused type that has a flat transmitting surface. Upon excitation, the entire surface of the transducer moves with the same velocity in the direction normal to the surface. Such a motion subsequently moves neighboring particles in the acoustic medium and results in the generation of acoustic waves (propagating along the direction of motion, i.e. normal to the surface). The wave propagation profile of any vibrating acoustic point source on the surface of the transducer is spherical. The intensity of the propagating wave at any given point in space is therefore the superposition of all the spherical waves emitted from all the points on the surface of the transducer. The resulting superposition has a complex intensity pattern (with many local maxima and minima) near the surface of the transducer as shown in Figure 2.5. On the contrary, the wave profile resembles a diverging *planar* wave at distances far away from the transducer (because relative delays and therefore phase differences between the travelling spherical waves become negligible at far distances). These two regions are known as near- and far-field regions. The Rayleigh distance determines the axial distance at which the pressure intensity profile transitions from the near- to the far-field region. For a transducer with diameter D , the Rayleigh distance is given by

$$\text{Rayleigh Distance} = \frac{D^2 - \lambda^2}{4\lambda} \quad (2.34)$$

where λ is the wavelength of the propagating wave in the medium. At distances larger than the Rayleigh distance, the wave diverges with a divergence angle of [5]

$$\theta_d = \sin^{-1} \left(\frac{1.22\lambda}{D} \right). \quad (2.35)$$

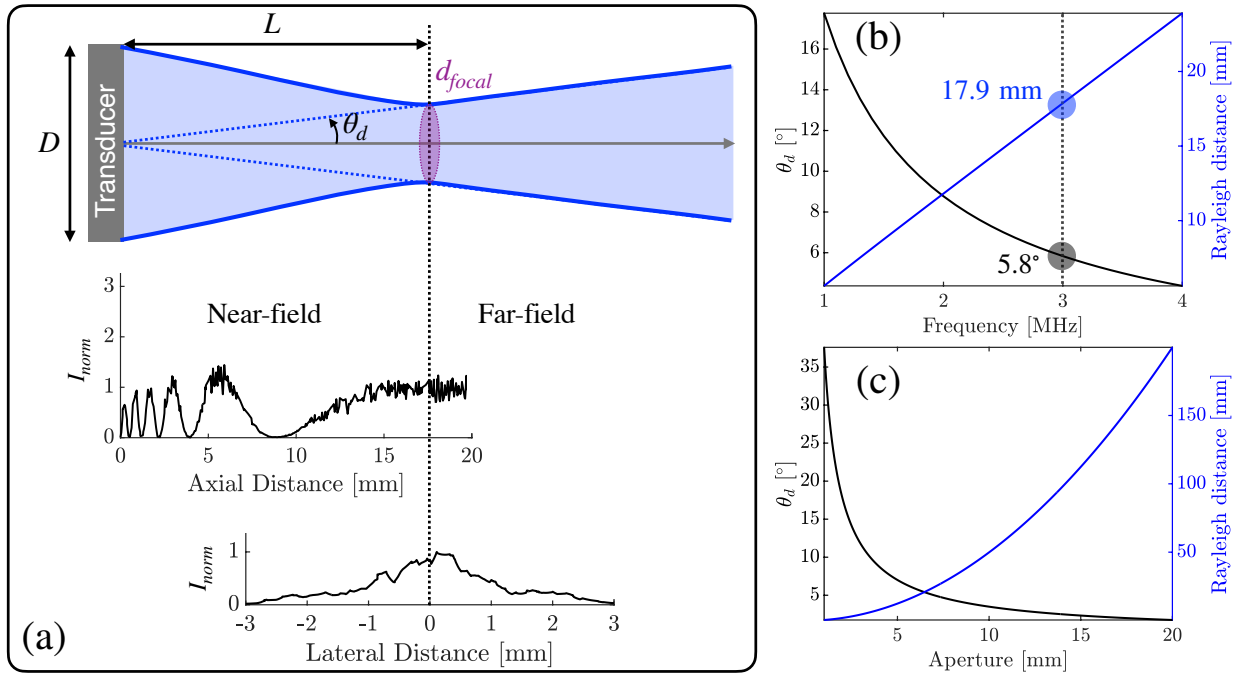


Figure 2.5: (a) Radiation profile of an unfocused single-element external transducer with aperture D . The generated beam has an inherent focal area at one Rayleigh distance away from the transducer. FEM simulated axial pressure intensity (normalized to that at the Rayleigh distance) profile and the lateral intensity at the Rayleigh distance for $D = 6$ mm operating at 3 MHz. Rayleigh distance and far-field divergence angle θ_d (b) for $D = 6$ mm at various frequencies and (c) at 3 MHz and various apertures.

As shown in Figure 2.5(b), for a fixed-diameter unfocused transducer, increasing the operation frequency increases the Rayleigh distance and reduces the divergence angle which ultimately results in a more planar propagation profile and therefore less focusing ability. A similar trend is observed when the aperture of the transducer is increased for a fixed operation frequency as shown in 2.5(c). Therefore, both the operation frequency and transducer aperture can be used to design for a required operation depth.

The local pressure intensity of some of the maxima in the near-field region is larger than that in the far field region (around the Rayleigh distance), but because of the non-uniformity of the near-field intensity profile, the harvested power in the near-field region would be sensitive to axial misalignment. Therefore, provided the axial pressure intensity at the Rayleigh distance is relatively large and uniform (Figure 2.5(a)), this region is often used as the optimal location for deep implants where the distance between the external transducer and the implant is poorly controlled.

As shown in Figure 2.5(a), however, the lateral diameter of the focal area is fairly narrow

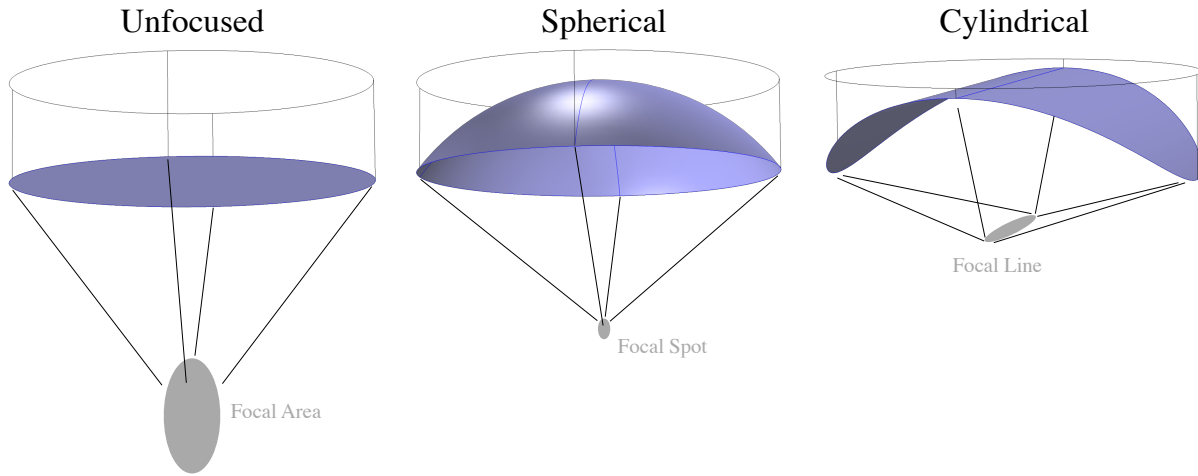


Figure 2.6: Comparison of unfocused, spherically and cylindrically focused external transducers.

for an unfocused transducer that results in high sensitivity to lateral misalignment. This can be remedied by increasing the diameter of the transducer (to laterally widen the focal area), but that would require decreasing the operation frequency (to keep the operation depth constant) which would result in a larger implant volume and lower communication bandwidth. The largest intensity maxima in the near-field region is problematic too because according to the FDA guidelines [48] the time-averaged acoustic intensity in tissue must always be kept smaller than 7200 W/m^2 , meaning that the achievable intensity at the Rayleigh distance of an unfocused transducer is always scaled down given the maxima of the intensity profile is in the near-field region. This issue is accentuated if one includes the propagation loss of the tissue. The sensitivity to lateral misalignment and the problem of near-field maxima can be solved using focused transducers described below.

Spherically and Cylindrically Focused Transducers

It is possible to geometrically shape the transmitting surface of the external transducer in order to sculpt arbitrary-shaped high-intensity regions. As shown in Figure 2.6 for instance, a single focal spot can be obtained if the transducer takes a spherical shape because in this case the waves generated by particles on the surface of the sphere travel the same distance and hence add up constructively only at the origin of the spherical transducer. Therefore, the spherically focused transducer has only a single intensity maxima, but is fairly sensitive to both axial and lateral misalignment.

The unfocused and spherically focused transducers are two extreme cases. A good com-

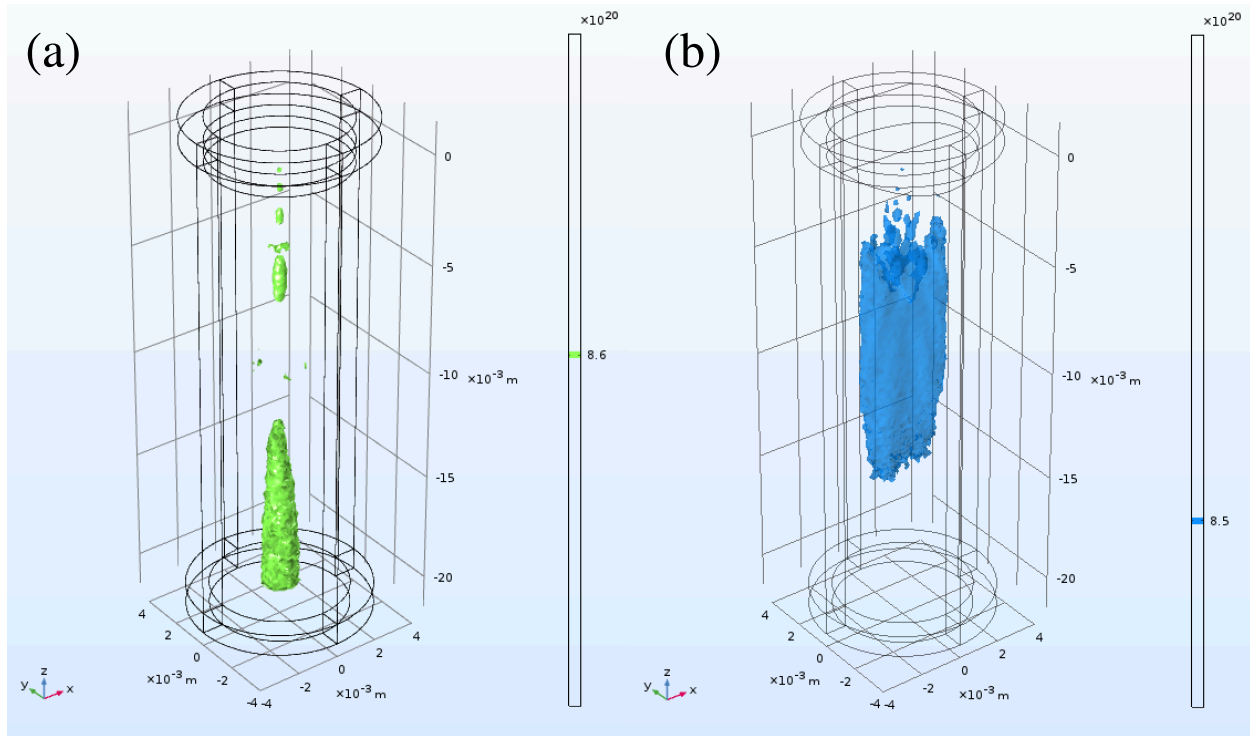


Figure 2.7: 3D simulated intensity profiles (with equal-intensity isosurfaces) of (a) an unfocused, and (b) a cylindrically focused external transducer with focal depth of 9 mm. The diameter of both transducers is 6 mm. Operation frequency is 3 MHz.

promise between these two is the cylindrically focused transducer. Compared to the unfocused transducer, it offers more design flexibility because of an extra degree of freedom that is the radius of the cylinder. Unlike the spherically focused transducer, it has a focal *line* that is along the height of the cylinder. Figure 2.7 compares the intensity profiles of an unfocused transducer with that of a cylindrically focused transducer both having a diameter of 6 mm and operating at 3 MHz. The radius (depth of operation) of the cylinder is 9 mm in this case. The axial and lateral pressure intensity profiles of the two transducers are shown in Figure 2.8 for various cylindrical radii of 4 mm, 9 mm, and 14 mm. It can be seen that compared to the unfocused transducer, increasing the curvature of the cylinder (decreasing radius) enhances the intensity and widens the lateral focal length but narrows the axial focal length. Therefore, the diameter and the radius of the cylindrical curvature are the two design parameters that can be tuned to achieve the focal area of interest.

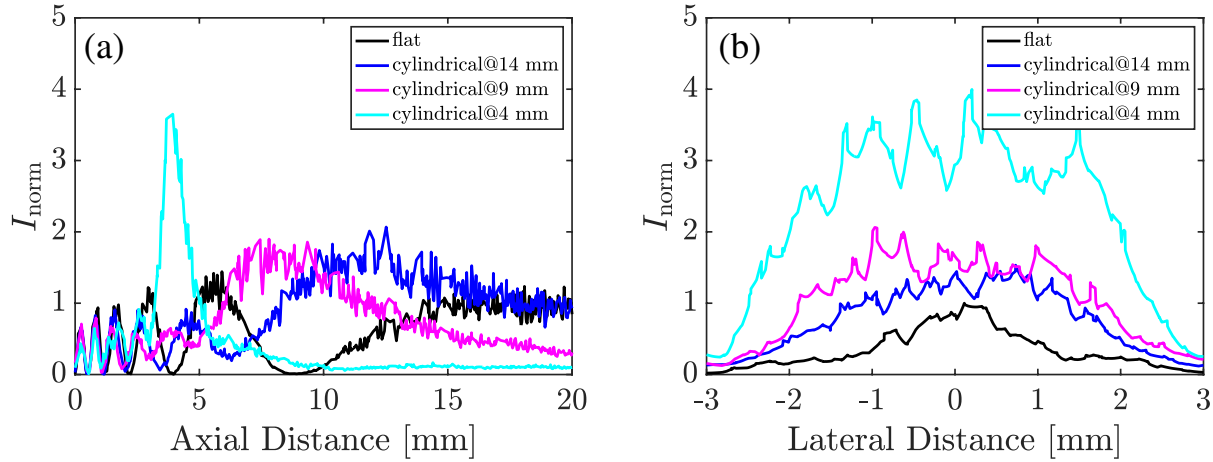


Figure 2.8: Comparison of simulated axial and lateral intensity profiles of an unfocused and cylindrically focused external transducers designed with various focal depths (4 mm, 9 mm, 14 mm). The diameter of all transducers is 6 mm. Operation frequency is 3 MHz. All intensities are normalized to the far-field peak intensity of the unfocused transducer.

2.3 Power Receiver Design

For neural implants, the geometry of the implant piezo is a critical design parameter since it determines the volume of the implant, the operating frequency, and the harvested power made available to the implant active circuitry. Design variables are the thickness (T) and aspect ratio (AR) of the piezo. We define AR as the ratio of the piezo width to its thickness as illustrated in Figure 2.9(a). In this section, we discuss different characteristics of the implant piezo from power harvesting and delivery perspectives and provide a systematic design approach for the implant piezo geometry and operation frequency with the objective of piezo miniaturization.

Mechanical resonant modes of bulk piezos with moderate aspect ratios suitable for implants can be classified to width expander (WE) and longitudinal expander (LE) for respectively large (>1) and small (<1) aspect ratios (AR s). In each mode, the piezo mechanically resonates along its major dimension, width or thickness respectively. Although, piezoelectric constitutive equations exist for the two resonant modes that can be used for analysis as briefly described earlier in this chapter and in detail in [9], for this study, we used a parametric FEM simulation (using COMSOL Multiphysics) because the two resonant modes are strongly coupled for $AR \sim 1$ and are not well-described by a single set of equations. We used a 2D axisymmetric model of the piezo with a surface area equivalent to that of a cuboid shown in Figure 2.9(a). A common piezo material (lead zirconated titanite, PZT-5H, with a mechanical quality factor of 50 and a dielectric loss tangent of 0.02) was used, while the model included a tissue phantom with the specific acoustic impedance of 1.5 MRayls sur-

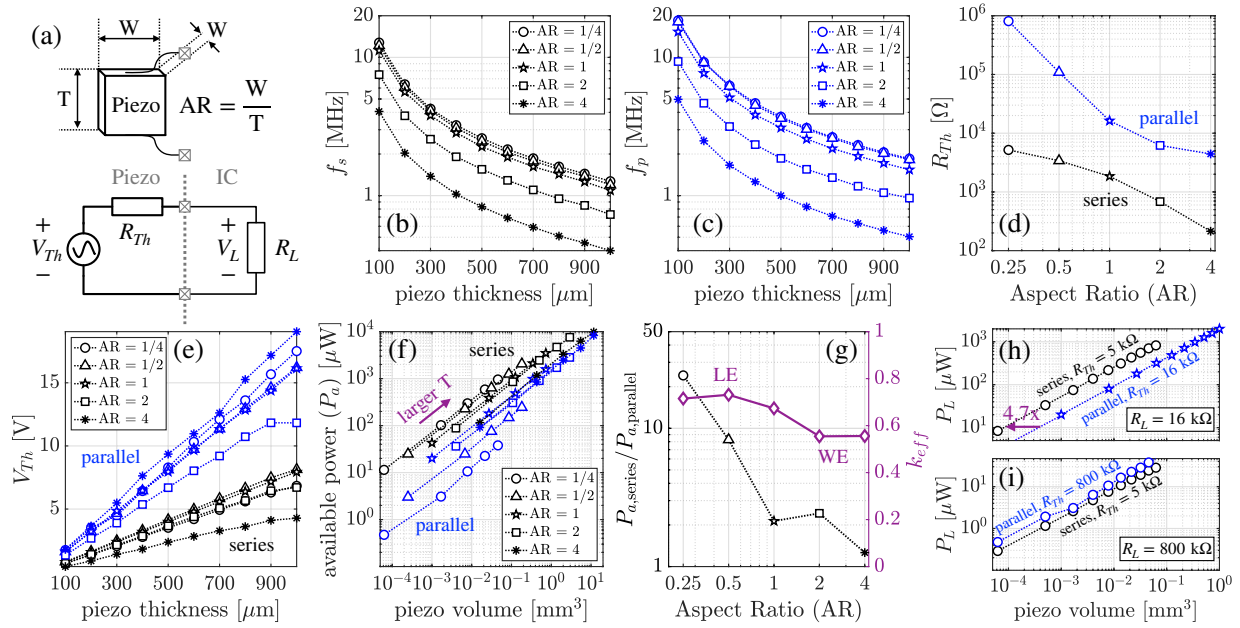


Figure 2.9: (a) Implant piezo geometry and its Thevenin equivalent circuit at resonance. Finite Element Simulation (FEM) results of the (b) series resonant frequency, (c) parallel resonant frequency, (d) resistance and (e) open circuit voltage with an incident pressure intensity of 720 mW/cm^2 for various piezo thicknesses and aspect ratios. (f) Simulated V_{Th} and R_{Th} values in (d) and (e) were used to calculate the available power per unit volume of the implant piezo (volumetric efficiency) at f_s and f_p . (g) Relative available power at f_s and f_p and its correlation with piezo resonant modes: Longitudinal Expander (LE) and Width Expander (WE) resonant modes determined using the effective electromechanical coupling factor of the piezo, k_{eff} . (h) A design example when operating at f_s with a relatively small impedance mismatch results in a smaller piezo volume compared to operating at f_p with a perfect piezo-load impedance matching. (i) A design example when operating at f_s with a relatively large impedance mismatch results in a larger piezo volume compared to operating at f_p with a perfect piezo-load impedance matching. Note: In all plots, each aspect ratio is shown using a unique marker (*e.g.*, Δ for $AR = 1/2$)

rounding the implant piezo. The model was encapsulated with a perfectly matched layer, while frequency domain analyses were used for simulating the impedance and harvested power.

The link operating frequency is often chosen to be the resonant frequency of the implant piezo because: (1) at resonance the piezo has the highest electromechanical transduction efficiency and exhibits a resistive internal impedance. Therefore, maximum power delivery to the IC can be obtained without impedance matching networks; (2) more importantly, as

demonstrated in Chapter 3, the implant uplink modulator has the maximum backscatter modulation strength at the piezo resonant frequencies. Figure 2.9(b) and (c) show the simulated series, f_s , and parallel resonant frequencies, f_p , of the piezo for thicknesses ranging from 100 μm to 1000 μm and aspect ratios ranging from 1/4 to 4. $\text{AR} < 1/4$ is impractical due to mechanical fragility and therefore ignored in this study.

At resonance, the piezo can be modeled by its Thevenin equivalent circuit, shown in Figure 2.9(a). It can be shown that in general R_{Th} is a function of AR and V_{Th} is linearly proportional to the piezo thickness as simulated and shown in Figures 2.9(d) and (e). The simulated V_{Th} in Figure 2.9(e) was found by applying an incident (background) pressure field of $p_i = 147$ kPa (equivalent to the regulated pressure intensity of 720 mW/cm^2 in tissue [48]), and recording the open-circuit voltage of the implant piezo for all the geometries. The impedance of the piezo was simulated in absence of the background field using a test voltage source connected across the piezo terminals. The simulated V_{Th} and R_{Th} were used to calculate the available power, P_a , by the piezo for all the possible geometrical configurations (T and AR). Because the implant piezo is non-planar, volumetric efficiency (P_a per unit volume) is used as a figure of merit when comparing different configurations, as shown in Figure 2.9(f).

The simulated volumetric efficiency shown in Figure 2.9(f) is grouped based on the aspect ratio and the type of the resonant frequency. It is observed for a fixed AR, the piezo thickness can be used as a proxy to trade P_a with the volume of the piezo. But because the slope of the curves in Figure 2.9(f) is only 6.6 dB/decade, trading P_a with the piezo volume degrades the volumetric efficiency of the piezo. For instance, increasing P_a by 100x requires the volume of the piezo to be increased by 1000x, ultimately degrading the volumetric efficiency by 10x. Instead of thickness, the aspect ratio of the piezo can be used to improve the volumetric efficiency. At f_s , decreasing the aspect ratio asymptotically improves the volumetric efficiency as shown in Figure 2.9(f). For example, at any given P_a , a ~ 10 x reduction in volume can be achieved by decreasing the AR from 4 to 1/4. A similar but opposite trend is found at f_p , that is increasing the AR enhances the volumetric efficiency.

The final parameter for improving the volumetric efficiency is the type of the resonant frequency. As shown in Figure 2.9(f), a piezo operating at f_s generally provides a larger P_a per unit volume compared to f_p . This discrepancy in P_a is more evident for smaller aspect ratios as demonstrated in Figure 2.9(g) and can be explained as follows. The piezo converts acoustical energy carried by pressure waves to electrical energy. The input acoustical energy to the piezo is maximum when the pressures exerted on the opposite sides of the piezo are in phase, *i.e.* out-of-phase pressures result in a net force acting on the piezo body without creating any internal stress/strain. The phase shift of the incident acoustic wave measured across the front and back faces of an implanted piezo in tissue is given by $\theta = 2\pi fT/v_{tissue}$, where f is the wave frequency and v_{tissue} is the propagation speed of sound in tissue (for most tissue types is ~ 1500 m/s [3]). Resonant frequencies of an LE-resonating piezo are $f_p = v_{piezo}/2T$ and $f_s = f_p\sqrt{1 - k_{eff}^2}$ [9], where v_{piezo} is the speed of sound in the piezo material (~ 4500 m/s for PZT-5H) and k_{eff} is the effective electromechanical coupling

factor of the piezo that is ~ 0.7 as shown in Figure 2.9(g). Therefore, $\theta_{parallel} \sim 3\pi$, but $\theta_{series} \sim 2\pi$ for small ARs.

That is, small aspect ratios increase k_{eff} and decrease θ_{series} ultimately resulting in an enhanced net pressure applied across the piezo terminals. The elevated net pressure results in a larger acoustical energy input to the piezo at f_s and therefore larger available electrical power from the piezo. Thus, the minimum piezo volume can be achieved when operating at f_s and as long as R_{Th} is scaled (using AR, see Figure 2.9(d)) to match the load impedance, R_L . According to Figure 2.9(d), however, R_{Th} at f_s has a finite range, meaning that for large R_L values (>5 k Ω in Figure 2.9(d)), impedance matching cannot be achieved at f_s . Therefore, for $R_L > 5$ k Ω , two possible designs exist: (I) operation at f_p with matched piezo-load impedances ($R_L = R_{Th,p}$), and (II) operation at f_s without impedance matching ($R_L \neq R_{Th,s}$). The general equation describing the relationship between the piezo available power, P_a , required power delivered to the load, P_L , the piezo and load impedances R_{Th} and R_L is given by

$$P_L = P_a \frac{4R_L}{R_{Th}} \left(1 + \frac{R_L}{R_{Th}}\right)^{-2}. \quad (2.36)$$

Using (2.36) and known R_L , the two previously described designs can be compared. Two design examples are to follow to demonstrate the process. At f_s , the piezo with an aspect ratio of 1/4 has the highest volumetric efficiency and the largest $R_{Th,s}$ compared to other configurations, making it the best geometry for power delivery to large R_L values. Therefore, only AR of 1/4 for design II needs to be considered for the comparison. Now let's compare the two designs when $R_L = 16$ k Ω (for moderately high power consumption ICs). A piezo with an aspect ratio of 1 at f_p has $R_{Th,p}$ of 16 k Ω , Figure 2.9(d). Therefore, according to (2.36), $P_L = P_{a,p}$ for this design. The series resonating piezo with AR of 1/4 has $R_{Th,s}$ of 5 k Ω , so $P_L = 0.72P_{a,s}$, meaning that for this configuration only 72% of the available power is delivered to $R_L = 16$ k Ω due to the piezo-load impedance mismatch. Therefore, the available power curves in Figure 2.9(f) for the two designs are respectively scaled by 1 and 0.72 for arbitrary P_L as shown in Figure 2.9(h) for comparison. It can be observed from Figure 2.9(h) that for $R_L = 16$ k Ω operation at f_s (without impedance matching) results in a 4.7x smaller piezo volume compared to operation under maximum power transfer condition at f_p . As another example for ultra-low-power ICs, consider the case where $R_L = 800$ k Ω . For this load, impedance matching and therefore $P_L = P_{a,p}$ can be obtained at f_p by choosing AR of 1/4, Figure 2.9(d). Conversely, the series resonating piezo with AR of 1/4 has $R_{Th,s} = 5$ k Ω , resulting in $P_L = 0.025P_{a,s}$, meaning that for this configuration only 2.5% of the available power is delivered to $R_L = 800$ k Ω . Therefore, the available power curves in Figure 2.9(f) for the two designs are respectively scaled by 1 and 0.025 for arbitrary P_L as shown in Figure 2.9(i) for comparison. Unlike the previous example, operation at f_s is found to require 2x larger piezo volume to deliver the same amount of power to the load compared to operation at f_p .

In summary, the design approach that results in the minimum implant piezo volume is as follows. For a given R_L and P_L , the aspect ratio of the implant piezo is designed to obtain

$R_{Th,s} = R_L$ at f_s . Using Figure 2.9(f) and known P_L and AR, the minimum volume of the implant piezo is found and the design is complete. If $R_{Th,s} = R_L$ cannot be achieved at f_s (due to prohibitively small AR), two cases are considered: (I) operation at f_p with matched piezo-load impedances, and (II) operation at f_s without impedance matching. For each case, the required available power by the piezo, P_a , to deliver P_L to the load is found using (2.36). For P_a calculation, $R_{Th,p} = R_L$ (achieved by proper choice of aspect ratio at f_p) for case (I), and the largest possible $R_{Th,s}$ (smallest possible aspect ratio) is used for case (II). Using calculated P_a and known AR, Figure 2.9(f) is used to obtain the piezo volume for case (I) and (II), respectively. Finally, the obtained piezo volumes are compared, and the smaller one is chosen to complete the design.

2.4 Design Case Study

In the previous section, we presented a systematic design approach for the geometrical design of the implant piezo for the case the electrical loading of the implant piezo was modeled by a resistor R_L . In most practical cases, however, the implant delivers power to an active integrated circuit (IC) whose input stage is a rectifier that is a non-linear load. In this section, we extend the design procedure for piezo active loads and provide a design example to illustrate the process.

Miniaturizing An Implantable Wireless Neurostimulator

In this section, we present a design methodology for minimizing piezo volume suitable for neural implants and we use deep-tissue neurostimulators that can be used for either peripheral nerve or brain tissue stimulation as our target application.

The ultrasonic power harvesting system of the stimulator can be modeled by the simplified circuit shown in Figure 2.10. The stimulator is represented by an ideal rectifier and a load current sink that requires a minimum voltage headroom of V_L to model the power consumption constraints. Note that this is a generic circuit model for implant ICs. The power source is a resonating piezo (actuated by incident ultrasound waves launched by an external transducer) that is modelled by its Thevenin equivalent circuit at resonance. The piezo is actuated by the local acoustic intensity that is regulated to a maximum of 7200 W/m² for diagnostic ultrasound [48]. The local ultrasound intensity is a complex function of the operation depth, acoustic properties (density and speed of sound) of the medium, type and geometry of the external transducer. We assume maximum acoustic intensity is locally available at the depth of interest, which is a valid assumption for focused external transducers, e.g. spherical, whose intensity profiles have a maxima at their designed focal point. In reality, the intensity in all tissue areas must not exceed 7200 W/m², and ensuring so requires careful modelling of the external transducer and entire channel, which is beyond the scope of this section.

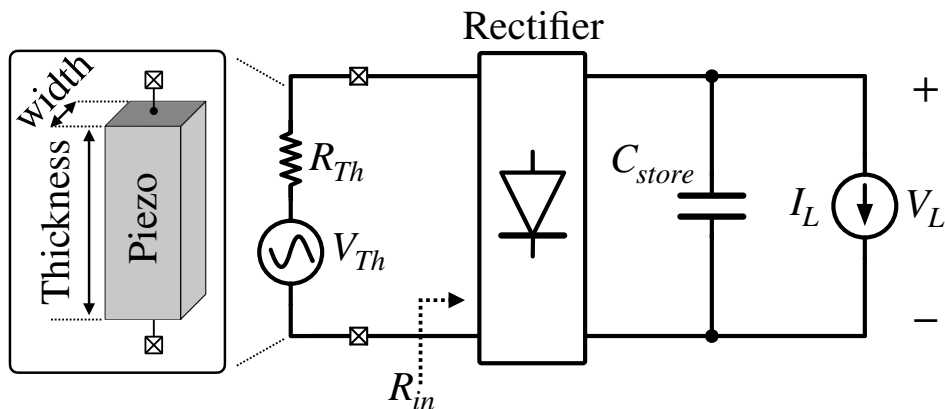


Figure 2.10: The generic ultrasonic implant model.

As shown in Figure 2.10, the design constraints are V_L and I_L , and the design space is the geometry (aspect ratio and thickness) of the piezo. For neural stimulation, we target an average current consumption of $100\mu\text{A}$ and a minimum rectified voltage V_L of 2.5 V. These numbers are consistent with those used in previously reported neuromodulating implants in the peripheral nervous system [13, 62], and the brain [73] that have been experimentally shown to invoke neural activity *in vivo*. The design process starts by characterizing the implant piezo, namely V_{Th} and R_{Th} , at the resonant frequency. A bulk piezo with a moderate aspect ratio ($\text{AR} = \text{width}/\text{thickness}$), used in most ultrasonic implants, mechanically resonates along its major dimension [9]. There are two fundamental resonant frequencies, namely series and parallel. At either resonant frequency, the reactive components of the piezo electrical impedance cancel out leaving only a resistance that is modeled by R_{Th} . The piezo model is completed with the open circuit AC voltage source V_{Th} . Finite element solvers are used to solve for the electrical impedance of the piezo, resonance frequencies, R_{Th} , and V_{Th} for various aspect ratios and thicknesses. Solving 3D finite element models provides a more accurate estimate of these parameters compared to available closed form 1D analytical expressions especially for $\text{ARs} = 1$ when there is a considerable mode coupling between different resonant modes that is not easily described with a single set of equations. The simulated parameters are then stored in look-up tables and used throughout the design process. For a lead-zirconate-titanate (PZT-5H) piezo with an $\text{AR} = 1$, these parameters are shown in Figures 2.11(a) and (b). At resonance, V_{Th} linearly scales with the piezo thickness, while R_{Th} is independent of thickness and is only a decaying function of AR. With known R_{Th} and V_{Th} for a given geometry (thickness and AR), the maximum available power per volume of piezo can be calculated. For a PZT-5H piezo with an $\text{AR} = 1$, this is shown in Figure 2.11(c) at the series resonance frequency.

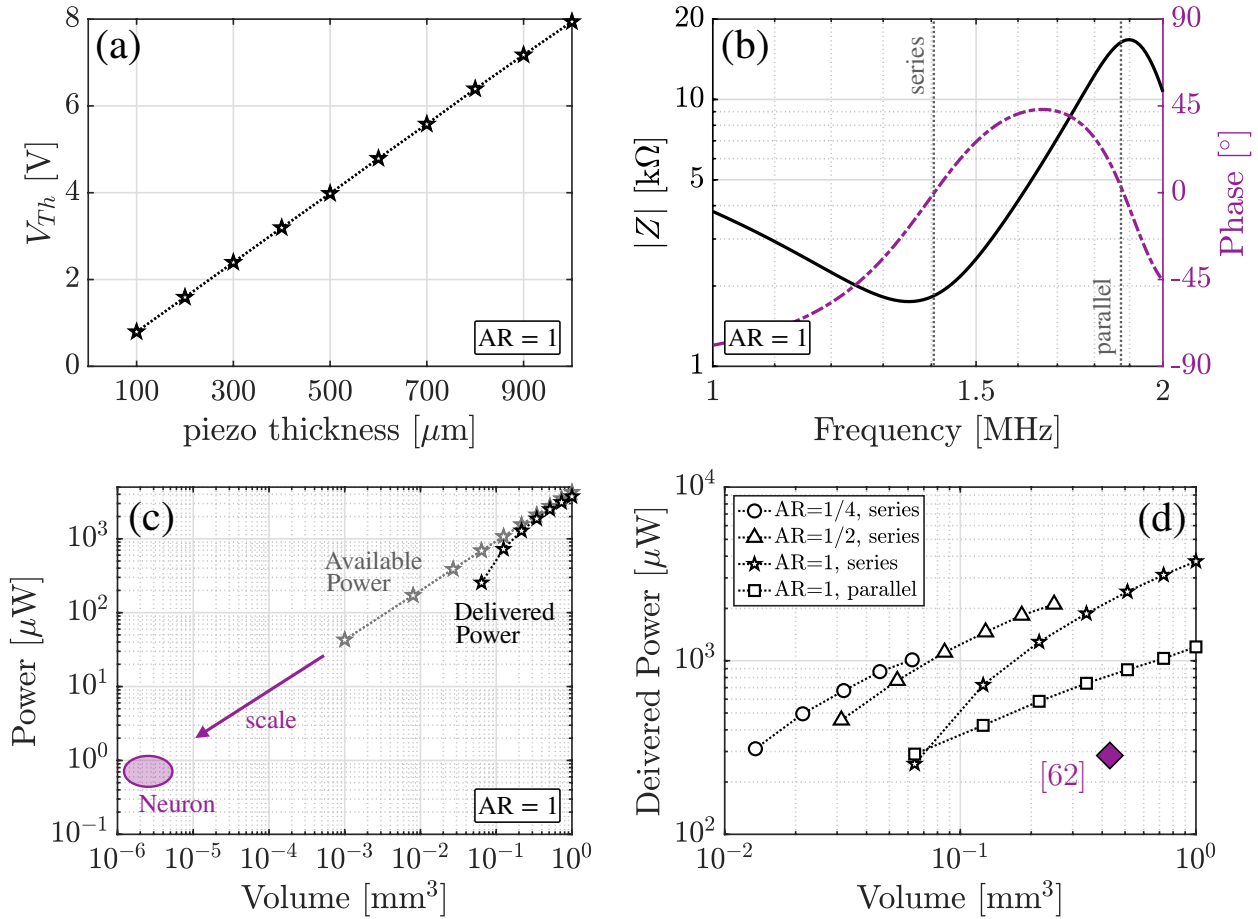


Figure 2.11: The piezo (a) open-circuit voltage, (b) impedance, and (c) calculated maximum available power with the unity aspect ratio (AR) at 7200 W/m^2 of local ultrasound intensity. The estimated maximum available power at the neuron dimensions is significant. (d) Designed piezo geometries and a comparison to prior art.

To harvest the maximum power, the input impedance of the chip R_{in} should be matched to the piezo resistance R_{Th} , and any mismatch will decrease the delivered power. The following equation, derived from the conservation of energy, can be used to approximate the delivered power to the load:

$$I_L \approx \frac{2}{\pi} \frac{V_{Th}}{R_{Th}} \left(1 - \frac{V_L}{V_{Th}}\right) \left(1 - \frac{2}{\pi} \text{asin}\left(\frac{V_L}{V_{Th}}\right)\right). \quad (2.37)$$

For a known load voltage, 2.5 V, the above expression can be numerically solved for I_L , for different combinations of V_{Th} and R_{Th} that are ultimately mapped to different geometries and volumes using previously introduced look-up tables. Any geometry that provides $I_L > 100 \mu A$ is a solution. The same process can be repeated for other aspect ratios at both series and parallel resonant frequencies. A summary of acceptable geometries is shown in Figure 2.11(d) for the neural stimulating implant constraints outlined earlier. Interestingly, we find that decreasing the aspect ratio of the piezo roughly maintains delivered power while decreasing the volume. The smallest piezo volume that delivers 250 μW of power while the rectifier maintains $V_L \geq 2.5 V$ is found to be 0.013 mm³ for a piezo with AR = 1/4. This is an order of magnitude smaller than the piezo used in [62]. In [62], a margin of error was included to account for non-idealities caused by the encapsulation, misalignment, and tissue inhomogeneity. Improved encapsulation and tissue modeling, and lower AR would allow the use of a significantly smaller piezo. Moreover, scaling the piezo size to the size of a neuron (Figure 2.11(c)) could potentially harvest non-negligible amounts of power (1 μW), enough to power a sensor. At these scales other elements such as the IC and interconnect would likely dominate the volume, but it demonstrates that there is significant room for innovation and advancing the state of the art for low-power miniature implants.

Power Transmitter Design

The design approach discussed above assumes the use of a focused transducer and that the maximum acoustic intensity of 7200 W/m² is locally available at the location of the implant. However, unfocused external transducers are frequently used to provide flexibility on the depth of operation and marginal resilience to lateral misalignment. In such cases, implants are typically placed close to the Rayleigh distance which provides a relatively wide and flat far-field focal arena.

An example of the axial acoustic intensity profile of an unfocused radial external transducer is shown in Figure 2.12, for a designed depth of 20 mm, R=4.5 mm, $\lambda=1$ mm, $\alpha=2.2$ dB/(cm·MHz) and at the operating frequency of 1.5 MHz. This axial intensity profile can either be found using finite element methods or by using available closed-form expressions [61]. Unlike a focused transducer, the maximum of the intensity profile occurs at an unintended depth, i.e., the near field region (Figure 2.12). Keeping the maximum intensity below the safety limit of 7200 W/m² results in a 5 \times smaller intensity at the intended operation depth (20 mm in this example). Since the harvested piezo voltage amplitude, V_{Th} , scales linearly with the square root of the ultrasound intensity, the previously obtained V_{Th} voltages would

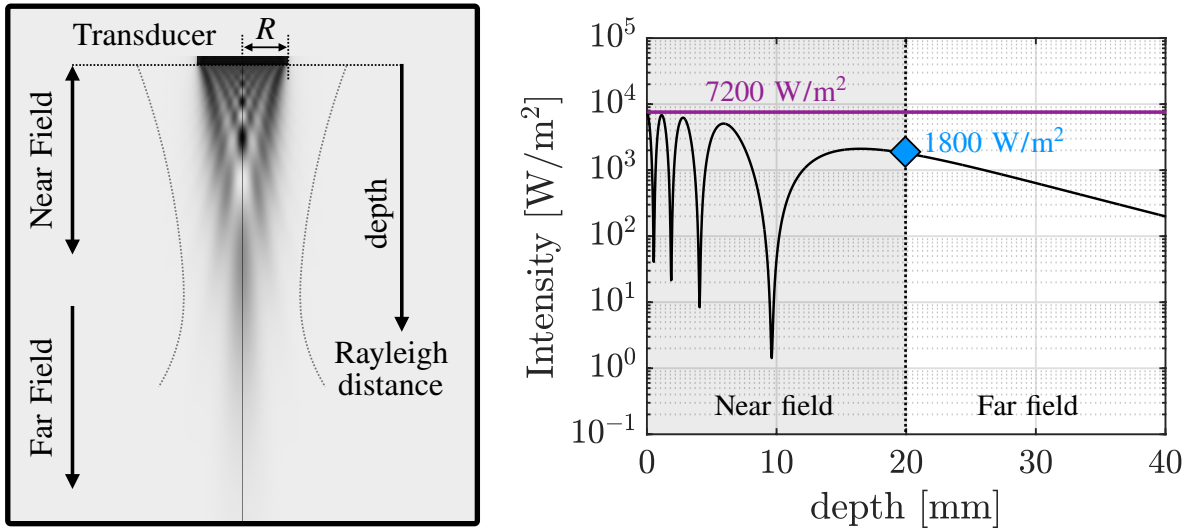


Figure 2.12: Axial intensity of an unfocused radial external transducer with a Rayleigh distance of 20 mm.

need to be scaled down according to the new local intensities at the depth of interest. The same design process described earlier can be repeated with the updated values of V_{Th} to obtain the minimum piezo volumes.

2.5 Summary

In this chapter, we provided the background information on piezoelectricity and discussed various aspects of ultrasonic wireless power transmission links. In particular, the fundamentals of piezoelectricity, its constitutive relations and equivalent circuit models for two common piezo resonance modes (TE and LE) were presented. Using piezo equivalent three-port network, the circuit model of the link was presented and used to describe the end-to-end link efficiency. Three different types of single-element external transducers (unfocused, spherically and cylindrically focused) were briefly described and compared. And finally, using the volumetric efficiency as a figure of merit, we presented a design guideline for the aspect ratio and thickness of the implant piezo that minimizes the overall implant volume as far as power harvesting is concerned. A practical design example for a neural stimulating implant was also presented to demonstrate the proposed design steps.

This chapter included a direct adaptation of two sections of the following articles:

- (a) R. Muller, **M. M. Ghanbari**, and A. Zhou. “Miniaturized Wireless Neural Interfaces: A tutorial.” *IEEE Solid-State Circuits Magazine* 13, no. 4 (2021): 88–97.
- (b) **M. M. Ghanbari**, and R. Muller. “Optimizing volumetric efficiency and backscatter communication in biosensing ultrasonic implants.” *IEEE Transactions on Biomedical Circuits and Systems* 14, no. 6 (2020): 1381–1392.

Personal contribution: I drafted the last section of article (a), generated the majority of the figures and discussed/reviewed the contents of the final manuscript with the co-authors. Regarding article (b), I wrote the original draft of the manuscript, performed all the analyses and experimental verification.

Acknowledgements: Regarding article (a), all authors contributed to the draft of the original manuscript. R. Muller reviewed the manuscripts and provided advice on the technical aspects of the research. R. Muller was the principal investigator of both works.

Chapter 3

Ultrasonic Wireless Data Transmission

A growing number of ultrasonic mm-scale implants have recently been proposed for interacting with deeply-seated human nerves [70, 23, 62, 39] and monitoring a wide range of physiological signals, such as pressure [81], temperature [61, 71], blood oxygen saturation [75], gastric waves [52] and tissue impedance [47] from deep anatomical regions. Reported implant volumes as small as 0.065 mm^3 [71], *in vitro* wireless operation ranges of up to 12 mm [81] and fully untethered *in vivo* implantation in live rodents [62] demonstrate the potential of miniature ultrasonically powered implants as a viable solution for deep-tissue therapy and biosensing.

The basic components of an ultrasonic implant, conceptually shown in Figure 3.1, are a piezoceramic resonator (or piezo) and an integrated circuit (IC). The implant piezo functions as an acoustic antenna enabling the implant to harvest energy from ultrasound waves launched by a distant external transducer (interrogator). The power management unit (PMU) of the implant IC conditions the harvested energy to perform signal acquisition and wireless data back telemetry. The acquired biological signal is wirelessly transmitted to the external transducer by the uplink modulator of the IC for further processing. For implantable devices, to reduce tissue displacement and enable minimally invasive non-surgical implantation techniques, *e.g.* injection, the overall implant volume should be kept small, *e.g.* sub- mm^3 . Given that the volume of the implant is dominated by the piezo, the majority of the aforementioned prior art use a single-piezo implant assembly where data uplink is realized by modulating the amplitude of the ultrasound echo reflected from the implant piezo (backscattering). For ultra-low power biosensing ICs, backscatter communication obviates the need for external capacitors or a secondary piezo and consequently results in the smallest possible implant form factor [23, 71].

In this chapter, we perform a thorough characterization of the ultrasonic backscatter communication channel to help advance state-of-the-art uplink backscatter modulators in terms of data rate and linearity. The uplink backscatter modulator in Figure 3.1 in its simplest representation is a variable shunt impedance Z_E connected across the piezo terminals

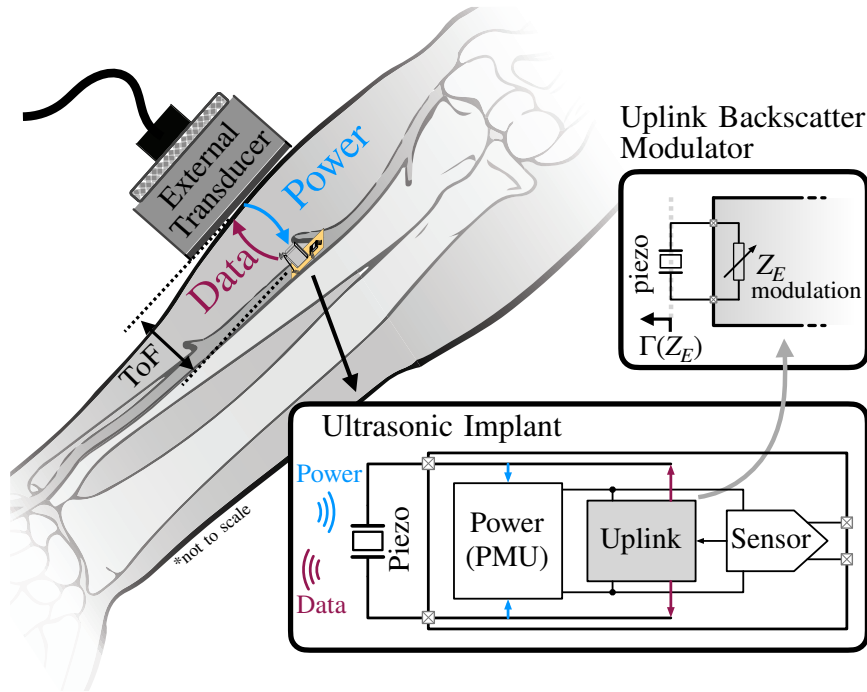


Figure 3.1: A single-piezo ultrasonic biosensing implant with backscatter uplink modulator.

that modulates the acoustic reflection coefficient of the piezo Γ . Resistive [32], capacitive [50] and FET [70, 71] shunt modulating networks have been previously explored. Due to lack of a tool for piezo-IC co-simulation or any known analytical relationship between Γ and the uplink modulating impedance Z_E , previous implementations of digital backscatter modulators have been limited to the most basic type of digital modulation (on-off keying, OOK) [75, 71], and previously reported analog backscatter modulators have been designed empirically and suffered from significant nonlinearity [70, 61]. We therefore pay special attention to the characterization of $\Gamma(Z_E)$ and provide an end-to-end equivalent circuit model of the channel for piezo-IC co-simulation in a common CAD tool. Moreover, we provide universal closed-form expressions for $\Gamma(Z_E)$ to include: 1) Γ 's dependence on Z_E at both the series and parallel resonant frequencies 2) the effect of low-Q mechanically damped piezo, and 3) the effect of air-backing. We briefly discuss how one can leverage the derived analytical closed form expressions to improve the linearity of an analog backscatter modulator or implement amplitude shift keying digital modulation to enhance the data rate of a digital backscatter modulator relative to the commonly used OOK modulation. The derived expressions require only a single parameter, piezo internal impedance, that can easily be measured or accurately simulated prior to any piezo-circuit codesign. The results (Γ vs. Z_E) predicted by the derived expressions are shown to be in good agreement with those obtained by the finite element method (FEM) simulation and experiments, validating their accuracy.

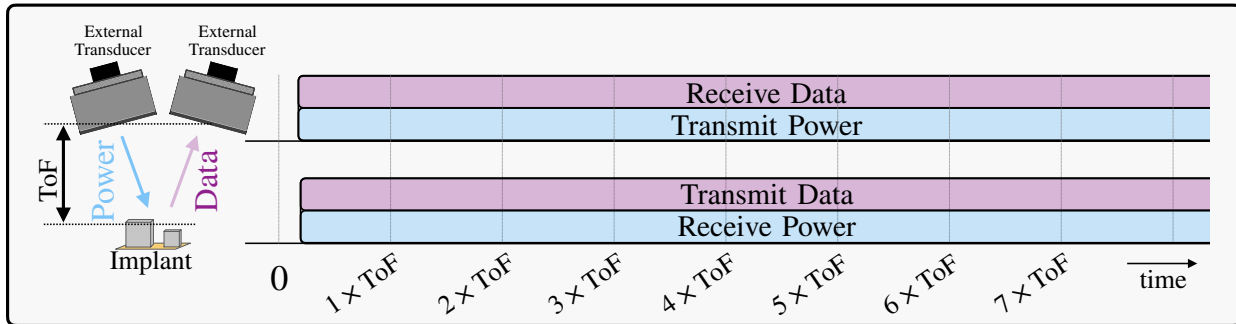
In Section 3.1, various aspects of wireless data transmission in ultrasonic links such as active and backscatter communication protocols, multiple-access protocols, and type of modulation schemes (analog vs. digital) are discussed. In Section 3.2, the backscatter protocol is discussed in detail where the main components of the round-trip channel path loss in backscatter links are highlighted and evaluated. An end-to-end SPICE friendly hybrid equivalent circuit model of the channel useful to numerically solve for $\Gamma(Z_E)$ is presented in Section 3.2. Closed-form expressions for $\Gamma(Z_E)$ under various boundary conditions are introduced in Section 3.3. Section 3.4 discusses optimal geometrical design of the implant piezo for backscatter communication. Experimental verification of the derived expressions is presented in Section 3.5.

3.1 Power+Data Transmission Protocols

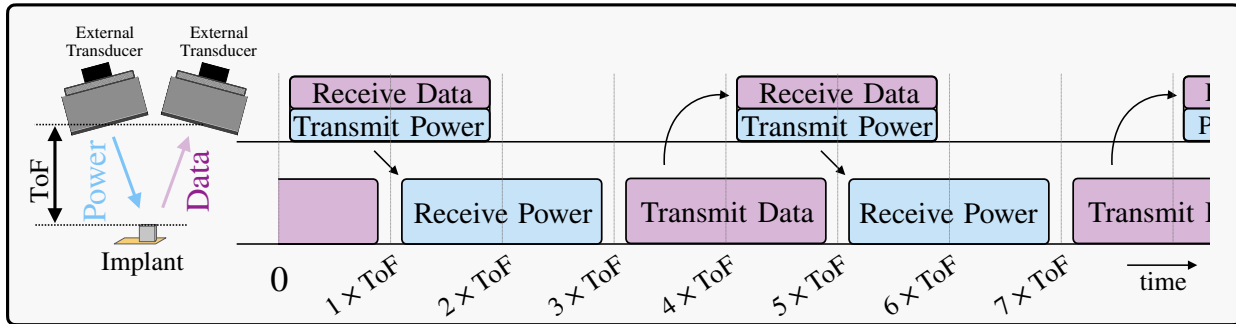
Active Drive vs. Pulse-echo

Bulk piezoceramic (piezo) resonators are ultrasound transducers that are commonly used as both implant energy harvesters and data transmitters/receivers [80, 23]. Separate power transmission and data communication links have been previously demonstrated in ultrasonic implants [11, 51]. This mode of operation, shown in Figure 3.2(a), enables continuous data transmission and high data rates, but limits the miniaturization of the implant volume since it requires two ultrasound resonators preferably tuned at distant frequencies to minimize carrier leakage. Therefore, it is desirable to reduce the number of piezos to one per implant. In a *single-piezo* implant, there exist two previously reported schemes that perform both power delivery and uplink data transmission: 1. sequential power harvesting followed by active drive [81], and 2. simultaneous power harvesting and echo modulation [24]. In both of the schemes, the ultrasound power pulse is generated by a distant external transducer. The former requires an additional transducer for receiving data as illustrated in Figure 3.2(b). In this case, once the power harvesting phase is over and energy is stored on a capacitor, the implant piezo is actively driven by the implant circuit to transmit data back to the second external transducer where it is acquired and subsequently demodulated and post-processed. In the second case, known as the pulse-echo/backscatter scheme, uplink data transmission is realized by modulating the amplitude of the echo of the power delivery pulse, Figure 3.2(c). In the pulse-echo scheme, the modulated echo carrying uplink data is received by the same external transducer that initially transmitted the power pulse. Therefore, to avoid an excessive dynamic range requirement of the analog front-end of the receive chain, the pulse/echo duration is restricted to twice that of the time of flight (ToF) between the external transducer and the implant resulting in a 50% duty cycle for data transmission. Although the data transmission period of the time-duplex active drive scheme is not constrained by the ToF, actively driving the piezo rapidly discharges the implant charge-reservoir and consequently must be short, usually <50% of the time, and immediately followed by another power pulse. Moreover, unlike the pulse-echo scheme, for the time-duplex active drive, *two* external trans-

(a) Continuous Active Drive



(b) Time Duplex Active Drive



(c) Pulse-Echo (Backscatter)

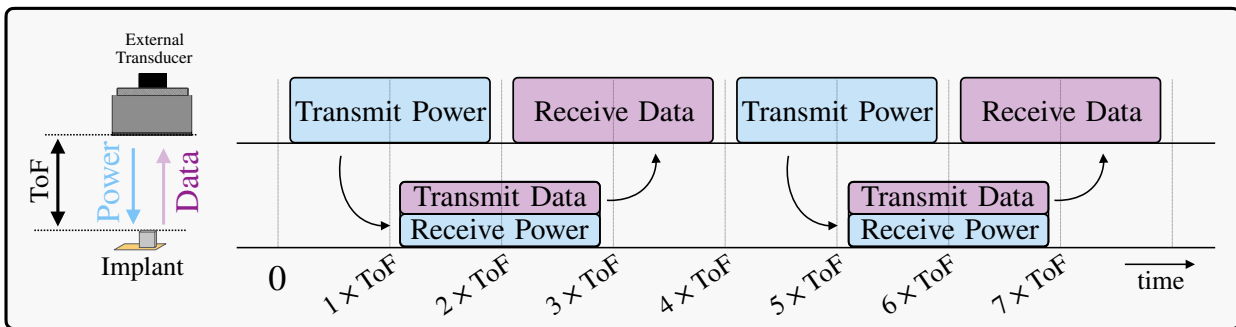


Figure 3.2: Previously reported power and uplink protocols for (a) continuous power and data communication with a dual-piezo implant. Single-piezo implant protocols include (b) active drive: sequential power harvesting and uplink data transmission, and (c) pulse-echo scheme: simultaneous power harvesting and uplink echo modulation.

ducers need to be aligned to the miniature implant piezo that increases the complexity and cost of the setup. Therefore, in this work we focus primarily on the pulse-echo scheme as it helps with implant miniaturization, requires a single interrogator, and does not compromise

the communication bandwidth relative to time-duplex active drive. In this chapter, we discuss the underlying mechanisms of ultrasound backscattering using piezos and obtain design equations that can be used to implement a backscatter modulation scheme, m-level ASK, that is spectrally more efficient than the commonly used OOK.

Multiple Access Protocols

The two single-implant wireless schemes described above can be modified to achieve multi-implant communications. Multi-site ultrasound power delivery has been previously demonstrated by external ultrasound phased-arrays [10] or a single-element transducers [24]. In either case, power is delivered to the implants during pre-determined time slots shared between all implants. A significantly more challenging problem in a multi-implant setting is the uplink data transmission from multiple implants. Classic RF multiple access communication protocols, namely frequency-division multiple access (FDMA), time-division multiple access (TDMA), and code-division multiple access (CDMA) are possible options.

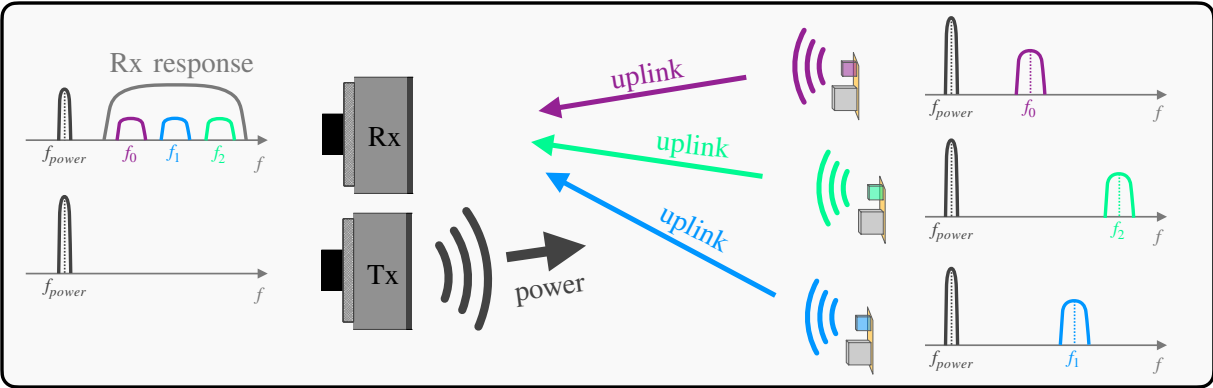
FDMA

In a frequency-division multiple-access channel, implants use non-overlapping frequency bands for data uplink. Given the constraints of the existing power+data protocols of ultrasonic neural implants, FDMA can be realized on either the main carrier or on subcarriers as shown in Figure 3.3(a) and (b). In the former, each implant actively drives a dedicated uplink piezo tuned at a unique frequency for data back telemetry. Although, continuous wireless power delivery and maximum uplink data rate is possible, implementation of this scheme is practically challenging because the geometry (thickness) of each implant's uplink piezo must be different from that of the other implants so each implant has a unique resonant frequency. Also, given backscattering is a linear transformation (i.e., reflected and incident waves are at the same frequency), FDMA on unique main carriers is not possible in backscatter links to the best of our knowledge.

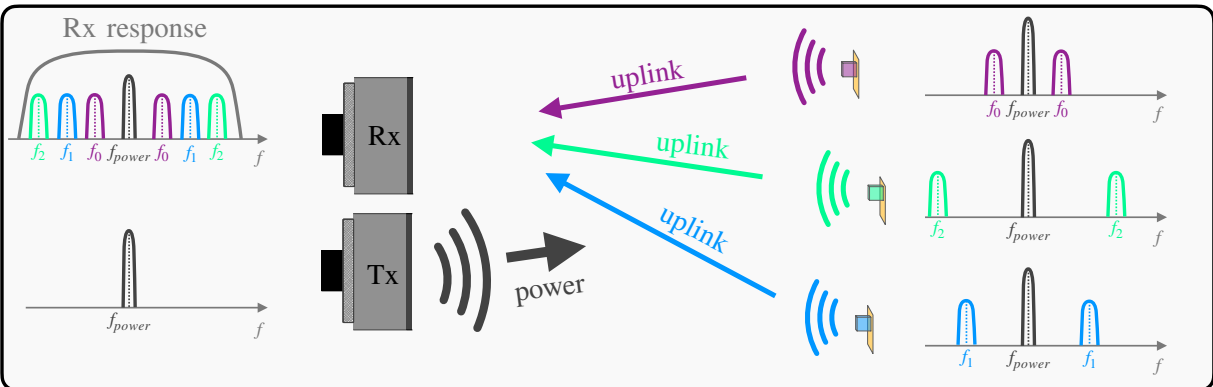
CDMA

FDMA can be realized on unique subcarriers as shown in Figure 3.3(b) to alleviate the practical challenges of the classic FDMA protocol mentioned above. In this scheme, each implant first modulates a unique (internally generated) subcarrier that is then used to modulate the main carrier. Unlike the classic FDMA scheme, this scheme lends itself better to single-piezo power+data protocols. A particularly interesting form of this scheme, CDMA, results if orthogonal subcarriers are used by the implants as shown in Figure 3.3(c). With orthogonal subcarriers, all implants share the available frequency band and have the same geometrical design [24], and the channel sensitivity to multipath reflections can be significantly reduced by using a simple multipath-correlator receiver, e.g. Rake [77]. Also, similar to cellular CDMA, the intermittent neural signal can be exploited (by squelching) to enhance the bit

(a) FDMA



(b) FDMA : Subcarrier



(c) CDMA : Subcarrier

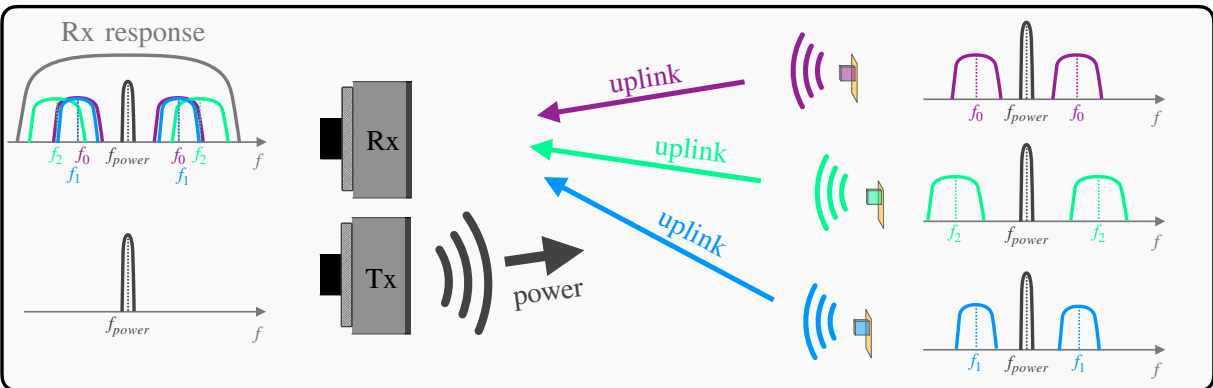


Figure 3.3: Multiple access protocols using (a) FDMA on main carrier, (b) FDMA on subcarriers, (c) CDMA on subcarriers.

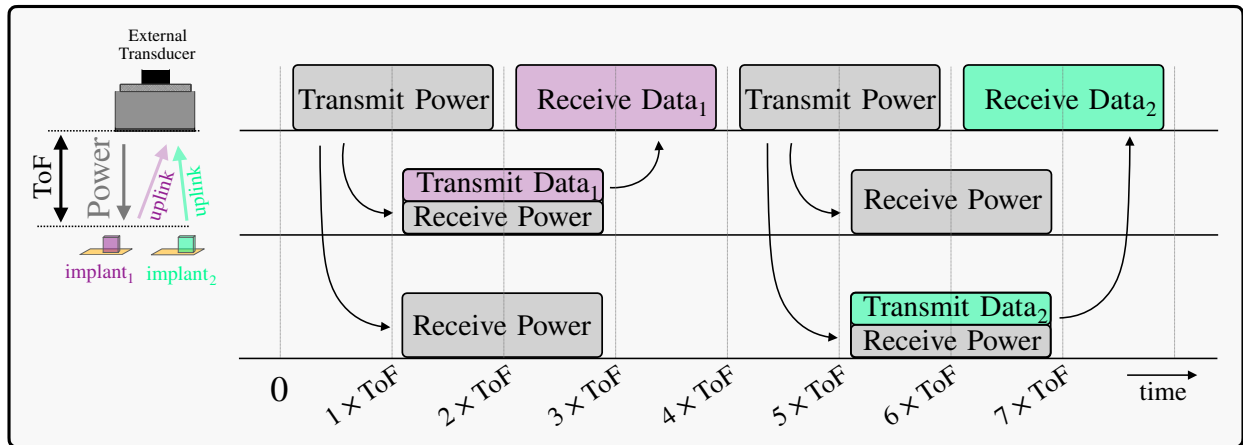


Figure 3.4: An example of a TDMA protocol for a pulse-echo channel with two implants

error rate (BER) at high data rates [25]. The orthogonality of subcarriers in a CDMA ultrasound channel can be compromised if the relative depths of the implants are altered. In Chapter 4, we demonstrate multi-implant communication using a CDMA scheme.

TDMA

The pulse-echo communication link in Figure 3.2(c) can also accommodate time-division multiple-access protocols as conceptually shown in Figure 3.4. Each implant has a dedicated time slot during which it has the full control of the uplink. Unlike the other multiple-access protocols, in this scheme, implants must have enough memory to store data collected prior to beginning of their uplink time slot. The implants must also have a *virtual* counter shared between them to keep track of the channel master at any time. In Chapter 6, we present the implementation of an implant that employs TDMA for multiple access.

Analog, Digital and Quasi-digital Uplink

Figure 3.5 shows a typical echo pulse of an ultrasonic implant when analog echo modulation (AM) is used for data back-telemetry. After implant power up and initialization, the amplitude of the echo is modulated according to the recorded neural signal. A comparison between the required echo period $T_{echo,min}$ for analog and digital echo modulation (DM) along with their bounce diagrams are shown in Figure 3.5. Assuming the same number of ultrasound cycles ($1/f_{main,carrier}$) is required for the amplitude to settle or switch between states, the required pulse period for the case of DM is larger than that of AM by roughly the number of digital bits transmitted in each echo. In other words, AM carries higher information per cycle than DM. To prevent overlapping the transmitted pulse and the echo, the

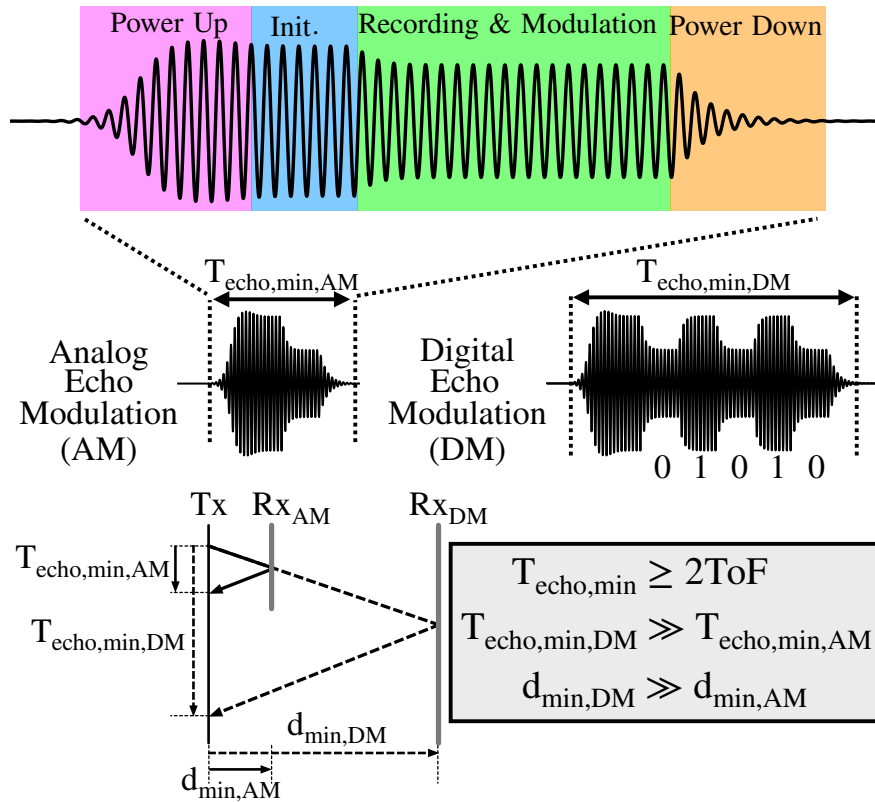


Figure 3.5: (top) A typical ultrasound pulse with analog echo modulation (AM); (bottom) comparison between Analog and Digital echo modulation schemes and their corresponding bounce diagrams

pulse duration must be smaller than the round-trip time between the external interrogator (Tx) and the implant (Rx), or $< 2\text{ToF}$. Thus, the minimum distance between the implant and the external transducer in the case of B-bit digital modulation, $d_{\min,DM}$, is B times larger than that of AM. For a $d_{\min,AM}$ distance shown in Figure 3.5, only a single bit of data can be transmitted using DM. The same principle holds true when subcarrier modulation takes place. The maximum interrogation frequency in a pulse-echo communication channel is given by $f_{\text{sample}} = 1/2T_{\text{echo,min}}$. In addition to extending the operating range (by allowing shorter distances between Tx and Rx), AM uplink requires shorter $T_{\text{echo,min}}$ and hence can enable higher interrogation frequencies and ultimately uplink data rates.

The AM uplink, however, has little immunity to the noise of the channel as the carrier noise contaminates the SNR of the transmitted signal [70]. Therefore, the acquired neural signal must be adequately amplified before transmission to maintain its SNR as shown in Chapter 4.

Digital OOK has the best noise efficiency while AM has the best spectral efficiency (ig-

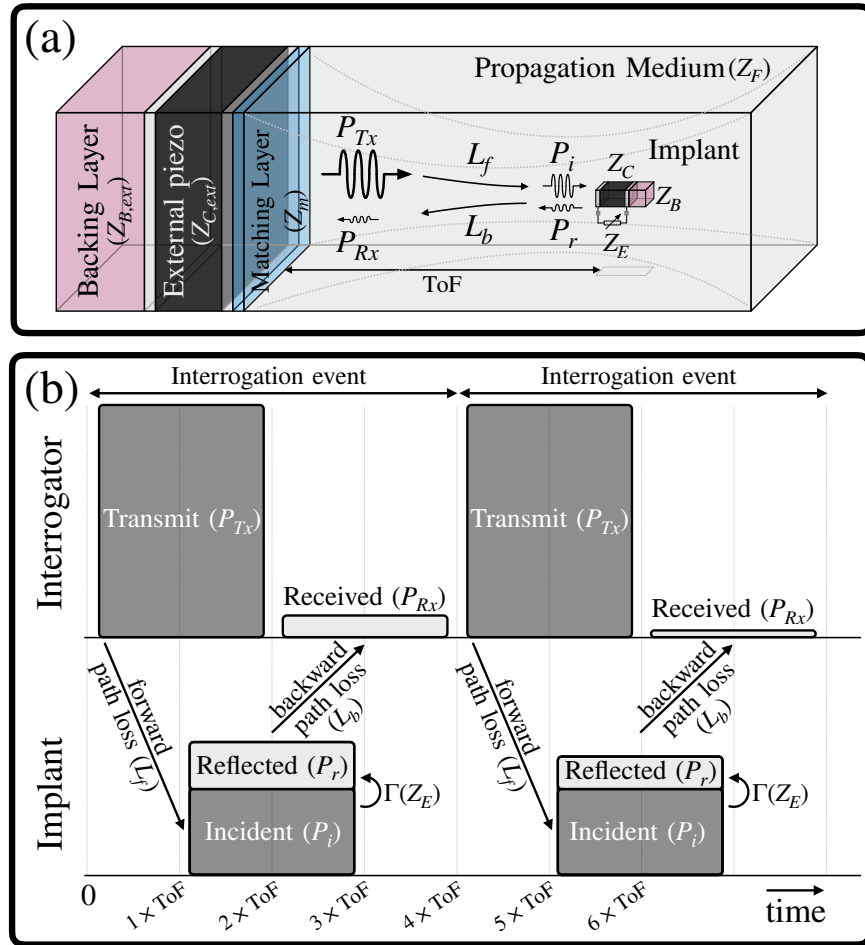


Figure 3.6: (a) Typical backscatter communication channel, and (b) timing diagram of each interrogation event.

noring phase modulation that is challenging for ultrasound backscatter links). A compromise between the two is perhaps the quasi-digital m -level ASK modulation scheme whose transmission data rate is $\log_2(m)$ times that of OOK, and m can be used as a proxy to trade noise immunity and data rate. The system and circuit implementations of an m -level backscatter modulator is discussed in great detail in Chapter 6.

3.2 Channel Equivalent Circuit Model

In a backscatter communication protocol, an interrogation event begins with the interrogator launching a wavelet (denoted as P_{Tx} in Figure 3.6) towards the implant. While propagating, P_{Tx} is attenuated and spread out such that only a fraction of its power, P_i , impinges the

front face of the implant piezo. The forward path loss (L_f) is used to formally quantify P_i/P_{Tx} . Due to the finite propagation speed of sound in the medium, P_i arrives at the location of the implant after a single time of flight (ToF). At this time, P_i branches into three components: P_E , P_r and P_{leak} : P_E is the harvested electric power available at the electrical terminals of the implant piezo, P_r is the reflected acoustic power and P_{leak} is the power of the wave passing by the implant piezo. The implant IC modulates the piezo acoustic reflection coefficient by adjusting Z_E to encode data for back telemetry, that is $P_r = \Gamma(Z_E)P_i$. It takes another ToF for the wave front of the reflected pressure field P_r to arrive at the location of the external transducer. P_r also experiences attenuation and spreading determined by the backward propagation path loss (L_b). Similar to L_f , L_b is characterized by P_{Rx}/P_r . Finally, the external transducer converts the received pressure field power P_{Rx} into electrical voltage to allow for signal conditioning, demodulation and data postprocessing. Because the same external transducer is used for receiving the backscattered field, the duration of the P_{Tx} wavelet should not exceed the roundtrip travel time ($2 \times$ ToF) as shown in the protocol timing diagram in Figure 3.6(b).

The complete analysis and end-to-end simulation of the backscatter communication channel described above is challenging mainly for its transient multi-domain electro-acoustical nature. Modeling acoustical systems with equivalent electrical elements is a well-established method for simplifying the analysis [36, 70, 5, 74]. Equivalent circuit models of the interrogator-implant pair have been used in [70, 5, 74] for the analysis of power delivery to the implant. Such equivalent circuit models however are best accurate when there is only a single degree of freedom for the wave to propagate. For instance, because the spreading component of the path loss cannot be easily modeled by 1D equivalent circuit models, [70, 5], and [74] ignore the wave spreading and only include the attenuation component of the path loss. It will be shown shortly, however, that the loss due to spreading is an order of magnitude larger than that due to attenuation. To address this, we use a hybrid FEM-circuit equivalent model of the channel.

We first characterize the round-trip channel path loss using a FEM solver. The results obtained from this FEM study are then incorporated into an equivalent circuit model to simulate the channel response. The roundtrip path loss of the backscatter channel shown in Figure 3.6 is given by

$$L_T = \frac{P_{Rx}}{P_{Tx}} = L_f \cdot \Gamma(Z_E) \cdot L_b. \quad (3.1)$$

In (3.1), $\Gamma(Z_E)$ is the backscatter modulating component which will be thoroughly dealt with in the following sections. L_f and L_b are the forward and backward path losses which are 0 dB for a lossless channel. The backscatter channel shown in Figure 3.6, has two contributing loss mechanisms in each direction; attenuation and spreading:

$$L_f = L_{f,a} \cdot L_{f,s} \quad (3.2)$$

$$L_b = L_{b,a} \cdot L_{b,s}. \quad (3.3)$$

In (3.2) and (3.3), $L_{f,a} \sim L_{b,a} = e^{-2\alpha}$ is the attenuation due to thermal loss of vibrating

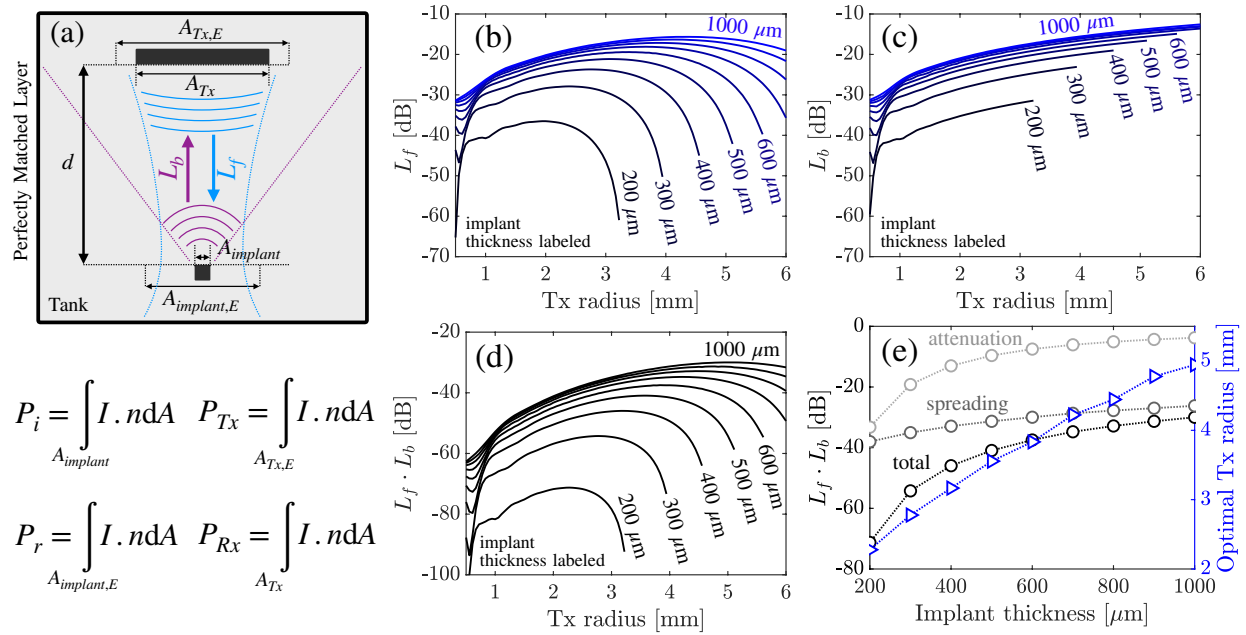


Figure 3.7: FEM simulation of channel path loss. (a) Simulation setup. Simulated (b) forward, (c) backward, and (d) round-trip path loss for various implant thicknesses (with aspect ratio of 1) and TX radii. (e) Optimal TX radius and relative contribution of spreading and attenuation components of the path loss.

particles in a viscous propagation medium, where $\alpha = a \cdot f^b$ is the attenuation constant for which a and b are found empirically for the medium of interest, *e.g.* $a = 2.2$ dB/cm.MHz, and $b = 0.8$ for muscle tissue [58]. The spreading loss $L_{f,s}$ is due to the suboptimal radiation pattern of the transmitted field P_{T_x} and the small aperture of the implant piezo. Ideally, all of the transmitted power P_{T_x} is focused on the aperture of the implant piezo and $L_{f,s}$ is 0 dB. But, $L_{f,s}$ degrades when the implant piezo becomes small relative to the dimensions of the foci.

For instance, the focal area of an unfocused 5 mm radius circular transducer is ~ 30 mm², and an implant piezo with a 1 mm² aperture receives only 3% of the power of the wave available at the foci.

Similarly, because the radiation pattern of the backscattered field P_r is approximately spherical, and the aperture of the external transducer is finite, only a fraction of the backscattered power is received by the external transducer resulting in backscattered spreading loss $L_{b,s}$. To quantify the channel path loss, we used a parametric FEM simulation using COMSOL Multiphysics. For the implant piezo with thicknesses ranging from 200 μm to 1000 μm , we simultaneously solved for the optimal aperture of the external transducer and its associated optimal link path loss for a sample depth of 20 mm.

A frequency-domain 2D axisymmetric simulation with a setup shown in Figure 3.7(a) was used for this study. For quantifying $L_f (= P_i/P_{Tx})$, P_{Tx} was simulated by assigning a reference pressure boundary condition to the aperture of the external transducer (A_{Tx}). The frequency of the operation was set to the resonant frequency of the implant piezo for each configuration, Figure 2.9(b). P_{Tx} and P_i were calculated by integrating the simulated pressure intensity over the cross-sectional area of the external transducer and the implant $A_{Tx,E}$ and $A_{implant}$, respectively, as shown in Figure 3.7(a). Here, $A_{Tx,E}$ extends beyond the actual aperture of the external transducer by 100% to account for the entire transmitted power including the side lobes. For each implant piezo thickness, the radius of the external transducer was changed from 0.5 mm to 6 mm and the forward path loss L_f was calculated, shown in Figure 3.7(b). It can be observed that for each implant piezo size there exists an optimal transducer radius that results in the minimum forward path loss. A similar parametric simulation was performed to characterize $L_b (= P_{Rx}/P_r)$. That is, a pressure boundary condition was assigned to $A_{implant}$, and P_r and P_{Rx} were calculated by integrating the simulated pressure intensity over $A_{implant,E}$ and A_{Tx} , respectively. The integration cross-sectional area for computing P_r is extended beyond the actual aperture of the implant, $A_{implant}$, by 100% to account for the entire reflected wave power from the implant. Simulated L_b for each implant piezo size and for various apertures of the external transducer are shown in Figure 3.7(c). Using simulated L_f and L_b , the roundtrip path loss $L_f \cdot L_b$ was calculated, Figure 3.7(d). Comparing Figure 3.7(b) and (d), it can be observed that the backward path loss contribution to the roundtrip path loss has moved the optimal radius of the external transducer to slightly larger values. Finally, the roundtrip path loss for a given implant piezo size is shown in Figure 3.7(e). The relative contribution of the spreading and attenuation components of the path loss is also shown in Figure 3.7(e). Across all implant piezo thicknesses (and consequently operating frequencies) the spreading component of the path loss is between 5 to 23 dB larger than the attenuation component. We use the FEM simulated results shown in Figure 3.7(e) in the next section to incorporate the effect of path loss in the equivalent circuit model of the channel.

In this section, we use an equivalent circuit model, shown in Figure 3.8(a), to simulate the backscatter response of the channel in a common CAD tool. As discussed in Chapter 2, low AR piezos resonating in the longitudinal expander (LE) mode provide higher volumetric efficiency for the implants. Due to their high ARs, the piezo elements of the external transducers are usually excited at the thickness extensional (TE) mode to create a directional field towards the target implant [35]. Both LE and TE modes can be represented by the same equivalent circuit model as long as the right material constants are used. Here, we use the Redwood [66] equivalent circuit model for the two piezo elements of the channel, because unlike the Mason [49] or KLM [37], the Redwood model is more SPICE friendly. In particular, KLM has a frequency dependent transformer turn ratio that cannot be easily simulated in SPICE. Similarly, Mason requires impedances with unconventional nonlinear frequency dependence that is challenging to implement in common simulation tools. Other derivations of the original Redwood model, such as Leach [40], can equivalently be used in the following analysis as well.

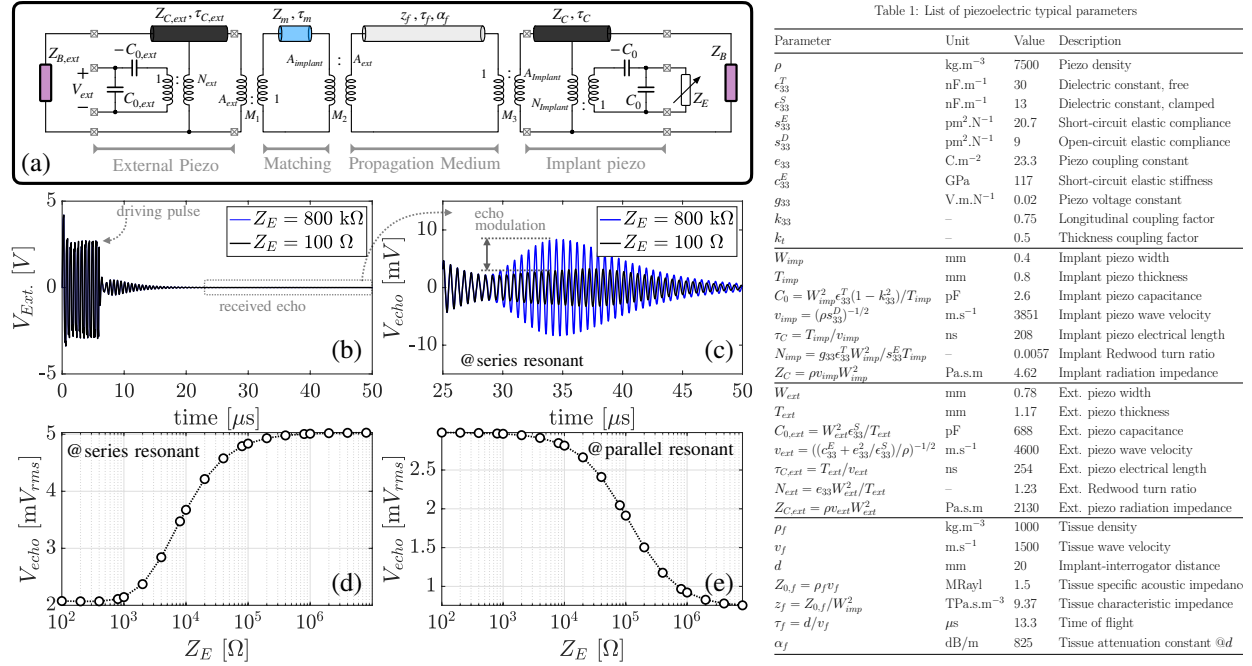


Figure 3.8: (a) end-to-end equivalent circuit model of channel. Simulated (b) transient response of channel (c) received echo signal. Received echo vs. Z_E at (d) the series resonant and (e) parallel resonant frequencies.

The LE and TE piezoelectric constitutive equations can be collapsed into a set of linear equations as follows [35]

$$\begin{bmatrix} F_1 \\ F_2 \\ V_3 \end{bmatrix} = \mathbf{P} \cdot \begin{bmatrix} v_1 \\ v_2 \\ I_3 \end{bmatrix} = \begin{bmatrix} m & n & p \\ n & m & p \\ p & p & r \end{bmatrix} \begin{bmatrix} v_1 \\ v_2 \\ I_3 \end{bmatrix} \quad (3.4)$$

$$\begin{bmatrix} F_1 \\ F_2 \\ V_3 \end{bmatrix} = \begin{bmatrix} Z_C & Z_C & N \\ j \tan(\beta l) & j \sin(\beta l) & j \omega C_0 \\ Z_C & Z_C & N \\ j \sin(\beta l) & j \tan(\beta l) & j \omega C_0 \\ N & N & 1 \\ j \omega C_0 & j \omega C_0 & j \omega C_0 \end{bmatrix} \begin{bmatrix} v_1 \\ v_2 \\ I_3 \end{bmatrix} \quad (3.5)$$

relating the electrical and the two acoustical ports of a bulk piezo, resonating primarily along its major dimension. In (3.4) and (3.5), F and v are respectively force and wave particle velocity at the two acoustical ports of the piezo, while V and I are the voltage and current at its electrical port. The description of the other parameters used in (3.5) for the external and implant piezo elements in Figure 3.8(a) and their typical values used in this study are listed in Table I. The Redwood model directly implements (3.5). The acoustical ports 1 and 2 are expressed in terms of force (F) and particle velocity (v), and therefore characteristic

impedance of the transmission line (Z_C and $Z_{C,ext}$) in the model is the radiation acoustic impedance of the piezo, *e.g.* $Z_{C,ext} = Z_0 A_{ext}$ where Z_0 is the specific acoustic impedance of the piezo material, and A_{ext} is its cross-section area. The electrical length of the transmission line in the model (τ_C and $\tau_{C,ext}$) is simply set by the physical thickness of the piezo divided by the wave propagation speed in the piezo (see Table I). All the parameters of the Redwood circuit model (C_0 , Z_C , τ and N) can be calculated once the piezo material, geometry and type of resonance mode are known. The second acoustical port of each piezo element in Figure 3.8(a) is terminated by the radiation acoustic impedance of the backing layer (Z_B and $Z_{B,ext}$). Two transformers M_1 and M_3 are used at the front face of the piezo elements (acoustical port 1) to properly scale F and v by the cross-section area of each piezo (A) and change variables to respectively pressure $p = F/A$ and volume velocity $u = vA$.

A quarter-wavelength matching layer is used at the front (emitting) acoustical terminal of the external transducer to acoustically match the impedance of the external transducer $Z_{C,ext}$ to that of tissue z_f . The characteristic impedance of the matching layer is the geometric mean of the impedances seen to the left and right of the matching layer. A composite of multiple matching layers can also be used to improve the impedance matching bandwidth or in cases where a single matching layer is not feasible (due to unavailability of a material for the required Z_m) [35]. The propagating medium is modeled by a transmission line with the characteristic impedance of z_f and electrical length of τ_f .

In Figure 3.8(a), transformer M_2 is used to model a perfect lossless focusing of the beam on the implant aperture. The total FEM simulated roundtrip path loss for an implant piezo with a thickness of 800 μm is -33 dB at the distance of 20 mm with roughly equal forward and backward loss contributions of -18 and -15 dB, respectively. To account for this path loss, the transmission line modeling the propagation medium is assumed to be lossy with a mean attenuation constant of $\alpha_f = 825$ dB/m. We used *Cadence Virtuoso* to simulate the response of the channel. In this simulation, the external transducer was first driven by 10 cycles of a square wave, and then is immediately short circuited to discharge any residual charge across its terminals. Then, the interrogator is switched to the receive mode to capture the backscattered voltage. A sample transient received backscattered voltage for Z_E of 100 Ω and 800 k Ω is shown in Figure 3.8(c) when the operation frequency is tuned to the series resonant frequency of the implant piezo. The implant has no backing layer in this setup. The associated rms voltage of the received echoes for various Z_E values at the series and parallel resonant frequencies of the implant piezo are shown in Figures 3.8(d) and (e). It can be observed that the received backscattered signal is a monotonic but nonlinear function of Z_E . Moreover, it behaves differently at the series (increasing function of Z_E) and parallel resonant frequencies (decreasing function of Z_E).

The end-to-end equivalent circuit model of the channel described above is useful not only for the transient analyses but also for noise analyses and evaluating the response of the channel when a custom active backscatter modulator is used [24]. This circuit, however, lacks simplicity and therefore is not as helpful in the *design* and *synthesis* of novel backscatter modulators. In the next section, we present simple analytically derived expressions for $\Gamma(Z_E)$ that provide insight into critical design aspects of the backscatter modulator.

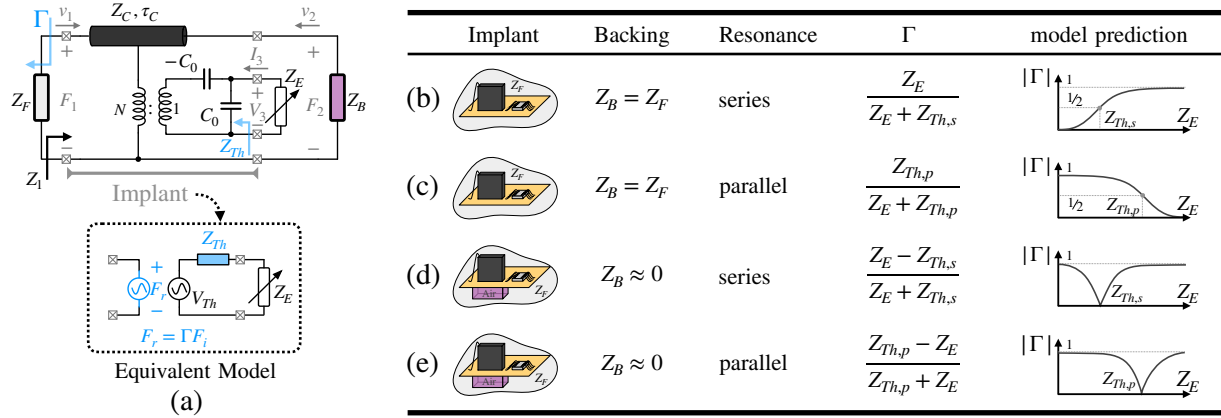


Figure 3.9: Proposed piezo electro-acoustical model (a) coupling the Thevenin equivalent circuit model of the piezo to its acoustic reflection coefficient. Expressions for reflection coefficient at parallel and series resonant frequencies for two common backing boundary conditions are listed in (b)-(e).

3.3 Simplified Implant Piezo Model

The Redwood equivalent circuit model of the implant piezo is redrawn in Figure 3.9(a)(top). Finding a closed-form relationship between the reflection coefficient evaluated at the front acoustical terminal of the piezo Γ and Z_E is of interest.

[60] formulated the relationship between Z_E and Γ for a resonant piezo and numerically solved for $\Gamma(Z_E)$. Here, we expand the analysis in [60] and analytically derived closed-form expressions for $\Gamma(Z_E)$ to include: 1) Γ 's dependence on Z_E at both the series and parallel resonant frequencies 2) the effect of low-Q mechanically damped piezo with arbitrary τ , and 3) the effect of the backing layer of the piezo, e.g. air-backing.

By definition, the series and parallel resonant frequencies of a piezo are found for an acoustically unloaded piezo, *i.e.* $Z_F = Z_B = 0$, at which the electrical impedance of the piezo is purely resistive. Therefore, at these two frequencies, the complex equivalent electro-acoustical circuit models of the piezo (Mason[49], KLM [37] and Redwood [66]) can be reduced to the piezo Thevenin Equivalent circuit model, using an open-circuit AC voltage source and the piezo internal impedance at the respective resonant frequency. Such a Thevenin equivalent circuit model is very helpful and intuitive due to its simplicity but fails to address the existing coupling between the electrical and acoustical ports of the piezo and ultimately the relationship between Z_E and Γ . Illustrated in Figure 3.9(a)(bottom) is the proposed equivalent circuit model of the piezo that fills the electro-acoustical coupling gap of the Thevenin Equivalent circuit model. The proposed model includes a force source and replaces the internal resistance of the piezo with a complex impedance. The force source explicitly generates the reflected acoustic wave (echo) flowing through Z_F , *i.e.* propagat-

ing towards the interrogator. F_i is the force generated by the incident pressure field at the acoustic terminal of the piezo, and Γ is the Z_E -dependent reflection coefficient.

Similar to electromagnetic waves, the acoustic reflection coefficient at port 1 of the implant piezo shown in Figure 3.9(a)(top) is given by

$$\Gamma = \frac{Z_1 - Z_F}{Z_1 + Z_F}, \quad (3.6)$$

where Z_1 is the acoustical impedance seen into port 1 when port 2 and 3 are respectively terminated by Z_B and Z_E which is given by

$$Z_1 = \frac{p^2(2n - 2m - Z_B) + (Z_E + r)(m^2 - n^2 + mZ_B)}{(Z_E + r)(m + Z_B) - p^2}. \quad (3.7)$$

Dummy parameters m, n, p and r in (3.7) are defined in (3.4)–(3.5). By substituting (3.7) in (3.6), $\Gamma(Z_E)$ can be found.

Using (3.4), (3.5) and the acoustical boundary conditions ($F_1 = -Z_F v_1$ and $F_2 = -Z_B v_2$) in Figure 3.9(a)(top), the impedance seen into the electrical port of the piezo (port 3) is found as follow

$$Z_3 = r - \frac{p^2(Z_B + Z_F + 2(m - n))}{Z_B Z_F + m(Z_B + Z_F) + m^2 - n^2}. \quad (3.8)$$

Piezo series resonant frequency is a frequency at which the electrical impedance of an acoustically unloaded piezo ($Z_B = Z_F = 0$) has no imaginary component. Therefore, (3.8) at f_s results in

$$r(m^2 - n^2) = 2p^2(m - n). \quad (3.9)$$

Here, we use Z_3 instead of the previously used Z_{Th} to make indices compatible with the port numbers used in Figure 3.9. Now, let's derive Γ_s for the piezo with $Z_B = Z_F \neq 0$ at f_s . By substituting (3.6) in (3.7), and using (3.8)–(3.9), Γ_s can be found

$$\Gamma_s = \frac{1}{Z_E + Z_3} \cdot \frac{Z_E(m^2 - n^2 - Z_F^2) - rZ_F^2}{m^2 - n^2 + 2mZ_F + Z_F^2}. \quad (3.10)$$

Given at f_s , $m^2 - n^2 \gg Z_F^2 + 2mZ_F$ for typical tissue and piezo material constants, (3.10) can be approximated by

$$\Gamma_s \approx \frac{Z_E}{Z_E + Z_3}, \quad (3.11)$$

when $Z_B = Z_F \neq 0$. The same procedure can be used to derive $\Gamma_{s,air}$ for an air-backed piezo $Z_B = 0$ operating at f_s . That is, for an air-backed piezo, (3.8) becomes

$$\begin{aligned} Z_{3,air} &= r - \frac{p^2(Z_F + 2(m - n))}{mZ_F + m^2 - n^2} \\ &= Z_F \frac{mr - p^2}{mZ_F + m^2 - n^2}, \end{aligned} \quad (3.12)$$

where the second equality is resulted using (3.9). By substituting (3.7) in (3.6), and using (3.9) and (3.12), $\Gamma_{s,air}$ can be found

$$\Gamma_{s,air} = \frac{Z_E - Z_F \frac{mr-p^2}{m^2-n^2-mZ_F}}{Z_E + Z_F \frac{mr-p^2}{m^2-n^2+mZ_F}} \approx \frac{Z_E - Z_3}{Z_E + Z_3}. \quad (3.13)$$

At the parallel resonant frequency, $\beta l \rightarrow \pi$ and it can be shown that in (3.4) and (3.5) $m \rightarrow \infty$, $(m-n) \rightarrow \infty$, $(m+n) \rightarrow 0$ and $(1-n/m) \rightarrow 2$. Using these approximations, when $Z_B = Z_F \neq 0$ at f_p , (3.8) and (3.7) can be simplified to

$$Z_3 = r - \frac{2p^2(Z_F + m - n)}{Z_F^2 + 2mZ_F + m^2 - n^2} \approx \frac{-2p^2}{Z_F}, \quad (3.14)$$

$$Z_1 = Z_F - \frac{4p^2}{Z_E + r} \approx Z_F \left(1 + \frac{2Z_3}{Z_E}\right). \quad (3.15)$$

Γ_p can therefore be found by substituting (3.15) in (3.6), that is

$$\Gamma_p \approx \frac{Z_3}{Z_E + Z_3}. \quad (3.16)$$

In a similar fashion, $\Gamma_{p,air}$ for an air-backed piezo $Z_B = 0$ operating at f_p can be derived. In this case, Z_3 and Z_1 are given by

$$Z_3 = r - \frac{p^2(Z_F + 2(m-n))}{mZ_F + m^2 - n^2} \approx \frac{-4p^2}{Z_F}, \quad (3.17)$$

$$Z_1 = -\frac{4p^2}{Z_E + r} \approx \frac{Z_F Z_3}{Z_E}, \quad (3.18)$$

and using (3.6), $\Gamma_{p,air}$ is found as

$$\Gamma_{p,air} \approx \frac{Z_3 - Z_E}{Z_3 + Z_E}. \quad (3.19)$$

for an air-backed implant piezo, *i.e.* $Z_B = 0$, where Z_3 (or Z_{Th}) is the electrical impedance of the piezo at the frequency of interest. Interestingly, for an air-backed piezo where there is no flow of energy to the backside acoustic port, the acoustic reflection coefficient at port 1 is equal to the electrical reflection coefficient at port 3, as described by (3.13) and (3.19). The proposed electro-acoustical model, shown in Figure 3.9(a)(bottom), is well-defined once Z_{Th} at the frequency of operation is known. A summary of the derived expressions under different boundary conditions is listed in Figures 3.9(b)-(e).

According to (3.11) and (3.16), the amplitude of the echo is equal to the voltage across the piezo termination impedance at f_s , but at f_p is equal to the voltage drop across the internal impedance of the piezo. In either case, thanks to the linear relationship between Γ and V_3 , in order to design a linear analog backscatter modulator, one can linearly modulate V_3 using a synchronous up-conversion current mixer as demonstrated in [24]. In a similar fashion, equidistant discrete values of V_3 can be used to realize amplitude shift keying modulation in a backscatter communication channel to carry higher information per symbol compared to the commonly used on-off keying modulation and ultimately improve the data rate.

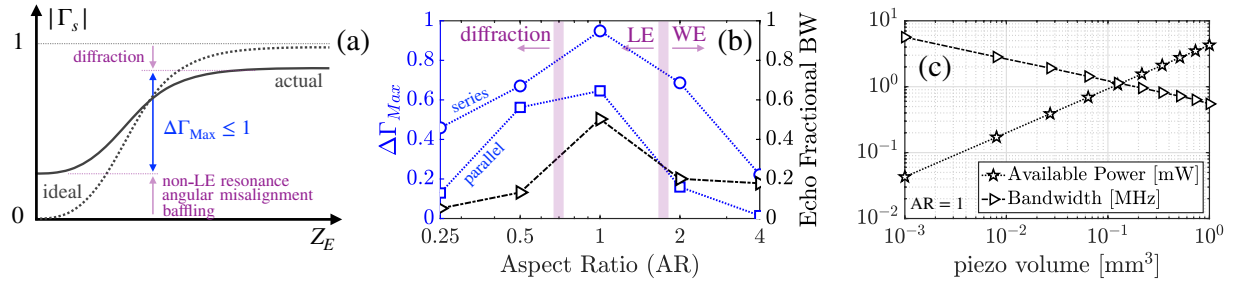


Figure 3.10: (a) Non-idealities that degrade $\Delta\Gamma_{Max}$. FEM simulation results show (b) decreasing the piezo AR initially enhances $\Delta\Gamma_{Max}$ as the piezo resonance mode changes from width expander (WE) to longitudinal expander (LE), but for $AR < 1$, $\Delta\Gamma_{Max}$ starts dropping due to diffraction. The simulated fractional bandwidth of the piezo follows a similar pattern. (c) Simulated available power and backscatter bandwidth for a piezo with an AR of unity.

3.4 Backscatter Bandwidth

The presented closed-form expressions for the reflection coefficient, (3.11), (3.16), (3.13) and (3.19), reveal how the amplitude of the echo can be modulated by the piezo termination impedance Z_E for backscatter communication. The modulation range of the echo amplitude is determined by $\Delta\Gamma_{Max}$, which according to (3.11), (3.16), (3.13) and (3.19), is ideally equal to 1. $\Delta\Gamma_{Max}$, however, degrades (and becomes < 1) due to second-order effects, mainly caused by the geometry of the implant piezo, that are not well modeled by the piezo constitutive equations used to derive (3.11), (3.16), (3.13) and (3.19). The type of the piezo resonant mode (LE vs. WE modes), diffraction, angular misalignment, non-ideal backing and baffling are responsible for $\Delta\Gamma_{Max}$ degradation. These are conceptually outlined in Figure 3.10(a) for the case of Γ_s , while FEM simulated $\Delta\Gamma_{Max}$ at f_s and f_p for various piezo aspect ratios is shown in Figure 3.10(b). For $AR \gg 1$ the piezo resonates more strongly along its width (WE mode) tangential to the direction of the incident wave resulting in reduced $\Delta\Gamma_{Max}$. For $AR < 1$, although the piezo resonates in the LE mode, its width becomes considerably smaller than the wavelength of the incident wave so that that wave-piezo interaction is dominated by diffraction rather than reflection. That is, the piezo becomes invisible to the incident wave at $AR \ll 1$, significantly reducing its echo modulation strength.

The simulated echo fractional bandwidth of the piezo is also reported in Figure 3.10(b). The settling time of the echo when switching Z_E from open- to short-circuit was used to estimate the fractional bandwidth in Figure 3.10(b). For $AR \ll 1$ and $AR \gg 1$, the piezo uniquely resonates in a distinct resonance mode, respectively LE and WE, resulting in a high quality-factor resonator. At $AR \sim 1$, the piezo is in transition from one mode to the other with a reduced quality factor and thus increased fractional bandwidth. Therefore, AR of ~ 1 is found to be optimal for backscatter communication.

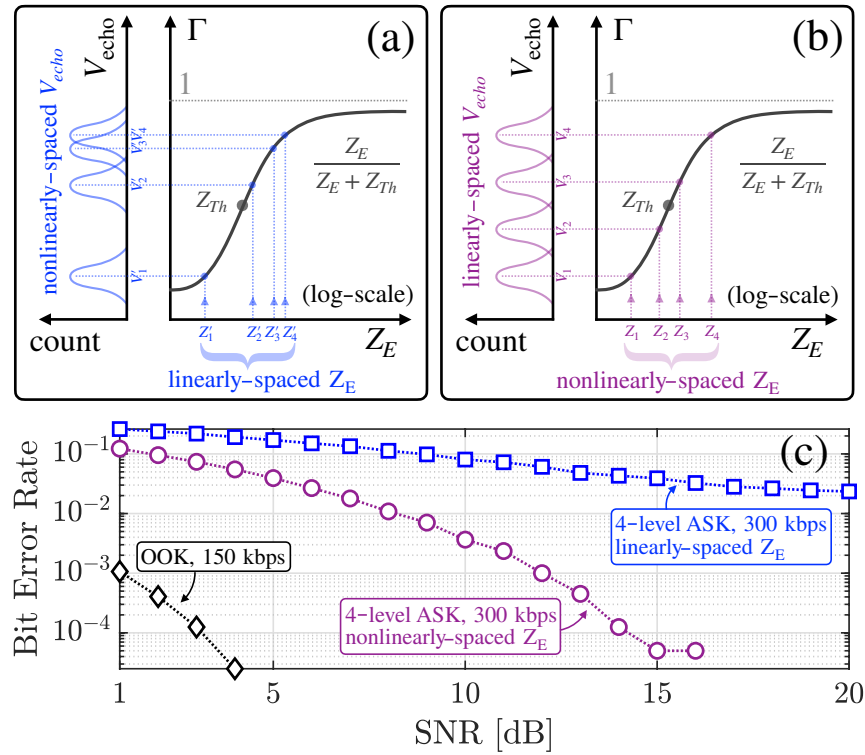


Figure 3.11: (a) 4-level ASK backscatter modulation with non-equidistant echo levels due to a suboptimal selection of linearly-spaced modulating Z'_E . (b) optimal 4-level ASK backscatter modulation with equidistant echo levels with nonlinearly-spaced modulating Z_E . (c) Numerically simulated bit error rates for (a), (b) and OOK; 1.5 MHz carrier frequency is used.

Using the echo fractional bandwidth and the carrier center frequency (Figures 2.9(b) and (c)), the available backscatter bandwidth per unit volume of the implant piezo can be calculated as shown in Figure 3.10(c). For a given AR (=1 in Figure 3.10(c)), increasing the piezo volume (or equivalently thickness) decreases the resonant frequency and ultimately the available backscatter bandwidth. The opposite trends of available power and backscatter bandwidth per unit volume of the implant piezo shown in Figure 3.10(c) clearly demonstrate an inherent tradeoff in the geometrical design space of the implant piezo. Thus, for high-speed applications, spectrally efficient backscatter modulation schemes are needed to decouple data rate and available power from the geometry of the implant. For instance, compared to OOK, an m -level amplitude shift keying (ASK) modulation increases the backscatter data rate by a factor of $\log_2(m)$. The selection of termination impedances required to implement an m -level ASK backscatter modulation, however, is not as straightforward as that of

OOK and should be made with care as demonstrated in Figure 3.11. The echo levels have distributions around their nominal values, due to the noise of the carrier. To reduce the transmission bit error rate (BER), the overlaps between these distributions should be minimized by having equidistant nominal echo levels. The optimal choice of Z_E for equidistant echo levels, shown in Figure 3.11(b), can be directly calculated using $Z_E(\Gamma)$ (obtained from (3.11)–(3.19)). For example, from (3.11), $Z_E = Z_{Th,s} \times \Gamma_s / (1 - \Gamma_s)$, and for 4 equidistant echo levels (*e.g.* $\Gamma_s = \{0.1, 0.36, 0.63, 0.9\}$), the required termination impedances should be $Z_E = Z_{Th,s} \times \{0.11, 0.58, 1.72, 9\}$. Any other choice for Z_E results in BER degradation. Figure 3.11(b) demonstrates how linearly-spaced termination impedances significantly increases the overlaps between the echo distributions. A comparison of the BER for the two cases in Figures 3.11(a) and (b) and OOK is shown in Figure 3.11(c) as a function of the carrier signal-to-noise ratio. It can be observed that linearly-spaced modulating Z'_E for the 4-level ASK modulation has an impractically high BER at all SNRs, but non-linearly spaced modulating Z_E can achieve a BER as small as that of OOK at SNR > 15 dB while achieving a data rate twice as large.

3.5 Measurement and Model Verification

Setup

In this section, we use FEM simulation and experimental results to verify the expressions derived in Section 3.3. Here, we only focus on non-air-backed implant piezo model, (3.11) and (3.16), as air-backing requires a sealed back-side cavity which complicates implant assembly and potentially degrades the longevity of the implant. The experimental setup is shown Figure 3.12. A piezoceramic cube (APC851, 0.51 mm³) mounted on a flexible board (~ 0.1 mm thick) was suspended at a distance of 20 mm away from a 0.25" diameter single-element external transducer (Olympus V323-SU) in oil (with attenuation constants $a \sim 0.1$ dB/cm.MHz and $b \sim 1.8$). The external transducer was driven by an ultrasound pulser (Maxim, MAX14808). Each interrogation ultrasound pulse contained 10 ultrasound cycles at a frequency precisely set by a function generator (Keysight 33522B). A waveform analyzer (Keysight CX3300A) was used to record the amplitude of the backscattered waveform received by the external transducer. A custom made capacitive/resistive bank was used to change the termination impedance of the piezo. A PC was used for measurement automation and data collection. An FEM model of the setup shown in Figure 3.12 was also generated in COMSOL Multiphysics and used to perform FEM simulations.

Results

In order to verify (3.11) and (3.16), the impedance of the test piezo was first measured, shown in Figure 3.13, using a precision LCR meter (Keysight E4980A). The series and parallel resonant frequencies of the piezo were measured to be 1.5 MHz and 1.745 MHz,

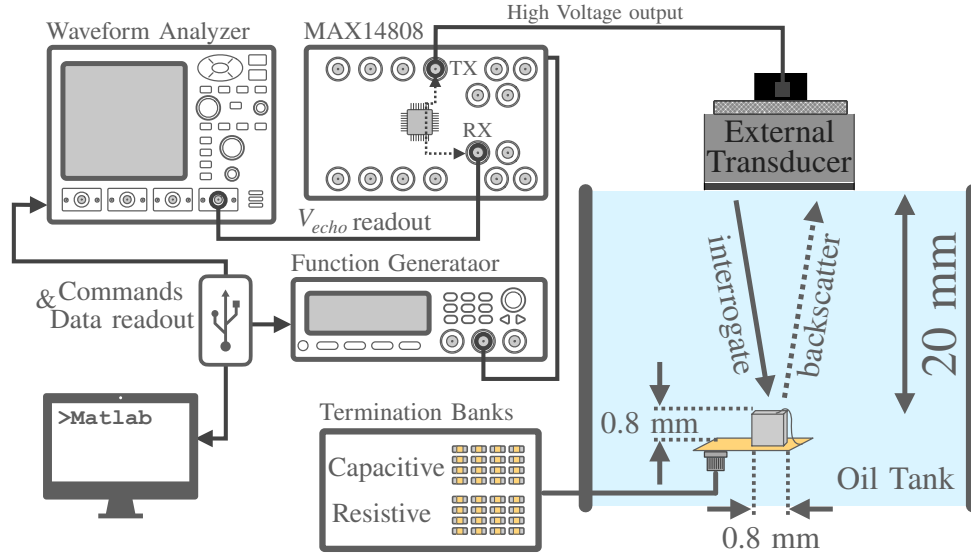


Figure 3.12: Experimental setup.

respectively. It can be observed in Figure 3.13 that submerging the piezo in a viscous fluid, *e.g.* oil, mechanically dampens the piezo and decreases its quality factor so that at f_s and f_p the piezo impedance is no longer purely resistive in oil for this originally low-Q piezo material. The impedance of the piezo is $Z_{Th,s} = 2.31 \text{ [k}\Omega\text{]}\angle - 32^\circ$ and $Z_{Th,p} = 9.78 \text{ [k}\Omega\text{]}\angle - 36^\circ$ at respectively f_s and f_p . The FEM simulated piezo impedance in oil is also shown in Figure 3.13 which is in good agreement with the measurement.

Next, the frequency response of the modulation index (MI) of the piezo was measured, for which the frequency of the interrogation pulse was changed from 1 to 2 MHz (in steps of 5 kHz) and the received echo voltage, V_{echo} , was measured. The MI was calculated for different values of termination impedances (ranging from 100 Ω to 800 k Ω , and 0.2 pF to 800 pF), using the measured V_{echo} and

$$\text{MI} = \frac{V_{echo}(Z_E) - V_{mid}}{V_{mid}}, \quad (3.20)$$

$$V_{mid} = \frac{1}{2} (\max(V_{echo}) - \min(V_{echo})). \quad (3.21)$$

The simulated and measured frequency response of the MI of the test piezo are shown in Figures 3.14(a)-(d). The absolute value of MI has a global and local maxima respectively at f_s and f_p , suggesting that operation at the series resonant frequency of the piezo provides a larger (relative to the midline) backscattered signal. Also, according to Figures 3.14(a) and (b), there exists an operation frequency midway between f_s and f_p (~ 1.6 MHz) at which no backscatter modulation is observed for any resistive load. No such frequency is found

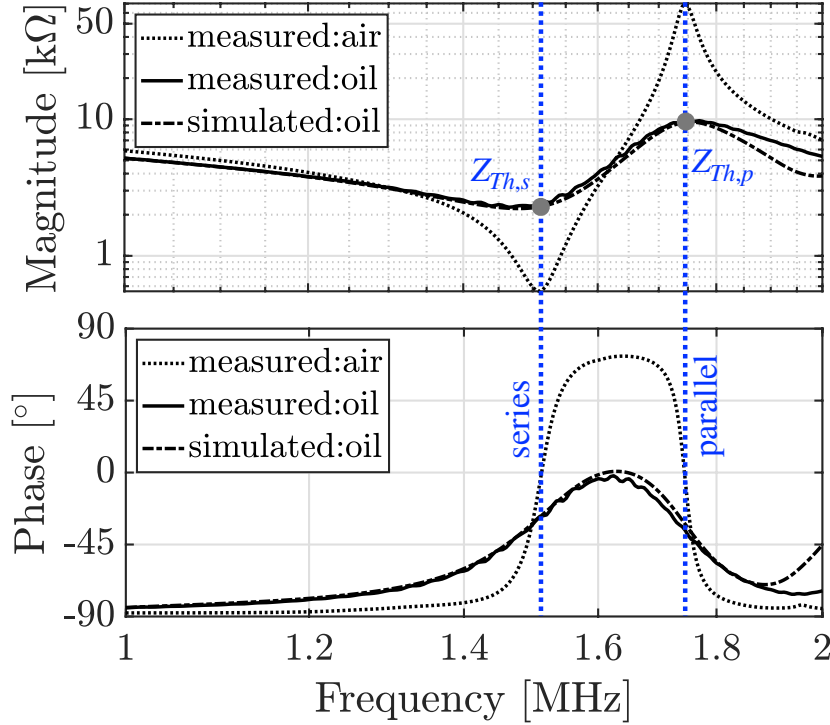


Figure 3.13: Measured and simulated piezo impedance.

for capacitive loads, Figure 3.14(c) and (d). Moreover, the MI has opposite trends at f_s and f_p with respect to the piezo termination impedance, meaning that at f_s , increasing the termination impedance increases the MI, but at f_p increasing the termination impedance decreases the MI. These trends are shown in Figures 3.14(e)-(h) for resistive and capacitive loads. The normalized reflection coefficient

$$\Gamma_{\text{norm}} = \frac{V_{\text{echo}}(Z_E) - \min(V_{\text{echo}}(Z_E))}{\max(V_{\text{echo}}(Z_E)) - \min(V_{\text{echo}}(Z_E))}, \quad (3.22)$$

is plotted in Figures 3.14(e)-(h) in order to subtract the measurement environment nonidealities such as non-flat frequency response of the external transducer, frequency dependence path loss and the reflection from the mounting stage of the test piezo. The reflection coefficient predicted by (3.11) and (3.16) (using measured $Z_{Th,s}$ and $Z_{Th,p}$ from Figure 3.13) is also plotted in Figures 3.14(e)-(h). A good agreement between the simulated, measured and predicted reflection coefficients across a wide range of conditions in Figure 3.14 validate the simplifying assumptions made in the derivation of (3.11) and (3.16).

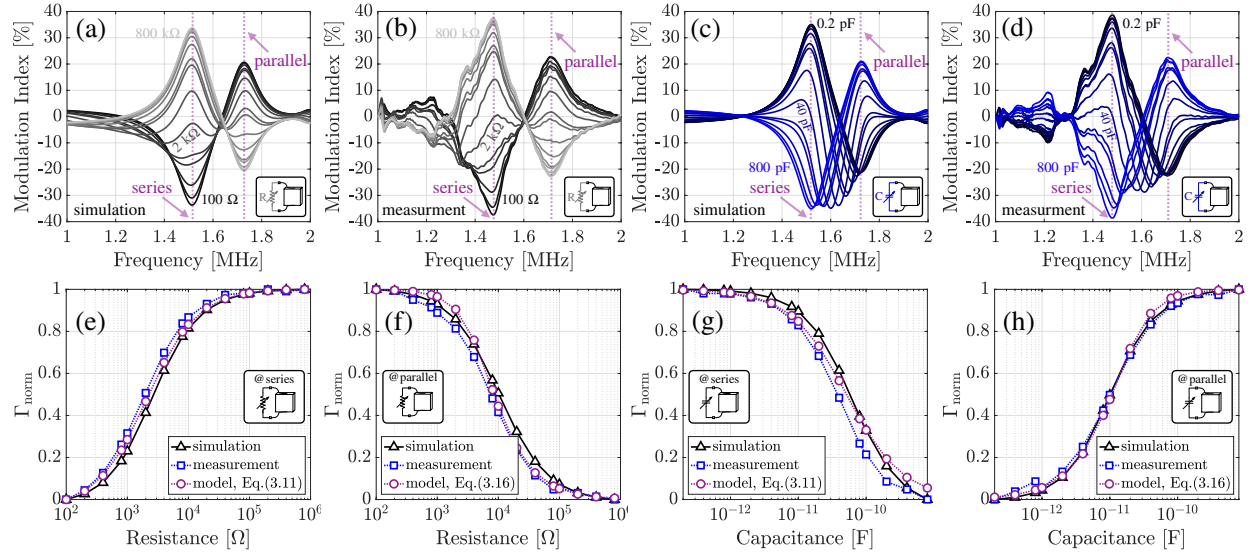


Figure 3.14: (a) simulated and (b) measured frequency response of the modulation index of the piezo for resistive. (c) simulated and (d) measured frequency response of the modulation index of the piezo for capacitive terminations. Comparison of simulated, measured and predicted Γ_{norm} at (e) f_s and (f) f_p for resistive loads. Comparison of simulated, measured and predicted Γ_{norm} at (g) f_s and (h) f_p for capacitive loads.

3.6 Summary

In this chapter, we briefly presented various existing wireless protocols that incorporate both data and wireless power transmission in ultrasound links. We also discussed available multiple-access protocols and compared analog, digital and quasi-digital modulation schemes in such links. We then presented an end-to-end SPICE friendly equivalent circuit model of the backscatter channel as a tool to simulate the channel response, while incorporating both the attenuation and spreading path loss components of the channel. The channel equivalent circuit model was then used to simulate $\Gamma(Z_E)$, a critical design parameter for backscatter uplink modulation. Last, to gain further insight into $\Gamma(Z_E)$, we presented simple closed form expressions for $\Gamma(Z_E)$ which link Γ to the commonly used Thevenin equivalent circuit model of the implant piezo under various boundary conditions. The experimentally validated closed-form expressions for $\Gamma(Z_E)$ are insightful for the design of ultrasound backscatter modulating circuits. These expressions are the backbone of the uplink modulators of the implants presented in Chapters 4 and 6.

This chapter was a direct adaptation of the following article:

M. M. Ghanbari, and R. Muller. “Optimizing volumetric efficiency and backscatter communication in biosensing ultrasonic implants.” *IEEE Transactions on Biomedical Circuits and Systems* 14, no. 6 (2020): 1381–1392.

Personal contribution: I wrote the original draft of the manuscript, performed all the analyses and experimental verification.

Acknowledgements: R. Muller reviewed the manuscript and provided advice on the technical aspects of the research. R. Muller was the principal investigator of this work.

Chapter 4

A mm-Scale Free-Floating Neural Recording Implant with Linear AM CDMA Uplink

4.1 Introduction

In this chapter, we present the design, implementation and verification of a miniature ultrasonically powered neural recording implant, conceptually shown in Figure 4.1, that achieves state-of-the-art neural recording performance when compared with recently reported sub-mm³ free floating wireless implants. The implant presented here occupies a volume of only 0.8 mm³, minimizing tissue displacement, scarring, and foreign body response. The implant is verified to operate at 50 mm depth in a tissue phantom (with ~ 0.5 dB/cm attenuation at 2 MHz), enabling recording of most peripheral nerve targets as well as deep brain targets through thinned skull [21].

To minimize the number of off-chip components and the overall implant volume, a pulse-echo power+data wireless protocol (previously introduced in Chapter 3 and) similar to [70] is used in this work, with three key differences. (1) The addition of a low-noise analog front-end in this work reduces the input referred noise by 34x compared to [70]. (2) The introduction of a technique to linearize the reflection coefficient, resulting in linear analog amplitude modulation of the echo and thereby lowering distortion as discussed in Section 4.3. The underlying principles of this linearizing technique was introduced and discussed in detail in Chapter 3. (3) By incorporating orthogonal subcarriers into the pulse-echo protocol, we realize CDMA and demonstrate simultaneous multi-implant interrogation without sacrificing interrogation frequency and with the use of a single-element external transducer. This not only simplifies the design of the external interrogator, but also maximizes operation depth and interrogation frequency (and hence temporal resolution of the acquired signal) in a multi-site recording setup.

In Section 4.2, the CDM pulse-echo wireless protocol is briefly discussed and compared

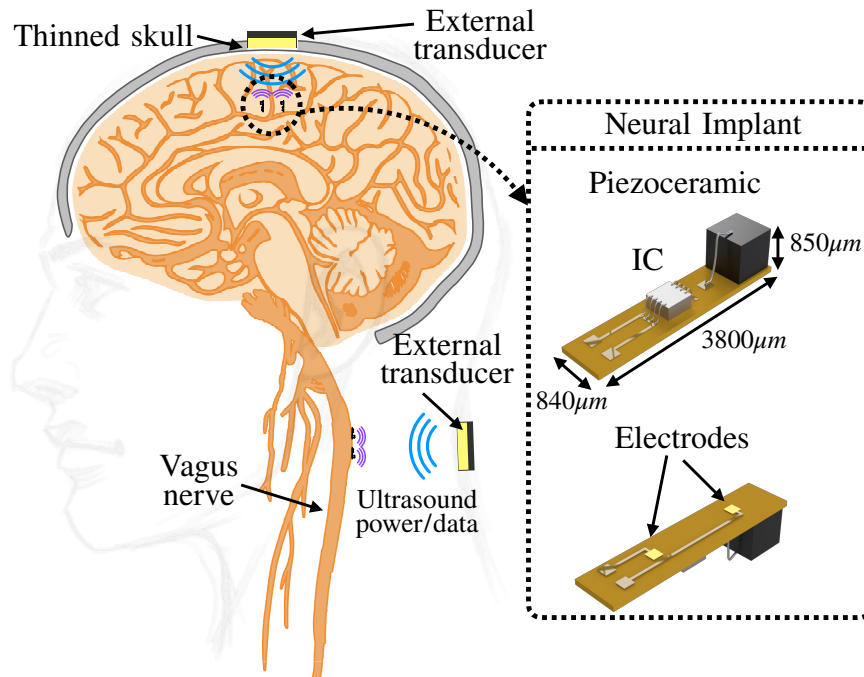


Figure 4.1: Untethered neural recording from deep regions of the peripheral/central nervous system using ultrasonically powered neural recording implant.

against other commonly used protocols. The main conclusions drawn in Chapter 3 regarding $\Gamma(Z_E)$ of the implant piezo are briefly reviewed in Section 4.3 as they are used to design a linear AM echo modulator of the implant presented in this chapter. Section 4.4 describes the circuit-level implementation of the integrated circuit (IC) of the implant and measurement results are presented in Section 4.5. Summary and comparison to the state-of-the-art are presented in Section 4.6.

4.2 CDMA Pulse-Echo Protocol

To miniaturize wireless implants below millimeter scales, the number and size of off-chip components must be minimized. This includes the elimination of off-chip capacitors and necessitates the realization of wireless power and data communication on a single link. Separate power transmission and data communication links have been demonstrated in ultrasonic implants [11, 51]. This mode of operation, shown in Figure 4.2(a), enables continuous data transmission and high data rates, but limits the miniaturization of the implant volume since it requires two ultrasound resonators preferably tuned at distant frequencies to minimize carrier leakage. A similar implant with a single power-data time-multiplexed piezo was presented in [81] to reduce the implant volume. However, actively driving the piezo increases the

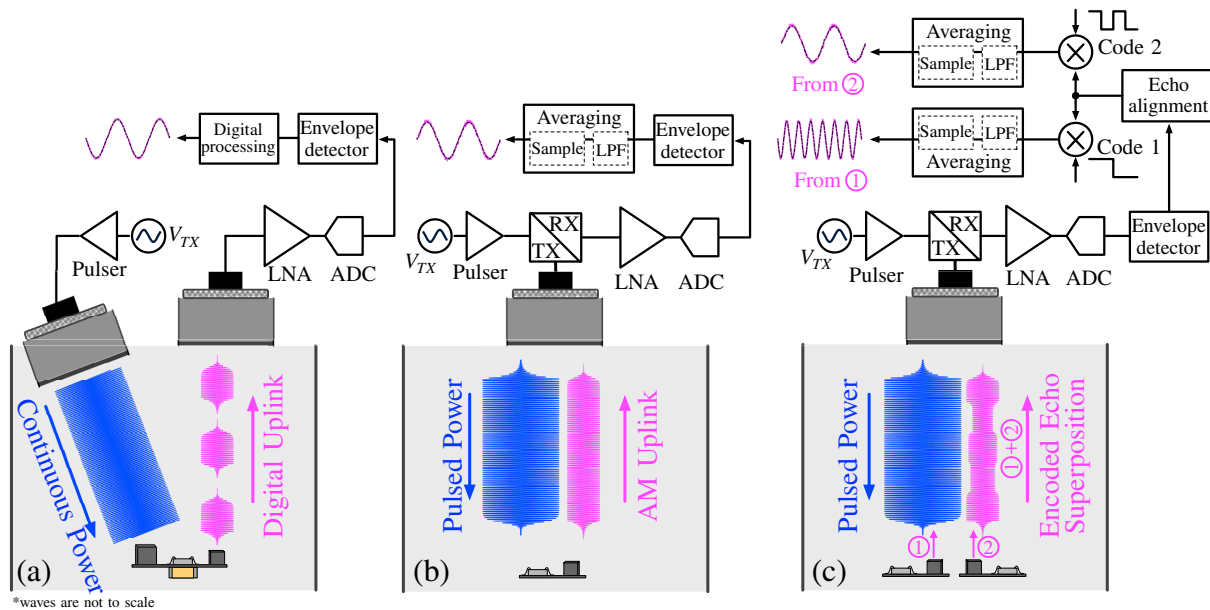


Figure 4.2: Various ultrasound operating protocols: (a) continuous mode operation where OOK is used for uplink data transmission (b) pulse-echo mode with classic AM uplink data transmission; (c) pulse-echo mode with simultaneous interrogation of two implants using orthogonally encoded AM.

number of off-chip components (storage and matching network capacitors) and ultimately its overall size. Alternatively, a single ultrasound link can be used for both power and uplink data transmission in a pulse-echo fashion [70], obviating the need for any secondary resonator or off-chip capacitor. In this scheme, shown in Figure 4.2(b), an ultrasound pulse is first launched towards the implant. After a single time of flight, the implant ultrasound resonator, realized by a bulk piezoceramic (Lead Zirconate Titanate, PZT), starts resonating and harvesting energy. Shortly after that, the integrated circuit (IC) on the implant wakes up and begins recording neural signals. At the same time, the amplitude of the echo (traveling towards the external transducer) is modulated according to the recorded neural signal. The AM-modulated echo is then received and reconstructed through the same external transducer. This pulse-echo interleaved scheme prevents overlapping of the high-voltage signals (up to $30 V_{\text{peak}}$) driving the external transducer, and the mV-level received echo signals, which would otherwise impose an impractically large dynamic range (e.g. 110 dB and 30 V input range) on the external receiver frontend. This pulse-echo protocol and its equivalent circuit model were discussed in detail in Chapter 3.

As discussed in Chapter 2, both focal length (Fresnel distance) and focal area of an unfocused single-element ultrasound transducer scale with its aperture. For instance, a low cost commercially available single-element 0.5" diameter unfocused external transducer has

a focal length of 52 mm and focal area of 50 mm² at 2 MHz in water. Therefore, we propose a network of sub-mm scale implants scattered over this 50 mm² focal area that simultaneously power up and perform data back telemetry. For uplink data transmission, each implant has a unique orthogonal subcarrier that utilizes code-division multiplexing (CDM), while modulating the amplitude of its echo. In this prototype, the chip internally generates a CDM code by dividing the clock (extracted from the main carrier) by a ripple counter. In a multi-implant setup CDM codes can be generated in the same fashion [41]; a frequency divider is clocked by the extracted global main carrier and followed by an encoder to generate CDM codes. A unique code may be chosen by trimming or hardwiring the device. The encoded echoes from multiple implants are superimposed in the acoustic medium and received by the external transducer as shown in Figure 4.2(c). The receive chain of the interrogator includes a low noise amplifier and a high-resolution ADC. Decoding an echo is only a matter of synchronized code multiplication and low-pass filtering (e.g. averaging). Upon echo and CDM code multiplication at the receiver, the signal associated with the CDM code is converted to baseband while those of other channels will remain spread across the spectrum. Averaging concurrently generates a single sample of the selected channel and filters out the non-selected channels. Decoding is possible regardless of the length of the encoded echo as long as it contains an instance of a CDM frame. This is crucial because the duration of the time-interleaved echoes is finite (and often short, ~ 10 's of microseconds). In addition, orthogonal codes can serve as a subcarrier signal that partially bypasses the low-frequency noise contents of the main carrier [68].

4.3 Linear Echo Modulation

The profile of the acoustic reflection coefficient Γ of the implant piezo as a function of its termination resistance R_E at its series resonance frequency is shown in Figure 4.3(a). It can be observed that if R_E is used for modulation, the modulated echo is significantly distorted due to the nonlinearity of Γ , especially when concurrent energy harvesting with echo modulation imposes a minimum value of termination resistance $R_E = R_{min}$. That is, R_{min} should be large enough to allow energy harvesting. This is not a serious problem for digital OOK modulation when transmission of only two states is needed. In this work, however, we use AM modulated echo for data back telemetry as it contains higher information per ultrasound cycle and would not require exceedingly long pulses (restricting the operation depth) for each sample of transmitted data as described in Chapter 3. Therefore, for AM modulation, Γ vs. R_E nonlinearity must be addressed to avoid distortion of the transmitted signal. The governing equations of bulk piezos as well as their equivalent circuit models (KLM [37] and Redwood [66]) are complex and provide little insight to describe this nonlinearity. We showed in Chapter 3 that at the series resonance frequency of the piezo,

$$\Gamma \approx \frac{Z_E}{Z_E + R_S} \propto V_3, \quad (4.1)$$

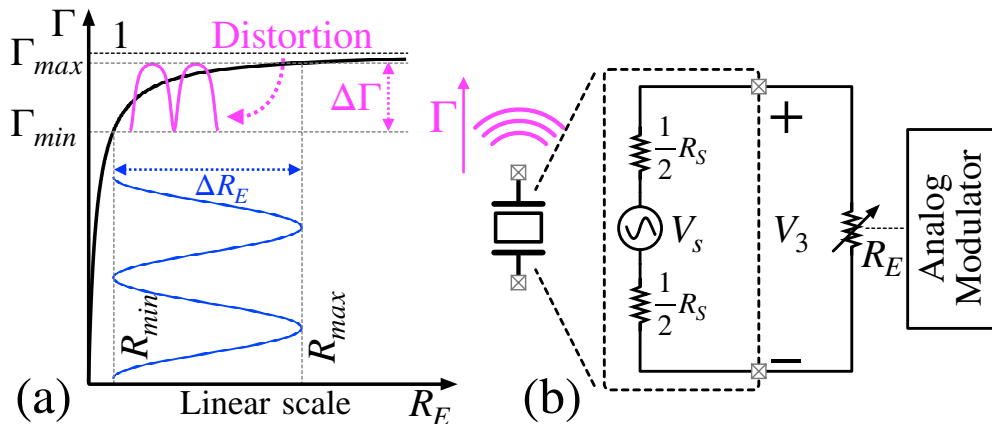


Figure 4.3: Conceptual Γ - R_E curve showing significant nonlinearity.

where R_s is the internal series resistance of the piezo, meaning at f_s , Γ is approximately linearly proportional to the *voltage* across the piezo, therefore for a linear echo modulation, the voltage across the piezo (rather than its electrical termination resistance) needs to be linearly modulated according to the acquired neural signal. Equation (4.1) has a single parameter, R_s , which can be obtained empirically or by finite element method (FEM) simulation. Experimental verification of this closed-form expression was demonstrated in Chapter 3. In the next section, we describe how the active rectifier can be repurposed to linearly modulate the voltage of the piezo to achieve a highly-linear ultrasound echo modulator.

4.4 Hardware Implementation

A simplified block diagram of the interrogator and the neural recording implant is shown in Figure 4.4. The implant IC contains a power management block that rectifies and regulates the received piezo voltage to a 1 V supply. A clock signal is directly extracted from the piezo-harvested voltage (using 2.5 V buffers), which is divided to generate the chopper signal. The analog front-end consists of a fully differential chopper stabilized amplifier followed by a linear gm-cell that linearly modulates the amplitude of the echo. After receiving and conditioning the echo at the external interrogator, digital post-processing, shown in Figure 4.2(c), is performed to reconstruct the transmitted signal. The implant is powered on as long as an ultrasound pulse is present, meaning that the implant is memory-less. This hinders electrode DC offset cancellation. Therefore, the input-output linear range of the implant should be extended to minimize distortion. The input linear range of the implant is beyond ± 10 mV. The output (echo) modulation linearity is achieved by linearly modulating the piezo voltage as discussed below.

The implant utilizes a $0.75 \times 0.75 \times 0.75$ mm³ piezo (840, APC International), whose $R_s =$

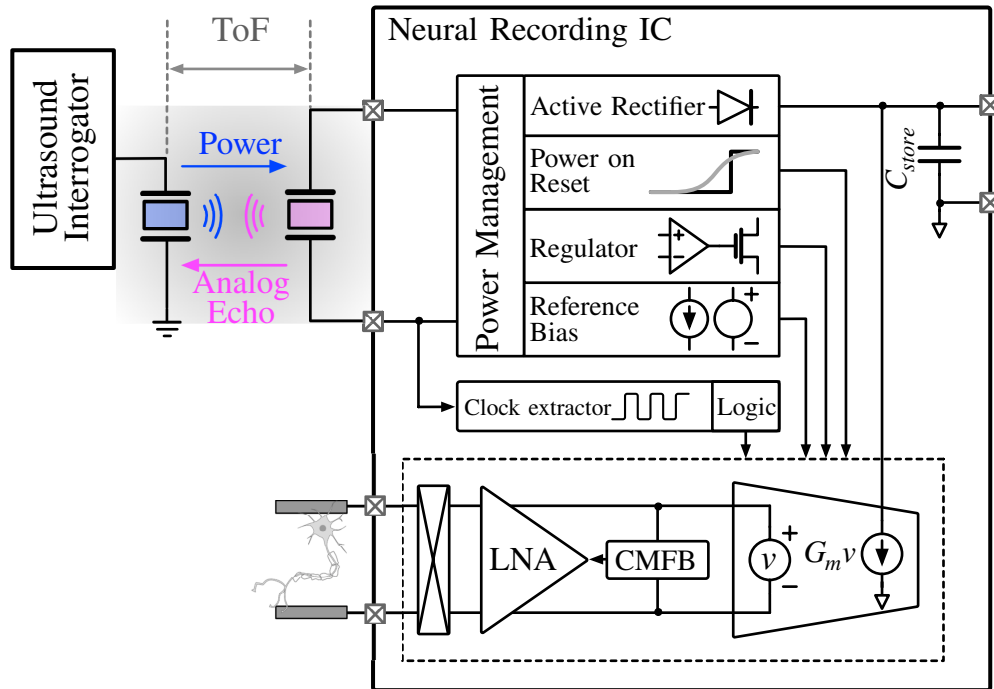


Figure 4.4: Simplified block diagram of the IC.

4 k Ω . When an ultrasound pulse is received at the piezo, the IC has a finite amount of time ($<2\text{ToF}$, e.g. $66 \mu\text{s}$ @ 50 mm depth) to power up, generate a stable supply, record neural signals and perform uplink data transmission. Therefore, rapid power-up and precise timing management of the sub-blocks are critical. The interconnection of power management blocks and the top-level timing diagram of the chip are shown in Figure 4.5. Due to the time constant associated with the on-chip storage capacitor (130 pF), the internal series resistance of the piezo, and the $<2\pi$ conduction angle of the rectifier, it takes $\sim 5 \mu\text{s}$ (~ 10 ultrasound cycles) to fully charge up the storage capacitor and for the supply-independent proportional-to-absolute-temperature (PTAT) source to generate two reference voltages ($V_{ref,1V}$ and $V_{ref,0.5V}$) on-chip. The PTAT core transistors M_{1-4} are designed to operate in the subthreshold region such that $I_{M5} = \eta V_T \text{Ln}(W_2/W_1)/R_{ref}$, where η and V_T are the subthreshold factor and thermal voltage, respectively. Initially, M_{1-8} are off and the gates of M_{7-8} track V_{rect} . Upon harvesting voltage from the piezo, V_{rect} rises, and M_{7-8} turn on pulling up/down the gates of M_{1-2}/M_{3-4} to speed up their transition from zero current to the desired current (500 nA) stable bias point. M_6 is designed to be strong enough to pull down the gates of M_{7-8} , charging C_{start} and disengaging the PTAT startup circuitry once M_{1-2} turn on. $V_{ref,1V}$ serves as the low dropout regulator (LDO) reference voltage, and a delayed version of $V_{ref,1V}$ triggers the power on reset (POR) to initialize the logic states. The amplifier initialization takes $3 \mu\text{s}$, which is followed by signal acquisition and uplink

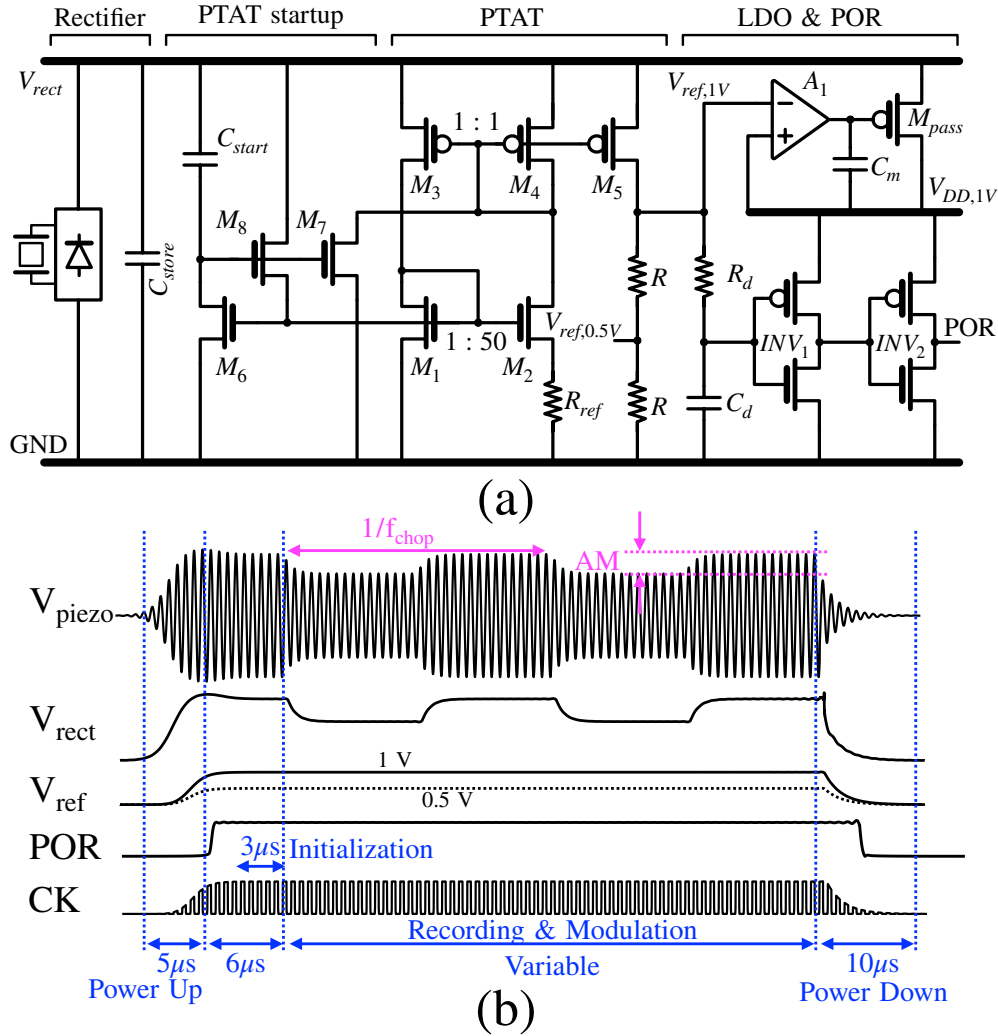


Figure 4.5: (a) Schematic diagram of power management blocks (b) chip-level timing diagram shown with 2 subcarrier cycles.

data transmission. In the absence of an ultrasound pulse, the on-chip storage capacitor discharges in $\sim 10 \mu s$, meaning that inter-pulse duration should be greater than $10 \mu s$ for proper re-initialization (POR triggering) of the IC. This translates to a minimum operation depth of 14 mm without requiring any acoustic spacer.

Low-noise Amplifier

The analog front-end (AFE) of the chip consists of a fully differential capacitive-feedback low noise amplifier (LNA) whose circuit diagram is shown in Figure 4.6. The values of the

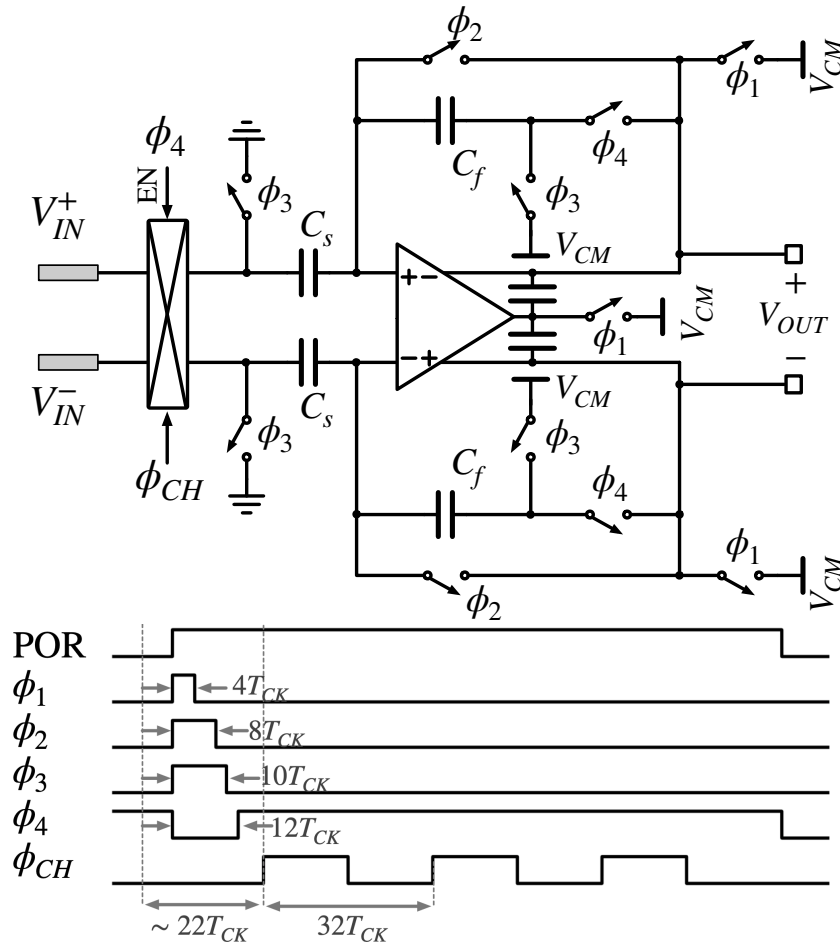


Figure 4.6: LNA topology and timing diagram.

feedback and load capacitors (0.44 pF and 4.7 pF respectively), and the feedback factor ($\beta \sim 1/16$) set the noise ($< 10 \mu V_{\text{rms}}$ in 180 kHz bandwidth) of the circuit, while the effective transconductance of the LNA sets the bandwidth. The amplifier is initialized by a set of switches controlled by ϕ_{1-4} , which bias the LNA as quickly as possible to maximize the signal acquisition period. V_{CM} is set to the 0.5 V mid-rail voltage using a power-gated linear regulator shown in Figure 4.7(b). The low impedance source charges 25 pF of capacitance in $< 1 \mu s$.

Since the LNA runs on a 1 V supply and has a gain of 16, auto-zeroing is implemented to cancel amplifier offset and improve the linear output voltage swing [17]. Auto-zeroing is implemented by sampling the offset of the amplifier on the feedback capacitors (C_f). The ϕ_1 switches are disabled first, placing the amplifier in the unity gain feedback. The sampled offset is then subtracted from the signal after sequentially opening ϕ_2 and ϕ_3 and

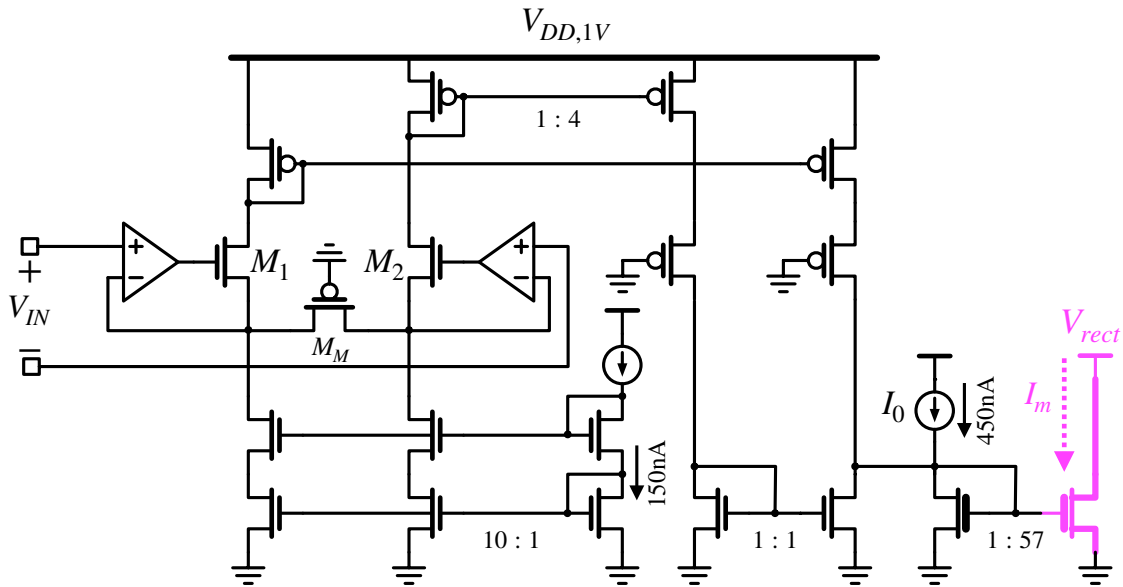


Figure 4.8: Linear gm-cell architecture.

a bandwidth of 180 kHz, high enough to pass the third harmonic of the highest subcarrier frequency (55 kHz). Although the amplifier has a broadband forward path of 180 kHz, the bandwidth of the post-processed signal, and therefore the effective noise bandwidth of the amplifier are reduced to 5 kHz at an interrogation frequency of 10 kHz. Along the signal chain, as shown in Figure 4.2(c), decoding and demodulation of the echo involves averaging the echo for the duration of the pulse. This averaging concurrently applies a sinc low pass filter with a 3dB bandwidth of $1/2T_{integration}$ to the received signal and translates every received echo to a single sample. Therefore, at a 10 kHz interrogation frequency (sampling frequency), the signal and noise bandwidth is reduced to 5 kHz. Lastly, the auto-zeroing noise foldover does not degrade the noise performance of the front-end for the amplifier is already a sampled one where the input-referred sampled thermal noise voltage of the broadband amplifier during the amplification phase is almost $6\times$ larger than that sampled and translated to baseband during the auto-zero phase. This is due to β and C_T being $16\times$ and $2.5\times$ larger respectively during the auto-zero phase compared to those during the amplification phase.

Linear G_m -cell design

The LNA drives a linear transconductance stage for converting the acquired signal to current. The G_m -cell therefore requires a ± 160 mV input voltage range with better than 0.5% nonlinearity. This is achieved by forcing the input voltage across a PFET device biased in

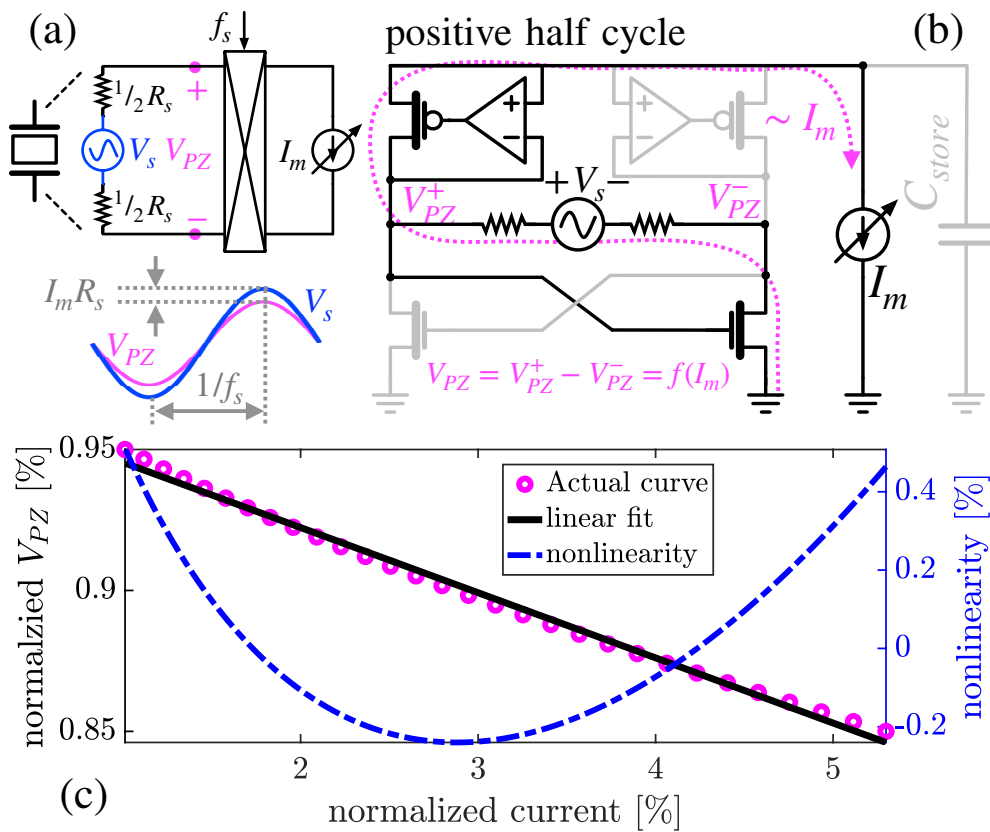


Figure 4.9: (a) Conceptual echo amplitude modulation using synchronous up-conversion current mixer (b) reusing active rectifier as synchronous mixer (c) nonlinearity induced by the rectifying modulator.

the triode region with a differential super source follower (Figure 4.8) [34]. A PFET device is used instead of a resistor to save area without sacrificing linearity. A Δ incremental increase of V_{in} results in both $|V_{DS}|$ and $|V_{GS}|$ of M_M to increase by respectively Δ and $\Delta/2$, which gives rise to $I_{M_M} \propto \Delta$ as long as M_M is in triode region which is ensured by designing M_M as a long-channel low- V_t device. The current generated through M_M creates a pair of differential current signals passing through M_1 and M_2 that is converted to single-ended in the last stage of the G_m -cell. The G_m stage has a nominal transconductance of $120 \mu\text{S}$. The 1 V supply powers this stage, except for the final current mirror, which is connected directly to the rectifier output and provides the signal for uplink data modulation. 2.5 V devices are used in the final mirror stage due to higher rectifier voltages.

Linear echo modulator

The linear relationship between Γ and V_3 , expressed in (4.1), reveals that linear amplitude modulation of the echo is possible by linearly modulating the amplitude of the piezo voltage ($V_{PZ} = V_{PZ}^+ - V_{PZ}^-$ in Figures 4.9(a) and (b)). At resonance, the piezo is modeled by an AC voltage source (V_s) and the series resistance of the piezo (R_s). Consider the conceptual circuit diagram shown in Figure 4.9(a) where it is assumed the signal modulating the echo amplitude is available in the current domain, I_m . To modulate the amplitude of the piezo voltage, I_m is upmodulated by a current mixer whose switching phase is synchronous to the piezo voltage. This results in the peaks and valleys of the piezo voltage dropping by $I_m R_s$. A similar AM modulation technique holds true for reflective antenna systems.

In this work, the synchronized up-conversion current mixer is implemented with minimal hardware overhead by reusing the active rectifier. The circuit diagram of the active rectifier is shown in Figure 4.9(b) where high-frequency common-gate RF amplifiers are used as comparators. Since the rectifiers are inherently nonlinear, rectifier-induced nonlinearity should be taken into account. It can be shown that the relationship between the DC voltage at the output of the rectifier V_{rect} and the load current I_m is given by

$$I_m \propto \frac{V_s}{R_s} \left(1 - \frac{V_{rect}}{V_s}\right) \left(1 - \frac{2}{\pi} \text{asin}\left(\frac{V_{rect}}{V_s}\right)\right), \quad (4.2)$$

where, V_s is the peak value of the piezo open-circuit voltage. Equation (4.2) is plotted in Figure 4.9(c) where the nonlinearity between V_{rect} (normalized to V_s) and I_m (normalized to V_s/R_s) is shown for 10% modulation depth. The voltage across the piezo (V_{PZ}) is the upmodulated version of V_{rect} , therefore V_{rect} and V_{PZ} voltages are equivalent in (4.2). For 10% modulation depth the maximum nonlinearity between V_{PZ} (and ultimately Γ) and I_m is less than 0.5%. Since rectifier nonlinearity was shown to be minimal, a single-ended Gm-cell was connected to the output of the rectifier, mitigating the need for the Gm-cell to sink current from both terminals of the piezo to maintain full conduction angle if connected to the input of the rectifier.

4.5 Hardware Verification

The IC was fabricated in the TSMC 65nm LP CMOS process. The die micrograph and the fully assembled implant are shown in Figure 4.10. The bulk piezo and the chip are bonded to a flex PCB interposer. A pair of $200 \times 200 \mu\text{m}^2$ electroless nickel immersion gold plated electrodes (ENIG) are designed on the backside of the PCB with 2 mm spacing. The measured impedance of the ENIG electrodes (mean of measurements for 6 electrode pairs, measurements made using a precision LCR meter, Keysight E4980A) submerged in phosphate-buffered saline (PBS 1 \times) and a model for a single electrode are shown in Figure 4.11. The maximum measured (24 hour post submersion) electrode DC offset was 1.1 ± 0.4 mV. The implant is encapsulated with $\sim 10 \mu\text{m}$ of Parylene-C [46]. The total area of the chip, including test pads and on-chip decoupling capacitors, is 0.25 mm^2 . The minimum

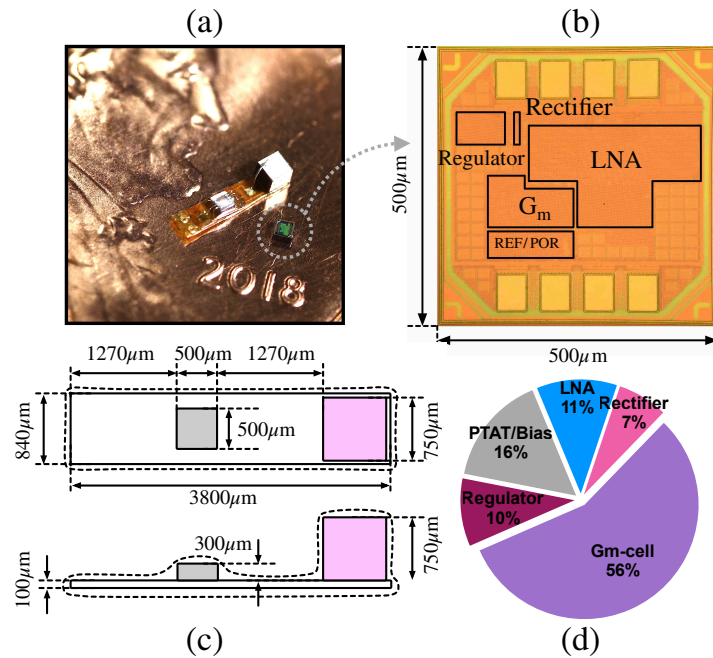


Figure 4.10: (a) Fully packaged implant micrograph (b) IC micrograph (c) dimensions of the fully packaged implant (d) power consumption breakdown.

voltage amplitude required at V_{rect} was measured to be 1.25 V. The circuit power dissipation after rectification was $\sim 30 \mu\text{W}$, and the total power consumption including the efficiency of the power management circuits were measured to be $37.7 \mu\text{W}$ during normal operation with a 50% duty cycle. The breakdown of the power consumption is shown in Figure 4.10(d).

The chip characterization setup and measurement results are shown in Figures 4.12-4.15. The setup includes a piezo model, an AC-coupled voltage source in series with a 4 k Ω resistor, connected to the piezo terminals of the chip. The output was measured using a fully differential lock-in amplifier for main-carrier demodulation. Subsequent signal processing steps, e.g. subcarrier demodulation, were performed on a PC. The output transient response of the chip, measured at the piezo voltage terminals, is shown in Figure 4.13(a) in response to a 20 mV_{PP} input sine wave for five consecutive interrogation events. The first interrogation event is shown in Figure 4.13(b) where 11 μs of power-on/startup time and the 27.5 kHz subcarrier signal are observable. The demodulated and reconstructed input signal for the same measurement is shown in Figure 4.13(c). Static and dynamic nonlinearity measurement results are shown in Figure 4.14. An end-to-end voltage gain ($\Delta V_{PZ}/v_{in}$) of 23 dB with maximum static non-linearity error of 1.2% was measured. The power spectrum of the reconstructed 313 Hz, 20 mV_{PP} sine wave is shown in Figure 4.14(b) and achieved an SFDR of 50 dB and a THD of -44 dB. No harmonic tones are visible for a 10 mV_{PP} input signal.

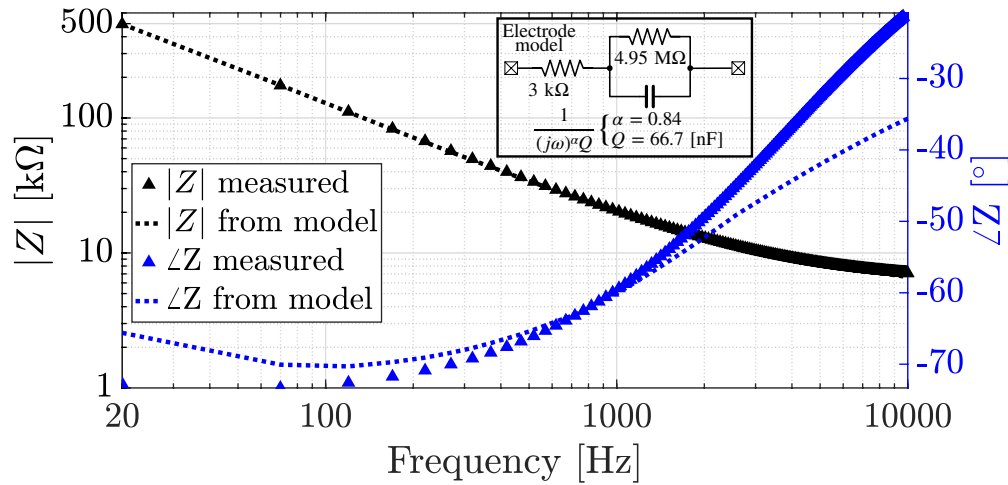


Figure 4.11: Measured ENIG electrode impedance (mean of measurements for 6 electrode pairs); (inset) single electrode model.

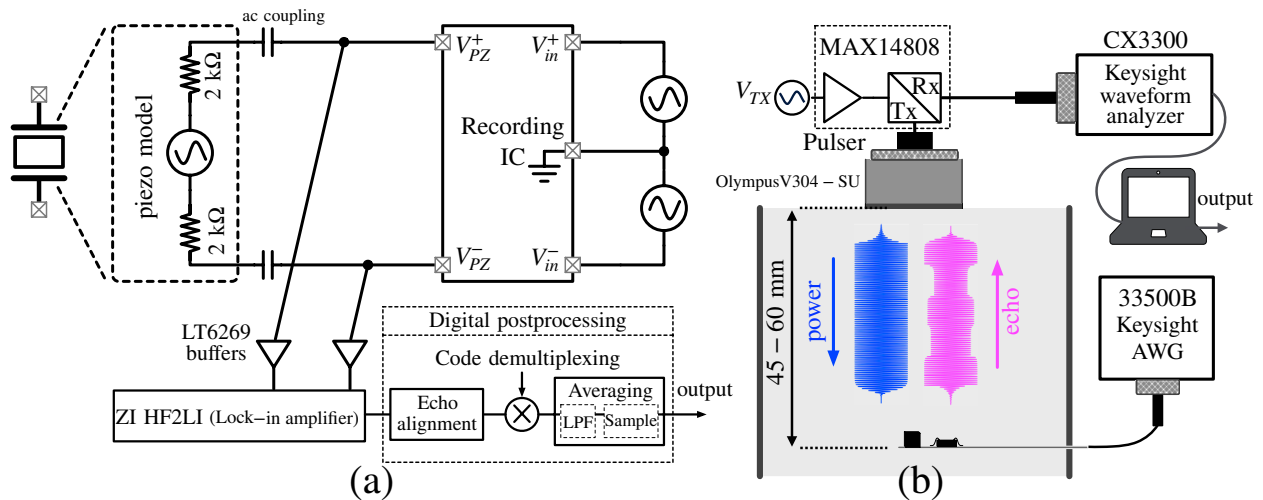


Figure 4.12: (a) benchtop measurement setup, (b) single-mote *in vitro* measurement setup

The noise measurement results are summarized in Figure 4.15 for an interrogation (sample) frequency of 10 kHz. There are two major contributors to the total input referred noise density: the AM noise of the carrier, and the noise contributed by the recording circuits. The total input referred noise spectral density was measured to be 328 nV/ $\sqrt{\text{Hz}}$. This is mainly dominated by the carrier noise, measured at 319 nV/ $\sqrt{\text{Hz}}$ in the absence of the chip (Figure 4.15(a)). Both the curves in Figure 4.15(a) are derived by down-chopping and averaging,

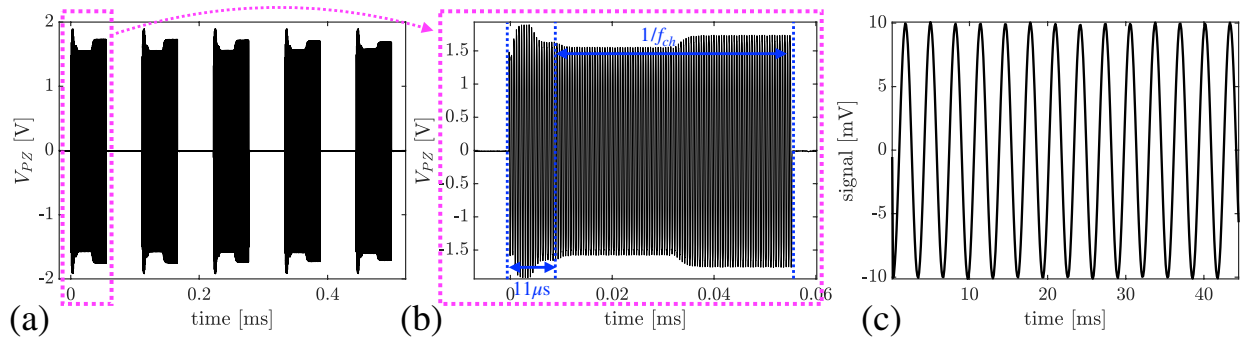


Figure 4.13: Benchtop measurement result showing amplitude modulation of the input voltage of the rectifier for (a) five consecutive sample pulses for a 313 Hz, 20 mV_{PP} input signal (b) first interrogation event where startup time and the subcarrier signal are visible (c) the demodulated input-referred signal.

which partially removes the $1/f$ noise of the carrier. Assuming the noise of the carrier and that of the chip are additive, the input referred noise of the chip alone can be estimated 76 nV/ $\sqrt{\text{Hz}}$, or $5.37 \mu\text{V}_{\text{RMS}}$ in a 5 kHz bandwidth. The effect of chopping in bypassing the low-frequency noise contents of the main carrier is demonstrated in Figure 4.15(b), where $1/f$ noise is clearly visible in the spectrum when chopping is disabled.

The single-mote *in vitro* measurement setup is shown in Figure 4.12(b), where a single assembled mote is suspended at a distance of 45–60 mm away from a single-element external transducer in oil (with ~ 0.5 dB/cm attenuation at 2MHz). The implant was interrogated at 8 kS/s. The main carrier frequency was set to the resonant frequency of the implant piezo at 1.78 MHz. A subcarrier frequency of 55 kHz was generated on chip. Two received sample echoes that form a peak and a valley of a 313 Hz, 20 mV_{PP} signal are shown in Figure 4.16 along with their demodulated signals. The reconstructed received signal and its spectrum are also shown in Figure 4.16(e) and (f). Although the noise of the carrier (generated by the external ultrasound pulser) dominates the overall noise of the link, for the 20 mV_{PP} input range of the implant, 47.96 dB of SNR is measured. Were the carrier noise absent, the SNR would improve by ~ 10 –12 dB. Figure 4.16(g) summarizes the measured SNR and equivalent uplink data rate measured at multiple other possible configurations with varied depth, interrogation frequency and subcarrier frequency using the same setup introduced earlier.

To make sure an even number of subcarrier cycles (e.g. 2 in Figure 4.16(d)) is used for demodulation, first, echo duration is chosen to be sufficiently long. For instance, $>29 \mu\text{s}$ and $>47 \mu\text{s}$ echoes are needed for 2 and 4 cycles of a 55 kHz sub carrier respectively. Since the startup time and consequently the start of the echo modulation period of the chip is consistent from sample to sample, and since the period of the subcarrier is known and referenced to the main carrier frequency (e.g. $1.78 \text{ MHz} \div 32 = 55 \text{ kHz}$), the subcarrier signal

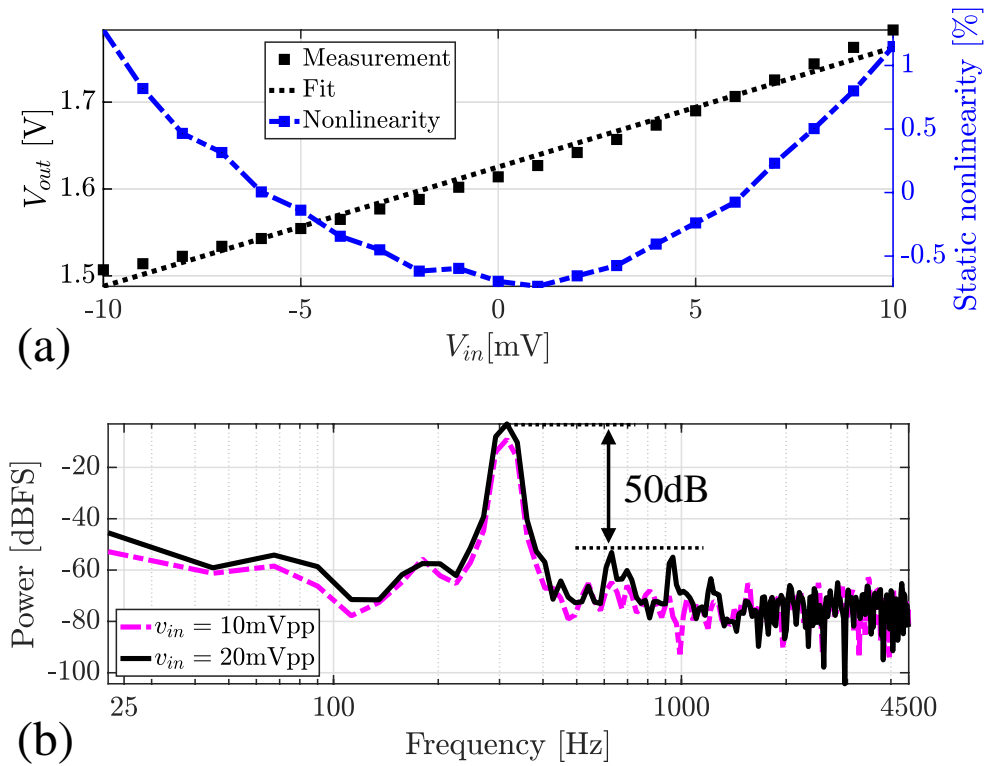


Figure 4.14: (a) The static input-output (defined as the input voltage of the rectifier) linearity curve of the chip. (b) power spectral density of the reconstructed signal shown in Figure 4.13.

can be determined at the interrogator receiver for demodulation. For pulses longer than the ones mentioned above ($29 \mu\text{s}$ and $47 \mu\text{s}$), the received echoes are truncated to $29 \mu\text{s}$ and $47 \mu\text{s}$ such that only an even number of cycles are used for demodulation.

Further *in vitro* verification of the mote was performed where an 800 ms stream of pre-recorded neural signal (acquired by Plexon multichannel acquisition processor) from an awake-behaving rat (Long-Evans) motor cortex was fed to the chip and wirelessly transmitted to the external interrogator. The mote was placed at the depth of 45 mm in a tissue phantom (with ~ 0.5 dB/cm attenuation at 2 MHz) and interrogated at 10 kS/s. Figure 4.17 shows the comparison between the reference pre-recorded neural signal with the signal recorded and wirelessly transmitted by the implant.

The effects of misalignment on the operating range of the device were also characterized. Figure 4.18 outlines a set of measurement results reporting the harvested piezo voltage and the maximum modulation depth of the echo at various relative locations of the external transducer and the implant piezo. The measurement medium was oil with ~ 0.5 dB/cm attenuation at 2 MHz. An unfocused $0.5''$ diameter external transducer was driven at 1.78

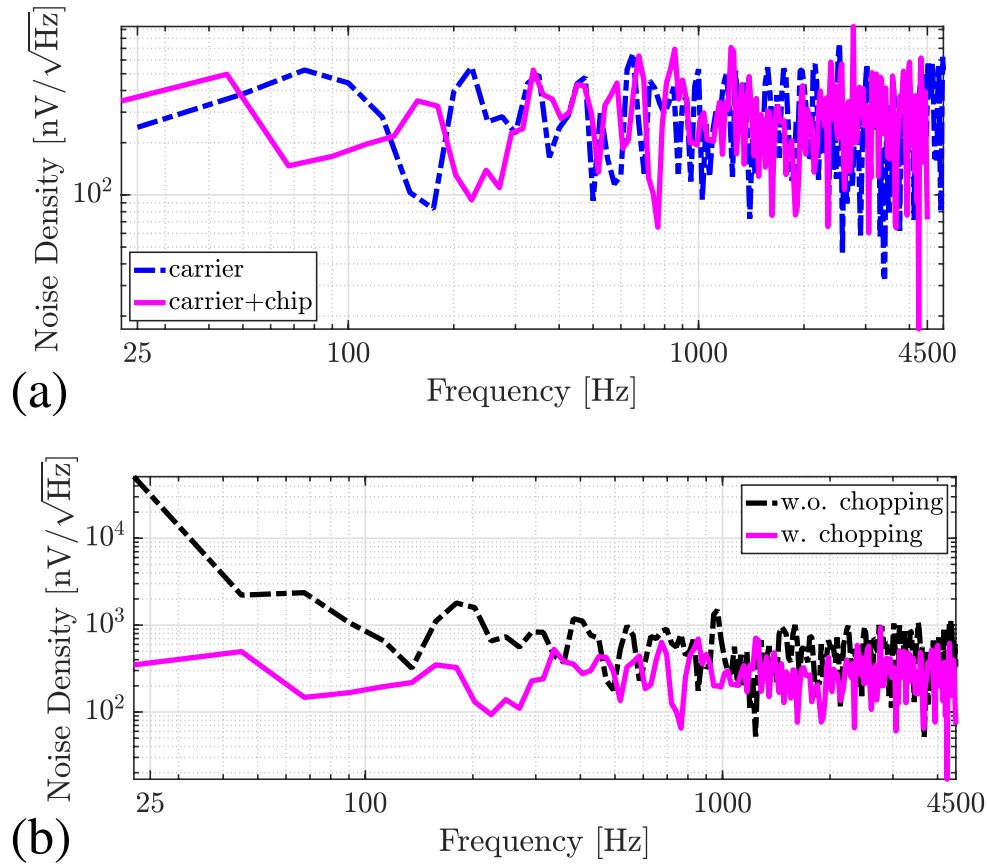


Figure 4.15: Noise measurement. (a) the noise spectral density of the carrier alone and that obtained from the chip: noise is dominated by the carrier noise. (b) effect of chopping in reducing the low-frequency noise contents of the main carrier.

MHz by a ± 15 V pulser. The maximum modulation depth is defined based on the received echo amplitude at two extreme piezo terminations, open- and short-circuited piezos. Figure 4.18(a) illustrates that the harvested power is maximized at the Fresnel distance of the external transducer (~ 52 mm), and that the optimal operation depth of the implants is ~ 50 mm where the harvested voltage and the modulation depth are concurrently large. Moreover, at 70 mm of depth, acceptable harvested voltages (> 4.5 Vpp) and maximum modulation depth (> 20 %) were measured. It is also observed that beyond the Fresnel distance, the modulation depth steadily decays at a rate of 6% per cm, allowing a large range of viable implant depths for the mote. Figures 4.18(b) and (c) demonstrate similar measurement results for horizontal x- and y-axis misalignment between the implant piezo and the external transducer. It can be observed that the effect of horizontal misalignment is symmetric with respect to the line of sight (LoS); a slight asymmetry in Figure 4.18(c) is

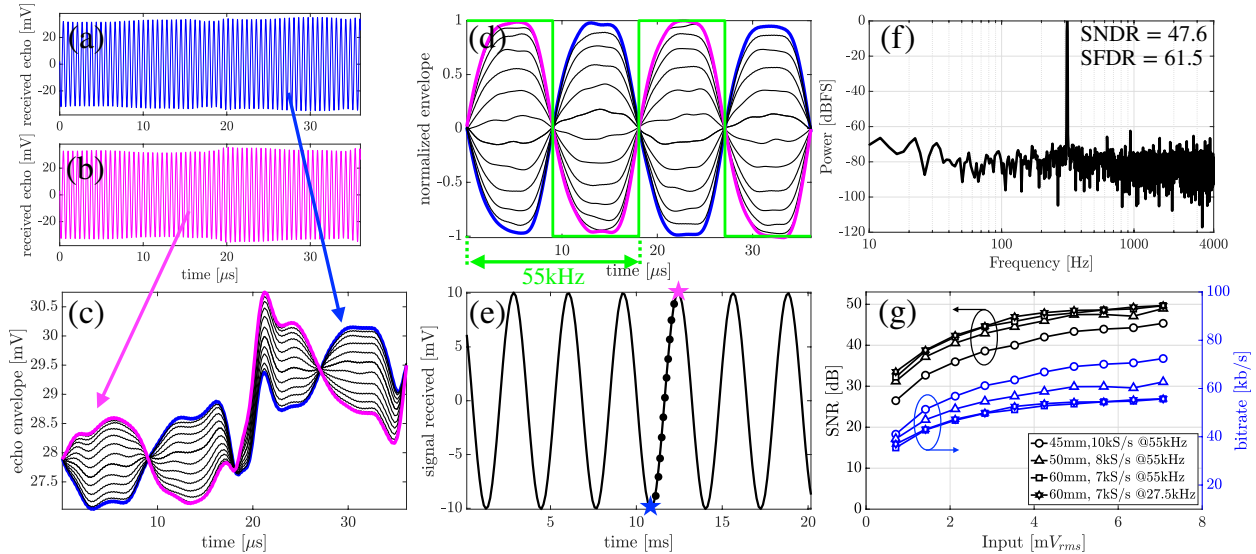


Figure 4.16: Single-mote *in vitro* measurement results. Implant is interrogated at 8 kS/s at 5 cm of depth (a-b) two received echo signals each translating into a sample shown in (e), (c) their corresponding AM demodulation (d) common-mode rejection of received echoes (e) reconstructed 313 Hz signal (f) SNR of received signal (noise dominated by carrier noise) and (g) measured SNR and equivalent uplink data rate vs. input range of the implant.

due to the setup, which includes a rod holding the piezo along the x-axis. Since the chip is fully operational at harvested voltages greater than 4.2 V_{pp}, horizontal misalignment of up to ± 1.75 mm is acceptable at a cost of a negligible drop in modulation depth. The ± 1.75 mm misalignment margin is directly proportional to the aperture of the external transducer, therefore the margin can be doubled by using a 1" external transducer.

Figure 4.19 demonstrates an *in vitro* measurement setup where two implants at a depth of 50 mm with a 2 mm separation were synchronously powered up by a single 0.5" unfocused external transducer. The setup environment limits the depth in this dual-mote measurement. The subcarrier frequencies of the implants are orthogonal to each other (55 kHz and 27.5 kHz) to enable simultaneous uplink data transmission in this dual-mote setup. Each implant transmitted a single tone (414 Hz and 313 Hz) to the external receiver. The reconstructed tones are shown in Figure 4.19(b) along with their spectra. Measured SNDR and SFDR are shown as a function of vertical misalignment between motes in Figures 4.19(e) and (f), respectively. It can be observed that the uplink data transmission quality is maintained over ± 2 mm of vertical misalignment. A given vertical misalignment ΔZ between two implants, results in the implants powering up with a delay equal to $\Delta t = \Delta Z/c$, where c is the propagation speed of sound in tissue. This delay, in turn, results in subcarriers becoming out of phase by Δt , which translates to inter-channel crosstalk and consequently degradation of SNDR and SFDR. Given the carrier frequency and the highest frequency of the orthogonal

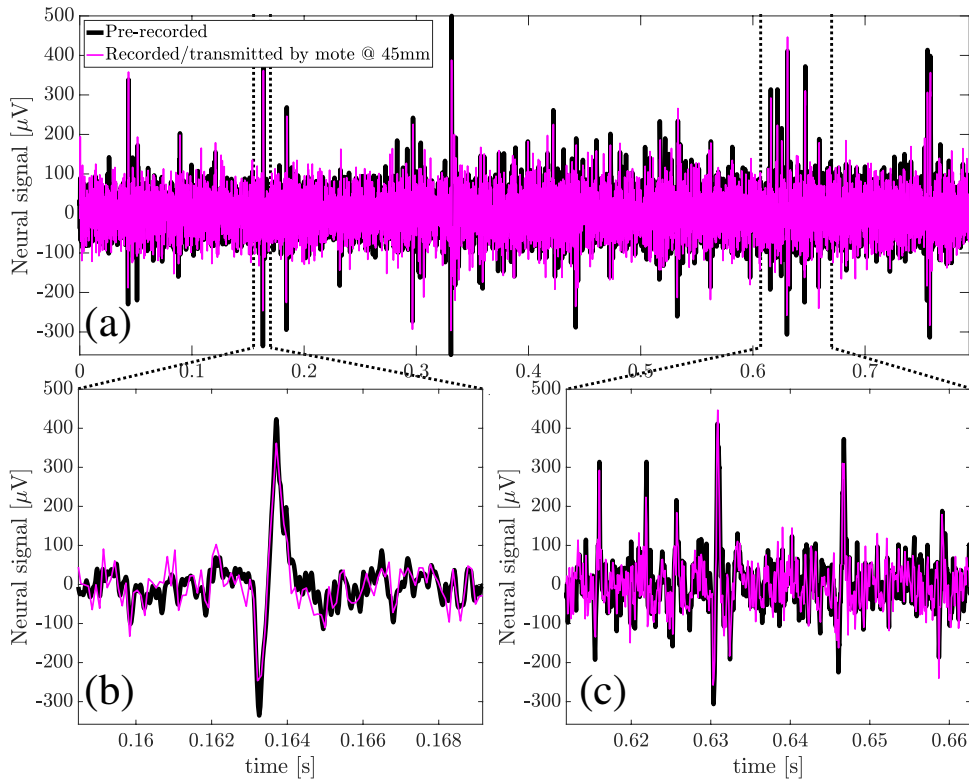


Figure 4.17: (a) 800 ms stream of pre-recorded neural signal recorded (at 10 kS/s) and wirelessly transmitted by the mote at 45 mm of depth. Comparison of reconstructed data between (b) single and (c) multiple action potential events.

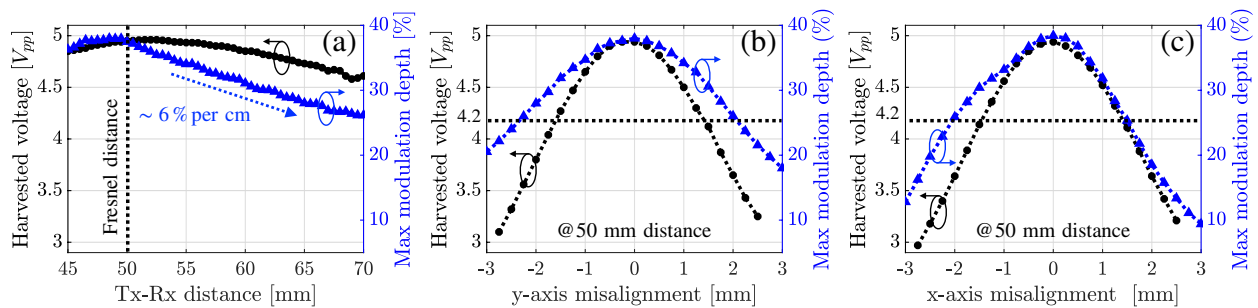


Figure 4.18: Measured piezo-interrogator relative misalignment characterization in (a) vertical (b) horizontal y-axis (c) horizontal x-axis dimensions

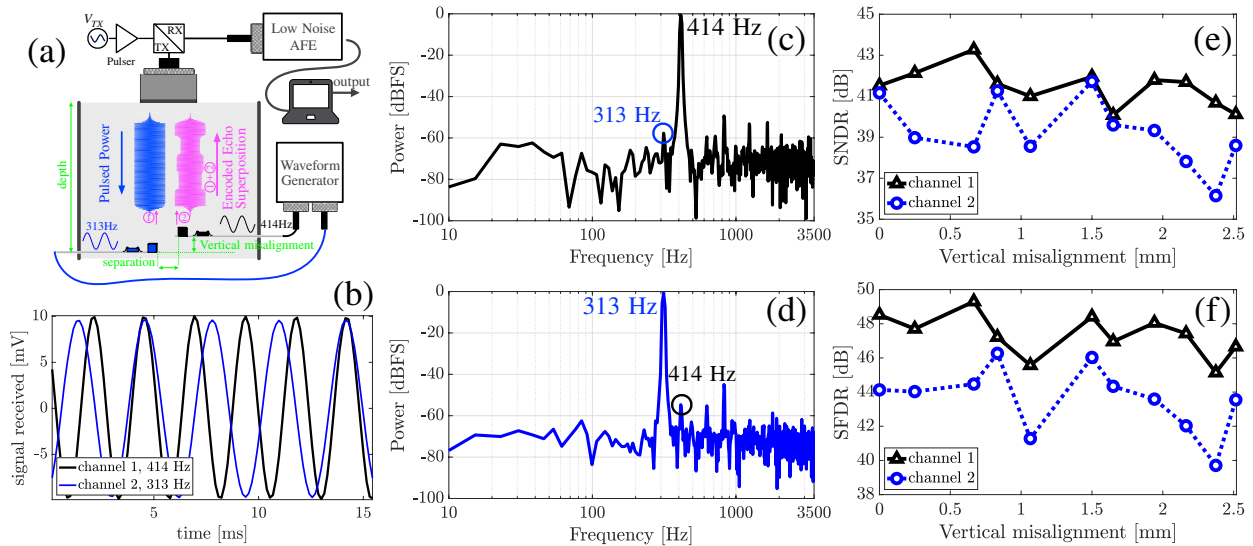


Figure 4.19: Simultaneous power up and data transmission of two implants at depth of 50 mm and separation of 2 mm. (a): *in vitro* measurement setup. (b): reconstructed signals at the external interrogator. (c-d) spectra of the reconstructed signals (e-f) measured SNDR and SFDR of each channel versus vertical misalignment between the notes

codes are 1.78 MHz and 55 kHz respectively, at depths between 35 and 70 mm, 4 implants can be simultaneously interrogated. At depths ≥ 70 mm, up to 8 devices can be simultaneously interrogated.

4.6 Summary

In this chapter, we presented a 0.8 mm^3 free floating implant that uses a single ultrasound link for wireless power harvesting and analog data back telemetry. The implant incorporated a linear amplitude modulated ultrasound echo modulation achieving a $20 \text{ mV}_{\text{PP}}$ end-to-end linear range across the wireless channel. A comparison with recently published fully integrated free-floating sub- mm^3 neural recording implants is shown in Table 4.1. This work advances the noise performance of [70] by 34x without sacrificing the implant volume. Compared to prior art [70, 83, 44], this work achieves the lowest nonlinearity at the highest input range, achieves a comparable NEF to that of the state-of-the-art, and improves operating depth by $>2.5\text{x}$, resulting in the highest measured depth/volume ratio by $\sim 3\text{x}$. We demonstrate, for the first time to our knowledge, simultaneous power-up and communication with two free-floating motes without requiring a specialized, e.g. beamformed, external transducer.

Table 4.1: Performance Comparison Table

	Neuron'16	TBioCAS'18	CICC'18	This work
Link	Ultrasound	Optical	RF	Ultrasound
Back telemetry	AM Backscatter	Analog PPM	IR-UWB	AM Backscatter
Implant depth (mm)	8.8	–	20	50
Total Volume (mm ³)	0.8	0.004	<1	0.8
Encapsulated	Yes	No	Yes	Yes
Depth/Volume (mm ²)	11	–	–	61.7
Simultaneous Multi-mote	No	No	No	Yes
Technology (nm)	65	180	350	65
Total power (μ W)	–	0.9	296*	61
IC area (mm ²)	500×450	90×330	1050×1050	500×500
Wake-up time (μ s)	3.3	15000	110	11
THD (dB)	–	-16@0.5mV _{pp}	–	-44@20mV _{pp}
Static nonlinearity (%)	–	49 [†] @6mV _{PP}	–	1.2@20mV _{PP}
LNA	noise floor (μ V _{rms})	180	15	3.78
	Bandwidth (kHz)	5	10	12
	power (μ W)	–	0.52	42.9
	NEF/ PEF	–	4.07/16.6	6.6/78.4
	Gain (dB)	0	30	53

[†]estimated
*after AC-to-DC

This chapter was a direct adaptation of the following article:

M. M. Ghanbari, D. K. Piech, K. Shen, S. Faraji Alamouti, C. Yalcin, B. C. Johnson, J. M. Carmena, M. M. Maharbiz, and R. Muller. “A sub-mm³ ultrasonic free-floating implant for multi-mote neural recording.” *IEEE Journal of Solid-State Circuits* 54, no. 11 (2019): 3017–3030.

Personal contribution: I developed the idea, designed the IC and performed chip characterization, data collection and analyses. I wrote the original draft of the manuscript.

Acknowledgements: S. Faraji Alamouti designed the PTAT circuit of the chip, and C. Yalcin helped with the layout. D. Piech helped with the ultrasound measurement setup. K. Shen assembled and encapsulated the implants. R. Muller, M. M. Maharbiz, J. M. Carmena, B. Johnson provided advice on the technical aspects of the research. All the co-authors reviewed the manuscript. R. Muller was the principal investigator of this work.

Chapter 5

High Throughput Ultrasonic Multi-implant Readout Using a Machine-Learning Assisted CDMA Receiver

5.1 Introduction

In any communications channel, reducing the symbol duration directly increases the data transmission rate. However, due to finite channel bandwidth, reduced symbol length often causes significant inter-symbol interference (ISI) and elevated bit error rates (BERs). In this chapter, we attempt to aggressively increase data rate of a prototype CDMA ultrasound link by decreasing the symbol duration and subsequently compensating for the resulting ISI using a machine-learning assisted CDMA decoder. In particular, we present an ultrasonic link consisting of a single-element external transducer and 4 implants that achieves a total data rate of 784 kbps (196 kbps/implant) and a spectral efficiency of 490 kbps/MHz, the highest reported to our knowledge. Scaling the operation frequency to 5 MHz provides data rates up to 2.45 Mbps.

The next section discusses the problem of ISI in more detail and presents the implementation of the proposed machine learning assisted CDMA decoder. Experimental results are presented in Section 5.3. Comparison with the state-of-the-art is summarized in Section 5.4.

5.2 ML-Assisted CDMA Decoder

The data transmission period (each packet length) is of finite duration limited by the time of flight (ToF). Since the packet transmission rate is also set by the ToF, increasing the data rate requires increasing the number of bits transmitted in each packet, resulting in fewer ultrasound cycles/bit. For instance for a packet length of 60 μ s, 96 cycles of a 1.6 MHz

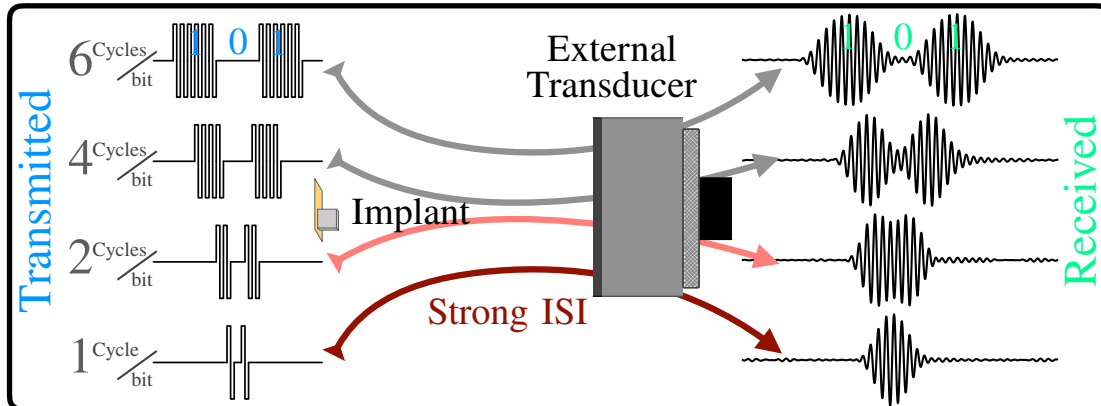


Figure 5.1: Illustration of bit expansion and resulted Inter Symbol Interference (ISI): transmission of a ‘101’ for various cycles/bit configurations.

carrier are available. Transmitting 16 and 96 bits/packet respectively results in allocation of 6 and 1 ultrasound cycles/bit. Fewer cycles per transmitted bit consequently result in inter-symbol interference (ISI). Fig. 5.1 shows signals received by the external transducer when an implant is transmitting a ‘101’ for various numbers of cycles/bit, assuming that on-off keying (OOK) base-band digital modulation is used. Due to the finite mechanical bandwidth of the piezo, the received signal is expanded in time. It can be observed that as the number of cycles/bit decreases the transmitted bits are merged together and become indistinguishable from one another. This results in a strong ISI, which significantly degrades the BER at high data rates if a conventional decoder is used. Here, we present an ISI tolerant machine learning (ML) assisted decoder to improve BER at high data rates.

Prior art has demonstrated the application of ML, especially Neural Networks (NN) in communication. [1] demonstrates that for a CDMA protocol, a NN approach can outperform conventional matched-filter implementations and deliver results close to that of an optimal decoder. In [20], an end-to-end approach was taken to enhance the performance of detectors for OOK and pulse amplitude modulation. Furthermore, bi-directional recurrent NN (RNN) model was shown to excel at continuous multi-symbol sequence detection in the presence of strong ISI.

In this work, the waveform of the packetized data is used to train the ML model. Each packet forms an image that includes all transition levels through the symbols in that packet. 1-D image processing is performed by a Convolutional Neural Network (CNN) that processes the raw waveform, eliminating the need for manually selecting input features. A CNN-based model benefits from parameter sharing to detect certain features that can appear anywhere along the image; as a result, fewer model parameters are required to achieve the desired pattern recognition accuracy, relaxing the data size and training time constraints.

Fig. 5.2 shows a block diagram of the receiver backend. The raw acquired waveform is

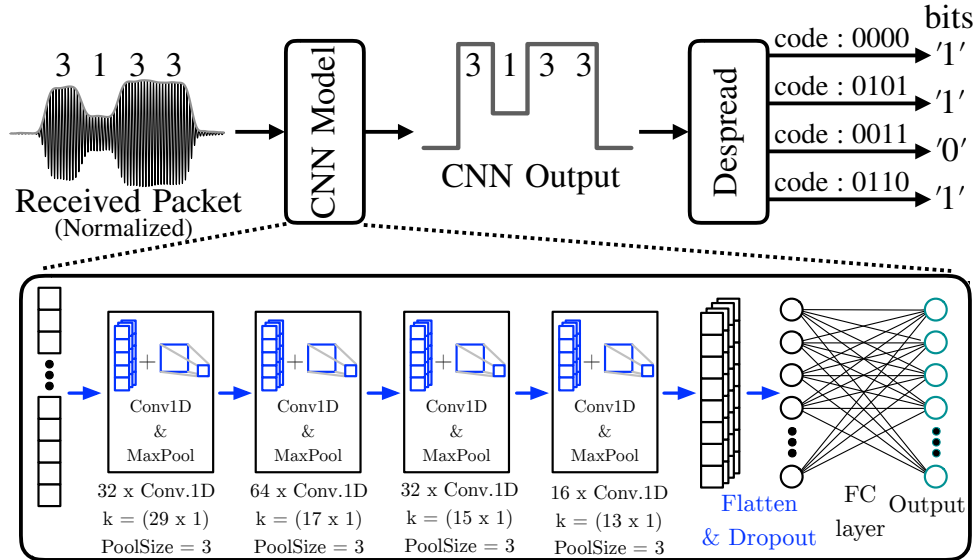


Figure 5.2: Block diagram of machine-learning assisted CDMA decoder.

input to a CNN-based regressor, with no prior filtering or demodulation. The CNN model is comprised of 4, 1-D Conv. layers with ReLU activation function, followed by Max Pooling operations and a final fully connected (FC) layer that maps to the outputs. The CNN is trained to predict the corresponding stream of CDMA levels. These arrays of predicted levels are then despread (using the assigned CDMA codes) to recover the actual data transmitted by each implant.

5.3 Experimental Results

To experimentally verify the efficacy of the ML-assisted decoder and specify the maximum achievable data rate, the setup shown in Fig. 5.3 was used for automated data generation and collection. In order to simplify the experimental setup, we used the active uplink protocol shown in Figure 3.2(b). Nevertheless, because 50%-duty-cycled data transmission period is considered in this work, our proposed ML-assisted decoder is compatible with backscatter links, Figure 3.2(c), as well. Pseudorandom OOK data generation and CDM encoding was performed on a PC. Four piezoceramic cubes (APC851, 0.51 mm^3 , 1.6 MHz) mounted on a flexible board (0.3 mm thick) were suspended at a distance of 50 mm away from a 0.5" diameter single-element unfocused external transducer (Olympus V304-SU-F1.88IN-PTF) in oil (with $\sim 0.5 \text{ dB/cm}$ at 2 MHz). Each piezo was driven by an ultrasound pulser (Maxim, MAX14808) whose command inputs were controlled by an FPGA (Xilinx Spartan-6 LX150) clocked at 57 MHz. CDM-encoded OOK pseudorandom data was generated by a PC and transferred to the FPGA for each packet of data. Once the packets are launched

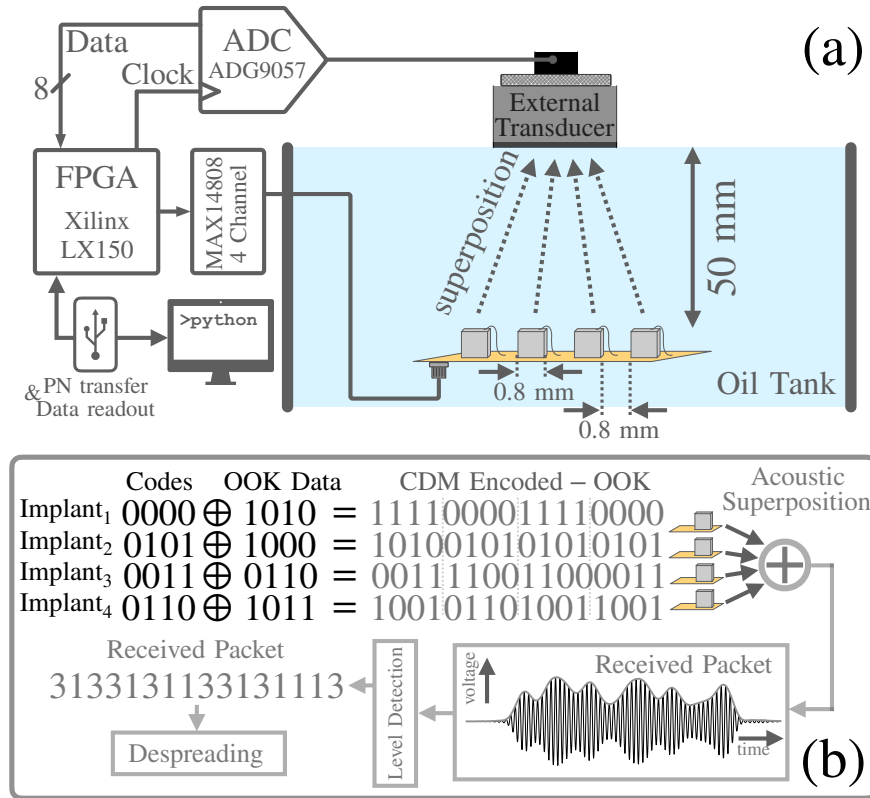


Figure 5.3: (a) Setup for automated data collection and (b) generation .

by driving the implant piezos, the output of the external transducer is sampled by an 8-bit analog to digital converter (ADG9057) to record the acoustically superimposed CDM-encoded data transmitted by all piezos. The recorded signal at the output of the external transducer was transferred to PC where labeling and subsequent digital processing were performed. Measurements were made for multiple data rate configurations at 10,000 packets per configuration. A set of 4,000 packets (~ 290 ms of recording) were used for model training. For the two highest data rate configurations, 6400 packets were used instead for training the CNN as in these configurations packets contained a significantly higher number of bits to be decoded. Pre-trained models and transfer learning techniques can be used to further shorten the training phase. All the measurements were performed with a 50% packet rate as explained in Section II. Since ToF is held constant, packet data transmission rate was set to 14 kHz, and the packet duration was maintained at $35 \mu\text{s}$ (56 ultrasound cycles at 1.6 MHz). The data rate was adjusted by changing the number of bits/implant per packet from 1 to 14, respectively resulting in 56 kbps to 784 kbps data rates. Measured packet streams received by the external transducer for 56 kbps and 392 kbps uplinks are shown in Fig. 5.4(a) and (b). The transition levels (superimposed codes transmitted by implants, e.g. 3133) for low

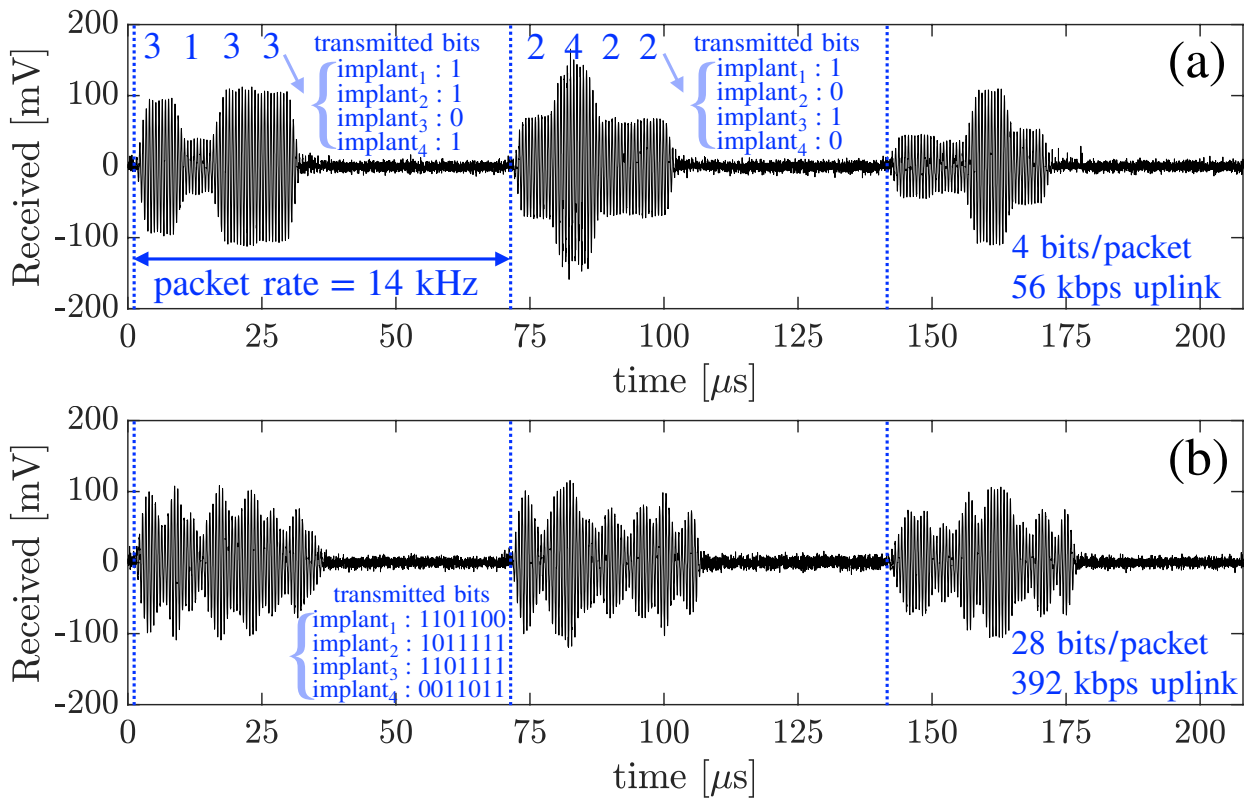


Figure 5.4: Simultaneous data transmission of 4 implants using OOK CDMA modulation. Measured waveforms received by external transducer for data rates of (a) 56 kbps and (b) 392 kbps.

data rates, e.g. 56 kbps in Fig. 6(a), are clearly visible. In Fig. 5.4(b), however, transition levels due to strong ISI cannot be easily observed.

The measured BER for different channel data rate configurations is shown in Fig. 5.5(a) for a signal-to-noise ratio (SNR) of 35 dB. A comparison was made with a more conventional approach, a Minimum Mean-Squared Error (MMSE) detector, which was implemented, trained and tested on the same data set. At low data rates where ISI is insignificant, both of the decoders can achieve a BER of $1E-5$. As the data rate increases, ISI significantly degrades the performance of the MMSE decoder. An optimal CDM decoder [77] could enhance this performance, but such an implementation would be computationally impractical for data rates greater than 224 kbps. The ML-assisted decoder achieves a BER better than $6.4E-4$ for data rates up to 784 kbps without the computational complexity of an optimal CDM decoder. To evaluate the system performance in lower SNR values, in-band gaussian noise was added to the collected samples to generate an SNR range of 0–35 dB. At each

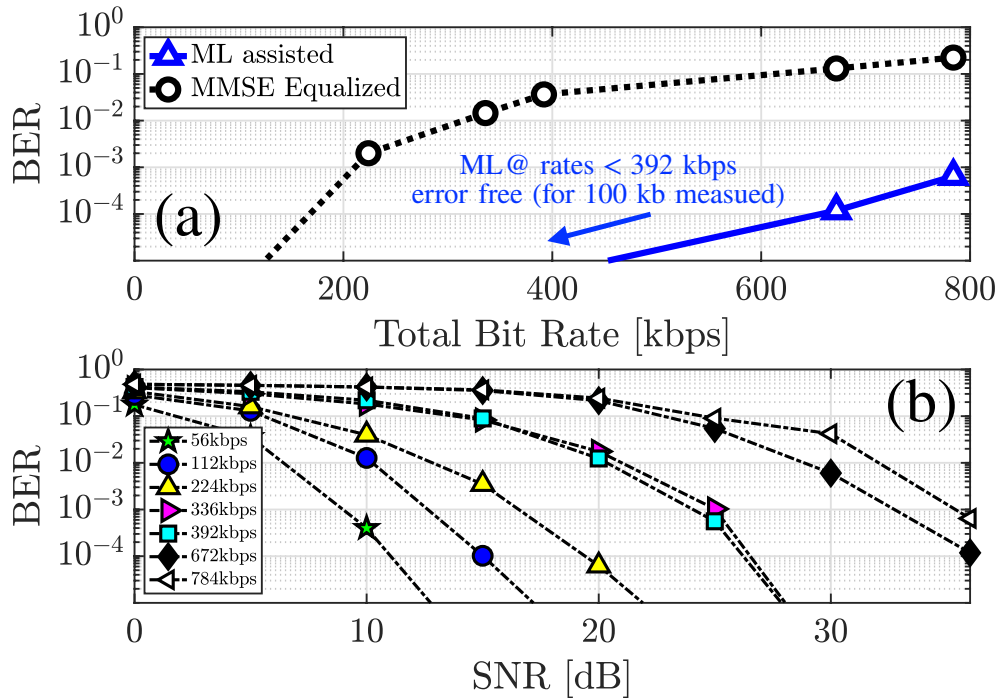


Figure 5.5: (a) Measured bit error rate (BER) vs. total data rate of the channel. (b) Measured bit error rate (BER) vs. received signal-to-noise (SNR) ratios for various total channel data rates.

SNR level, the model was retrained with noisy samples and retested with the data set. Fig. 5.5(b) summarizes the achieved BER by the ML-assisted CDMA decoder at different rates and SNR values. As an example, for 30 dB of SNR, BER of $5E-7$ can be achieved for data rates up to 392 kbps.

5.4 Summary

Table 5.1 summarizes the performance metrics of the CDMA communication channel presented in this work compared to those of the prior art. This work incorporates 4 single-piezo implants operating at a total data rate of 784 kbps, the highest reported to our knowledge. Introducing a CNN-assisted CDMA receiver improves BER by more than 2 orders of magnitude when compared with a common MMSE decoder. This work also achieves the highest reported spectral efficiency $\sim 10\times$ higher than the best reported single-piezo implant [80], and $\sim 6.4\times$ higher than the best dual-piezo implant[10]. Moderate carrier scaling to 5 MHz would increase the number of implants supported in this work to 12, resulting in an overall channel datarate of 2.45 Mbps.

Table 5.1: Comparison of Recently Published Ultrasound Links

	[80]	[11]	[81]	[51]	[10]	This work	This work	This work
No. of Implants	2	1	1	1	2	4	4	4
Piezos per Implant	1	2	1	2	2	1	1	1
External Elements	32	2	2	2	32	1	1	
Depth [mm]	60	85	120	37.5	65	50	50	50
f_c [MHz]	1	2.5	0.79	1	2.52	1.6	1.6	1.6
Uplink [kbps]	50	100	10	75	194	392	672	784
SE* [kbps/MHz]	50	40	12.6	75	77	245	420	490
BER	–	1E-4	1E-5	–	1E-4	1E-5	1.2E-4	6.4E-4

*Spectral Efficiency

This chapter was a direct adaptation of the following conference paper:

S. Faraji Alamouti*, **M. M. Ghanbari***, N. T. Ersumo, and R. Muller. “High throughput ultrasonic multi-implant readout using a machine-learning assisted cdma receiver.” In 2020 42nd Annual International Conference of the IEEE Engineering in Medicine & Biology Society (EMBC), pp. 3289–3292. IEEE, 2020.

Personal contribution: I developed the idea, designed and implemented the experimental setup and performed data collection. I wrote the majority of the original draft of the manuscript.

Acknowledgements: S. Faraji Alamouti implemented the CNN-based decoder, helped with the measurement setup and performed data post-processing. N. T. Ersumo performed piezo micro-dicing. R. Muller reviewed the manuscript and provided advice on the technical aspects of the research. R. Muller was the principal investigator of this work.

Chapter 6

A mm-Scale Free-Floating Neural Recording Implant with M-level ASK TDMA Uplink

6.1 Introduction

The human hand has 27 degrees of freedom the majority of which are controlled by two main nerves known as the ulnar and median nerves as illustrated conceptually in Figure 6.1(left). It has been shown that neural signals indirectly recorded from these nerves through muscle activation, by means of surface electromyography (EMG), can be decoded to infer intention and control custom-made active prostheses with 12 degrees of freedom [54]. This is possible because there is correlation between certain hand gestures and activation of certain (anterior) forearm muscles (as shown in [54]), but for the same reason, significantly lower degrees of freedom can be inferred in the case of transradial/transhumeral amputation when those muscles are absent [85]. These amputation types, however, account for roughly 40% of upper limb amputation cases in the Untied States [4].

There are two approaches to access neural activity in such amputation cases: 1. Targeted muscle reinnervation (TMR), and 2. *In situ* neural implants. In the former, residual nerves are surgically transferred to muscle grafts or muscles that are not mechanically functional due to amputation. The activation of these reinnervated proxy muscles acts as a stable biological amplifier for the EMG signal and subsequently helps with intention inference for active control of prostheses. Decoding hand gestures with a few degrees of freedom have been reported using this technique [85, 79]. *In situ* recording of neural activity from the ulnar and median nerves from amputees with upper limb loss (e.g. wrist disarticulation or transradial amputation) has shown to support natural hand gestures that are composites of up to 12 degrees of freedom [82], thanks to high selectivity and signal quality of *in situ* neural recording. The most commonly-used *in situ* neural recording method, however, involves implantation of microelectrodes on deeply-seated nerves that are connected to an external

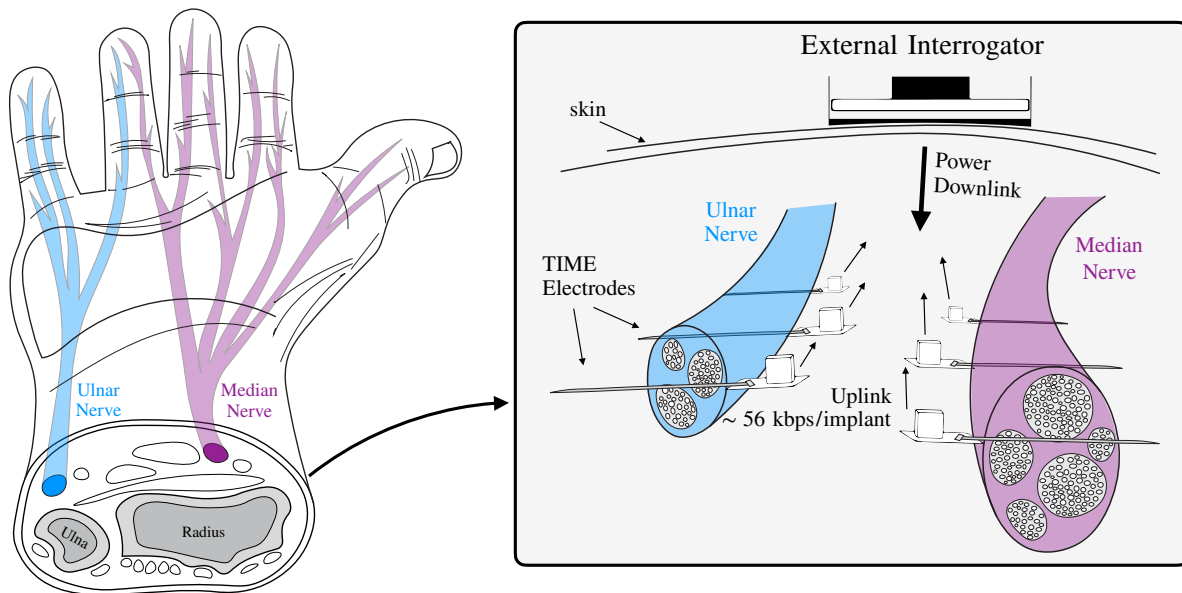


Figure 6.1: The ulnar and median nerves are centimeters apart around the wrist and each control the movement of a particular finger. Concept of distributed miniature wireless neural implants shown in the right. Each implant is ultrasonically powered and communicated and uses a transverse intrafascicular multichannel electrode (TIME) for enhanced nerve selectivity.

device, using transdermal wires, that performs recording and decoding of neural data to infer intention. The *tethered* nature of this method results in a relatively short implant lifetime (a few weeks) due to infection [82], displacement of the implanted electrodes caused by externally applied force on the wires and subsequent signal quality degradation, all of which ultimately limit the application of such implants to basic neuroscience research. In order to increase the longevity of these implants and extend their application to beyond neuroscience research, we propose a network of battery-less sub-mm scale implants that wirelessly communicate with an interrogating device, as shown in Figure 6.1(right), eliminating the wires and substantially reducing the likelihood of infection and implant displacement. In order to reach the target nerves, centimeters-deep operation ranges are required while the wireless data communications link should support greater than 56 kbps (8 bits at 7 kS/s data acquisition [19]) per channel for raw data transfer. This is a major challenge in ultrasound links given the operation frequency is often limited by the amount of harvested power and is often smaller than 3 MHz. In soft tissue, acoustic wave propagation loss (in dB) increases linearly with frequency, and at the same time, the dimensions of the implant piezo resonator are scaled down (so its resonance frequency is properly tuned to the operation frequency). Both of these trends result in a severe penalty in the harvested power by the implant piezo as

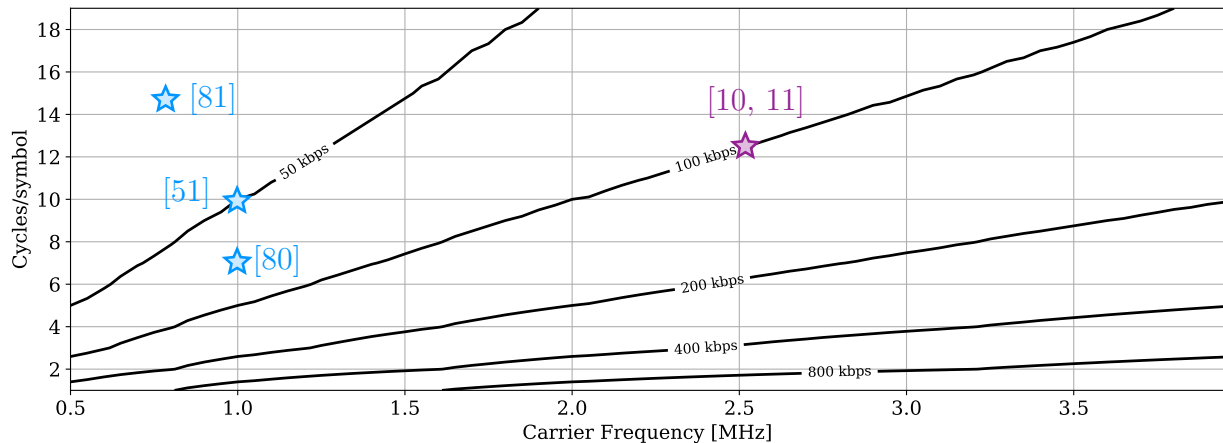


Figure 6.2: Contours show the maximum achievable data rate as a function of cycles/symbol and carrier frequency using OOK modulation in a pulse-echo protocol. Performance of prior art with OOK uplink using [pulse-echo](#) and [continuous-time](#) protocols.

the operation frequency increases. Moreover, for the purpose of miniaturization, pulse-echo communications protocol is often preferred which further reduces the available link capacity by a factor of two because in a backscatter channel data can be transferred only 50% of the time. In practice, this is an optimistic figure though, as the the external interrogator cannot immediately switch from (power) transmit to (data) receive mode (due to finite settling time of the receive chain) and therefore the channel capacity is in reality reduced by more than 50% compared to continuous-time protocols.

Therefore, given the operation frequency/bandwidth is bounded, the only other option to increase the data rate is employing a spectrally efficient modulation scheme to trade the available signal to noise ratio (SNR) according to Shannon’s theorem, i.e.,

$$DR = B \log_2(1 + SNR), \tag{6.1}$$

where DR and B are the achievable data rate and bandwidth of the link, respectively. Unfortunately, the majority (if not all) of the prior art uses the most basic (least efficient) digital modulation scheme, that is on-off keying (OOK) [11, 10, 80, 51, 75], and therefore suffer from poor spectral efficiency, Figure 6.2. Encoding more information in each symbol can be achieved by amplitude modulation (ASK), phase modulation (PSK) or a combination of both (e.g., Quadrature Amplitude Modulation). For single-piezo implants, these modulation types must however be incorporated into the echo that has proven to be challenging. This is in part due to the complexity and nonlinearity of the piezo reflection coefficient Γ with respect to its termination impedance. For instance, this nonlinearity in case of amplitude modulation can result in poor bit error rates if not addressed properly, and that explains why

the majority of the prior art uses OOK which is inherently a linear modulation scheme. In Chapter 3, we developed a powerful yet simple echo backscattering model and introduced a general echo-level linearization technique [22]. In this work, we leverage our echo model and propose a linear multi-level Amplitude Shift Keying (m-level ASK) ultrasound backscatter modulator to enhance the data rate of backscatter links by $\log_2(m)$ relative to OOK. The implemented prototype can perform up to 16-level ASK, meaning a 4x improvement in data rate can be achieved relative to OOK. The bit error rate performance is of course contingent on the SNR of the echo in the channel of interest. In this work, we also introduce a custom wireless protocol that is suitable for the setup shown in Figure 6.1(right). The protocol incorporates pulsed wireless power transmission, downlink (for implant specific configurations) and high-speed uplink backscatter communications with time-division multiple access (TDMA) protocol to avoid packet collision. The wireless protocol and modulation scheme presented in this work are generic and can be used for any application that requires high data rates such as miniature ultrasonic lensless image sensors [64].

The rest of this chapter is organized as follows. Section 6.2 provides an overview of the implant IC, discusses the proposed ultrasound wireless protocol and circuit implementation of the m-level ASK backscatter modulator and other critical blocks of the IC. Experimental verification of the prototype IC is presented in Section 6.3, and Section 6.4 concludes this chapter.

6.2 Hardware Implementation

System Overview

A simplified block diagram of the proposed implant is shown in Figure 6.3. The implant is comprised of a bulk piezo, an external capacitor and an IC. The piezo acts as a dual-purpose acoustic antenna for both wireless energy harvesting and backscatter data communications. In short, the piezo mechanically resonates in response to incident acoustic pulses (launched by an external transducer) and converts mechanical energy to electrical energy. This energy is conditioned by an active rectifier and stored on the capacitor to allow for continuous data acquisition and uninterrupted operation of other key blocks during inter-pulse gaps. For data back telemetry, the chip actively modulates the amplitude of the reflected echo by modulating the electrical termination impedance of the piezo. During inter-pulse gaps and when performing echo modulation, the chip solely relies on the charge stored on the capacitor as its source of energy. The chip has four low-dropout regulators (LDO) to generate stable supply voltages for sensitive analog blocks (1.1 V for low-noise amplifier and analog-to-digital converter) and a programmable 0.8–1.1 V supply for the digital back-end of the chip. The majority ($\sim 80\%$) of the simulated power consumption of the digital back-end block is due to leakage, and reducing the digital supply voltage helps reduce the leakage contribution. The reference voltages of all the LDOs are generated by a proportional-to-absolute-temperature (PTAT) reference circuit realized by subthreshold CMOS devices. An analog timer is used

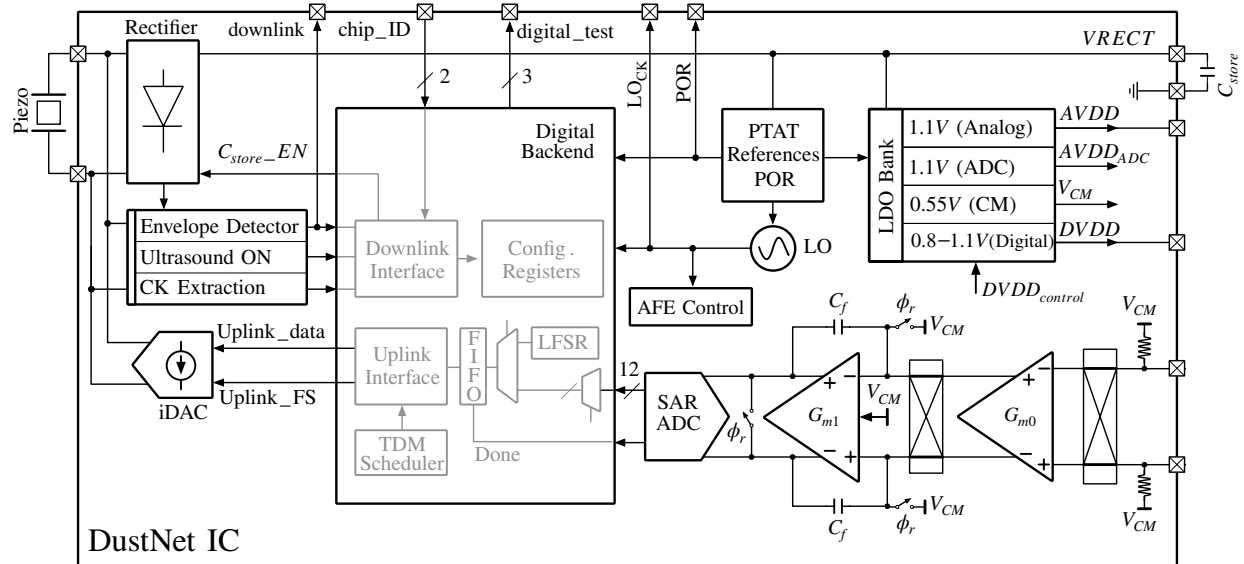


Figure 6.3: Simplified block diagram of the implant system, comprising a bulk piezo for power harvesting and data communications, an external capacitor for energy storage and the DustNet IC.

as a power-on reset (POR) signal to initialize the chip once all the supply voltages are established. The analog front-end is an open-loop $G_m C$ resetting integrator. The integration time of the integrator is controlled by a local oscillator (LO) whose frequency is automatically adjusted (using replica circuits) to compensate for the process and temperature variations of G_{m1} and C_f of the integrator to achieve a ratiometric and well-defined DC gain of 40 dB. The output voltage of the integrator is digitized by a monotonic-switching [45] successive approximation register (SAR) analog to digital converter (ADC) with a dedicated supply voltage. The digital backend assembles the ADC data into packets and commands the uplink modulator to perform piezo load modulation for data transmission. The chip uses an envelope detector as a downlink modulator, and keeps track of the incident pulses using an ultrasound-on detector. A clock signal synchronous to the ultrasound carrier frequency is extracted from the piezo voltages. This synchronous clock signal is necessary for locking into downlink symbols for demodulation and uplink data modulation.

Wireless Protocol

The proposed implant in this work is a fully wireless system that in essence is an ultrasound transceiver, supporting multi-implant bi-directional data communications and wireless power transmission on a single ultrasound link established between the implant(s) and a single-

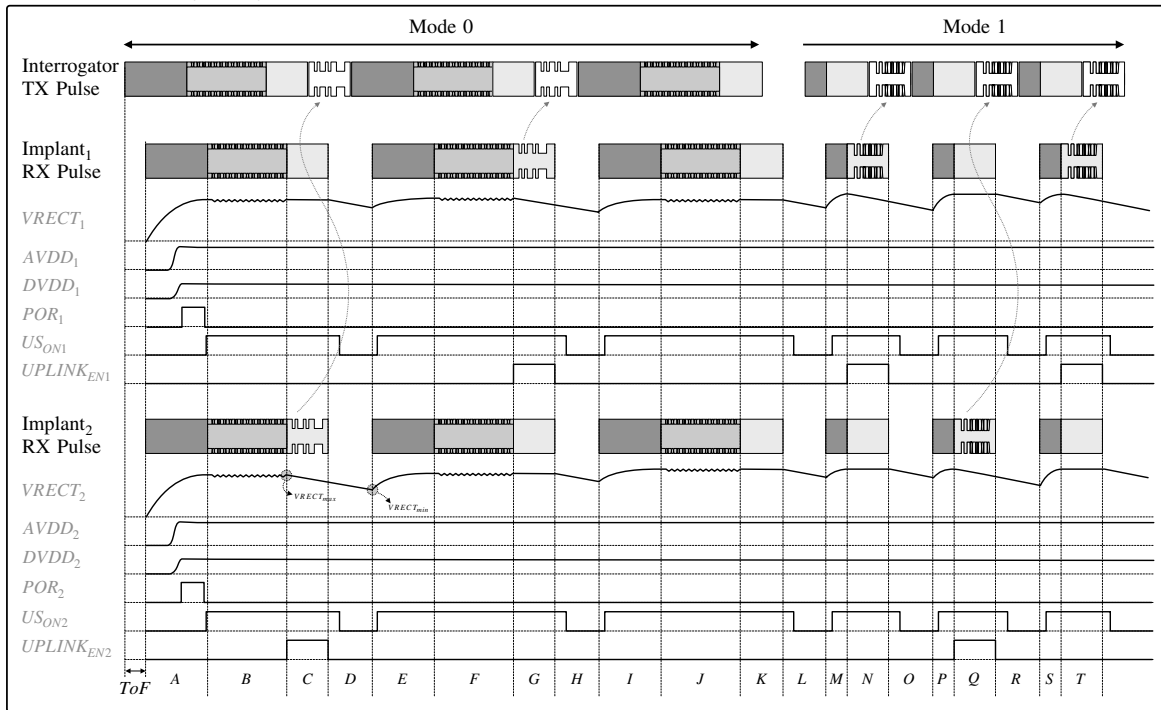
element low-cost external transducer (interrogator). The timing diagram of the proposed wireless protocol is shown in Figure 6.4. For simplicity and without loss of generality, we describe the protocol assuming the channel is comprised of two implants, Figure 6.4.

The protocol has two modes of operation: Mode 0 and Mode 1. The default mode of operation upon power up is Mode 0. Mode 0 pulses have three segments allocated for recharging the capacitor, downlink and uplink communications. This mode is mainly used for implant identification, configuration and setting up the link parameters (e.g., number of ASK levels, uplink symbol duration, etc.). During the downlink segment, the pulse envelope is modulated by the interrogator, while during the uplink segment the envelope of the echo is modulated by the implant(s). Each implant has an identification (ID) number that in the prototype IC is set through IO pads, but because Mode 0 has an ID discovery feature, the implant IDs need not be known in advance and therefore can also be implemented using Physically Unclonable Functions (PUFs). Two reserved IDs are used for broadcasting in Mode 0. Once all the implants are configured, the channel transitions to Mode 1 using the broadcast feature of Mode 0. Mode 1 pulses have only two segments for recharging and uplink data transfer. In this mode, the implants use the channel in a time-division multiple-access (TDMA) fashion. In both modes, the duration of the uplink segment must not exceed 2x the time of flight given the pulse-echo nature of the uplink. Subsequently, the inter-pulse gap should also be longer than the duration of the uplink segment so the interrogator can obtain/process the echo before transmitting the next pulse.

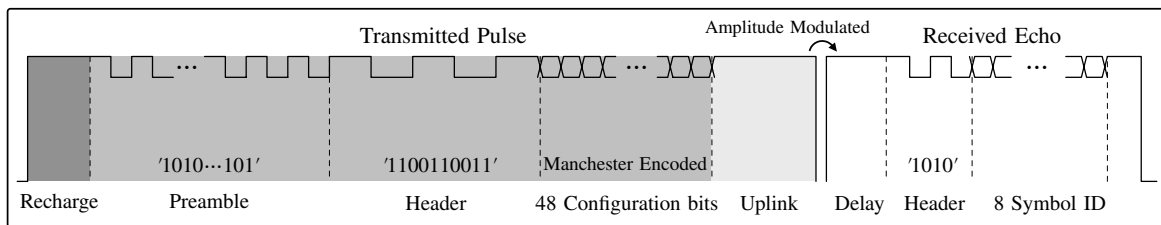
All the phases (A–T) of the protocol as well as critical signals of the implants are shown in the example diagram of Figure 6.4 (top). The following is a brief description of each phase.

- **A:** The implants receive the very first Mode 0 pulse. The harvested piezo voltage is rectified to charge the external capacitor. Once V_{RECT} exceeds the minimum required voltage headroom of the PTAT generator (1.2 V), the PTAT/LDO voltages are established and the POR is triggered to initialize the internal states of the digital circuitry. The ultrasound ON signal is also asserted given the presence of the ultrasound pulse in this phase.
- **B:** This is the downlink segment of Mode 0 during which the envelope of the pulse is modulated by the interrogator according to a certain pattern shown in Figure 6.4(middle). The downlink segment begins with a preamble that is an even number of ‘10’ sequence. The preamble is used by the implant to estimate the symbol duration that is subsequently used for correct (mid-symbol) sampling of the following symbols. Symbol estimation is performed by counting the number of carrier cycles within each ‘1’ and ‘0’ symbol of the preamble and dividing it by the total number of symbols used for estimation. The estimation process is done over 32 symbols and therefore the preamble must contain at least 32 symbols. After the symbol length estimation is complete, the chip waits for a hard-coded header ‘1100110011’ immediately after which follow the configuration bits. The chip disregards any data that follow a wrong header pattern.

Protocol Timing Diagram



Mode 0



Mode 1

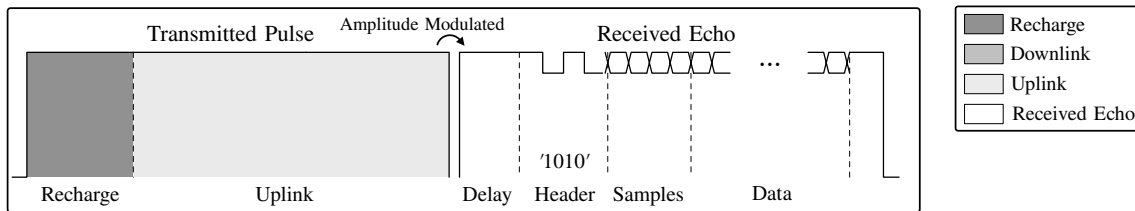


Figure 6.4: Simplified timing diagram of the proposed protocol when two implants are in operation is shown in top. The two implants are assumed to have the same distance to the external interrogator. Critical signals of each implant are also illustrated. The pattern of the envelope of mode 0 and mode 1 pulses are also shown.

There are 48 configuration bits that are Manchester encoded to avoid long sequences of ones and zeros that would skew the average of the envelope towards either level, reducing the demodulation error margin. This is necessary because the symbols are demodulated by comparing the pulse envelope with a low-pass filtered version of it. It is important to note that pulses are inevitably broadcast to all the implants. Therefore, to target and configure a specific implant, 8 of the 48 configuration bits are allocated for the target implant ID that is used for ID discovery as well (see below). Two target IDs are reserved for the purpose of broadcasting. All the implants register the configuration bits of a Mode 0 pulse if ‘11111111’ is used as the target implant ID. The other reserved ID is ‘00000000’ that cues all the implants to transition from Mode 0 to Mode 1 upon receiving it.

- **C:** After the last configuration bit is transmitted in Mode 0 downlink, the uplink segment of Mode 0 begins during which the chip modulates the envelope of the echo that is received by the external interrogator one ToF later. After a programmable delay, the uplink segment starts with a hard-coded ‘1010’ header. The external interrogator can use the header to estimate the modulation index and the symbol duration of the following uplink symbols. The Mode 0 uplink is only used for the purpose of ID discovery. That is, the implant acknowledges and transmits its ID using the uplink segment of a given Mode 0 pulse, once its ID is pinged during the downlink of that pulse. This feature allows the external interrogator to search for all the available IDs and (if not known a priori) discover the ones that are active. In the example of Figure 6.4(top), Implant₂’s ID is pinged during phase B, and it acknowledges its presence during phase C. Similarly, Implant₁’s ID is queried during phase F, and it acknowledges its presence in phase G. Unlike the modulator in [24], in order to maximize the modulation index, the piezo load modulation in this work is performed at the input of the rectifier and in order to minimize the undesired impact of drooping $VRECT$ on the envelope of the echo, the piezo is disconnected from the rest of the circuit during the uplink segment. This is achieved through the $UPLINK_{EN}$ signal. In fact, assertion of $UPLINK_{EN}$ commands the active rectifier to disconnect the piezo from the rest of the chip.
- **D:** This is an inter-pulse gap during which the implants do not receive any energy from the piezo and therefore solely rely on the energy stored on their capacitor causing $VRECT$ of both implants to drop linearly with a slope of I_L/C_{store} , where I_L is the total current consumption of the chip. Because the LDOs require at least 100 mV of voltage headroom, C_{store} and the inter-pulse gap are chosen so $VRECT$ does not drop below 1.2 V at any time. The minimum C_{store} for a required $VRECT_{min}$ can be numerically computed as follows. Assuming the piezo open-circuit voltage and series resistance are V_{Th} and R_{Th} , the relationship between the total current consumption of the chip and the maximum of $VRECT$ is given by

$$I_L = \frac{2}{\pi} \cdot \frac{V_{Th}}{R_{Th}} \left(1 - \frac{VRECT_{max}}{V_{Th}} \right) \cdot \left(1 - \frac{2}{\pi} \text{asin}\left(\frac{VRECT_{max}}{V_{Th}}\right) \right). \quad (6.2)$$

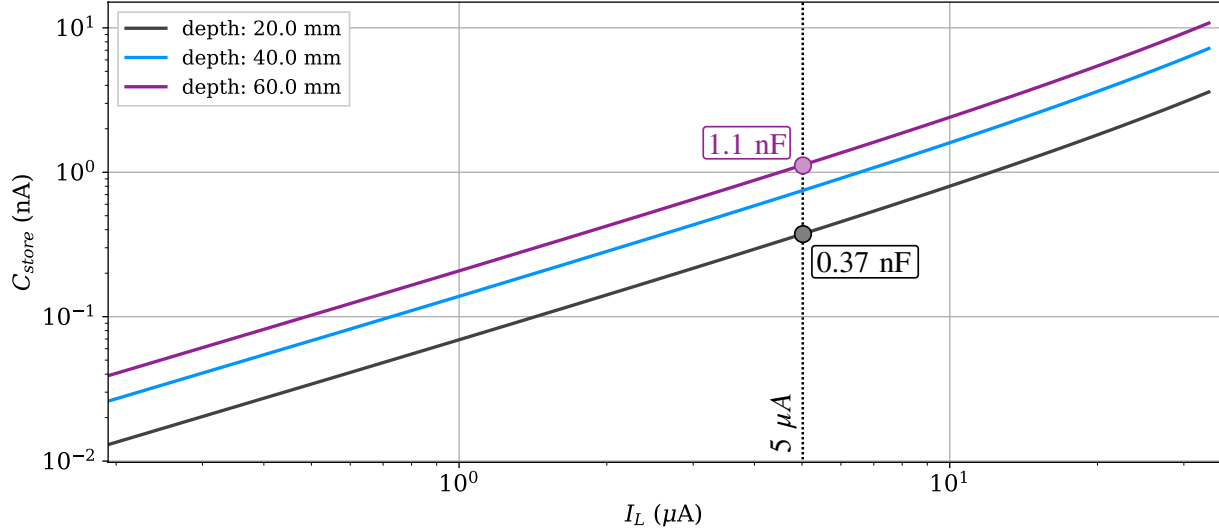


Figure 6.5: Minimum required C_{store} for a given total chip current at various depths of operation. The open-circuit piezo voltage and its series resistance are assumed to be 2 V and 2 k Ω , respectively. Target $VRECT_{min}$ is 1.2 V.

Using the relationship between I_L , $VRECT_{max}$, and $VRECT_{min}$ during the linear voltage drop region, i.e.,

$$VRECT_{max} = VRECT_{min} + \frac{2I_L T_{uplink}}{C_{store} \cdot \nu}, \quad (6.3)$$

where ν and T_{uplink} are the wave propagation speed (~ 1500 m/s) and width of the uplink segment, the minimum C_{store} can be numerically calculated. For a target $VRECT_{min} = 1.2$ V, Figure 6.5 shows the minimum required C_{store} as a function of I_L at various depths of operation. The open-circuit piezo voltage and its series resistance are assumed to be 2 V and 2 k Ω , respectively. The larger the depth of operation and I_L , the larger C_{store} is required. The total power consumption of the implant in this work is roughly 5 μA , and therefore according to Figure 6.5 a minimum of 1.1 nF of C_{store} is required for operation depths of up to 60 mm. In reality to reduce the voltage ripple of $VRECT$, a considerably larger C_{store} should be used. Lastly, during this phase after a slight delay, the ultrasound ON signal is reset given the absence of any harvested piezo voltage.

- **E, F, G and H:** These four phases are essentially the same as respectively A, B, C, and D except that in this Mode 0 pulse, Implant₁ is the target implant for downlink instead of Implant₂, and subsequently it is Implant₁ that sends back its ID as an acknowledgement. In case another implant was present in the channel, this process would continue until all implants are configured.

- **I, J, K and L:** This is the last Mode 0 pulse and is used to broadcast (using target ID of ‘00000000’) a cue to the implant(s) that the following pulses are Mode 1 pulses and therefore the beginning of the TDMA uplink. This cue is basically a single-bit flag within the downlink 48-bit configuration word. The primary parameters of the Mode 1 TDMA uplink must be set prior to this Mode 0 pulse and before transitioning to Mode 1. These primary parameters are: 1. the total number of implants ($N_{implants}$) and 2. the uplink index ($<N_{implants}$) uniquely assigned to the implant(s). Each implant decides whether it is the channel master by simply counting Mode 1 pulses, $N_{Mode1,pulse}$ (using the ultrasound ON signal) and computing $N_{Mode1,pulse}$ modulo $N_{implants}$. The implant is the channel master once the result of the modulo calculation equals this implant’s assigned uplink index. With this scheme, all the implants are synchronized and take turns during Mode 1 to use the channel. Unlike the TDMA protocols presented in [43], the proposed TDMA protocol in this work is inherently collision free and obviates the need to continuously query the implants for uplink data transmission.
- **M, N and O:** This is the very first Mode 1 pulse. Mode 1 pulses have two segments. The first segment (whose width is programmable) is allocated for recharging C_{store} . M-level ASK echo modulation is performed once the recharge segment is over. As shown in Figure 6.4(bottom), the uplink segment begins with a hard-coded ‘1010’ header to allow the external interrogator to estimate the symbol width and the extreme echo levels of the m-level ASK modulation. The following 4 symbols are reserved for the number of ADC samples being transmitted in this current pulse. The uplink modulator can perform 2-level, 4-level, 8-level and 16-level ASK modulation hereafter referred to as ASK2, ASK4, ASK8 and ASK16, respectively. Each symbol of ASK2, ASK4, ASK8 and ASK16 carries 1, 2, 3, and 4 bits of information, respectively. Depending on the number of ASK levels, 8 (ASK2, ASK4 and ASK16) or 9 (ASK8) bits of the ADC output are used for transmission. This way, an integer number of ADC samples can be transmitted in a single pulse. The implant has two data source: 1. the output of the ADC and 2. a Linear Feedback Shift Register (LFSR) that is used as a pseudo random number generator for bit error rate (BER) characterization. Note that no downlink segment is used in Mode 1 to maximize the width of the uplink segment or equivalently the number of symbols that can be transmitted in each pulse. Once transitioned into Mode 1, all the implants remain in Mode 1 and continuously record neural data and use uplink in a synchronous TDMA fashion. In the example protocol shown in Figure 6.4, $implant_1$ ’s uplink index is configured to be 0 and that of $Implant_2$ is 1. Therefore, $Implant_1$ is the channel master during even-numbered pulses and $Implant_2$ is the channel master during odd-numbered pulses.
- **P, Q, R, S and T:** The two implants take turns and transmit their data during their assigned pulse. In a multi-implant setting, the implants cannot immediately transmit the recorded neural data, and therefore must store their data between their scheduled uplink slots. A first-in first-out (FIFO) memory (12 bits wide and depth of

16) is incorporated in the digital back-end block to serve that purpose. It is important to note that transitioning into Mode 1 is a one-way operation. Therefore, if at any point during Mode 1, new configurations were needed to be loaded to implants, the implants would need to be first powered down and then powered up in Mode 0 for reconfiguration.

M-level ASK Uplink Modulator/Rectifier

We derived two closed-form expressions (when operating at series and parallel resonance) describing the relationship between the reflection coefficient Γ and the electrical termination impedance of the implant piezo Z_E in Chapter 3, equations (3.11) and (3.16). We further discussed that due to the non-linearity of $\Gamma - Z_E$, the most straightforward digital modulation is the on-off keying (OOK) because the performance (or the BER) of OOK is not altered by the nonlinear relationship of $\Gamma - Z_E$ as long as the two selected modulating Z_E values are *distant* enough to minimize the overlapping regions of the distribution of the received echo levels as shown in 6.6(a). Given $\Gamma - Z_E$ is monotonic, the simplest and most optimal choice for the two Z_E are open- and short-circuits for OOK. For an m-level backscatter ASK modulation scheme, however, the Z_E values must be chosen strategically. For instance, if equally-distant Z_E values were chosen, then due to the non-linearity of $\Gamma - Z_E$, the distribution of the received echo levels would have significant overlaps resulting in severe BER degradation. An example of such a sub-optimal selection of Z_E for ASK4 is shown in Figure 6.6(b). Alternatively, the modulating impedances Z_E can be selected in a (nonlinear) way to compensate for the

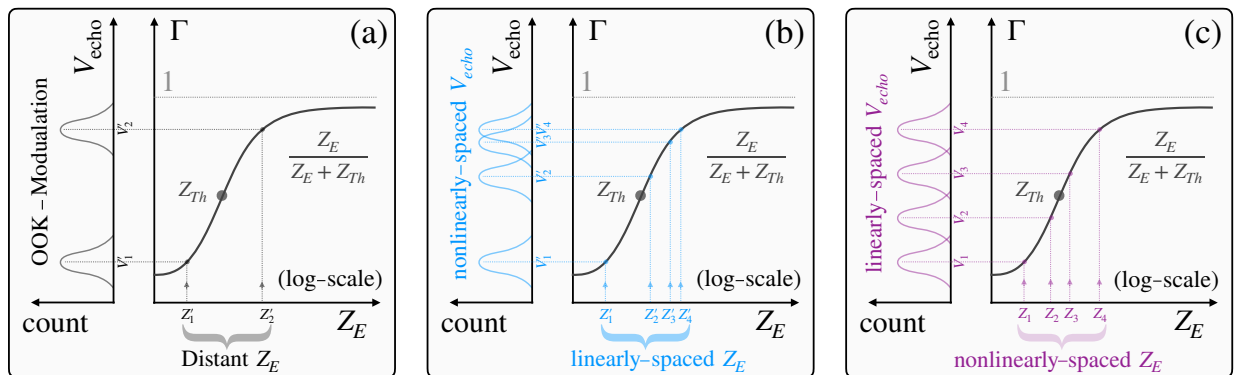


Figure 6.6: (a) OOK echo modulation using two distant (open/short) piezo electrical terminations. (b) Linearly spaced piezo termination results in heavily overlapped echo levels (and high BER) due to the inherent nonlinearity of Γ vs. Z_E . (c) Equidistant echo levels can be achieved by nonlinearly-spaced Z_E values. Note that the x-axis in these plots is log-scale, and operation at the series resonance frequency is assumed.

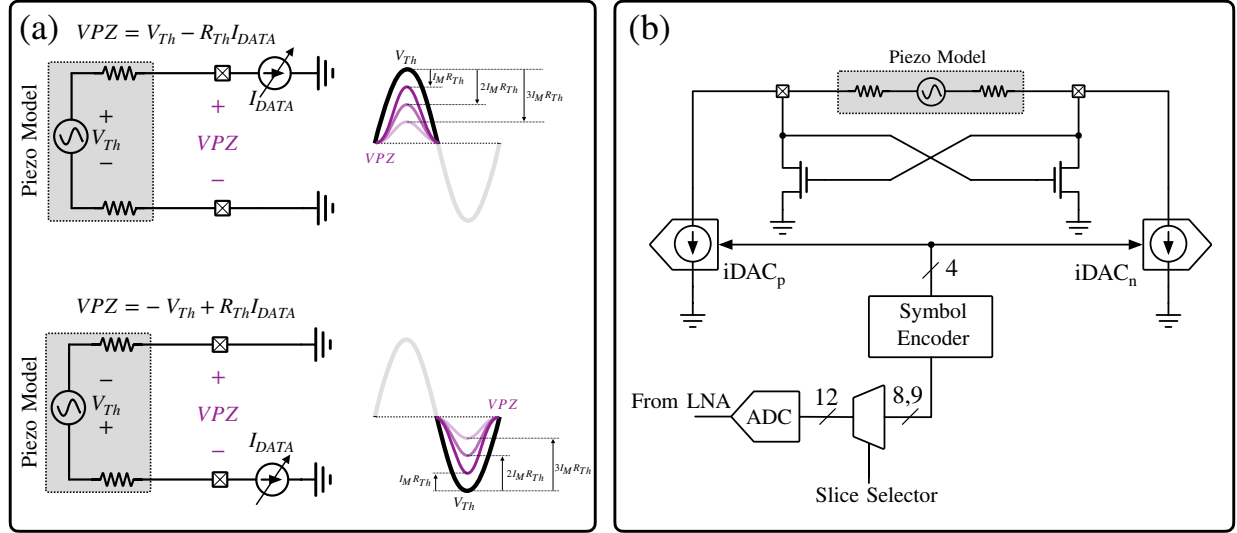


Figure 6.7: (a) ASK4 linear echo modulation shown conceptually, i.e., $\Gamma \propto VPZ \propto I_{DATA}$ (b) Simplified circuit diagram of the current-mode echo modulator consisting of two matched iDACs and a pair of cross-coupled NMOS clamp. Signal flow is shown from the input of the SAR ADC to the piezo terminals.

Table 6.1: Summary of ASK modulation Configurations

	Default Selected ADC bits for Uplink [†]	bits/Symbol	Symbols/ADC Sample	iDAC Levels
ASK2	$B_{11}, B_{10}, B_9, B_8, B_7, B_6, B_5, B_4, B_3, B_2, B_1, B_0$	1	8	2:0,15
ASK4	$B_{11}, B_{10}, B_9, B_8, B_7, B_6, B_5, B_4, B_3, B_2, B_1, B_0$	2	4	4:0,5,15,15
ASK8	$B_{11}, B_{10}, B_9, B_8, B_7, B_6, B_5, B_4, B_3, B_2, B_1, B_0$	3	3	8:0,2,4...14
ASK16	$B_{11}, B_{10}, B_9, B_8, B_7, B_6, B_5, B_4, B_3, B_2, B_1, B_0$	4	2	16:0,1,2...15

[†]symbols separated by , and grayed out bits not used

inherent non-linearity of $\Gamma - Z_E$ to achieve equi-distant echo levels and enhance the BER as shown in Figure 6.6(c). Because the $\Gamma - Z_E$ relationship is completely defined by the internal resistance of the piezo R_{Th} , i.e. $\Gamma \propto R_E / (R_E + R_{Th})$, equi-distant echo levels can be simply obtained by a set of nonlinearly-spaced termination resistances implemented as resistor banks integrated on the chip. This implementation however is not area efficient especially when $m > 8$ and operating at parallel resonance since that would require on-chip integration of multiple large (100's of $k\Omega$) resistor banks. Alternatively, since $\Gamma \propto VPZ$, equidistant echo levels can be achieved by modulating the envelope of VPZ using a current-mode circuit conceptually shown in Figure 6.7(a). In the positive half-cycle of V_{Th} , a variable current source I_{DATA} is connected between the two terminals of the piezo to create a voltage drop equal to $I_{DATA}R_{Th}$ across the piezo terminals, that is $VPZ = V_{Th} - R_{Th}I_{DATA}$. In the negative half-cycle of V_{Th} , the polarity of the current source is reversed to create the same

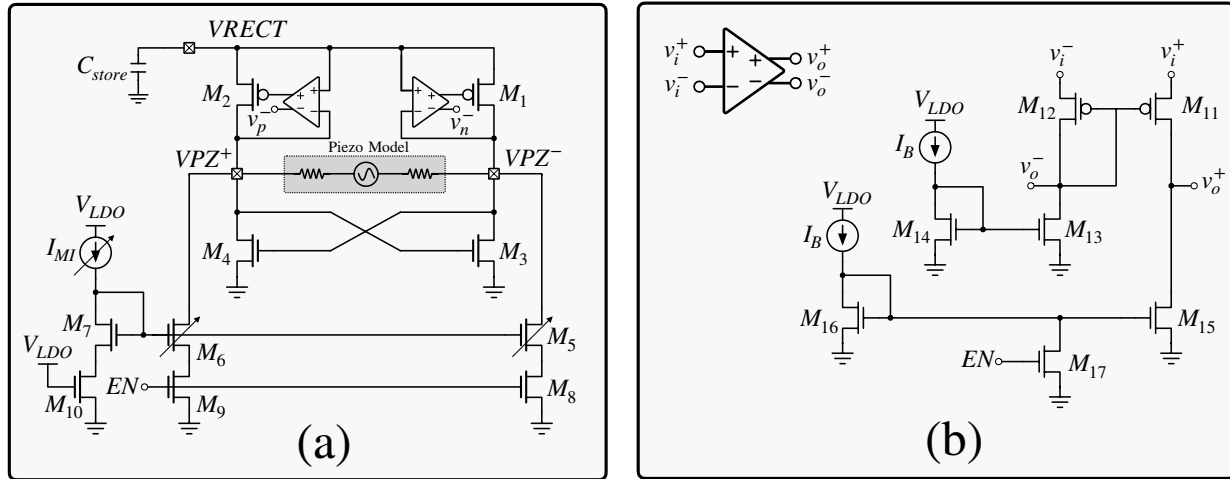


Figure 6.8: (a) Simplified circuit diagram of the proposed modulating active rectifier and (b) its common-gate high-speed comparators. The circuit has two modes: active rectifier (Figure 6.9) and linear echo (piezo load) modulator (Figure 6.10).

voltage drop across the piezo terminals. With m linearly-spaced I_{DATA} values associated with m -level symbols, e.g. $0, I_M, 2I_M$ and $3I_M$ for ASK4, linearly-spaced VPZ amplitudes and subsequently echo levels are achieved. This current-mode echo modulation can be simply implemented by: 1. a pair of current digital to analog converters, iDACs, and 2. a pair of cross-coupled clamping NMOS devices as shown in Figure 6.7(b). The iDACs are matched and share the same inputs. This prototype uses 4-bit iDACs since up to 16 levels are needed for ASK16. For smaller modulation levels, a subset of iDAC levels are used for modulation as listed in the last column of Table 6.1. For instance, for ASK4, iDAC codes 0, 5, 10 and 15 are used for the four required symbol levels. In each half-cycle of the piezo voltage, one of the piezo terminals is tied to ground by the cross-coupled NMOS pair while I_{DATA} is drawn from its other terminal by the corresponding iDAC. Since the circuit is symmetric, in the other piezo half-cycle the same current is drawn from the piezo but in the opposite direction essentially modulating VPZ and the echo amplitude.

After amplification, the acquired neural signal is digitized by a 12-bit SAR ADC. In this prototype, in order to reduce the required data rate per implant, an 8- or a 9-bit slice of the 12-bit ADC output word is selected for uplink transmission. The default bits selected for transmission for each ASK configuration are listed in Table 6.1. A slice selector would allow to select any 8- or 9-bit slice from the 12 bit ADC word as shown in Figure 6.7(b). Non-default slices (with missing MSBs) would inevitably cause signal wrapping and therefore would require unwrapping on the interrogator side. In order to convert the raw ADC data to ASK symbols (or equivalently iDAC levels), a symbol encoder takes the raw ADC slice, groups bits into symbols and maps every symbol into iDAC input according to the ASK

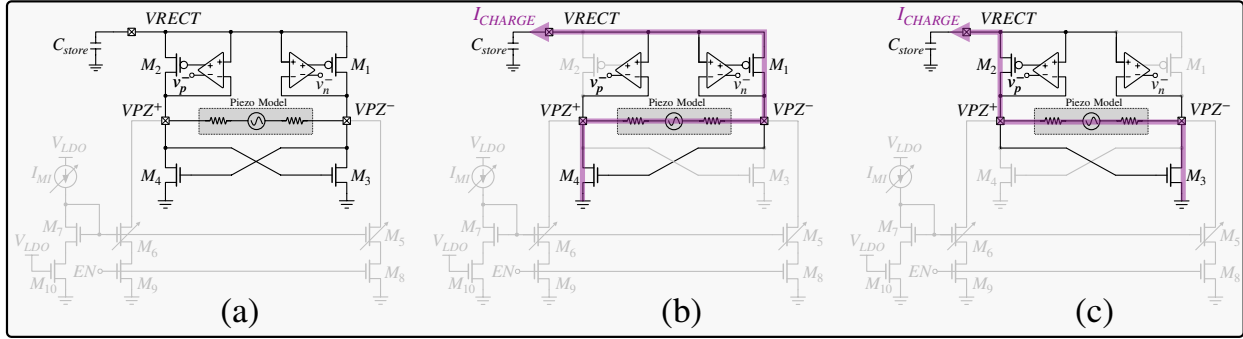


Figure 6.9: (a) During active rectification, the load modulating devices (M_5 and M_6) are disabled and the piezo current is properly steered through the PMOS pass transistors, M_1 and M_2 , in both the (b) negative and (c) positive half cycles of the harvested piezo voltage to charge C_{store} .

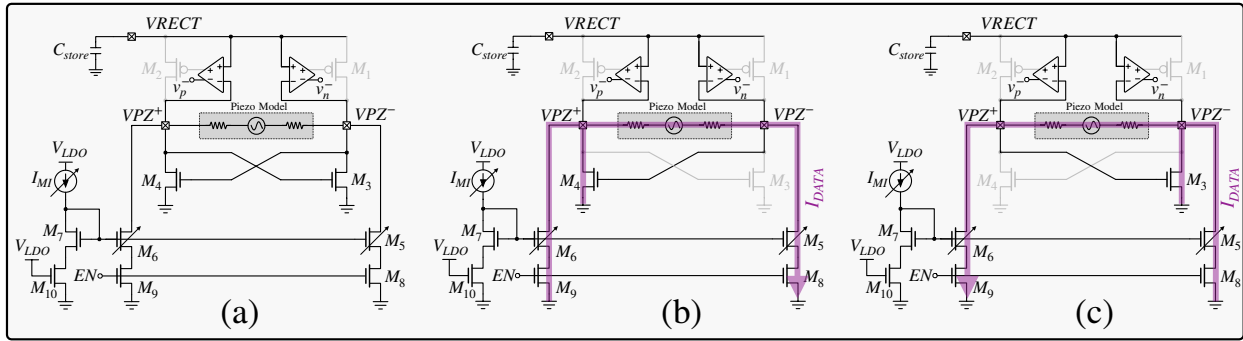


Figure 6.10: (a) For echo modulation, the non-inverting outputs of the comparators are forced to a high-state, disabling both the PMOS pass transistors, M_1 and M_2 , disconnecting C_{store} and protecting its stored charge from the large modulating current drawn from the piezo terminals. Quasi digital data in terms of current I_{DATA} is drawn from the piezo causing a linear voltage drop in both (b) negative and (c) positive half cycles of the piezo effectively modulating the envelope of the echo.

scheme as shown in Table 6.1. For instance, for ASK8, the 9-bit ADC slice is grouped into three 3-bit symbols. These 3-bit symbols are then mapped into 8 iDAC codes (0, 2, 4, . . . 14).

The uplink modulator shown in Figure 6.7(b) can be incorporated into the active rectifier of the implant as shown in Figure 6.8(a). M_3 and M_4 are the cross-coupled NMOS devices that tie one terminal of the piezo to ground in each half cycle. M_5 and M_6 are the output branches of the two 4-bit iDACs of the uplink modulator, while M_1 and M_2 are the PMOS pass transistors of the active rectifier whose gates are controlled by the high-speed common-gate comparators, Figure 6.8(b).

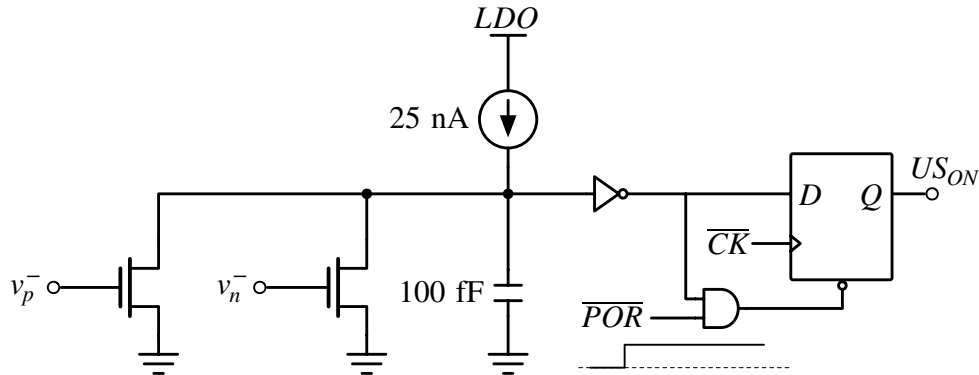


Figure 6.11: Ultrasound ON detector. Control signals v_p^- and v_n^- are the inverting output terminal of the high-speed rectifier comparators.

During the power harvesting mode, Figure 6.9, the uplink enable signal EN is low, and the outputs of the iDACs are disabled. Moreover, the pull-down switch inside the comparators M_{17} is off, and the comparators alternately pull down the gates of M_1 and M_2 to charge C_{store} , Figures 6.9(b) and (c). When the uplink enable signal EN is asserted, the circuit is transformed into the uplink modulator, Figure 6.10(a). That is, in Figure 6.8(b), M_{17} turns M_{15} off and the v_o^+ outputs of both the comparators are charged to $VRECT$ (through M_{11}) turning off both M_1 and M_2 disengaging C_{store} from the piezo terminals. At the same time, the output branches of the iDACs are enabled to create linear voltage drops (proportional to I_{DATA}) across the piezo voltage VPZ effectively modulating the amplitude of the echo. It is important to reiterate that M_1 and M_2 must be kept off during echo modulation to protect the stored charge on C_{store} from the large echo modulating current I_{DATA} , shown in Figure 6.10.

Ultrasound-ON Detector

In the wireless protocol described earlier, the implants need to know the presence of an ultrasound pulse. This is particularly important in Mode 1 when the implants rely on a synchronous pulse counter to determine their scheduled uplink time slot. The implemented ultrasound ON detector circuit is shown in Figure 6.11. The main devices are two pull-down NMOS switches that are activated once an ultrasound pulse is detected. The gates of these devices are simply controlled by the inverting output terminals of the rectifier comparators, drain of M_{12} in Figure 6.8(b), that for non-zero VPZ swing between ground and $VPZ/2 - V_{GS,12}$. Therefore, in presence of an ultrasound pulse when $VPZ/2 \geq V_{TH} + V_{GS,12}$, the NMOS switches are activated and quickly discharge the 100 fF capacitor. In the absence of a pulse, M_{14} in Figure 6.8(b) pulls down v_p^- and v_n^- to ground turning off both the NMOS switches of the ultrasound ON detector allowing the 25 nA current source to recharge the

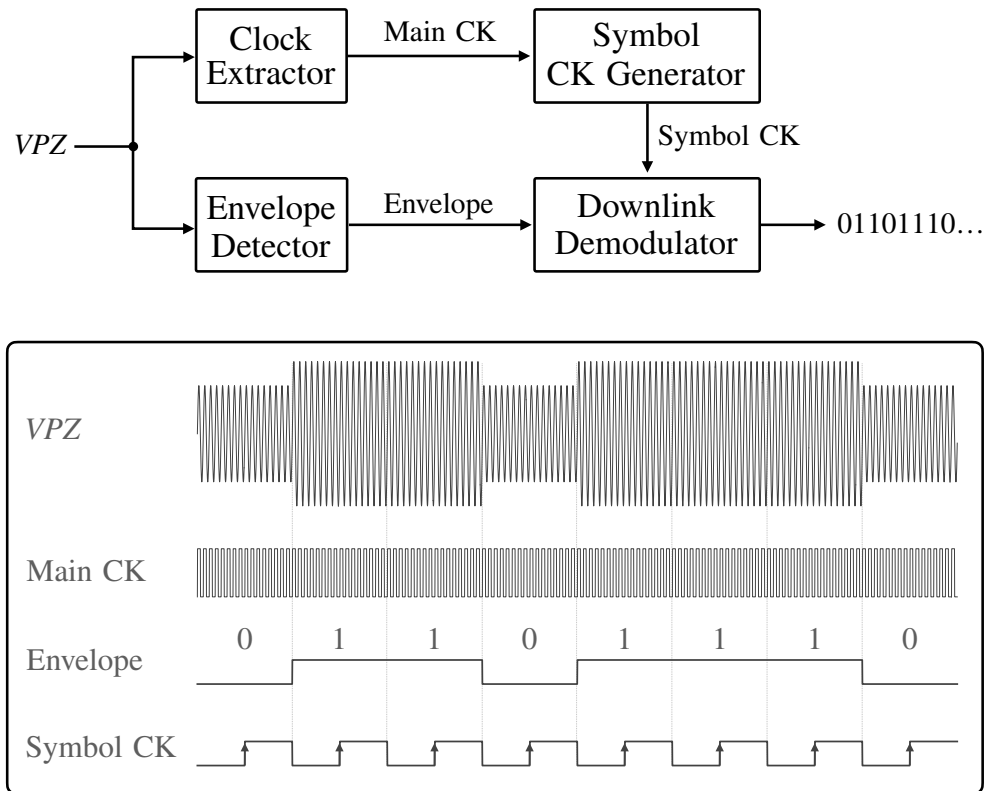


Figure 6.12: Downlink demodulator block diagram. The received *VPZ* carries both data and clock. The extracted (and hence synchronous) main clock is divided to generate the symbol sampling clock.

100 fF capacitor that asynchronously clears the output of the D-latch.

Clock Extraction

The ultrasound communication link in this work is a single-line link that carries both the data and clock signals. As shown in Figure 6.12, the data (symbols) are simply encoded into the envelope of the ultrasound pulse, or equivalently the harvested piezo voltage *VPZ*. The correct sampling of the downlink symbols requires a clock that is time-aligned with the middle of each symbol. This symbol-sampling clock is generated on-chip from a main clock that is extracted from *VPZ* (see Figure 6.12) using a comparator discussed below. Since the symbol width is constant, the symbol sampling clock is in fact generated by dividing the main clock by the estimated number of cycles per symbol and shifting it by half the symbol width. The uplink symbols width is also programmable in terms of the ultrasound cycles per symbol (that can be selected from the following widths: 4, 8, 12 and 16 cycles/symbol). Therefore,

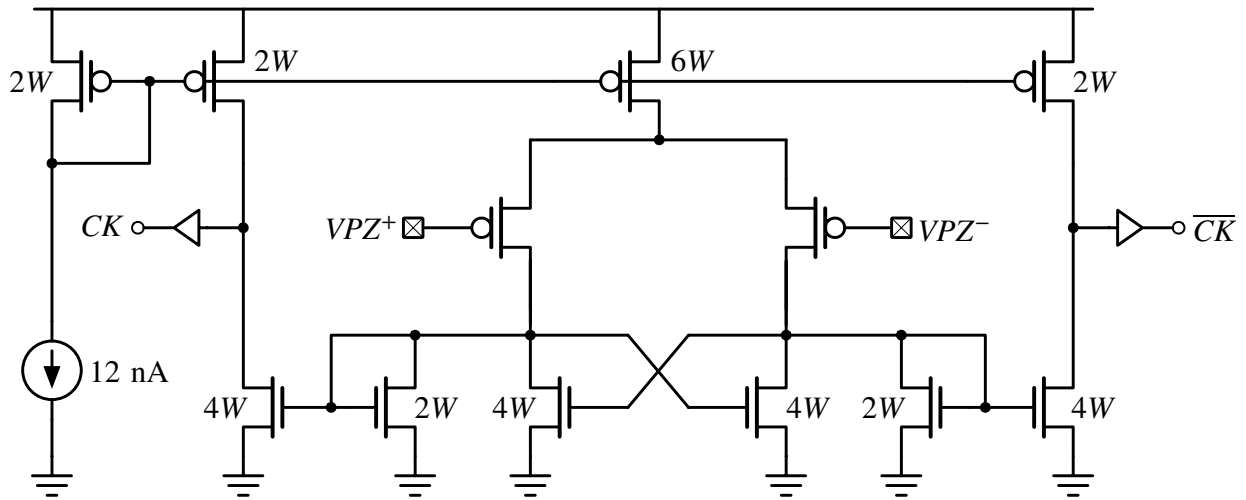


Figure 6.13: Clock extraction from VPZ using a high-speed comparator with a built-in hysteresis.

the uplink interface also uses the main extracted clock to synchronize the uplink symbols with the ultrasound carrier signal. Because the pulse duration is short (especially in the uplink mode), a fast phased-locked loop would be needed to lock into the carrier frequency that would result in a power-hungry design. Alternatively, given the carrier frequency is in the MHz range, a moderate-speed low-power comparator is used in this work to extract the clock directly from VPZ .

The circuit diagram of the clock extractor is shown in Figure 6.13 which uses the large-swing piezo signals VPZ^+ and VPZ^- as its input. Note that the inputs of the comparator swing between ground and $VPZ/2$, therefore PMOS input devices are chosen so the clock is extracted even with small voltage swings on VPZ (i.e., during ramp up and ramp down at the beginning and end of each pulse). The clock extractor is a high-gain (~ 38 dB) open-loop amplifier with a bandwidth of 2.5 MHz. In order to enhance its noise immunity, a pair of double-sized cross-coupled NMOS devices are used as an active load of the first stage to build a ± 10 mV of hysteresis. The core comparator (excluding the output buffers) consumes ~ 70 nA of static current from the digital supply rail.

Envelope Detection

A simplified circuit diagram of the envelope detector of the implant is shown in Figure 6.14. The input NMOS pair and the 50 fF tail capacitor act as a peak detector [53]. The output of this stage is followed by two low-pass filters (LPF) with corner frequencies of 1 MHz and 12 kHz. The first LPF extracts the symbols and cleans out the output of the peak

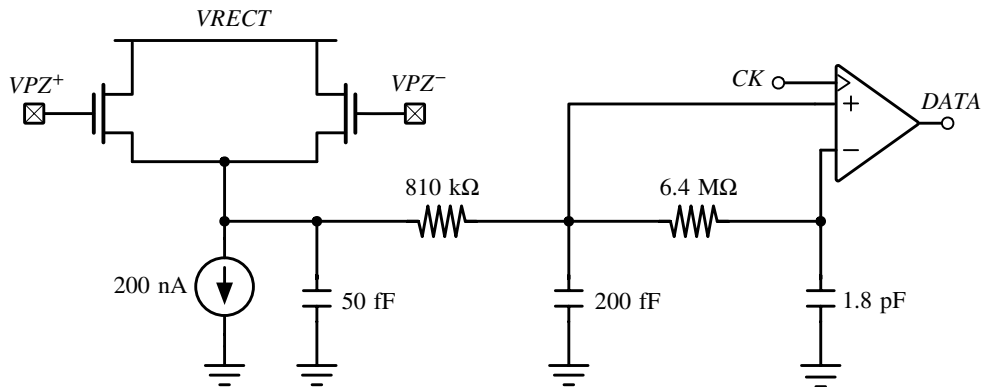


Figure 6.14: Simplified circuit diagram of the envelope detector.

detector by filtering its high-frequency (ultrasound carrier) contents, while the second LPF extracts the mean of the envelope. The outputs of the two LPFs are then compared using a single-bit quantizer (strongArm comparator) to digitize the envelope. For random data, the average of the envelope is most likely the average of the two levels, but for highly skewed data (containing a long sequence of 1's or 0's), the average will move towards one of the levels and narrows the noise margin of the comparator. Therefore, the data is Manchester encoded on the interrogator side to make sure the average of the envelope always equals the average of the two levels.

PTAT Reference and POR

All the LDO reference voltages and bias currents (except for the LNA that has a dedicated PTAT generator) are generated by the main PTAT reference generator of the chip whose circuit diagram is shown in Figure 6.15. In the core circuit, the PMOS current mirror ensures that the currents of M_1 and M_2 are the same. Given M_1 and M_2 are biased in the subthreshold region, the voltage drop across the source resistor R_s is given by

$$\Delta V_{GS} = V_{GS2} - V_{GS1} = \eta V_T \log\left(\frac{W_1}{W_2}\right), \quad (6.4)$$

where $\eta \sim 1.1$ is the subthreshold slope coefficient and $V_T = kT/q \sim 26$ mV is the thermal voltage. For $R_s = 640$ kΩ, the current of each branch of the PTAT core settles to 50 nA. This reference PTAT current is mirrored to a resistor ladder (with resistors having the same type as that of R_s) to generate five reference voltages that are used throughout the chip. The PTAT core circuit has two stable operating points one of which is undesired as it results in $I_1 = I_2 = 0$. To avoid the undesired operating point, a start-up circuit, comprising M_{s1} and C_s , forces a non-zero start-up current through the two branches of the PTAT core.

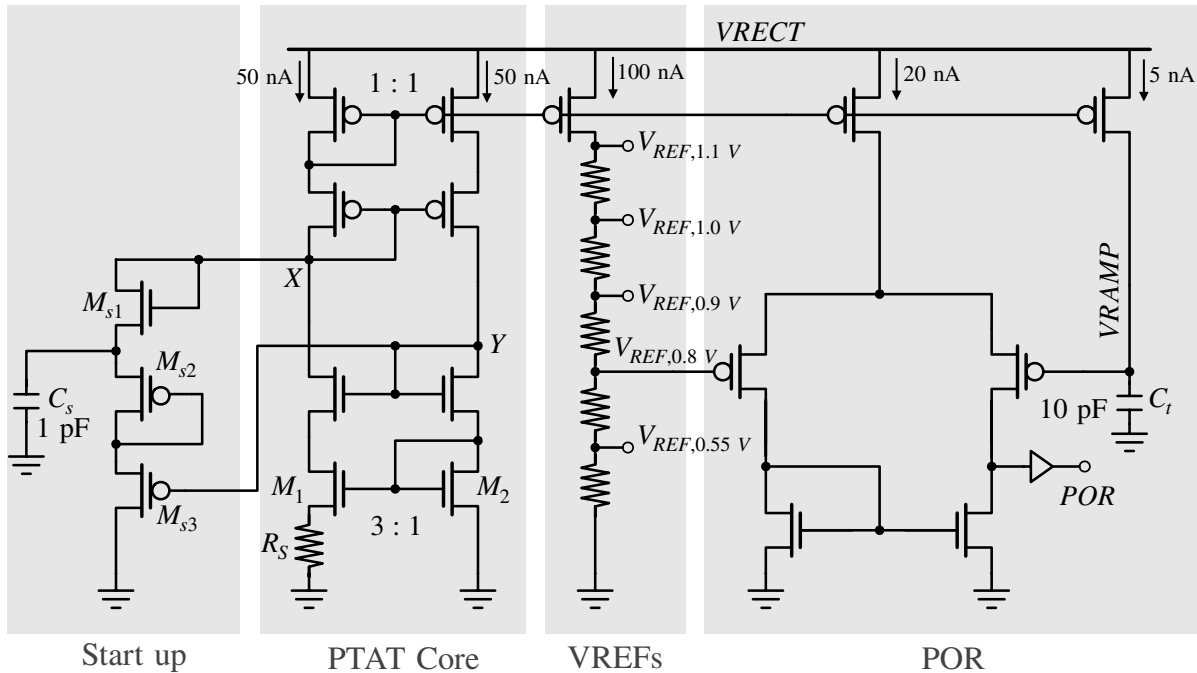


Figure 6.15: Simplified circuit diagram of PTAT reference generator and the POR.

During the power-up phase, C_s has no stored charge. Therefore, the diode-connected M_{s1} draws current from the left branch of the PTAT core to charge up C_{store} to approximately $VRECT - 2V_{GS} - V_{Th}$, at which point M_{s1} turns off and no current is drawn from the PTAT core (except for negligible M_{s1} subthreshold current to compensate for leaked charge out of C_s). After power-down M_{s2} and M_{s3} provide a discharge path for C_s .

The power-on reset on the chip must be triggered when all the reference voltages are settled. Based on the simulation results, it takes about 1 ms for the PTAT core reference current and all the reference voltages to be established, therefore a 1.5 ms analog timer is used to trigger the power-on reset (POR) signal. The analog timer is implemented by a 5 nA current source and a 10 pF capacitor. A continuous-time comparator detects when $VRAMP$ equals 0.8 V that takes approximately 1.5 ms after all the reference voltages are settled. Because $VRAMP$ monotonically rises from ground to $VRECT$, the POR signal is triggered only once.

CG-Compensated Regulators

There are four low-dropout regulators (LDO) on the chip that regulate $VRECT$ and convert it to: 1. a 1.1 V analog supply rail, 2. a 1.1 V supply rail dedicated for the SAR ADC, 3. a 0.55 V supply for the common-mode voltage of the low-noise amplifier, and 4. a configurable

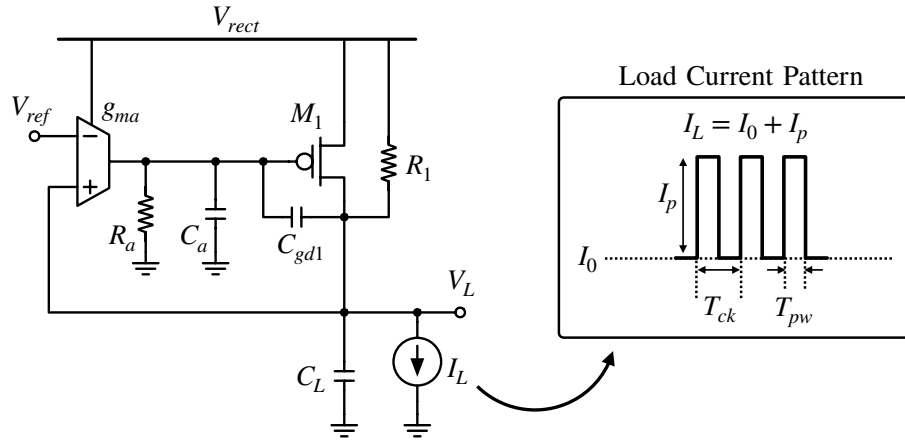


Figure 6.16: Simplified circuit diagram of the classic low-dropout regulator. The loop amplifier is modelled by a G_m -cell and its parasitic output load R_a and C_a . Load is modelled by a constant current sink I_L .

0.8–1.1 V digital supply rail.

The classic LDO topology is shown in Figure 6.16 which is a closed-loop system comprising a PMOS pass transistor M_1 , a loop amplifier and a load capacitor. The load circuit is modeled by a current sink I_L . Because of its finite bandwidth, the LDO responds to only slowly varying I_L . In other words, the feedback loop is *broken* when dealing with high-frequency contents of the load current I_p . Therefore, a load capacitance C_L is often placed at the output of the LDO to immediately provide current for fast transitioning currents. The minimum required C_L is determined by the maximum amount of ripple $V_{L,ripple}$ that can be tolerated on V_L . That is,

$$C_{L,min} = \frac{I_p T_{pw}}{V_{L,ripple}}. \quad (6.5)$$

Since the LDO is a feedback system, its stability is of paramount importance. In fact, it is critical that these LDOs remain stable at all times including the start-up phase when their load currents rise from zero to their steady-state levels. The loop-gain transfer function of

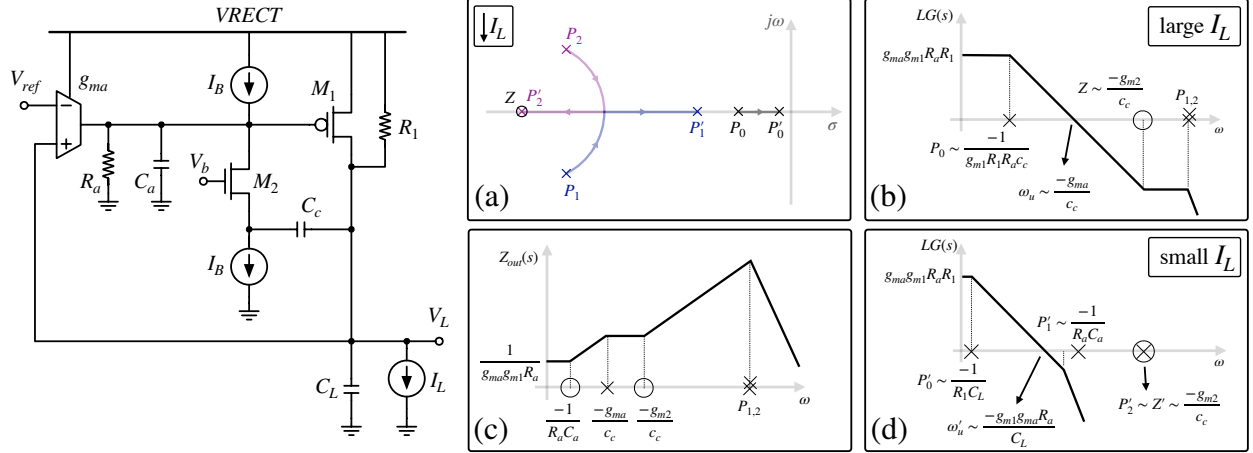


Figure 6.17: (left) Simplified circuit diagram of the common-gate compensated low-dropout regulator. (right) The root-locus of the loop-gain for decreasing I_L is shown in (a). The bode diagram of the loop-gain for (b) relatively large I_L and (d) relatively small I_L . The bode-diagram of the output impedance is shown in (c).

the classic LDO can be simply found as

$$H(s) = H_0 \frac{(1 - s/\omega_z)}{(1 - s/\omega_{p1})(1 - s/\omega_{p2})}, \quad (6.6)$$

$$H_0 \simeq g_{ma}g_{m1}R_aR_1, \quad (6.7)$$

$$\omega_{p1} \simeq -\frac{1}{R_a(c_{gs1} + (1 + g_{m1}R_1)c_{gd1}) + R_1(c_{gd1} + C_L)}, \quad (6.8)$$

$$\omega_{p2} \simeq -\frac{R_a(c_{gs1} + (1 + g_{m1}R_1)c_{gd1}) + R_1(c_{gd1} + C_L)}{R_aR_1(c_{gs1}c_{gd1} + c_{gs1}C_L + c_{gd1}C_L)}, \quad (6.9)$$

$$\omega_z = +\frac{g_{m1}}{c_{gd1}}, \quad (6.10)$$

which is a second-order system with a problematic zero in the right half plane. A phase margin greater than 45° can be achieved by pushing the zero past the unity gain bandwidth of the loop ($\omega_u \simeq g_{ma}/c_{gd1}$), i.e. $g_{m1} \gg g_{ma}$, which is possible with large output current I_L . During start-up phase, however, I_L can be small which places the zero closer to the unity gain bandwidth decreasing the phase margin and making it challenging to guarantee stability. The root cause of the instability issue with the classic LDO at $I_L \approx 0$ is the presence of the right half plane zero associated with the feed-forward path through the miller compensation capacitor C_{gd1} that can be avoided by a common-gate stage as shown in Figure 6.17(left).

The loop gain transfer function of the CG-compensated LDO is given by

$$H(s) \simeq \frac{g_{ma}g_{m1}R_aR_1(1 + s\frac{C_c}{g_{m2}})}{(1 + sR_1(C_L + g_{m1}R_aC_c))(1 + s\frac{C_L R_a C_a}{C_L + g_{m1}R_a C_c} + s^2\frac{R_a C_a C_c C_L}{g_{m2}(C_L + g_{m1}R_a C_c)})}, \quad (6.11)$$

$$H_0 \simeq g_{ma}g_{m1}R_aR_1, \quad (6.12)$$

$$\omega_{p0} \simeq -\frac{1}{R_1(C_L + g_{m1}R_aC_c)}, \quad (6.13)$$

$$\omega_{p1,2} \simeq -\frac{g_{m2}}{C_c} \left(1 \pm \sqrt{1 - 4\frac{C_c}{g_{m2}} \cdot \frac{C_L + g_{m1}R_aC_c}{R_aC_aC_L}} \right), \quad (6.14)$$

$$\omega_z = -\frac{g_{m2}}{C_c}, \quad (6.15)$$

which is a 3rd-order system with a left half plane zero. The root locus of the poles and the zero of the loop-gain transfer function is shown in Figure 6.17(a) as a function of decreasing I_L . Reducing I_L pushes the dominant pole ω_{p0} towards the origin and causes the complex-conjugate poles to split on the real axis. One of split poles moves towards the origin, while the other one moves towards the zero, effectively making the loop a second order loop whose stability can be guaranteed by design. The bode diagrams of the loop gain transfer function for large and small I_L values are shown in Figures 6.17(b) and (c), respectively. At small I_L values, for a phase margin greater than 45°,

$$C_L \geq g_{m1}g_{ma}R_a^2C_a. \quad (6.16)$$

At large I_L values, the loop can also be treated as a second-order system if the complex conjugate poles are aligned with the zero. Assuming the complex-conjugate poles are under-damped, this can be achieved by equating their natural frequency with the location of the zero, that is

$$\frac{g_{m2}}{g_{m1}} = \frac{C_c^2}{C_aC_L}. \quad (6.17)$$

In this case, for a phase margin greater than 45°, the non-dominant pole must be larger than the unity-gain bandwidth of the loop, $\omega_u \approx g_{ma}/C_c$, that is

$$g_{m2} \geq g_{ma}. \quad (6.18)$$

Equations (6.16)–(6.18) can be used as design equations to guarantee stability at two extreme I_L values. The stability of the final design, however, must be verified for I_L values between the extreme cases through extensive simulations.

The output impedance of the LDO determines its power-supply rejection (PSR). Given *VRECT* has a high-frequency tone at 2x the carrier frequency, the PSR at that frequency should be small. The output impedance of the CG-compensated LDO is given by

$$Z_{out} \approx \frac{1}{g_{m1}g_{ma}R_a} \cdot \frac{(1 + sR_aC_a)(1 + s\frac{C_c}{g_{m2}})}{(1 + s\frac{C_c}{g_{ma}})(1 + s\frac{C_aC_L}{g_{m1}C_c} + s^2\frac{C_LC_a}{g_{m1}g_{m2}})} \quad (6.19)$$

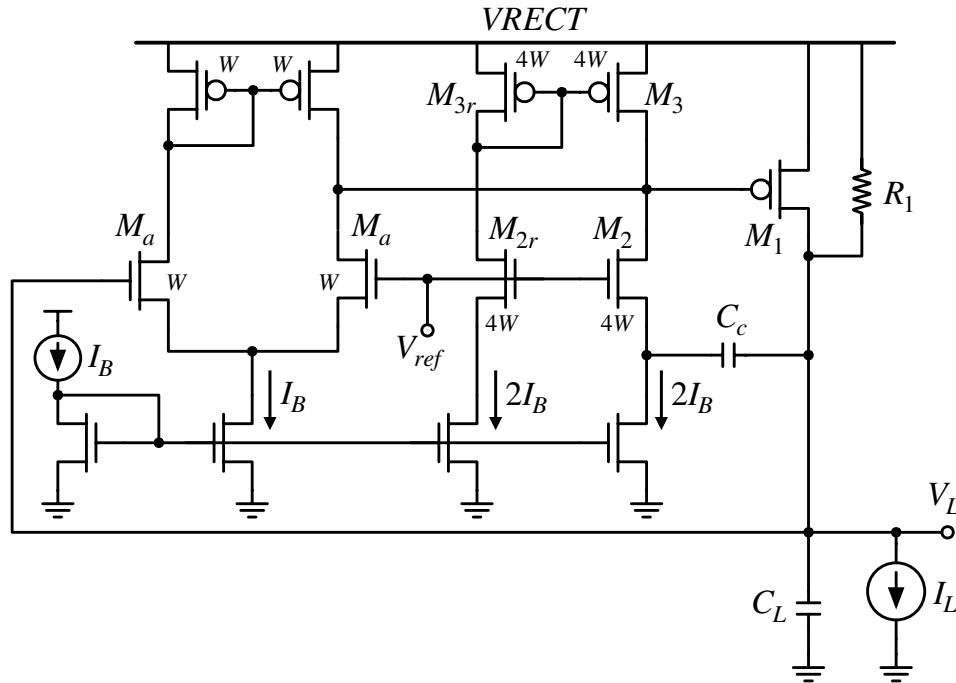


Figure 6.18: The circuit implementation of the CG-compensated LDO.

The bode diagram of the output impedance of the LDO is also shown in Figure 6.17(c).

A straightforward circuit implementation of the CG-compensated LDO topology is shown in 6.18 where g_{ma} is implemented by a 5-transistor OTA. In this design, $g_{m2} = 2g_{ma}$ is chosen as a compromise between power consumption and phase margin. This choice also makes it simpler to use a replica bias branch and hence the available V_{ref} to bias M_2 as shown in Figure 6.18. To keep M_a devices in saturation at all times,

$$VRECT - |V_{GS1}| \geq V_{ref} - V_{GS,a} + V_{dsat,a}, \quad (6.20)$$

where $V_{dsat,a}$ is the drain-source saturation voltage of M_a devices. Therefore, M_1 and M_a should be strong (large W/L) and weak (small W/L), respectively.

Low Noise Amplifier

A simplified circuit diagram of the analog front-end (AFE) is shown in Figure 6.19 along with the timing diagram of its critical command signals and detail circuit diagrams of its main blocks. The open-loop integrating-sampler AFE architecture is chosen in this work since it inherently has a large input impedance which is essential to prevent signal attenuation when micrometer-scale electrodes are used. Similar to [15], the input devices of the first stage are biased at V_{CM} by long-FET devices (M_1 and M_2 in Figure 6.19(c)) carrying a nominal DC

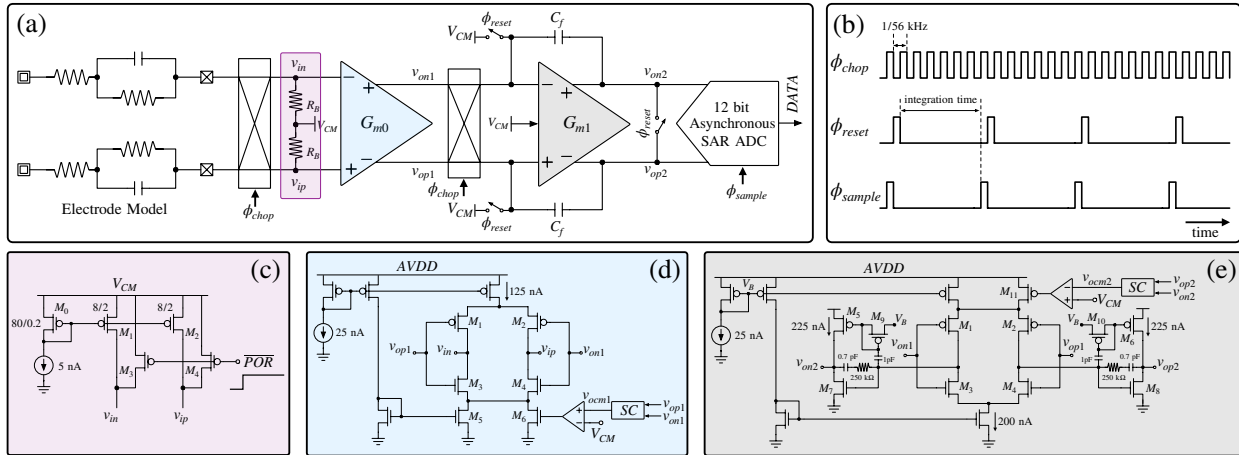


Figure 6.19: (a) Simplified block diagram of the analog front-end. (b) timing diagram of critical switches. (c) Simplified circuit diagram of the input biasing network. Simplified circuit diagram of the (d) first and (e) second G_m cells.

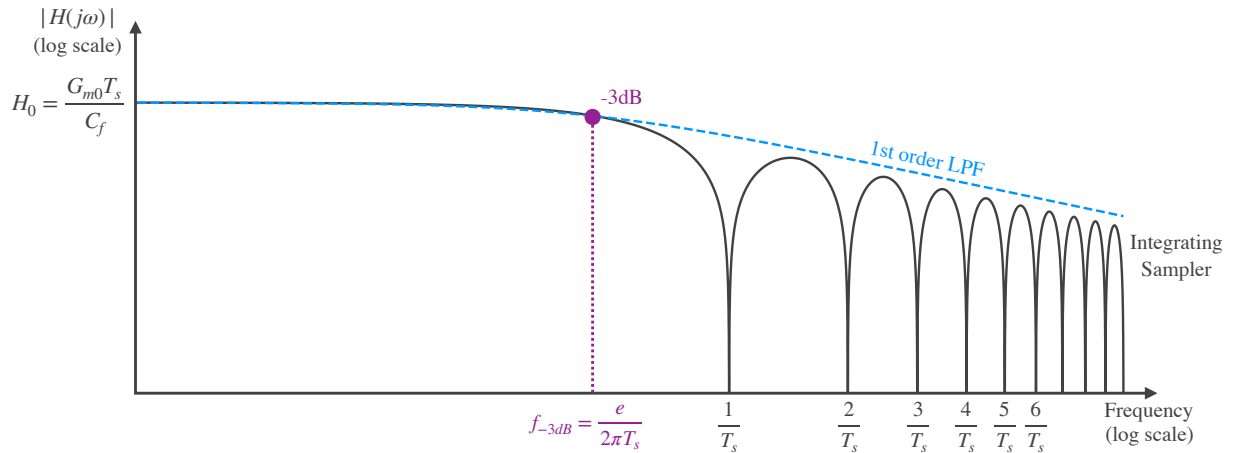


Figure 6.20: Transfer function of the integrating sampler with the integration period of T_s has a -3 dB bandwidth at $\approx 0.44/T_s$, and notches at integer multiples of $1/T_s$.

current of 50 pA, translating to 20 G Ω differential input resistance (assuming electrodes are biased at the IC ground). In order to speed up the biasing at the start-up phase, M_3 and M_4 provide a quick charge-up path for the electrode capacitance to V_{CM} before the POR is triggered. The main G_m cell, G_{m0} , is realized as a fully complementary OTA for its superior noise-power performance. G_{m0} converts the input voltage to current that is subsequently

(LO) shown in Figure 6.21. The constant- g_m biasing technique, shown in Figure 6.21(a), uses a dedicated PTAT current generator to bias the input pairs of G_{m0} . That is,

$$I_{PTAT} = \frac{\eta V_T \text{Ln}(W_2/W_1)}{R}, \quad (6.23)$$

$$G_{m0} = \frac{I_{PTAT}}{2\eta V_T} \propto \frac{\text{Ln}(W_2/W_1)}{R}, \quad (6.24)$$

where η and V_T are the subthreshold constant and thermal voltage (≈ 26 mV), respectively.

The oscillator shown in Figure 6.21(b) uses the same PTAT current, generated by the dedicated PTAT core, to alternately charge and discharge a capacitor, C_0 . Two continuous-time comparators with embedded systematic input-referred offsets are used to determine the state of the oscillator, e.g. charging or discharging. Assuming devices are in subthreshold,

$$V_{OS} = \eta V_T \text{Ln}(W_6/W_7), \quad (6.25)$$

$$T_{LO} = \frac{4C_0 V_{OS}}{\beta I_{PTAT}} \propto RC_0 \frac{\text{Ln}(W_6/W_7)}{\text{Ln}(W_2/W_1)}, \quad (6.26)$$

and therefore if T_{LO} or a fraction of it (e.g., T_{LO}/M) is used for the integration time, (6.22), (6.24) and (6.26) result in

$$H_0 \propto \frac{C_0}{C_f} \cdot \text{Ln}(W_6/W_7) \cdot \zeta, \quad (6.27)$$

where ζ is a well-defined proportionality factor. Therefore, the low-frequency gain of the open-loop integrating amplifier is defined by ratios of capacitor values and transistor sizes. For best PVT tracking, it is important that C_0 and C_f are of the same capacitor type. Similarly, G_{m0} should also use the same transistor type as that used for generation of the PTAT current, i.e. NMOS in this work. However, we found minor differences between the subthreshold slope coefficients of the PMOS and NMOS devices in this technology and therefore used a complimentary G_{m0} to improve the power efficiency of this cell by a factor of two, even though the PTAT cell uses NMOS devices.

The noise analysis of the integrating sampler can be done using a single-ended version of the amplifier shown in Figure 6.22(a). The noise of G_{m0} and G_{m1} are modeled as an output noise current sources i_{n0} and i_{n1} . The noise of G_{m0} is merely integrated on C_f for T_s seconds and sampled. The power of the sampled noise associated with i_{n0} at v_{out} is given by [2]

$$\overline{v_{n,out0}^2} = 2 \times \frac{S_{in0}}{2C_f^2} T_s, \quad (6.28)$$

$$S_{in0} = 4kT\gamma G_{m0}, \quad (6.29)$$

where k , T and γ are Boltzmann constant, absolute temperature and excess noise factor, respectively. The factor of 2 on the right hand side of (6.28) is due to the differential implementation. Using (6.22), this noise can be referred to the input as follows

$$\overline{v_{n,in0}^2} = \frac{4kT\gamma}{C_f H_0}, \quad (6.30)$$

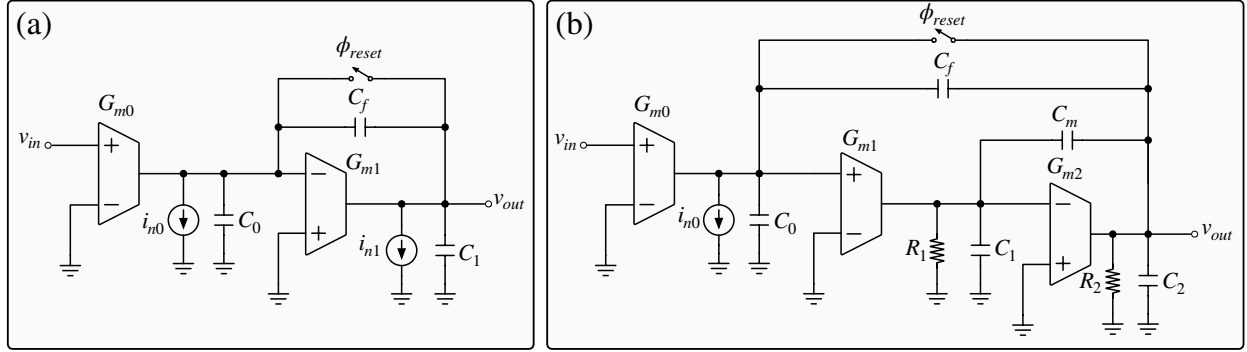


Figure 6.22: Simplified circuit model of the integrating sampler using (a) a single-stage and (b) a two-stage integrator.

where H_0 is the nominal low-frequency gain of the integrating sampler. During the integration phase, the transfer function of i_{n1} to v_{out} is approximately

$$\frac{v_{out}}{i_{n1}} \approx \frac{1}{\beta G_{m1}} \frac{1}{1 + s \frac{C_T}{\beta G_{m1}}}, \quad (6.31)$$

$$\beta = \frac{C_f}{C_f + C_0}, \quad (6.32)$$

$$C_T = C_1 + (1 - \beta)C_f, \quad (6.33)$$

where, β and C_T are the feedback factor and the total capacitance at the output node, respectively. Equation (6.31) is the transfer function of a leaky integrator with an equivalent resistance and capacitance of $(\beta G_{m1})^{-1}$ and C_T , respectively. Therefore, the sampled noise at the output node contributed by i_{n1} can be found as follows [2]

$$\overline{v_{n,out1}^2} = 2 \times \frac{S_{in1}}{2C_T^2} T_s \times \frac{1 - e^{-2\theta}}{2\theta}, \quad (6.34)$$

$$\theta = T_s \frac{\beta G_{m1}}{C_T}, \quad (6.35)$$

$$S_{in1} = 4kT\gamma G_{m1}. \quad (6.36)$$

The last term on the right hand side of (6.34) is due to the leaky integration. Equation (6.34), can be referred to the input simply by dividing it by H_0^2 as follows

$$\overline{v_{n,in1}^2} = \frac{2kT\gamma}{\beta C_T H_0^2} (1 - e^{-2\theta}) \approx \frac{2kT\gamma}{C_1 H_0^2}, \quad (6.37)$$

because $\theta \gg 1$ and $\beta \approx 1$.

Comparing (6.30) and (6.37), it can be concluded that for a large DC gain of $H_0 \approx 100$ the noise contribution of G_{m1} is negligible compared to that of G_{m0} and can be safely ignored for hand calculations, and that (6.30) is a good estimate of the total input referred noise of the integrating sampler which is solely set by the size of the integration capacitance C_f as long as a desired H_0 is known. For an input referred noise of $6 \mu V_{rms}$, with $H_0 = 100$, C_f should be ≥ 4.6 pF. The bandwidth of the integrating sampler is set by the integration period, T_s . For instance, for a 3 kHz bandwidth, $T_s \approx 146 \mu\text{Second}$, and therefore the required G_{m0} is approximately $3.2 \mu\text{S}$. With a fully complementary G_m cell shown in Figure 6.21(d), $3.2 \mu\text{S}$ of transconductance can be achieved by roughly 110 nA of tail current with all devices biased in deep subthreshold region, i.e. with $g_m/I_D \approx 29$.

In order to maximize the output swing of the integrator, G_{m1} is implemented by a two-stage OTA as shown in Figure 6.22(b). The stability of the feedback loop in Figure 6.22(b) merits some analysis and provides some design equations. The unity gain bandwidth and non-dominant pole of the loop gain transfer function of the feedback network are $\omega_u \approx G_{m1}/C_m$ and $\omega_{nd} \approx G_{m2}/C_2$, respectively. It also has a right-half plane zero at G_{m2}/C_m that is nulled by a nulling resistor. Therefore, to achieve a 60° phase margin

$$\frac{G_{m2}}{G_{m1}} \geq \sqrt{3} \frac{C_2}{C_m}. \quad (6.38)$$

Lastly, ω_u of the loop should be large enough for the loop to process the chopping frequency and its harmonics. In this work, the chopping frequency is 56 kHz, therefore, ω_u of $2\pi(1 \text{ MHz})$ is chosen. Given the total input capacitance of the ADC is $C_2 = 1$ pF, $G_{m2} = 12 \mu\text{S}$ achieves the 60° phase margin. G_{m1} and C_m are accordingly chosen to be $4 \mu\text{S}$ and 600 fF. In order to reduce the power required for G_{m2} by a factor of roughly two, 1-pF floating capacitors are used to couple the AC signal to the gates of M_5 and M_6 in order to turn this stage into a fully complementary transconductor as shown in Figure 6.19(e) [65].

6.3 Experimental Verification

The prototype implant IC was fabricated in TSMC 28 nm HPM CMOS process occupying an area of $1 \times 0.4 \text{ mm}^2$ as shown in Figure 6.23. The simulated breakdown of the average current consumption of the sub blocks of the IC is also shown in the same figure. For the implant assembly, the IC, a $500 \times 500 \times 500 \mu\text{m}^3$ bulk piezo and a storage capacitor will be assembled on a flexible printed-circuit board (PCB) following the process previously described in [62]. Characterization of the prototype IC was performed using a bring-up board discussed below.

Benchtop Measurement Setup

The benchtop characterization of the chip was performed using a bring-up board whose primary circuit is shown in Figure 6.24. The board is essentially an arbitrary waveform generator specifically tailored to generate the VPZ signal that the chip would receive from

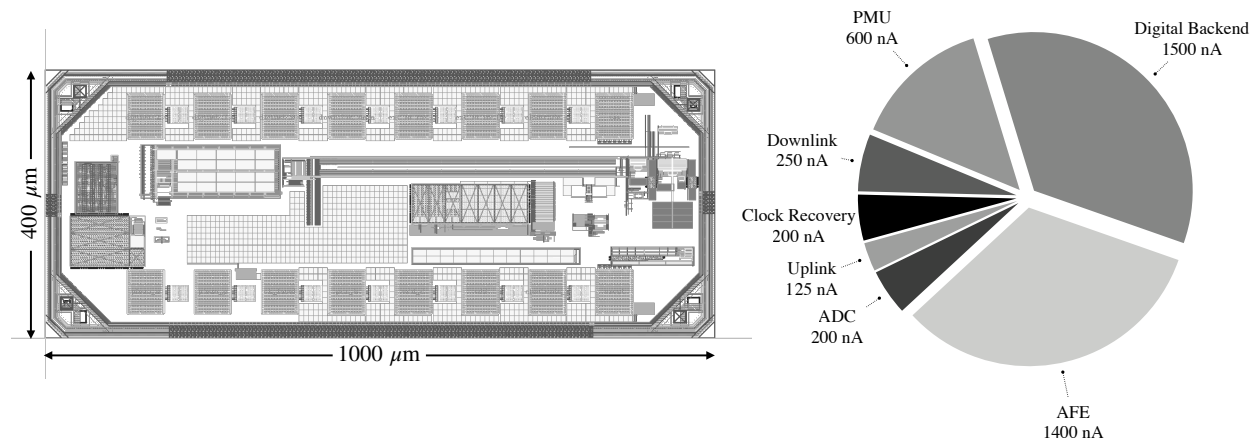


Figure 6.23: Layout of the prototype chip, and the breakdown of the simulated current consumption of the subblocks.

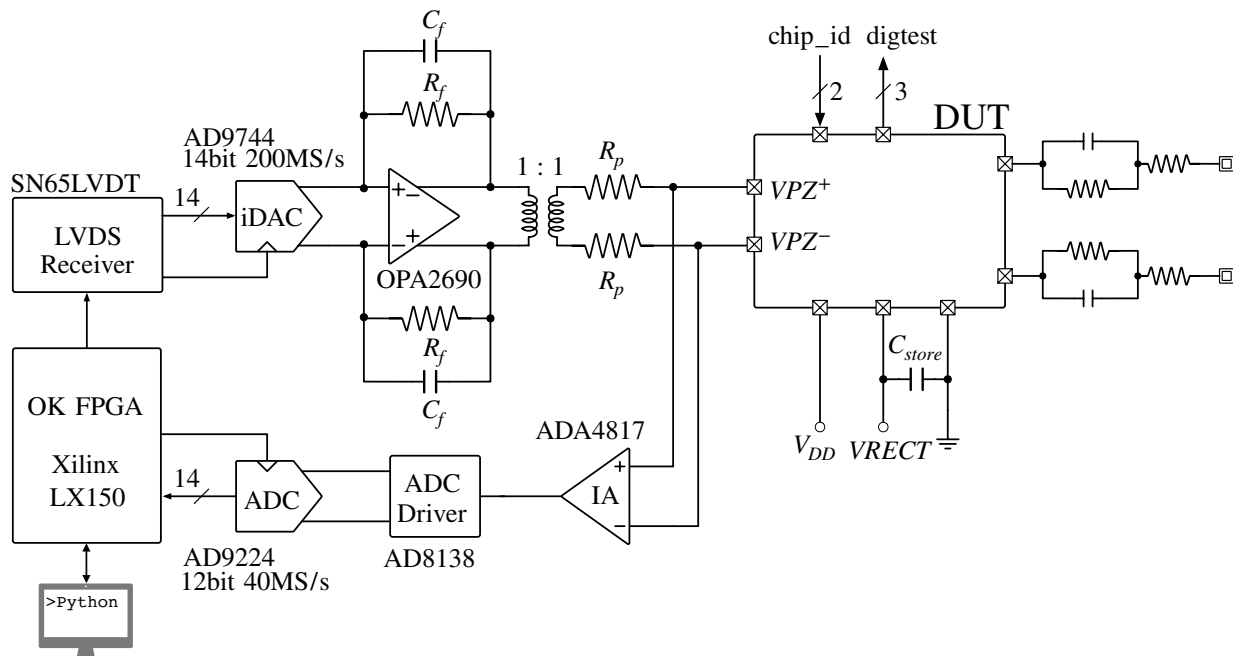


Figure 6.24: Simplified block diagram of the benchtop measurement setup.

the implant piezo when powered acoustically. VPZ is a pulsed carrier signal. In Mode 0,

its amplitude is OOK modulated for downlink, and in Mode 1, its amplitude is constant but modulated by the chip for backscatter uplink. To generate the complex (and dynamic) patterns of VPZ in Mode 0, and be able to immediately transition to Mode 1 (note that there must not be any pause between the transmitted pulses otherwise the chips would power down), the forward path of the test board is used. This path begins with an LX150 Xilinx FPGA (that receives command from a computer through a Python interface). For generating VPZ , the FPGA drives a high-speed 14-bit iDAC whose output current is low-pass filtered and converted to voltage by a fully-differential trans-resistance amplifier. Because of the relatively high-frequency of the command signals between the FPGA and the iDAC, an LVDS link is used between these blocks. The generated signal is coupled to the inputs of the device under test (DUT) by a transformer to create a floating voltage source that best models the piezo. Two 1 k Ω resistors are also used to model the internal resistance of the piezo (assuming a cubic shape). In Mode 1, the uplink data is embedded in the envelope of VPZ that needs to be recorded and processed. The feedback path of the bringup board serves this purpose. VPZ is probed by a custom-made (using ADA4817 fast JFET amplifiers from Analog Devices) high input-impedance (0.1 pF and 500 G Ω) three-OpAmp instrumentation amplifier. The output of the instrumentation amplifier is quantized by a 12-bit ADC, captured by the FPGA and transferred to the computer for post processing.

Measurement Results

Power Management Blocks

Figure 6.25 shows the trend of $VRECT$, the analog supply rail and the 0.55V supply rail of the chip immediately after the chip receives the first VPZ pulse at time 0. Upon receiving the very first pulse, the rectifier operates in a passive mode and starts charging C_{store} . The rectifier switches to the active mode once the PTAT reference bias currents are established at approximately 2 ms after. The analog supply rail and the 0.55 V common-mode supply rail of the AFE are also settled to their steady-state values within 5 ms of receiving the first VPZ pulse.

The voltage across C_{store} , or $VRECT$, linearly drops during the inter-pulse gaps as shown in Figure 6.26. The measured slope of $VRECT$ is 56 V/s which translates to the total current consumption of 5.6 μ A (given a 100 nF storage capacitor was used in this measurement). Note that this measured current consumption excludes the dynamic current consumption of the digital backend as during the inter-pulse gaps the main clock is not extracted, and the digital backend is in a hold state. It is also worth noting that $VRECT$ starts dropping slightly earlier than the gap itself, Figure 6.26. This is because, the last segment of Mode 0 pulses is allotted for uplink modulation (see Figure 6.4) for which C_{store} is disconnected to protect the stored charge from large uplink modulating currents.

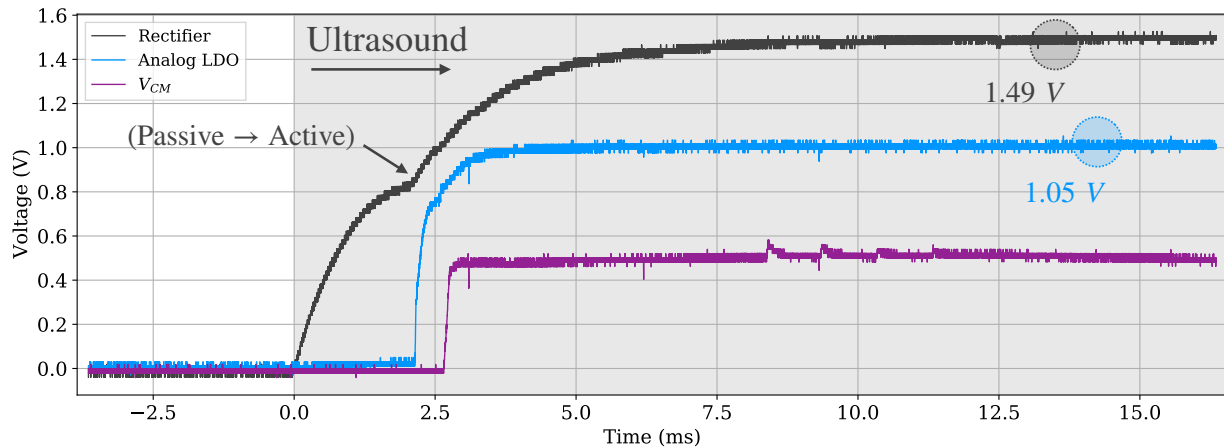


Figure 6.25: V_{RECT} , analog supply and the 0.55 V supply during start-up. VPZ is initiated at time 0.

Mode 0

A sample Mode 0 pulse is shown in Figure 6.27. The digital backend of the chip has a Finite State Machine (FSM) whose state (numbered in binary) is also shown in the same figure. The FSM state is used to verify to operation of the FSM upon receiving a Mode 0 pulse. The FSM switches back and forth between states 3 and 4, 16 times to estimate the width of the downlink symbols that follow. Once this estimation is over, the FSM advances to the next state which is waiting for the hard coded header. The FSM stays in this mode unless it receives a pattern other than ‘... 10101...’, after which it determines whether the pattern is the actual header or not. If the header (‘1100110011’) is detected, the FSM advances to the next state which is streaming in the Manchester encoded data. After registering in all the data, the FSM advances to its last state which is the uplink segment of Mode 0. This measurement verifies the correct operation of the ultrasound-ON detector, clock-extraction block, envelope detector and the downlink interface of the digital backend.

The close-up of the uplink segment of a Mode 0 pulse is shown in Figure 6.28. The uplink segment begins with a programmable delay that is allocated to partially recharge C_{store} before disconnecting it from VPZ for uplink. After the delay, the hard coded uplink header begins ‘00001010’, and immediately after that is the payload. The uplink payload in Mode 0 is merely the hard wired chip ID that is left padded with ‘110’. Payload data is sent out LSB first. Mode 0 uplink only uses ASK2 modulation for improved reliability. High-speed communications is not the goal of this mode. The uplink segment is repeated as long as VPZ is detected. The uplink segment shown in Figure 6.28(b) uses 5% modulation index. The mode 0 uplink modulation index of every pulse, however, can be programmed through the downlink segment of the pulse. Two other example pulses are shown in Figures 6.28(c)

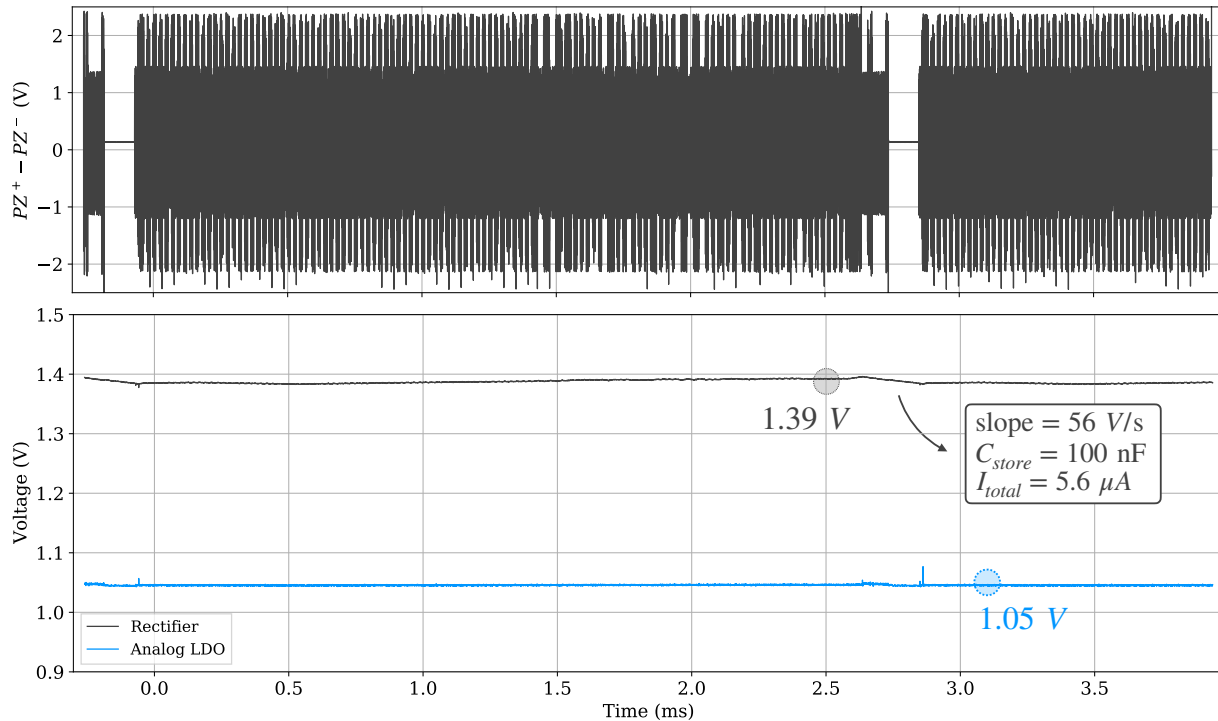


Figure 6.26: Mode 0 operation with inter-pulse gaps during which the chip only relies on charge stored on C_{store} . The slope of the linear voltage drop of V_{RECT} determines the total current consumption of the chip that is 5.6 μ A.

and (d) for which the chip is programmed to use 25% and 50% uplink modulation indexes, respectively. Note that this is done by changing the full-scale range of the modulating iDACs, that is the I_{MI} current source in Figure 6.8. I_{MI} is a 10-step iDAC whose measured range is 240 μ A with a differential nonlinearity (DNL) of better than 1 LSB. The uplink symbol duration is also programmable as shown in Figure 6.29. The possible choices are 4, 8, 12 and 16 cycles per symbol, and this can be used as a knob to adjust the bit rate and the bit error rate for a given channel.

Mode 1

Once the implant is configured and the uplink parameters (i.e., cycles/symbol, number of implants etc.) are set, the link transitions to Mode 1 which is specifically designed for high-speed data communications by using short pulses with m-level ASK modulation. A number of sample Mode 1 pulses are shown in Figure 6.30. A Mode 1 pulse, begins with a programmable C_{store} recharge segment. After the recharge segment is over, the uplink segment starts with a hard coded header of ‘1010’. This header can be used by the external interrogator to lock

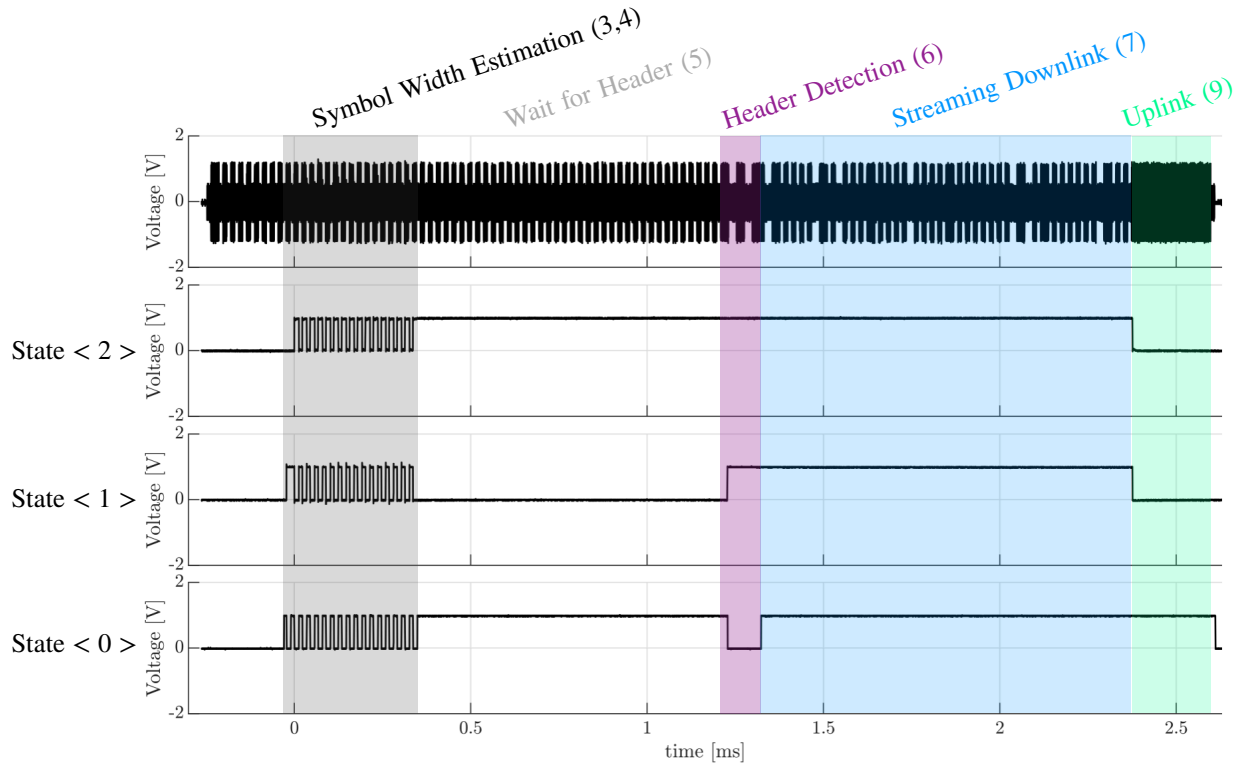


Figure 6.27: Mode 0 pulse showing various states of the internal FSM showing the chip locking into symbol width and performing demodulation.

into the symbol width and have an estimate of the maximum and minimum echo levels. The next four symbols (highlighted in purple) are the number of 8- or 9-bit data (depending on the modulation scheme) that the pulse is carrying. The symbols containing data immediately follow the data count segment. The chip can perform ASK2, ASK4, ASK8 and ASK16 as shown in Figures 6.30(a)–(d). In the sample pulse of Figure 6.30(a), the pulse is carrying 2 8-bit data using ASK2. The pulses shown in Figures 6.30(b) and (d), are carrying one 8-bit data using respectively ASK4 and ASK16, and the pulse shown in Figure 6.30(c) is carrying a single 9-bit data using ASK8. Increasing the number of modulation levels reduces the required width of the pulse (for the same number of bits) and subsequently allows to increase the pulse-repetition rate and ultimately the data rate of the link.

The chip has an LFSR source that is used as a pseudo-random number generator for the purpose of BER characterization. The LFSR can be activated during Mode 0. If activated, the output of the LFSR is used for uplink in Mode 1 instead of the ADC. Figures 6.31 – 6.34 summarize the measured data when the chip used the LFSR as the data source. The histogram of the ASK levels are shown in the top along with bi- or multi-modal kernel density functions whose minima are used as the optimal threshold level for symbol demodulation.

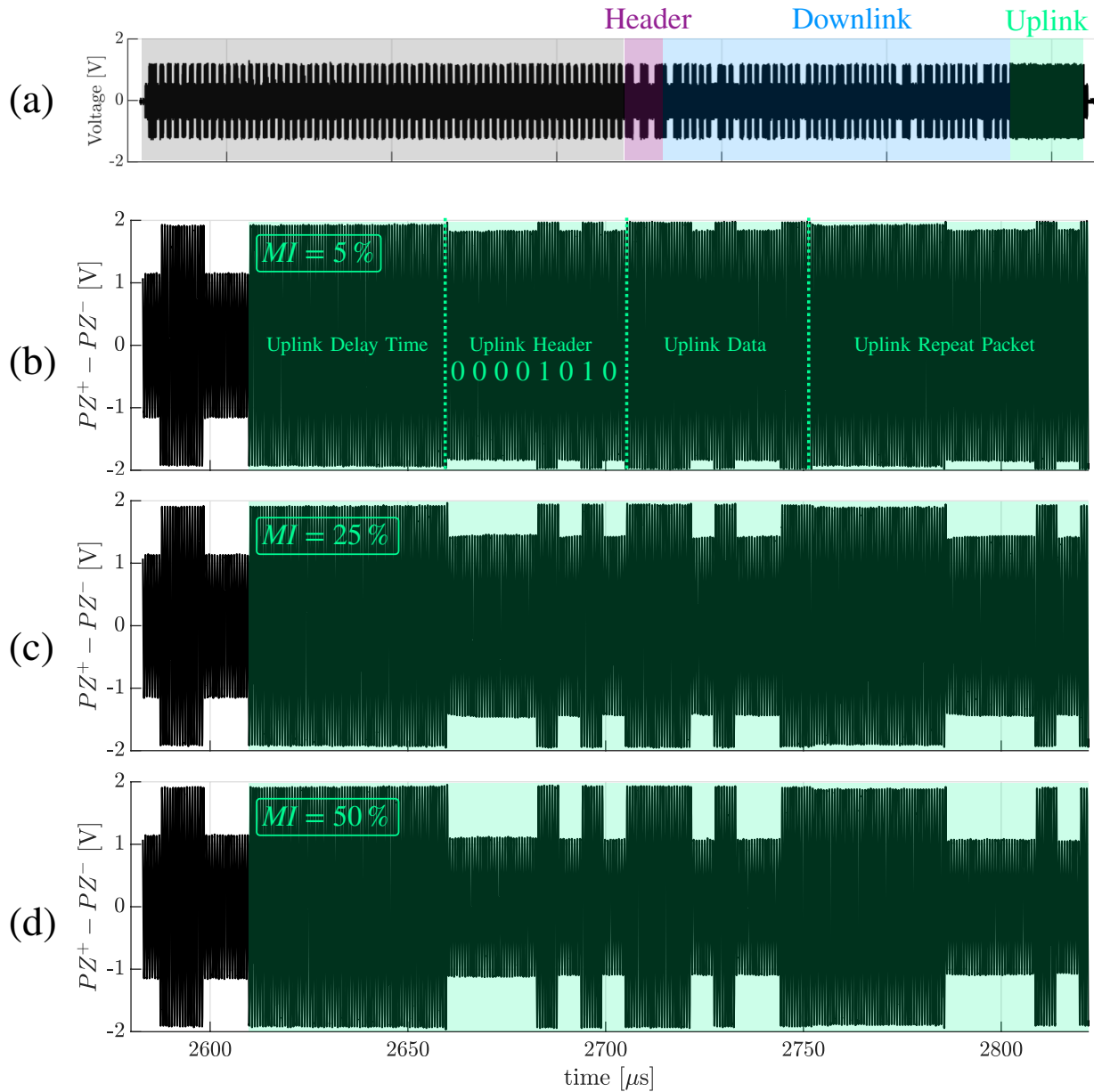


Figure 6.28: (a) A mode 0 pulse. (b) The close-up of the uplink segment of the pulse where the uplink header and payload are identifiable. The uplink modulation index is set to 5% in this pulse. The same uplink segment when the chip is programmed through the downlink segment of the pulse to use (c) 25% and (d) 50% uplink modulation index.

Using these thresholds, the reconstructed LFSR data are shown in the middle, while the golden LFSR data is shown in the bottom. LFSR data reconstruction was found error free

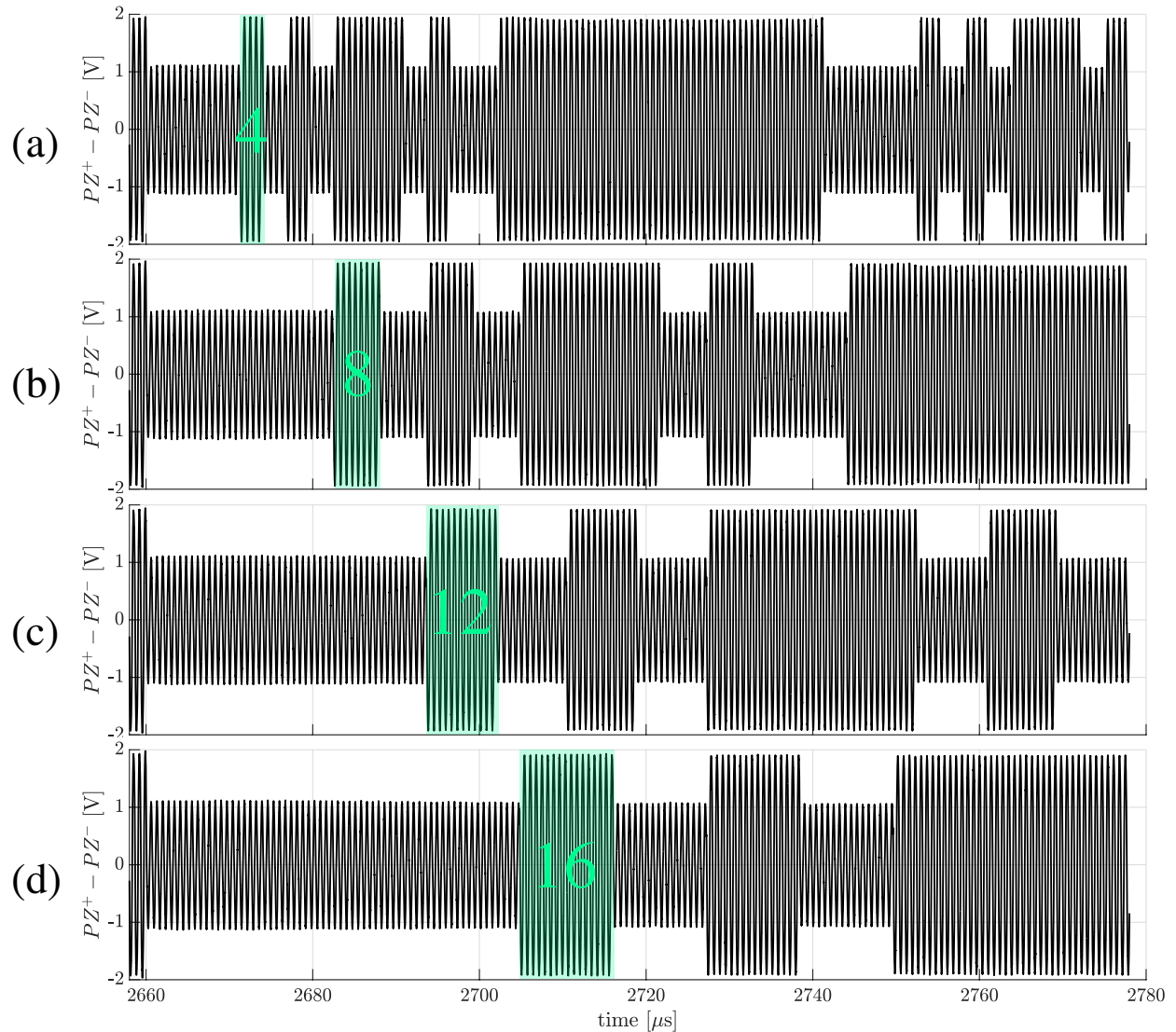


Figure 6.29: An uplink segment is shown with various symbol widths. Possible choices are (a) 4 cycles/symbol, (b) 8 cycles/symbol, (c) 12 cycles/symbol, and (d) 16 cycles/symbol.

when using ASK2, ASK4 and ASK8, while ASK16 showed approximately 3% BER. The purpose of this measurement is merely the functional verification of the uplink interface of the chip as well as data processing performed off-chip for data reconstruction. The BER characterization must be performed through the actual wireless link.

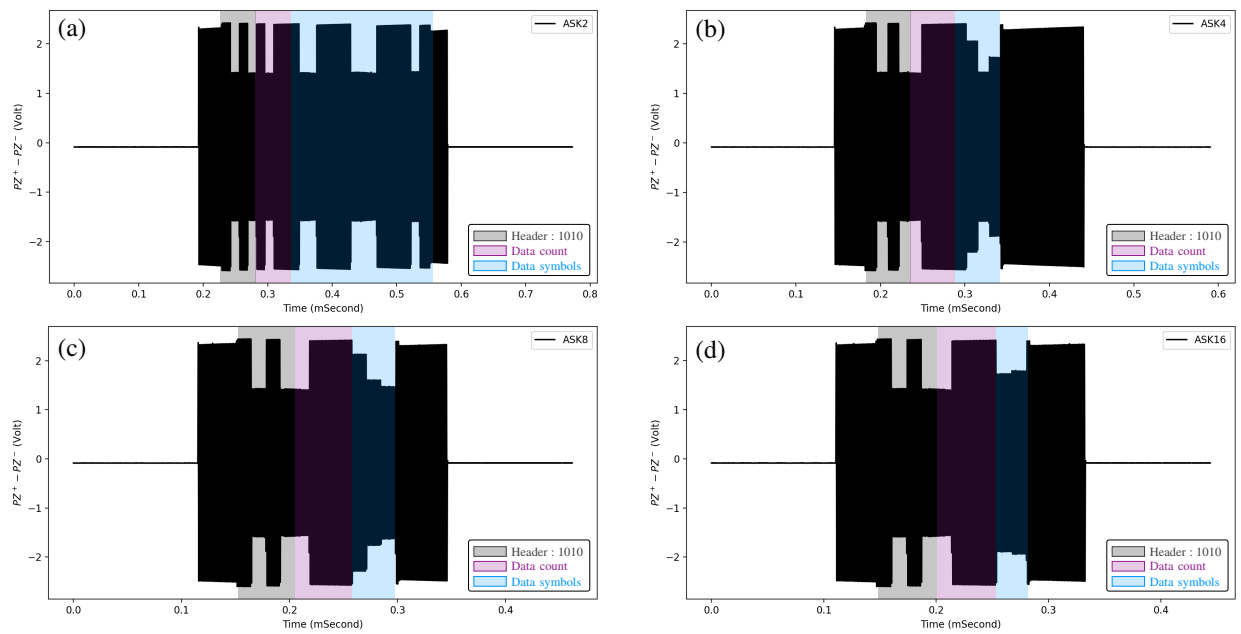


Figure 6.30: Sample Mode 1 pulses using (a) ASK2, (b) ASK4, (c) ASK8 and (d) ASK16 in the uplink segment.

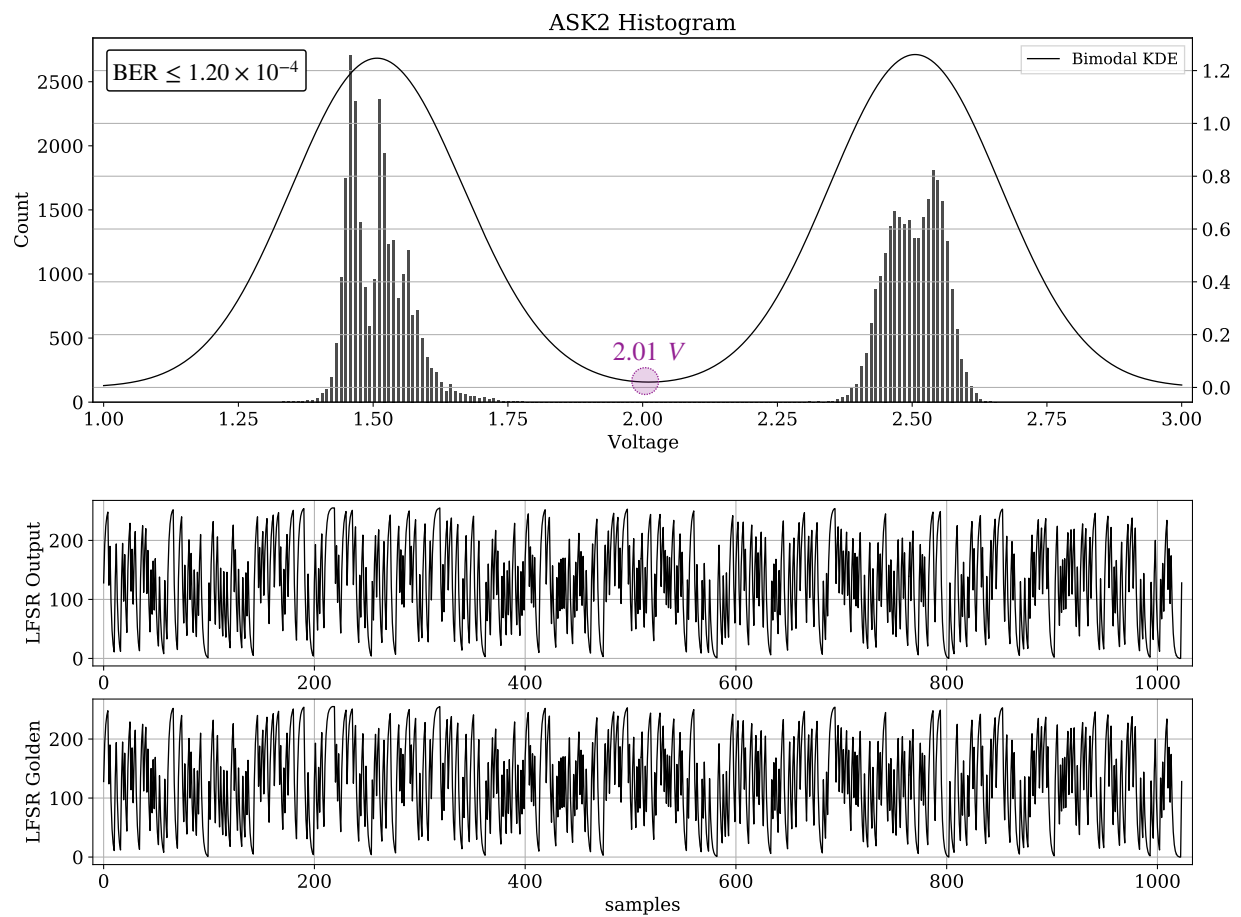


Figure 6.31: Mode 1 uplink transmitting LFSR data. (top) Histogram of the ASK2 levels. (middle) The reconstructed LFSR data and (bottom) the golden LFSR data.

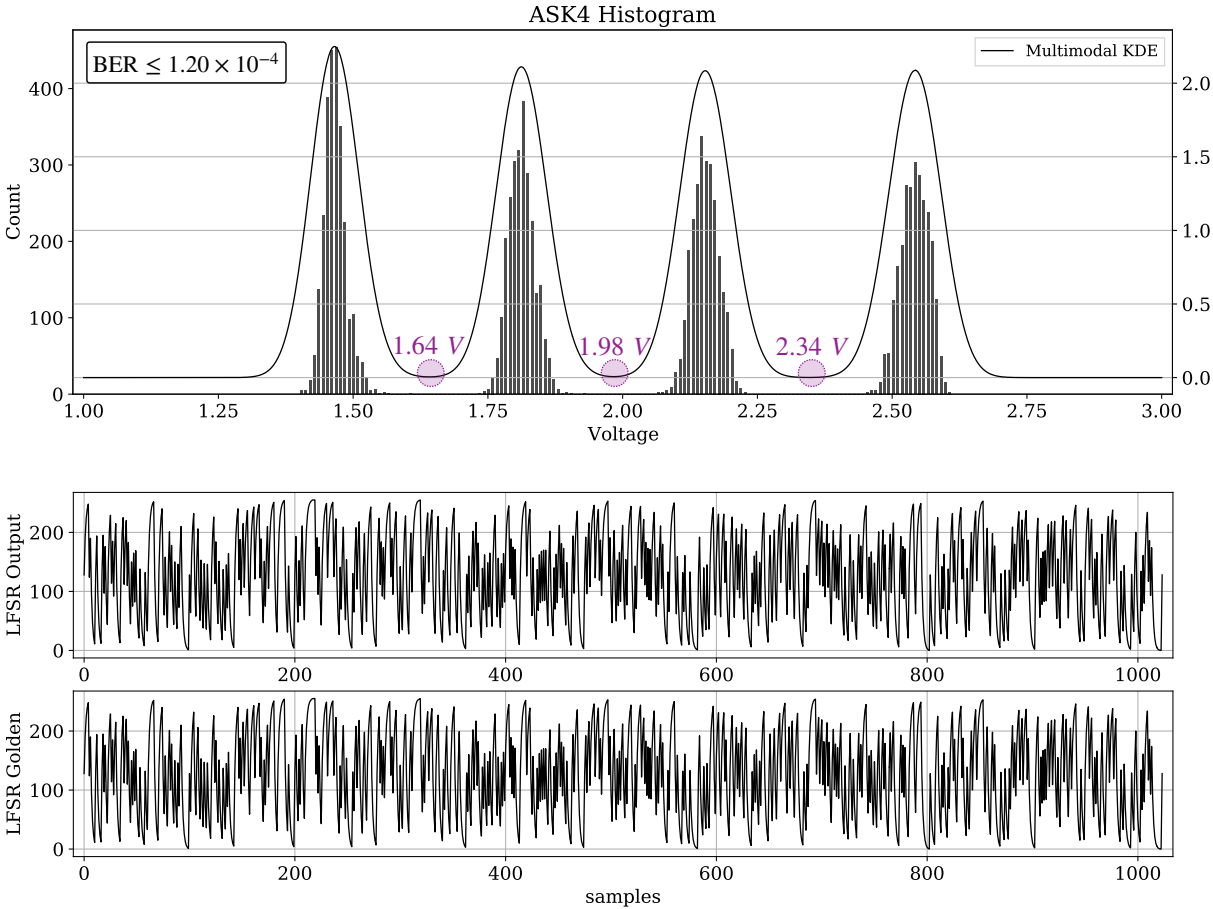


Figure 6.32: Mode 1 uplink transmitting LFSR data. (top) Histogram of the ASK4 levels. (middle) The reconstructed LFSR data and (bottom) the golden LFSR data.

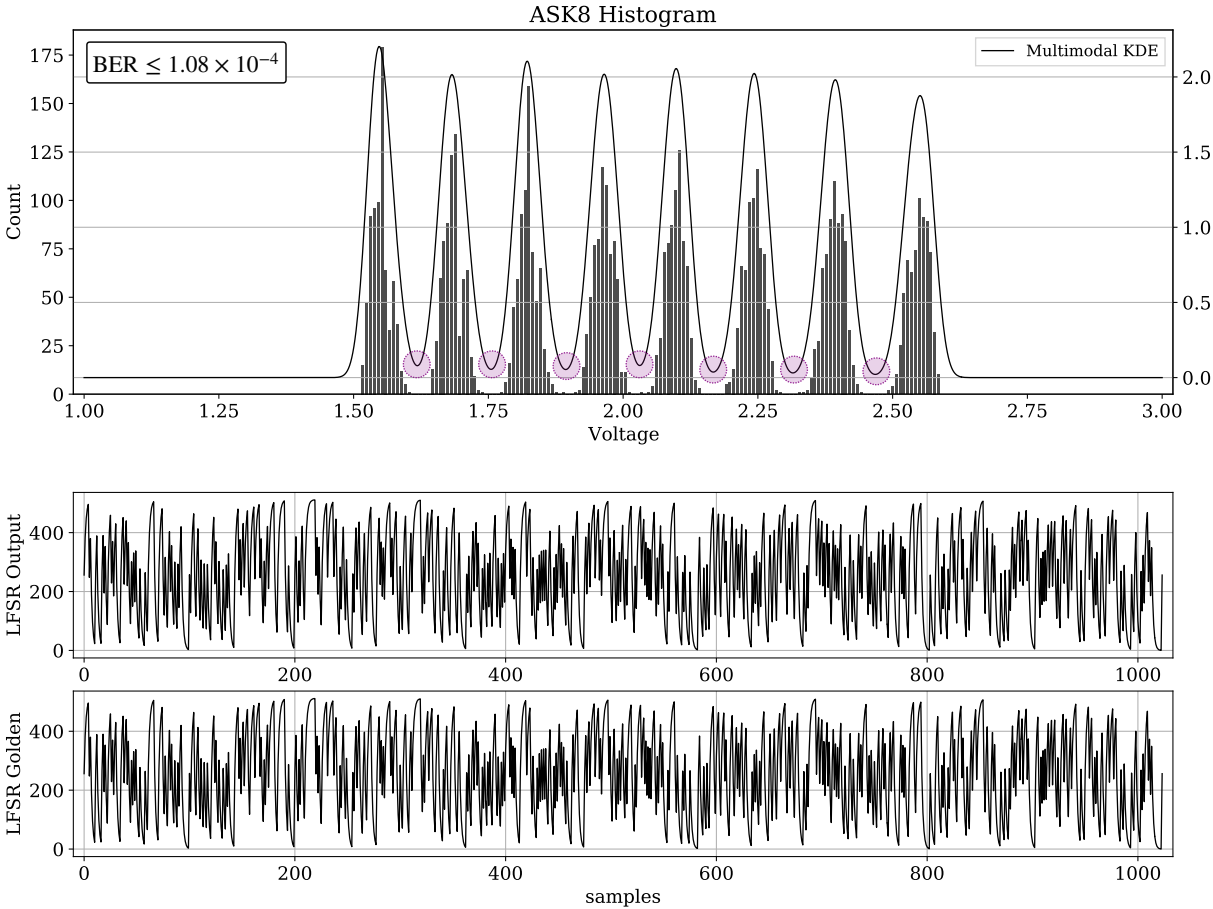


Figure 6.33: Mode 1 uplink transmitting LFSR data. (top) Histogram of the ASK8 levels. (middle) The reconstructed LFSR data and (bottom) the golden LFSR data.

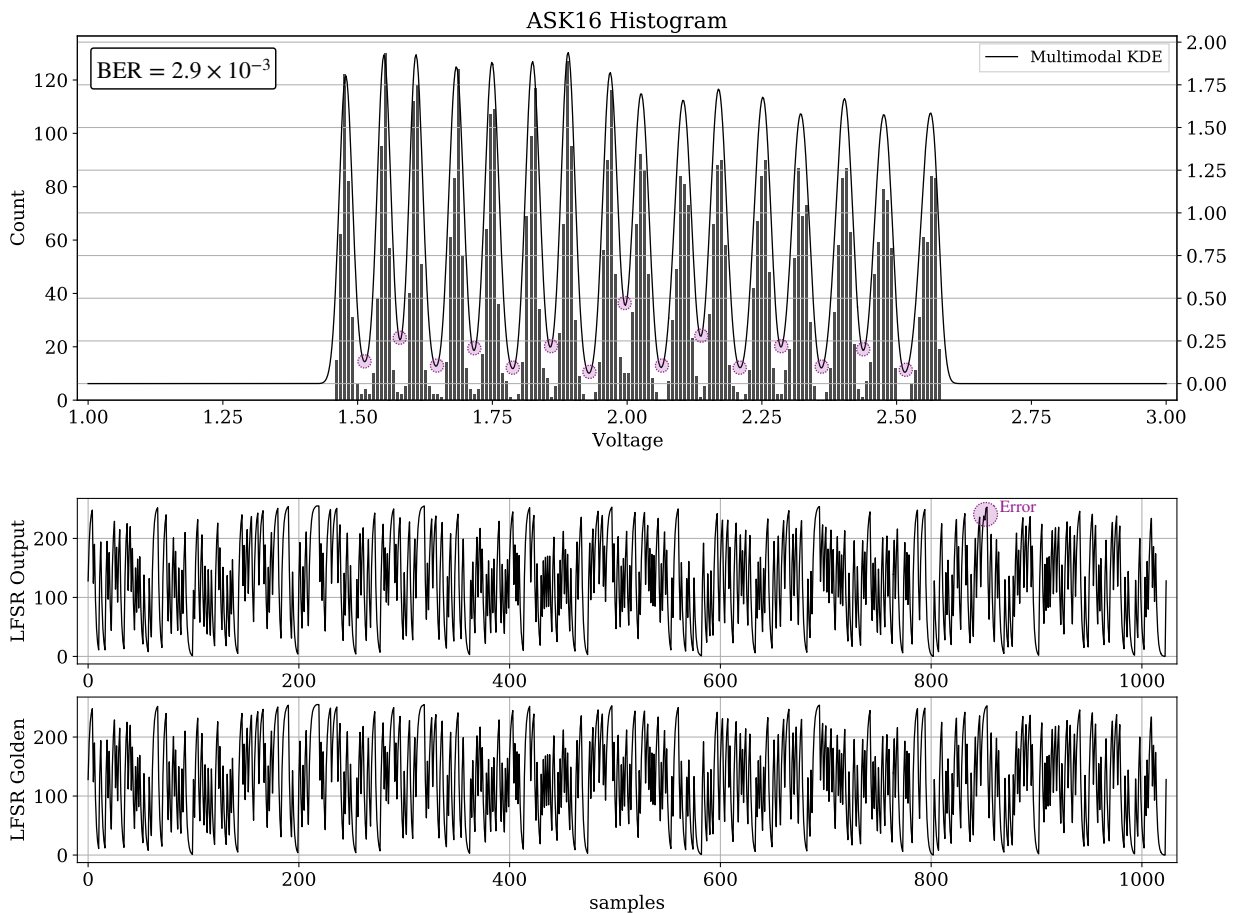


Figure 6.34: Mode 1 uplink transmitting LFSR data. (top) Histogram of the ASK16 levels. (middle) The reconstructed LFSR data and (bottom) the golden LFSR data.

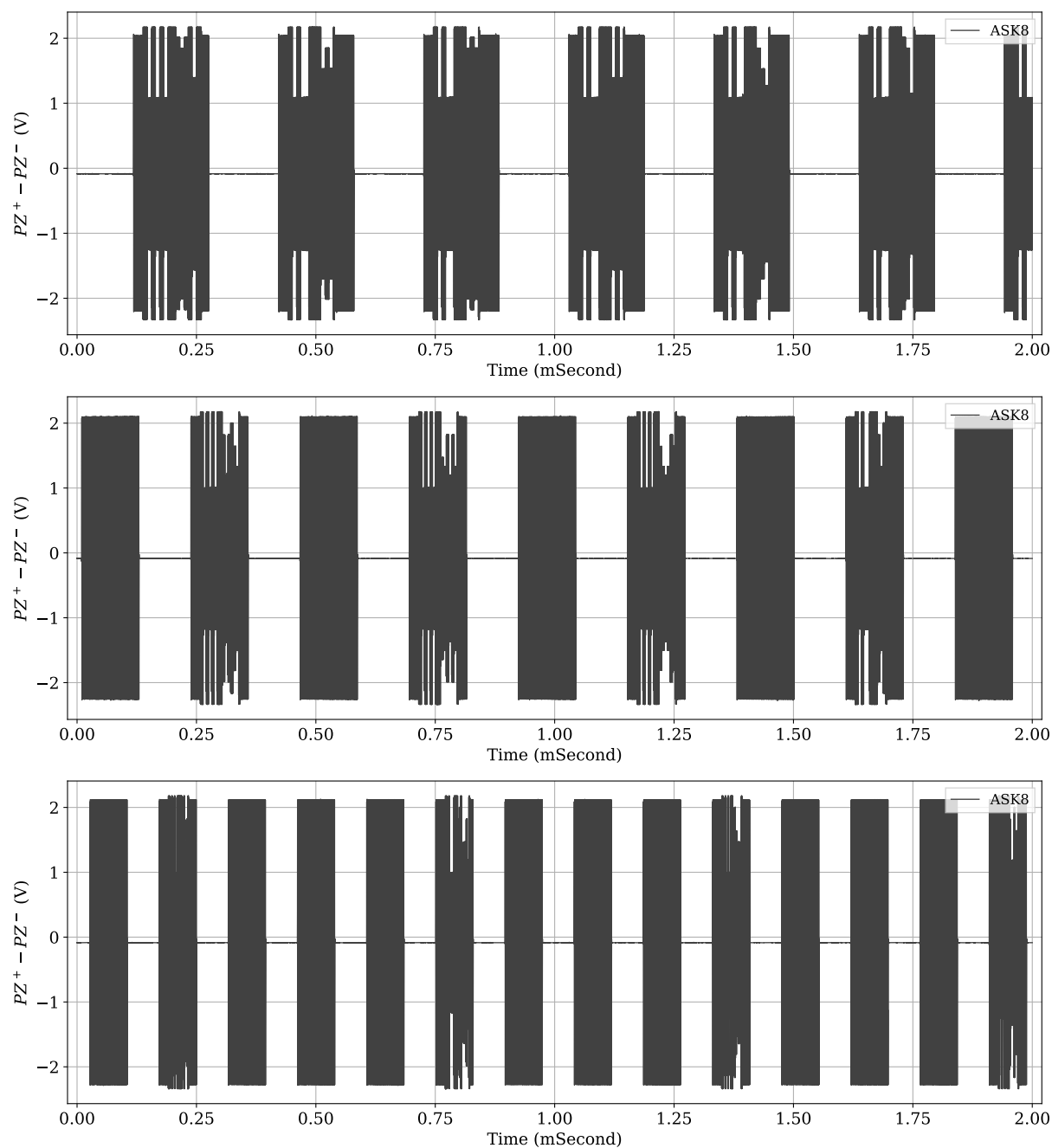


Figure 6.35: Functional verification of TDMA using a single test chip. The chip is programmed with (top) $N_{implants} = 1$, (middle) (top) $N_{implants} = 2$, and (bottom) $N_{implants} = 4$. For each configuration, the implant correctly decides when to activate its uplink modulator.

TDMA

Functional verification of the TDMA sequencer was tested using a single chip on the bring-up board. The chip was programmed with various $N_{implants}$ in Mode 0 and then transitioned to Mode 1 where it was observed that the implant correctly determined when to activate its uplink modulator. For instance, when the chip was programmed with $N_{implants} = 1$ (there is only one implant in the link), it decided that it is the channel master all the time as shown in Figure 6.35 (top). Moreover, the implant performed uplink modulation once every two pulses when programmed with $N_{implants} = 2$ (there are two implants in the link), Figure 6.35 (middle).

AFE+ADC

Figures 6.36 and 6.37 summarize measurement results for the purpose of characterizing the low-noise amplifier and the ADC. Figure 6.36(a) shows a 2-Hz $10 mV_{pp}$ sine wave input to the AFE. The spectrum of this recorded signal is shown in Figure 6.36(b) where an SFDR of about 40 dB is measured. The measured input-referred noise spectral density of the front-end is also shown in 6.36(c), where the integrated noise is found to be approximately $24 \mu V_{rms}$. This input referred noise is more than 4x larger than the designed value. There are two factors that contribute to this elevated noise level: 1. the non-linearity and thus elevated quantization noise of the ADC due to a layout error, and 2. noise injected from the supply of the ADC. After investigating the layout of the ADC it was found that the substrate under the capacitive FIFOs of the ADC was softly floating that caused a parasitic capacitive FIFO in parallel with the main FIFO. Since the parasitic FIFO was not binary-weighted, it injects significant non-linearity to the ADC. Moreover, although the SAR ADC used in this prototype was fully-differential, due to the monotonic switching scheme, the noise injected by the reference does not appear as a common-mode signal at the input of the comparator and degrades the input-referred noise of the ADC and subsequently the analog front end.

In order to characterize the non-linearity of the analog front-end, a histogram test was performed as shown in Figure 6.37. A slow full-scale ramp was input to the LNA. The histogram of ADC codes was used to quantify the differential and integral non-linearity of the signal chain that were found to be ≤ 1 LSB and ≤ 8 LSB, respectively.

6.4 Summary

In this section, a chip architecture suitable for miniature ultrasonically powered implants was presented. We also presented a wireless protocol for an ensemble of these implants to perform uplink in a TDMA fashion. Moreover, in order to increase the achievable data rate of the wireless link by $\log_2(m)$, we presented a novel m-level ASK backscatter modulator that is incorporated in the active rectifier of the chip. Functional verification of all the sub-blocks of the prototype IC was demonstrated through measurements.

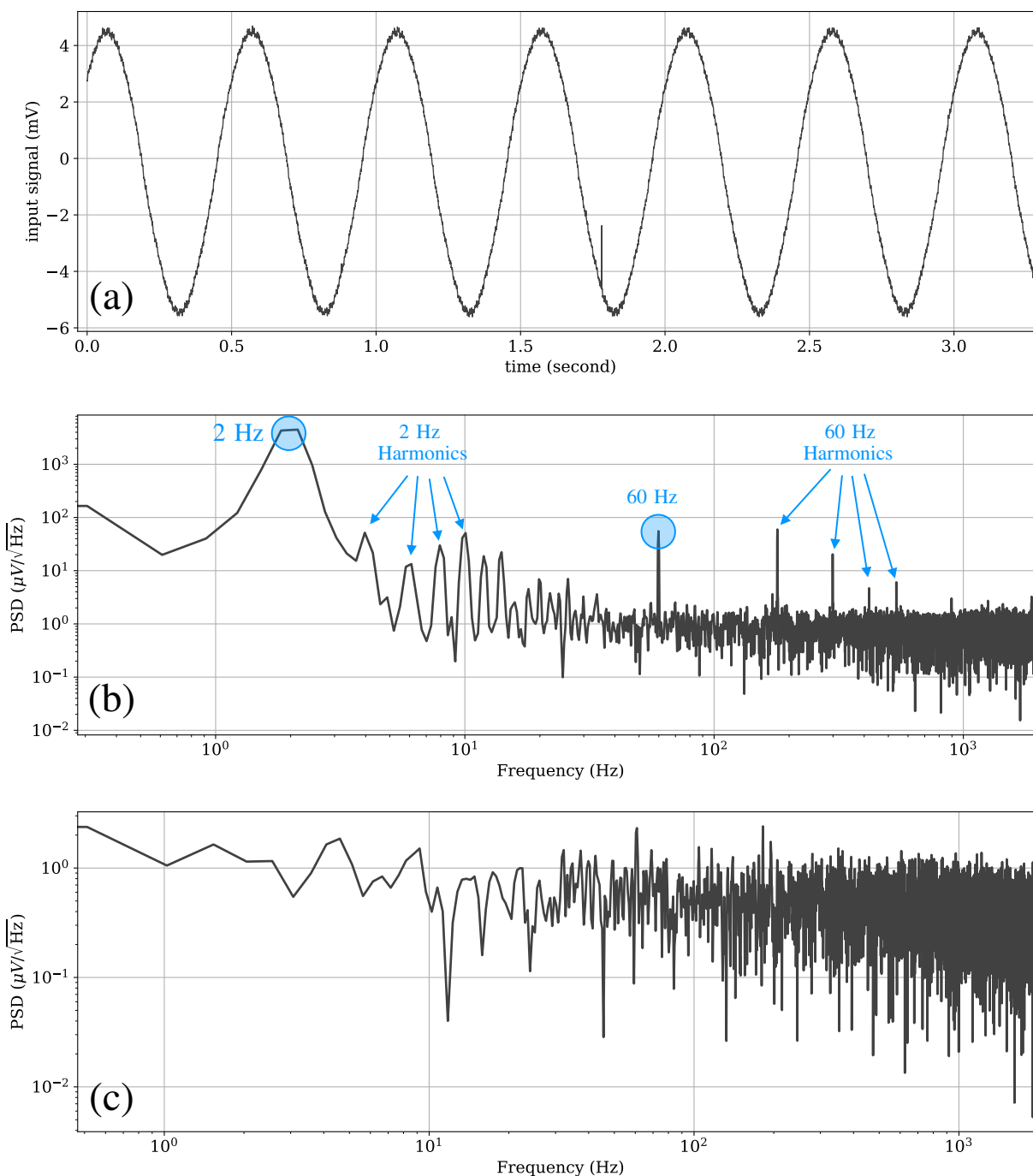


Figure 6.36: (a) A 10 mV_{pp} , 2 Hz sine wave recorded, transmitted and reconstructed. (b) the spectrum of the reconstructed sine wave. (c) Measured input-referred noise spectral density of the implant. Measured input-referred integrated noise is $24\ \mu\text{V}_{rms}$.

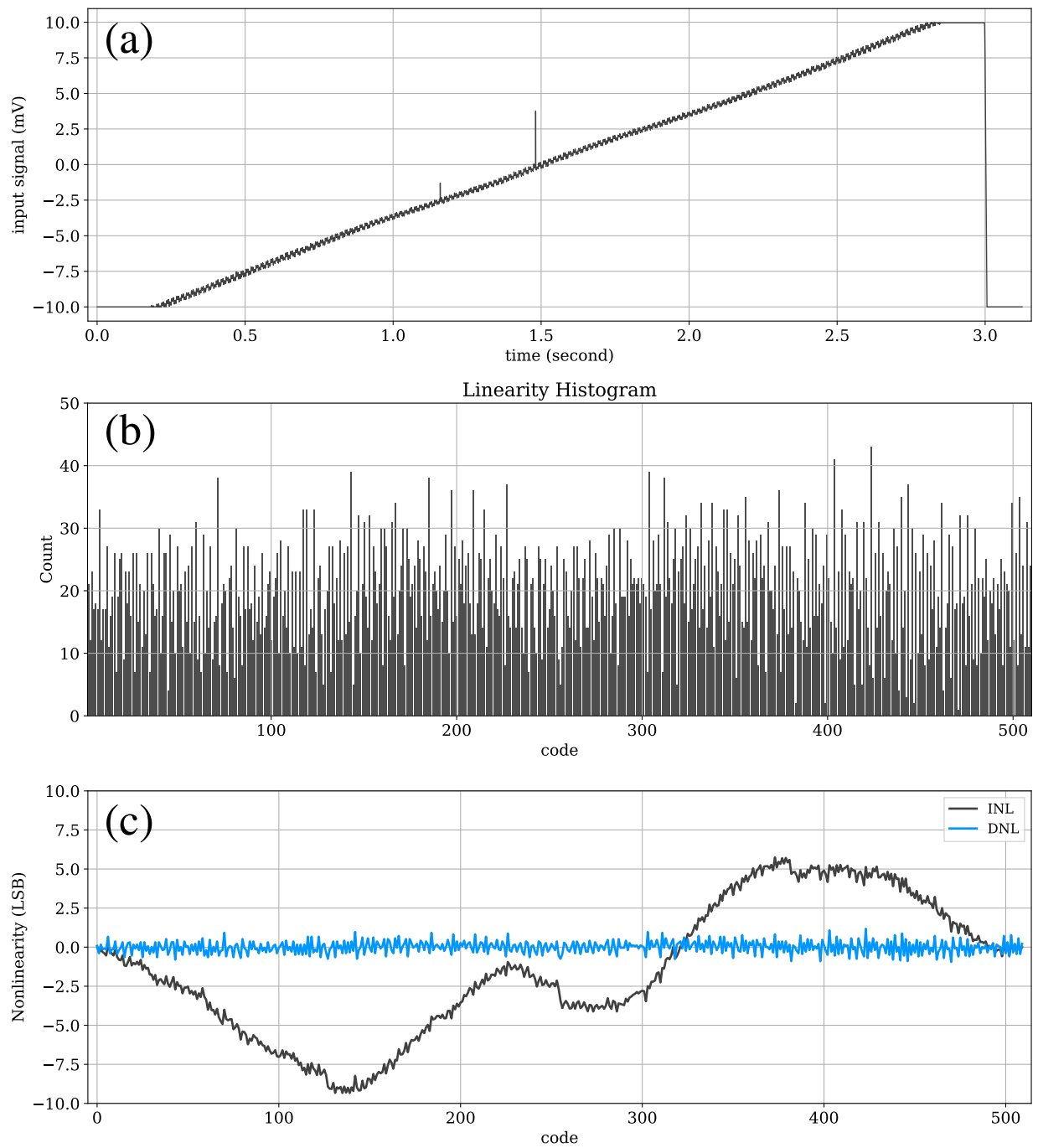


Figure 6.37: Measured linearity of the combined AFE and ADC (a) full-scale input ramp, and (b) its histogram (the first and last bins are removed for better visibility). (c) INL and DNL.

This chapter used material from collaborative work that needs proper acknowledgements.

Personal contribution: I developed the idea, designed the system-level architecture of the chip as well as the wireless protocol. I designed and implemented the majority of the analog and mixed-signal blocks of the chip, and performed all the bench-top chip characterization, data collection and analyses.

Acknowledgements: Cem Yalcin designed and implemented the digital backend block of the chip and helped with layout and top-level routing. Braeden Benedict designed and implemented the envelope detection block and helped with layout and top-level mixed-signal simulation. Rahul Kumar implemented the local oscillator and helped with layout. Rikky Muller provided advice on the technical aspects of the research. Rikky Muller was the principal investigator of this work.

Chapter 7

Summary and Future Research Directions

7.1 Summary

In this work, we presented two miniature wireless neural implants capable of recording and transmitting neural activity from deeply-seated peripheral nerves. In order to reduce implant-induced trauma and the likelihood of post-implant infection and to enable minimally-invasive implantation techniques such as injection, the primary design goals of these implants were miniaturization and wireless operation.

Power and data were wirelessly transmitted over acoustic wavelets repeatedly launched by an external interrogator. The implants used a single bulk piezoceramic as an acoustic antenna for converting acoustic energy to electric energy. For the purpose of miniaturization, data back telemetry was performed by load modulation of the implant piezo; a technique known as backscattering. We performed a comprehensive analysis on ultrasound backscattering and described the relationship between the acoustic reflection coefficient Γ (of the wave reflected from the front face of the piezo) and the electric termination impedance of the piezo Z_E . It was concluded that Γ is approximately linearly proportional to the voltage across the piezo when operating at the series or parallel resonant frequencies. This backscatter linearization technique ($\Gamma \propto V_{pz}$) subsequently enabled utilizing a gain stage at the sensing front-end of the implants and helped reduce the input-referred noise by more than an order of magnitude relative to the prior art [70]. We designed two linear uplink backscatter modulators and incorporated them into the active rectifier of the implant ICs. One of these modulators performed end-to-end linear analog modulation which deemed sensitive to carrier noise that degraded the overall noise floor of the implant by 10–12 dB. The other quasi-digital m-level ASK modulator was designed to provide better immunity to carrier noise while achieving a substantially higher data rate (by a factor of $\log_2(m)$) relative to OOK.

Additionally, a critical aspect of the wireless communication channel for these miniature neural implants was the multiple-access feature of the link. Therefore, we demonstrated

how code-division and time-division multiple-access (CDMA and TDMA) can be incorporated into the uplink communications protocols of these implants. These protocols allow communications with a network of these implants using a single-element low-cost external interrogator. The functionality of both of the proposed implants were experimentally verified.

7.2 Future Research Directions

Future research directions of this work can be viewed from three perspectives: scale, robustness and application. These directions are briefly discussed below.

Scale

It is unknown how many implants/electrodes are needed when creating an interface with the nervous system. Therefore, the general trend has been to increase the number of implants/electrodes to as many as possible since it enhances the specificity of the interface allowing it to target individual cells. The number of implants in a wireless channel, however, is strictly limited to the maximum data rate that the channel can support. For instance, in a 224 kbps channel, only 4 implants (56 kbps/implant) can be accommodated.

Despite our effort to enhance the ultrasound channel utilization in this work, the throughput of the channel with our proposed m-level ASK modulation is smaller than 1 Mbps, and this severely limits the number of implants that can be communicated. Therefore, to scale the number of implants to hundreds, two approaches exist: 1. increasing the total data rate of the channel 2. reducing the wireless data rate required by each implant.

In this work, we demonstrated that m-level ASK modulation enhances the data rate by $\log_2(m)$ relative to OOK. Another possibility to further enhance the channel utilization is the phase modulation of the symbols in addition to m-level amplitude modulation. Incorporating both phase and amplitude modulation into the pulse-echo modulation scheme, requires careful analysis of the phase of Γ with respect to the termination impedance Z_E similar to what presented in Chapter 3.

The pulse-echo communication protocol used commonly in single-piezo implants wastes 50% of the channel capacity because the interrogator repeatedly alternates between transmit and receive modes to avoid saturating the front-end of the receive chain by the large transmit signals. If this time-duplexing between transmit and receive modes were avoided, the implants would be able to use uplink all the time improving the channel capacity by 2x. One possibility of this continuous pulse-echo communication is conceptually shown in Figure 7.1. In this scheme, the interrogator continuously drives the external transducer, and the implant continuously performs echo modulation. Therefore,

$$V_R = A\sin(\omega_o t + \phi_s) + B(t)\sin(\omega_o t + \phi_b), \quad (7.1)$$

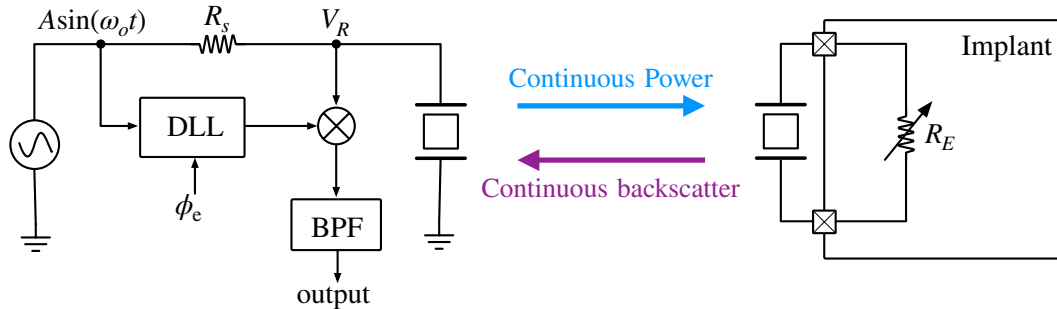


Figure 7.1: A conceptual diagram for the continuous pulse-echo communication scheme.

where ϕ_s is the phase shift caused by the impedance of the external transducer, ϕ_b is the phase shift due to the time of flight, and $B(t)$ ($\ll A$) is the amplitude of the echo picked up by the external transducer. As shown in Figure 7.1, if an excess phase ϕ_e is added to the driver signal ($A \sin(\omega_o t + \phi_e)$) using a delay-locked loop and mixed with V_R , the result would be

$$\text{Mixer output} = \frac{1}{2} A (\cos(\phi_e - \phi_s) - \cos(2\omega_o t + \phi_s + \phi_e)) \quad (7.2)$$

$$+ \frac{1}{2} B(t) (\cos(\phi_e - \phi_b) - \cos(2\omega_o t + \phi_b + \phi_e)). \quad (7.3)$$

Therefore, $\phi_e = \phi_b$ enables the extraction of $B(t)$ in the frequency domain using a band pass filter centered at the symbol rate of the uplink.

The other approach to scale the number of implants, as mentioned earlier, is reducing the data rate required by each implant. For instance, if instead of raw data that would require >56 kbps/implant, only neural spikes were transmitted, the data rate required by each implant would reduce by roughly 100x (assuming 500 Hz spike rate). This would subsequently allow to increase the number of implants by 100x. Transmitting spikes requires on-chip signal processing for spike detection that has been shown to require insignificant power [31], and therefore this is considered an effective technique in scaling the number of miniature wireless implants in channels with finite capacities such as ultrasound.

Robustness

The majority of ultrasonically-powered implants use piezoceramic as acoustic antennas. Due to the directivity of the implant piezo, the amount of harvested power and the quality of the data communications are sensitive to misalignment between the external transducer and the implant piezo. One way to address this issue is to employ a phased-array instead of a single-element external transducer to enable dynamic focusing of the beam on the location of the implants. An example of a 52-element beamforming external transducer to focus the transmitted wave pattern on the implants was demonstrated in [8, 7].

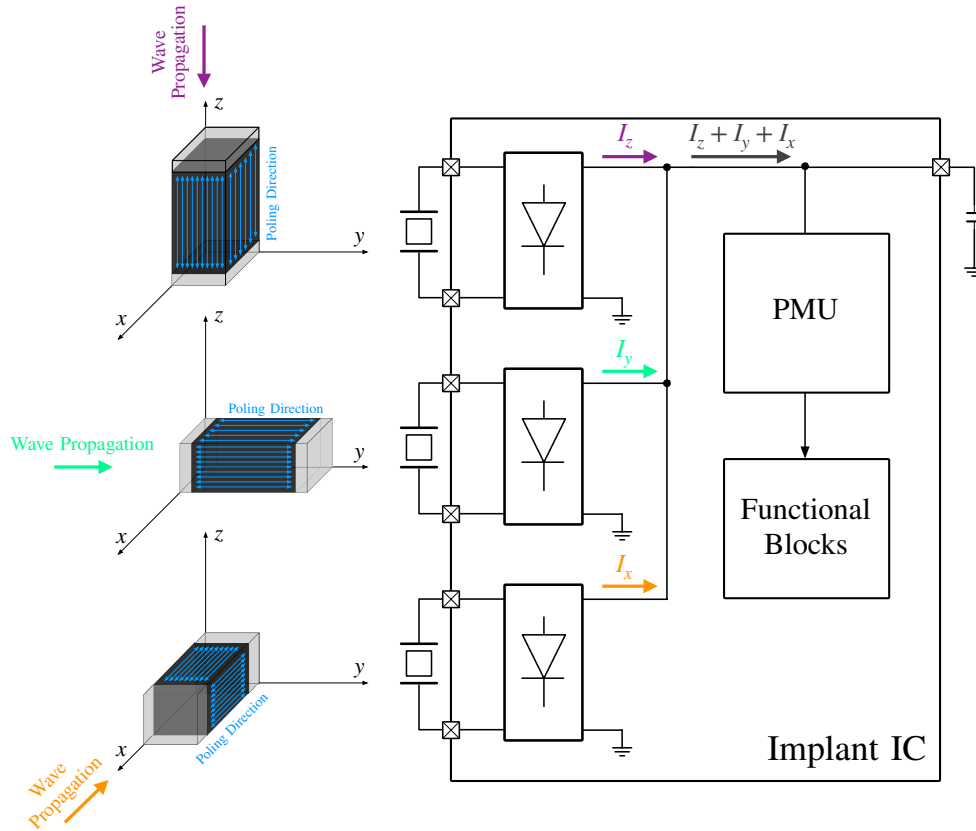


Figure 7.2: A conceptual diagram of a three-piezo implant to reduce sensitivity to angular misalignment.

A major challenge that is not addressed by phased arrays is the angular misalignment of the implant piezo. Typically, the implant piezo poling direction is assumed to be aligned with the direction of the propagation of the wave. Such a perfect alignment maximizes the harvested power by the piezo, but cannot be guaranteed for *in vivo* settings. As the angular misalignment between the piezo poling direction and the direction of propagation increases the harvested power reduces. A non-zero (thanks to the Poisson ratio of the piezo material) minima occurs at 90° angular misalignment. In order to solve this issue, a three-piezo implant architecture conceptually shown in Figure 7.2 can be used. In this architecture, the poling direction of each piezo is aligned with one of the Cartesian axes, and the power harvested by the piezos are combined in the current domain by using three rectifiers whose outputs are short circuited. The piezo that harvests the most power can be detected on chip and used for data backscattering in a similar fashion described in Chapter 3. This architecture directly trades to the overall volume of the implant and the sensitivity of the harvested energy, but because of the non-zero power harvested at 90° angular misalignment, the overall volume of

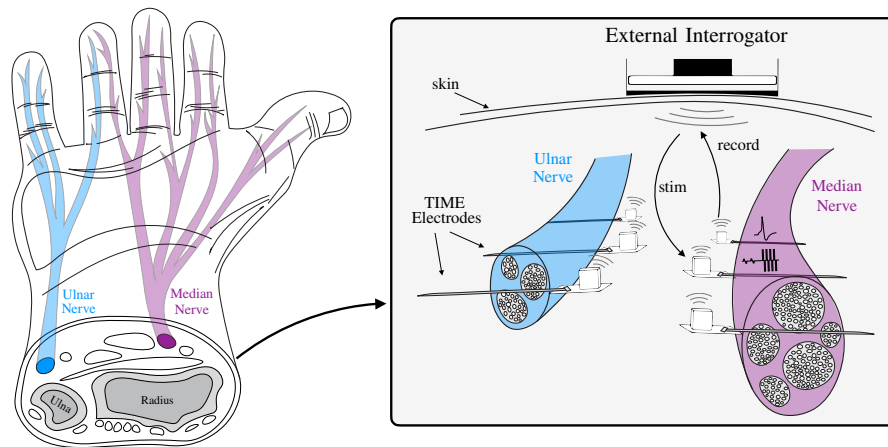


Figure 7.3: Concept of closed-loop neuromodulation using miniature wireless implants.

this three-piezo implant is likely to be smaller than 3x compared to a single-piezo implant.

Application

In contrast to non-invasive nerve interfaces (e.g., EMG), in-situ interfaces provide the opportunity to efficiently stimulate the nerves to restore sensory functions to greatly improve the agility of active prostheses. For instance, signals from pressure sensors embedded into an active prosthesis can be encoded and used to provide feedback to the user while grasping a fragile object just like how the human somatosensory system works. This is known as closed-loop neuromodulation when the neural interfaces can both read from and write into the nerves.

Minimally-invasive closed-loop neuromodulation, as conceptually shown in Figure 7.3, is *the* ultimate goal of this project. In this work, we demonstrated two mm-scale ultrasonic implants that are completely wireless. Minimally invasive neurostimulation using an ultrasonically-powered implant was previously demonstrated *in vivo* in [62]. These recording and stimulating implants, however, operate as standalone devices since their wireless protocols are incompatible. The root cause of this incompatibility is the stark contrast between the requirements of these implant types. A neural recording implant is a low-to-moderate power implant that requires low downlink data rate but a high uplink data rate. A neurostimulating implant, on the other hand, is a power intensive implant that requires moderate-to-high downlink data rate but a low uplink data rate. Encompassing these different power and data requirements in a universal wireless protocol is a technically challenging task that needs to be addressed to enable the ultimate goal of closed-loop neuromodulation using miniature wireless implants.

Bibliography

- [1] Behnaam Aazhang, B-P Paris, and Geoffrey C Orsak. “Neural networks for multiuser detection in code-division multiple-access communications”. In: *IEEE Transactions on Communications* 40.7 (1992), pp. 1212–1222.
- [2] Assad A Abidi. “Phase noise and jitter in CMOS ring oscillators”. In: *IEEE journal of solid-state circuits* 41.8 (2006), pp. 1803–1816.
- [3] Haim Azhari. *Basics of biomedical ultrasound for engineers*. John Wiley & Sons, 2010.
- [4] Galinos Barmparas et al. “Epidemiology of post-traumatic limb amputation: a National Trauma Databank analysis”. In: *The American Surgeon* 76.11 (2010), pp. 1214–1222.
- [5] Hamid Basaeri, David B Christensen, and Shad Roundy. “A review of acoustic power transfer for bio-medical implants”. In: *Smart Materials and Structures* 25.12 (2016), p. 123001.
- [6] Mel Bazes. “Two novel fully complementary self-biased CMOS differential amplifiers”. In: *IEEE Journal of Solid-State Circuits* 26.2 (1991), pp. 165–168.
- [7] Braeden C Benedict et al. “Time reversal beamforming for powering ultrasonic implants”. In: *2021 10th International IEEE/EMBS Conference on Neural Engineering (NER)*. IEEE. 2021, pp. 647–650.
- [8] Braeden C. Benedict, Mohammad Meraj Ghanbari, and Rikky Muller. “Phased Array Beamforming Methods for Powering Biomedical Ultrasonic Implants”. In: *IEEE Transactions on Ultrasonics, Ferroelectrics, and Frequency Control* 69.10 (2022), pp. 2756–2765. DOI: 10.1109/TUFFC.2022.3197705.
- [9] Don Berlincourt. *Ultrasonic transducer materials*. Springer, 1971.
- [10] Ting Chia Chang, Max Wang, and Amin Arbabian. “Multi-Access Networking with Wireless Ultrasound-Powered Implants”. In: *2019 IEEE Biomedical Circuits and Systems Conference (BioCAS)*. IEEE. 2019, pp. 1–4.
- [11] Ting Chia Chang et al. “27.7 A 30.5 mm³ fully packaged implantable device with duplex ultrasonic data and power links achieving 95kb/s with $< 10^{-4}$ BER at 8.5 cm depth”. In: *2017 IEEE International Solid-State Circuits Conference (ISSCC)*. IEEE. 2017, pp. 460–461.

- [12] Ting Chia Chang et al. “End-to-end design of efficient ultrasonic power links for scaling towards submillimeter implantable receivers”. In: *IEEE transactions on biomedical circuits and systems* 12.5 (2018), pp. 1100–1111.
- [13] Jayant Charthad et al. “A mm-sized wireless implantable device for electrical stimulation of peripheral nerves”. In: *IEEE transactions on biomedical circuits and systems* 12.2 (2018), pp. 257–270.
- [14] TS Davis et al. “Restoring motor control and sensory feedback in people with upper extremity amputations using arrays of 96 microelectrodes implanted in the median and ulnar nerves”. In: *Journal of neural engineering* 13.3 (2016), p. 036001.
- [15] Tim Denison et al. “A $2\mu\text{W}$ 100 nV/rtHz Chopper-Stabilized Instrumentation Amplifier for Chronic Measurement of Neural Field Potentials”. In: *IEEE journal of solid-state circuits* 42.12 (2007), pp. 2934–2945.
- [16] Gurpreet S Dhillon et al. “Residual function in peripheral nerve stumps of amputees: implications for neural control of artificial limbs”. In: *The Journal of hand surgery* 29.4 (2004), pp. 605–615.
- [17] Christian C Enz and Gabor C Temes. “Circuit techniques for reducing the effects of op-amp imperfections: autozeroing, correlated double sampling, and chopper stabilization”. In: *Proceedings of the IEEE* 84.11 (1996), pp. 1584–1614.
- [18] Ali Ersen et al. “Chronic tissue response to untethered microelectrode implants in the rat brain and spinal cord”. In: *Journal of neural engineering* 12.1 (2015), p. 016019.
- [19] Nir Even-Chen et al. “Power-saving design opportunities for wireless intracortical brain–computer interfaces”. In: *Nature biomedical engineering* 4.10 (2020), pp. 984–996.
- [20] Nariman Farsad and Andrea Goldsmith. “Neural network detection of data sequences in communication systems”. In: *IEEE Transactions on Signal Processing* 66.21 (2018), pp. 5663–5678.
- [21] FJ Fry and JE Barger. “Acoustical properties of the human skull”. In: *The Journal of the Acoustical Society of America* 63.5 (1978), pp. 1576–1590.
- [22] Mohammad Meraj Ghanbari and Rikky Muller. “Optimizing volumetric efficiency and backscatter communication in biosensing ultrasonic implants”. In: *IEEE Transactions on Biomedical Circuits and Systems* 14.6 (2020), pp. 1381–1392.
- [23] Mohammad Meraj Ghanbari et al. “17.5 A 0.8 mm³ Ultrasonic Implantable Wireless Neural Recording System With Linear AM Backscattering”. In: *2019 IEEE International Solid-State Circuits Conference-(ISSCC)*. IEEE. 2019, pp. 284–286.
- [24] Mohammad Meraj Ghanbari et al. “A Sub-mm³ Ultrasonic Free-Floating Implant for Multi-Mote Neural Recording”. In: *IEEE Journal of Solid-State Circuits* 54.11 (2019), pp. 3017–3030.

- [25] Klein Gilhousen et al. “On the capacity of a cellular CDMA system”. In: *IEEE Transactions on vehicular technology* 40.2 (1991).
- [26] Sohmyung Ha et al. “Silicon-integrated high-density electrocortical interfaces”. In: *Proceedings of the IEEE* 105.1 (2017), pp. 11–33.
- [27] Pieter JA Harpe et al. “A 26mW 8 bit 10 MS/s asynchronous SAR ADC for low energy radios”. In: *IEEE Journal of Solid-State Circuits* 46.7 (2011), pp. 1585–1595.
- [28] Leigh R Hochberg et al. “Reach and grasp by people with tetraplegia using a neurally controlled robotic arm”. In: *Nature* 485.7398 (2012), pp. 372–375.
- [29] Allan L Hodgkin and Andrew F Huxley. “Currents carried by sodium and potassium ions through the membrane of the giant axon of Loligo”. In: *The Journal of physiology* 116.4 (1952), p. 449.
- [30] Benjamin C Johnson et al. “An implantable 700 μ W 64-channel neuromodulation IC for simultaneous recording and stimulation with rapid artifact recovery”. In: *2017 Symposium on VLSI Circuits*. IEEE. 2017, pp. C48–C49.
- [31] Vaibhav Karkare, Sarah Gibson, and Dejan Marković. “A 75- μ W, 16-channel neural spike-sorting processor with unsupervised clustering”. In: *IEEE Journal of Solid-State Circuits* 48.9 (2013), pp. 2230–2238.
- [32] Hideyuki Kawanabe et al. “Power and information transmission to implanted medical device using ultrasonic”. In: *Japanese journal of applied physics* 40.5S (2001), p. 3865.
- [33] Adam Khalifa et al. “The microbead: A highly miniaturized wirelessly powered implantable neural stimulating system”. In: *IEEE transactions on biomedical circuits and systems* 12.3 (2018), pp. 521–531.
- [34] Chul Kim et al. “A 1.3 mW 48 MHz 4 channel MIMO baseband receiver with 65 dB harmonic rejection and 48.5 dB spatial signal separation”. In: *IEEE Journal of Solid-State Circuits* 51.4 (2016), pp. 832–844.
- [35] Gordon S Kino. *Acoustic waves: devices, imaging and analog signal processing*. 43 KIN. 1987.
- [36] Lawrence E Kinsler et al. “Fundamentals of acoustics”. In: *Fundamentals of Acoustics, 4th Edition, by Lawrence E. Kinsler, Austin R. Frey, Alan B. Coppens, James V. Sanders, pp. 560. ISBN 0-471-84789-5. Wiley-VCH, December 1999.* (1999), p. 560.
- [37] Richard Krimholtz, David A Leedom, and George L Matthaei. “New equivalent circuits for elementary piezoelectric transducers”. In: *Electronics Letters* 6.13 (1970), pp. 398–399.
- [38] Daniel Laqua, Thomas Just, and Peter Husar. “Measuring the attenuation characteristics of biological tissues enabling for low power in vivo RF transmission”. In: *2010 Annual International Conference of the IEEE Engineering in Medicine and Biology*. IEEE. 2010, pp. 1437–1440.

- [39] Kjeld Laursen et al. “Ultrasonically Powered Compact Implantable Dust for Optogenetics”. In: *Ieee Transactions on Biomedical Circuits and Systems* 14.3 (2020), pp. 583–594.
- [40] W Marshall Leach. “Controlled-source analogous circuits and SPICE models for piezoelectric transducers”. In: *IEEE Transactions on ultrasonics, ferroelectrics, and frequency control* 41.1 (1994), pp. 60–66.
- [41] DONG-HAHK LEE. “Logic Design of Orthogonal Variable Spreading Factor Code Generator”. In: *Journal of Circuits, Systems, and Computers* 14.03 (2005), pp. 507–513.
- [42] Jihun Lee et al. “An Implantable Wireless Network of Distributed Microscale Sensors for Neural Applications”. In: *2019 9th International IEEE/EMBS Conference on Neural Engineering (NER)*. IEEE. 2019, pp. 871–874.
- [43] Jihun Lee et al. “Neural recording and stimulation using wireless networks of microimplants”. In: *Nature Electronics* 4.8 (2021), pp. 604–614.
- [44] Sunwoo Lee et al. “A $250\mu\text{m}\times 57\mu\text{m}$ Microscale Opto-electronically Transduced Electrodes (MOTES) for Neural Recording”. In: *IEEE transactions on biomedical circuits and systems* 12.6 (2018), pp. 1256–1266.
- [45] Chun-Cheng Liu et al. “A 10-bit 50-MS/s SAR ADC with a monotonic capacitor switching procedure”. In: *IEEE Journal of Solid-State Circuits* 45.4 (2010), pp. 731–740.
- [46] Gerald E Loeb et al. “Parylene as a chronically stable, reproducible microelectrode insulator”. In: *IEEE Transactions on Biomedical Engineering* 2 (1977), pp. 121–128.
- [47] Michel M Maharbiz et al. *Implants using ultrasonic backscatter for sensing electrical impedance of tissue*. US Patent App. 16/313,860. 2019.
- [48] *Marketing Clearance of Diagnostic Ultrasound Systems and Transducers*. <https://www.fda.gov/media/71100/download>. Accessed: 06-09-2020.
- [49] Warren P Mason. “Electromechanical transducers and wave filters”. In: (1948).
- [50] Francesco Mazzilli et al. “In-vitro platform to study ultrasound as source for wireless energy transfer and communication for implanted medical devices”. In: *2010 Annual International Conference of the IEEE Engineering in Medicine and Biology*. IEEE. 2010, pp. 3751–3754.
- [51] Miao Meng and Mehdi Kiani. “Gastric Seed: Toward Distributed Ultrasonically Interrogated Millimeter-Sized Implants for Large-Scale Gastric Electrical-Wave Recording”. In: *IEEE Transactions on Circuits and Systems II: Express Briefs* 66.5 (2019), pp. 783–787.
- [52] Miao Meng et al. “An Ultrasonically Powered Wireless System for In Vivo Gastric Slow-Wave Recording”. In: *2019 41st Annual International Conference of the IEEE Engineering in Medicine and Biology Society (EMBC)*. IEEE. 2019, pp. 7064–7067.

- [53] Robert G Meyer. “Low-power monolithic RF peak detector analysis”. In: *IEEE Journal of Solid-State Circuits* 30.1 (1995), pp. 65–67.
- [54] Ali Moin et al. “A wearable biosensing system with in-sensor adaptive machine learning for hand gesture recognition”. In: *Nature Electronics* 4.1 (2021), pp. 54–63.
- [55] Rikky Muller et al. “A minimally invasive 64-channel wireless μ ECoG implant”. In: *IEEE Journal of Solid-State Circuits* 50.1 (2015), pp. 344–359.
- [56] Boris Murmann. “Thermal noise in track-and-hold circuits: Analysis and simulation techniques”. In: *IEEE solid-state circuits magazine* 4.2 (2012), pp. 46–54.
- [57] Elon Musk et al. “An integrated brain-machine interface platform with thousands of channels”. In: *Journal of medical Internet research* 21.10 (2019), e16194.
- [58] DK Nassiri, D Nicholas, and CR Hill. “Attenuation of ultrasound in skeletal muscle”. In: *Ultrasonics* 17.5 (1979), pp. 230–232.
- [59] Craig T Nordhausen, Edwin M Maynard, and Richard A Normann. “Single unit recording capabilities of a 100 microelectrode array”. In: *Brain research* 726.1-2 (1996), pp. 129–140.
- [60] Shaul Ozeri and Doron Shmilovitz. “Simultaneous backward data transmission and power harvesting in an ultrasonic transcutaneous energy transfer link employing acoustically dependent electric impedance modulation”. In: *Ultrasonics* 54.7 (2014), pp. 1929–1937.
- [61] B Arda Ozilgen and Michel M Maharbiz. “Ultrasonic thermal dust: A method to monitor deep tissue temperature profiles”. In: *2017 39th Annual International Conference of the IEEE Engineering in Medicine and Biology Society (EMBC)*. IEEE. 2017, pp. 865–868.
- [62] David K Piech et al. “A wireless millimetre-scale implantable neural stimulator with ultrasonically powered bidirectional communication”. In: *Nature Biomedical Engineering* 4.2 (2020), pp. 207–222.
- [63] F Pothof et al. “Comparison of the in-vivo neural recording quality of floating and skull-fixed silicon probes”. In: *2017 8th International IEEE/EMBS Conference on Neural Engineering (NER)*. IEEE. 2017, pp. 158–161.
- [64] Rozhan Rabbani et al. “Towards an Implantable Fluorescence Image Sensor for Real-Time Monitoring of Immune Response in Cancer Therapy”. In: *2021 43rd Annual International Conference of the IEEE Engineering in Medicine & Biology Society (EMBC)*. IEEE. 2021, pp. 7399–7403.
- [65] Jaime Ramirez-Angulo et al. “A free but efficient low-voltage class-AB two-stage operational amplifier”. In: *IEEE Transactions on Circuits and Systems II: Express Briefs* 53.7 (2006), pp. 568–571.
- [66] M Redwood. “Transient performance of a piezoelectric transducer”. In: *The journal of the acoustical society of America* 33.4 (1961), pp. 527–536.

- [67] Paolo M Rossini et al. “Double nerve intraneural interface implant on a human amputee for robotic hand control”. In: *Clinical neurophysiology* 121.5 (2010), pp. 777–783.
- [68] HARRISON E Rowe. “Amplitude modulation with a noise carrier”. In: *Proceedings of the IEEE* 52.4 (1964), pp. 389–395.
- [69] Kunal Sahasrabuddhe et al. “The Argo: a high channel count recording system for neural recording in vivo”. In: *Journal of neural engineering* 18.1 (2021), p. 015002.
- [70] Dongjin Seo et al. “Wireless recording in the peripheral nervous system with ultrasonic neural dust”. In: *Neuron* 91.3 (2016), pp. 529–539.
- [71] Chen Shi et al. “A 0.065-mm³ Monolithically-integrated Ultrasonic Wireless Sensing Mote for Real-time Physiological Temperature Monitoring”. In: *IEEE Transactions on Biomedical Circuits and Systems* (2020).
- [72] Amanda Singer et al. “Magnetolectric materials for miniature, wireless neural stimulation at therapeutic frequencies”. In: *Neuron* 107.4 (2020), pp. 631–643.
- [73] Tara L Skarpaas, Beata Jarosiewicz, and Martha J Morrell. “Brain-responsive neurostimulation for epilepsy (RNS® System)”. In: *Epilepsy research* 153 (2019), pp. 68–70.
- [74] Seung Hyun Song, Albert Kim, and Babak Ziaie. “Omnidirectional ultrasonic powering for millimeter-scale implantable devices”. In: *IEEE Transactions on Biomedical Engineering* 62.11 (2015), pp. 2717–2723.
- [75] Soner Sonmezoglu and Michel M Maharbiz. “34.4 A 4.5 mm³ Deep-Tissue Ultrasonic Implantable Luminescence Oxygen Sensor”. In: *2020 IEEE International Solid-State Circuits Conference-(ISSCC)*. IEEE. 2020, pp. 454–456.
- [76] Nicholas A Steinmetz et al. “Neuropixels 2.0: A miniaturized high-density probe for stable, long-term brain recordings”. In: *Science* 372.6539 (2021), eabf4588.
- [77] Don Torrieri. *Principles of spread-spectrum communication systems*. Vol. 1. Springer, 2005.
- [78] Pin-Chien Tsai, Hesam Sadeghi Gougheri, and Mehdi Kiani. “Skull impact on the ultrasound beam profile of transcranial focused ultrasound stimulation”. In: *2019 41st Annual International Conference of the IEEE Engineering in Medicine and Biology Society (EMBC)*. IEEE. 2019, pp. 5188–5191.
- [79] Philip P Vu et al. “A regenerative peripheral nerve interface allows real-time control of an artificial hand in upper limb amputees”. In: *Science translational medicine* 12.533 (2020), eaay2857.
- [80] Max L Wang et al. “Closed-loop ultrasonic power and communication with multiple miniaturized active implantable medical devices”. In: *2017 IEEE International Ultrasonics Symposium (IUS)*. IEEE. 2017, pp. 1–4.

- [81] Marcus J Weber et al. “A miniaturized single-transducer implantable pressure sensor with time-multiplexed ultrasonic data and power links”. In: *IEEE Journal of Solid-State Circuits* 53.4 (2018), pp. 1089–1101.
- [82] Suzanne Wendelken et al. “Restoration of motor control and proprioceptive and cutaneous sensation in humans with prior upper-limb amputation via multiple Utah Slanted Electrode Arrays (USEAs) implanted in residual peripheral arm nerves”. In: *Journal of neuroengineering and rehabilitation* 14.1 (2017), p. 121.
- [83] Pyungwoo Yeon, Muhannad S Bakir, and Maysam Ghovanloo. “Towards a 1.1 mm² free-floating wireless implantable neural recording SoC”. In: *2018 IEEE Custom Integrated Circuits Conference (CICC)*. IEEE. 2018, pp. 1–4.
- [84] Zhanghao Yu et al. “MagNI: a magnetoelectrically powered and controlled wireless neurostimulating implant”. In: *IEEE transactions on biomedical circuits and systems* 14.6 (2020), pp. 1241–1252.
- [85] Ping Zhou et al. “Decoding a new neural–machine interface for control of artificial limbs”. In: *Journal of neurophysiology* 98.5 (2007), pp. 2974–2982.
- [86] Tao Zhou et al. “Syringe-injectable mesh electronics integrate seamlessly with minimal chronic immune response in the brain”. In: *Proceedings of the National Academy of Sciences* 114.23 (2017), pp. 5894–5899.

Glossary

- AC** Alternate Current. 48, 69, 70, 78, 113
- ADC** Analog-to-Digital Converter. ix, xi, 61, 90, 95, 97–99, 104, 110, 115, 118, 127, 129
- AFE** Analog Front-End. xi, 64, 66, 108, 115, 127, 129
- AM** Amplitude Modulation. vi, vii, 8, 10, 40, 41, 59–61, 69, 71, 75, 78
- AR** Aspect Ratio. v, vi, 24–31, 45, 51, 52
- ASK** Amplitude Shift Keying. iii, vi, xii, 1, 8, 10, 38, 42, 52, 53, 86–132
- BER** Bit Error Rate. viii, ix, 10, 40, 53, 79, 80, 83, 84, 95–97, 118, 120
- CAD** Computer Aided Design. 35, 45
- CDM** Code Division Multiplexing. 58, 61, 81–83
- CDMA** Code-Division Multiple-Access. ii, iii, vi, viii, 1, 9, 10, 38–40, 58, 59, 79–85, 132
- CMOS** Complementary Metal Oxide Semiconductor. 4, 69, 89, 113
- CNS** Central Nervous System. 3
- DC** Direct Current. 62, 69, 78, 90, 108, 113
- DM** Digital Modulation. 40, 41
- DNL** Differential Non Linearity. xi, 117, 129
- DUT** Device Under Test. 115
- ECoG** Electrocorticography. 2
- EEG** Electroencephalography. 2
- EMG** Electromyography. 86, 135

- ENIG** Electroless Nickel Immersion Gold. vii, 69, 71
- FDMA** Frequency-Division Multiple-Access. vi, 5, 38, 39
- FEM** Finite Element Method. v, vi, 12, 18, 21, 24, 25, 35, 43–45, 47, 51, 53, 54, 62
- FET** Field Effect Transistor. 35, 108
- FIFO** First-in First-out. 95, 127
- fMRI** functional Magnetic Resonance Imaging. 2
- FPGA** Field Programmable Gate Array. 81, 115
- FSM** Finite State Machine. x, 116, 118
- IC** Integrated Circuit. vii, viii, 1, 25, 27, 28, 31, 34, 35, 43, 59, 60, 62–64, 69, 70, 78, 89–91, 109, 113, 127, 131
- INL** Integral Non Linearity. xi, 129
- ISI** Inter-Symbol Interference. viii, 79, 80, 83
- LDO** Low Drop-Out Regulator. ix, 63, 89, 91, 93, 103–108
- LE** Longitudinal Expander. v, vi, 12, 17, 18, 24–26, 32, 45, 46, 51
- LED** Light Emitting Diode. 6
- LFSR** Linear Feedback Shift Register. x, 95, 118, 119, 122–125
- LNA** Low-Noise Amplifier. vii, 64–67, 103, 127
- LO** Local Oscillator. 90, 111
- LoS** Line of Sight. 74
- LPF** Low Pass Filter. 102, 103
- LSB** Least Significant Bit. 116, 117, 127
- LVDS** Low-Voltage Differential Signaling. 115
- MEA** Microelectrode Array. 3
- MI** Modulation Index. 54, 55
- ML** Machine Learning. 80, 81, 83, 84

- MMSE** Minimum Mean Squared Error. 83, 84
- MSB** Most Significant Bit. 98
- NEF** Noise Efficiency Factor. 77
- NN** Neural Network. 80
- OOK** On-Off Keying. vi–ix, 8, 10, 35, 38, 41, 42, 52, 53, 60, 61, 80, 81, 83, 88, 89, 96, 115, 131, 132
- OTA** Operational Transconductance Amplifier. vii, 66, 108, 109, 113
- PBS** Phosphate-Buffered Saline. 69
- PCB** Printed Circuit Board. 69, 113
- PMU** Power Management Unit. 34
- PNS** Peripheral Nervous System. 1, 3, 6
- POR** Power-on Reset. ix, 63, 64, 90, 91, 103, 104, 109
- PSK** Phase Shift Keying. 88
- PSR** Power Supply Rejection. 107
- PTAT** Proportional to Absolute Temperature. ix, 63, 78, 89, 91, 103, 104, 111, 115
- PUF** Physical Unclonable Function. 91
- PVT** Process, Supply Voltage and Temperature. 110
- PZT** Lead Zirconate Titanate. 24, 26, 29, 60
- RF** Radio Frequency. 5, 6, 38, 69
- SAR** Successive Approximation Register. ix, 90, 97, 98, 104, 110, 127
- SFDR** Spurious-Free Dynamic Range. viii, 70, 75, 77, 127
- SNDR** Signal-to-Noise-and-Distortion Ratio. viii, 75, 77
- SNR** Signal-to-noise Ratio. vii, viii, 2, 41, 53, 72, 75, 83, 84, 88, 89
- SPICE** Simulation Program with Integrated Circuit Emphasis. 8, 15, 36, 45, 56
- TDMA** Time-Division Multiple-Access. iii, vi, x, 1, 5, 10, 38, 40, 86–130, 132

TE Thickness Extensional. iv, 12, 15–18, 32, 45, 46

THD Total Harmonic Distortion. 70

TIME Transverse Intrafascicular Multichannel Electrode. viii, 87

TMR Targeted Muscle Reinnervation. 86

ToF Time of Flight. 36, 41, 43, 63, 79, 82, 93

WE Width Expander. v, vi, 24, 25, 51

WPT Wireless Power Transmission. 3–5, 7